

Design and Optimization of Gearless Drives using Multi-Physics Approach

Andersen, Søren Bøgh; Santos, Ilmar

Publication date:
2012

Document Version
Publisher's PDF, also known as Version of record

[Link back to DTU Orbit](#)

Citation (APA):
Andersen, S. B., & Santos, I. (2012). Design and Optimization of Gearless Drives using Multi-Physics Approach. Kgs. Lyngby: Technical University of Denmark (DTU).

DTU Library

Technical Information Center of Denmark

General rights

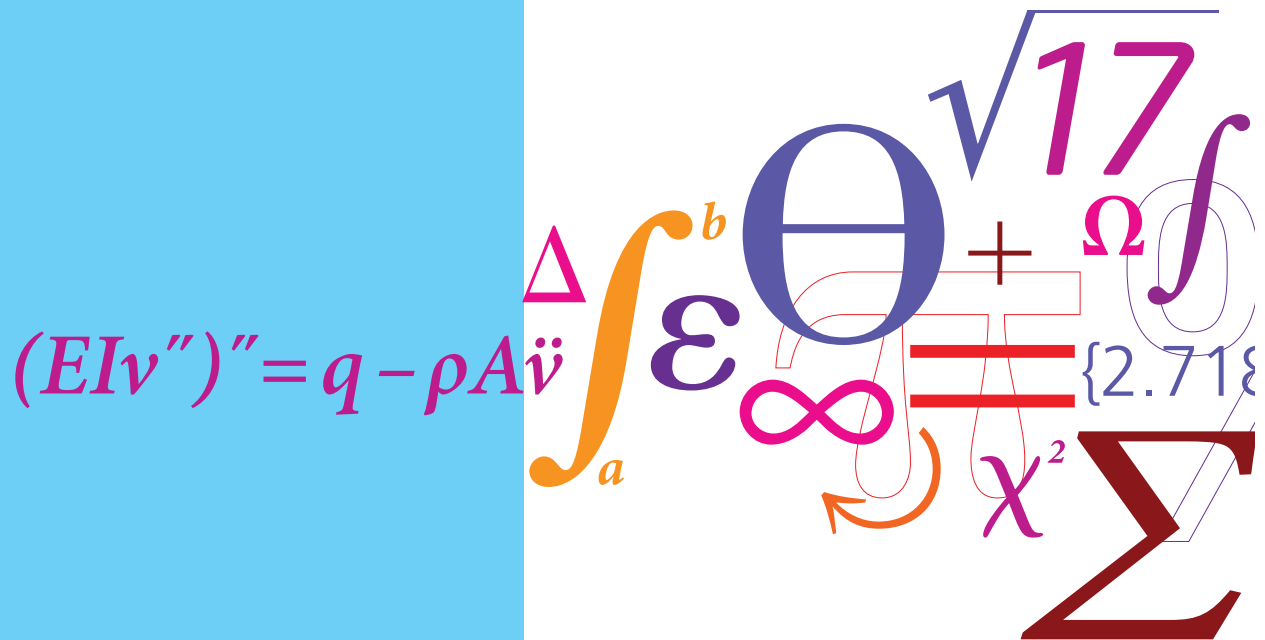
Copyright and moral rights for the publications made accessible in the public portal are retained by the authors and/or other copyright owners and it is a condition of accessing publications that users recognise and abide by the legal requirements associated with these rights.

- Users may download and print one copy of any publication from the public portal for the purpose of private study or research.
- You may not further distribute the material or use it for any profit-making activity or commercial gain
- You may freely distribute the URL identifying the publication in the public portal

If you believe that this document breaches copyright please contact us providing details, and we will remove access to the work immediately and investigate your claim.

Design and Optimization of Gearless Drives using Multi-Physics Approach

PhD Thesis



Søren Bøgh Andersen
 DCAMM Special Report No. S147
 September 2012

Design and Optimization of Gearless Drives using Multi-Physics Approach

by

Søren Bøgh Andersen

DEPT. OF MECHANICAL ENGINEERING
Solid Mechanics



TECHNICAL UNIVERSITY OF DENMARK

Title of the thesis:

Design and Optimization of Gearless Drives using Multi-Physics Approach

Ph.D. student:

Søren Bøgh Andersen

E-mail: sban@mek.dtu.dk

Supervisor:

Prof. Ilmar F. Santos

E-mail: ifs@mek.dtu.dk

Address:

Department of Mechanical Engineering, Solid Mechanics

Technical University of Denmark

Nils Koppels Allé, Building 404, 2800 Kgs. Lyngby, Denmark

Copyright © 2012 Søren Bøgh Andersen

DCAMM Special Report no.: S147

ISBN: 978-87-90416-95-9

Preface

This thesis is submitted in partial fulfillment of the requirements for obtaining the degree of Ph.D. in mechanical engineering at the Technical University of Denmark (DTU). The Ph.D. project was funded partially by the Danish Agency for Science, Technology and Innovation, Technical University of Denmark Department of Solid Mechanics and ABB Switzerland Ltd. Minerals & Printing which initiated the project as they had just formed a new R&D department and wanted a multi-physics tool for modeling their drives. The project was mainly carried out at the Technical University of Denmark, Department of Solid Mechanics, in the period 1st of October 2009 to 28th of September 2012.

I would like to send many thanks to my supervisor Prof. Ilmar F. Santos from Department of Mechanical Engineering at DTU for setting time aside for discussion of any potential issues regarding the work and for his constructive criticism and guidance.

Once a year doing the Ph.D. study, I have worked for a period of 2-3 month at ABB Research Center, Dättwil Switzerland as part of the agreement with ABB Switzerland Ltd. and would like in connection with this to thank all for their warm welcome and helpful nature. Specifically I would like to thank the following persons at ABB for providing data for verification of the work performed in this thesis and for their time to discuss any potential questions. Special thanks to Head of product management Dr.-Ing. Axel Fuerst, Dr.-Ing. Iossif Grinbaum, Daniel Hartermann, Christian Horstmann, David Casado, Daniel Bermudez, Dr.-Ing. Macarena Montenegro and all others who have been helpful during my work.

Kgs. Lyngby, 28th of September 2012.

Søren Bøgh Andersen



Resumé (in Danish)

Mange forskellige tekniske områder skal medtages i en designproces af store gearløse drev til mineindustrien for at kunne beskrive drevs elektrisk-mekanisk-termiske opførsel korrekt. Indtil videre behandles disse forskellige tekniske områder mere eller mindre separat, og ingen beskrivelser eller citationer er fundet vedrørende modellering af disse store drev ved brug af koblede multi-fysiske modeller, hvilket giver mulighed for en samlet optimering af den slags maskineri. Målet har derfor været at skabe pålidelige og sammenhængende tværfaglige matematiske modeller baseret på en multi-fysisk tilgang. Afhandlingens originalitet findes i den fuldstændige sammenkoblede model af et gearløst drev. Yderligere er anvendelsen af "Evolution Strategies" i optimering af et gearløst drev også en nyhed. Den foreslåede matematiske multi-fysiske model inkorporerer de fysiske hovedområder som et gearløst drev består af. Disse tekniske områder er elektromagnetisme, strukturdynamik, varme- og massetransport, hvilket er tæt sammenkædet med hinanden, da resultater fra et område har indvirkning på et andet og omvendt. Denne model er derefter blevet anvendt i en meta-heuristisk optimering ved hjælp af "Evolution Strategies". Den elektromagnetiske, termiske og strukturelle opførelser er blevet modeleret med Finite Element Metode i både 2D og 3D. Massetransporten er blevet beskrevet ved hjælp af en diskret model og løst ved hjælp af Newton-Raphsons Metod. En af de store udfordringer har været at få simplificeret de forskellige undermodeller for at minimere beregningstiden uden at miste præcisionen på de endelige resultater. Dette har muliggjort at modellerne kan anvendes i en iterativ optimeringsproces. Det er vist at den foreslåede multi-fysiske model fører til andre resultater end de hidtidigt anvendte afkoblede modeller, da disse anvender konstante værdier fra de andre fysiske områder selv om disse værdier er afhængige af hinanden. Den multi-fysiske model fører derfor til en mere præcis bestemmelse af de forskellige parametre. Afhandlingen giver et klart overblik over de koblede modellers nødvendighed og afgørende parametre. Det største bidrag til modellering af gearløse mølle drev, skal findes i den fulde integration af de forskellige tekniske områder, der muliggør en mere nøjagtig bestemmelse af de forskellige værdier, der karakteriserer mølledrevet. Dette muliggør samtidig en samlet optimering som ellers ikke ville have været mulig. Denne optimering er i dette tilfælde minimering af massen og tabene i drevet som i sidste ende vil være en minimering af købs- og driftsomkostningerne. Optimeringen resulterede i en massereduktion på 4,0% og en formindskelse af tabene på 9,9% i forhold til det oprindelige drev. Afhandlingen åbner også nye forskningsfronter og fremhæver tre nye nødvendige forskningsaspekter for videre udvikling af designprocesser af store gearløse drev baseret på multi-fysik: a) eksperimentelle test på det fysiske mølledrev til verifikation og tilretning af de præsenterede modeller er af afgørende betydning, da modellerne kun er blevet sammenlignet med andre matematiske modeller; b) simulering af den termiske del i 3D for at undersøge effekten af den aksiale varmefluks;

c) undersøgelse af effekten af ende-vindingerne og køle-luft-kanalerne i rammen med en detaljeret 3D CFD model.

Abstract

Many different technical areas are involved in the design process of large gearless drives for the mining industry, aiming at correctly describing the electrical-mechanical-thermal behavior of the drive. So far, these various technical areas are being treated more or less separately, and no descriptions or references are found concerning the modeling of these large drives using coupled multi-physics models, which allow an overall optimization of this kind of machinery. In this framework, the goal of this thesis is to create reliable and coherent interdisciplinary mathematical models based on a multi-physics approach. The originality of the thesis is to be found in the full interlinked model of a gearless drive. The use of "Evolution Strategies" in the optimization is also an original contribution to the field of gearless drive design. The proposed mathematical multi-physics model incorporates the key technical areas of a gearless drive. These technical areas are electromagnetism, structural dynamics, heat and mass transfer. Such technical areas are closely linked to each other, with results from one area affecting the others and vice-versa. The multi-physics model of the drive is connected to a meta-heuristic optimization procedure based on "Evolution Strategies". The electromagnetic, thermal and structural behaviors have been modeled using the Finite Element Method in 2D and 3D. The mass transport has been described by means of a discrete model and solved using the Newton-Raphson method. One of the major challenges has been to simplify the different sub-models to minimize calculation time without losing accuracy of the final results. This has allowed the models to be utilized in an iterative optimization process. It is shown that the proposed multi-physics model leads to different results than the decoupled models previously used, as the decoupled models use constant values from the several technical areas even though these values are interdependent. The multi-physics model therefore leads to a more precise determination of the design parameters. The thesis gives a clear overview of the necessity of the coupled models and highlights the vital design parameters. As already mentioned, the main contribution to the modeling of gearless mill drives is to be found in the full integration of the various technical areas, enabling a more accurate determination of the different physical parameters that characterize mill drive behavior. This enables an overall optimization that would not have been possible by other means. In this work, the optimization is based on the minimization of the mass of the drive components and losses in the drive, leading to a minimization of purchase and operating costs. The optimization resulted in a mass reduction of 4.0% and a decrease of losses of 9.9% compared to the original drive design. The thesis also opens new research fronts and highlights three new necessary research aspects for further development of the design processes of large gearless drives based on a multi-physics approach: a) experimental tests on the physical mill drives for verification and adjustment of the presented models are crucial, since the multi-physics models have only been compared with other mathematical models; b) 3D

simulation of the thermal part in order to investigate the effect of the axial heat flux; and finally c) investigation of the effect of the end-windings and the cooling-air channels in a frame with a detailed 3D CFD model.

Publications

The following publications are part of the thesis

- [P1] S. B. Andersen and I. F. Santos, Evolution strategies and multi-objective optimization of permanent magnet motor, *Applied Soft Computing*, 2012, **vol. 12** pp. 778-792
- [P2] S. B. Andersen, I. F. Santos, and A. Fuerst, Investigation of model simplification and its influence on the accuracy in FEM magnetic calculations of gearless drives, *IEEE Transactions on Magnetics*, July 2012, **vol. 48**, No. 7, pp. 2166-2177
- [P3] S. B. Andersen, S. Enemark and I. F. Santos, Dynamics and Stability of Rigid Rotors Levitated by Passive Cylinder-Magnet Bearings and Driven/Supported Axially by Punctual Contact Clutch, *Submitted to Journal of Sound and Vibration (ref. JSV-D-12-01433)*
- [P4] S. B. Andersen, I. F. Santos, and A. Fuerst, Multi-physics Modelling of Large Ring Motor for Mining Industry - Combining Electromagnetism, Fluid mechanics, Mass and Heat Transfer in Engineering Design, *Submitted to Journal of Applied Mathematical Modelling (ref. AMM13853)*

Contents

Preface	i
Publications	vi
Contents	vii
Nomenclature	xiii
1 Introduction	1
1.1 State of the art	1
1.2 Goals and main originality of this work	2
1.3 Structure of this work	4
2 Gearless mill drives	6
2.1 Mill drum	8
2.2 Rotor pole	8
2.3 Frame	9
2.4 Stator	11
2.5 Fan and cooling system	11
3 Electromagnetic forces, torque and losses in gearless drives - Electromagnetic model	13
3.1 Basic equation	14
3.2 Rotor and stator windings	18
3.3 Full and reduced finite element motor model	19
3.4 Estimation of force and torque	22
3.4.1 Zero torque phase angle	22
3.4.2 Torque & magnetic pull	23
3.4.3 Verification of force & torque model	24
3.5 Core and coil resistive losses	25
3.5.1 Eddy current & hysteresis losses	26
3.5.2 Determination of hysteresis & eddy current loss coefficients	29
3.5.3 Copper resistive losses	29
3.5.4 Verification of loss models	30
4 Estimation of cooling flows in gearless drives - Flow model	33
4.1 Energy equation - Bernoulli's equation	33
4.2 Head losses	34

4.2.1	Minor losses	34
4.2.2	Major losses	35
4.3	Reynolds number	35
4.4	Friction factor	36
4.4.1	Laminar flow	36
4.4.2	Turbulent flow	36
4.4.3	Moody's diagram	36
4.5	Volume flow	36
4.6	Non-circular channels and hydraulic diameter	37
4.7	Cooling channel geometry model	38
4.8	Mathematical model	40
4.9	Fan/cooler losses	41
4.10	Verification of flow model	42
5	Determination of heat distribution in gearless mill drives - Thermal model	44
5.1	Finite difference thermal calculations	45
5.2	Forced convection	48
5.3	Heat transfer in the solid parts	50
5.4	Losses in the solid parts	52
5.5	Dependency of fluid characteristics on temperatures and altitude changes	53
5.6	System parameters	55
5.7	Heat expansion	55
5.8	Verification of thermal models	56
5.9	Effects of neglecting the axial heat flux	60
6	Structural investigations of gearless drives - Structural model	62
6.1	Hexahedron 20 nodes isoparametric	62
6.1.1	Element stiffness matrix	63
6.1.2	Shape functions	64
6.1.3	Derivative of shape functions with respect to ξ	65
6.1.4	Derivative of shape functions with respect to η	66
6.1.5	Derivative of shape functions with respect to ζ	67
6.1.6	Jacobian matrix	68
6.1.7	Strain-displacement relationship	68
6.1.8	Constitutive matrix	69
6.1.9	The principal stresses in three dimensions	70
6.1.10	Von Mises stress	71
6.1.11	Surface traction	71
6.1.12	Volume forces	72
6.2	Performance of hexahedron 8 nodes and 20 nodes elements	72
6.3	External programs	75
6.4	Stator & frame	76
6.4.1	Frame model	76

6.4.2	Frame stiffener model	77
6.4.3	Stator model	80
6.5	Mill drum, rotor poles & bearings	80
6.5.1	Mill drum model	81
6.5.2	Rotor pole model	82
6.5.3	Bearings	83
6.6	Stator/rotor/frame forces and torque	83
6.7	Static deflection	84
6.8	Static stress	87
6.9	Rotor/stator air gap	87
6.10	Natural frequencies & mode shapes	90
6.11	On damping sources in mill drives	93
6.12	Simulating in time	93
6.12.1	Equation of Motion	94
6.12.2	Pseudo modal reduction	94
6.13	Verification of structural model	95
7	Metaheuristic optimization of multi-physics model of a gearless drive	100
7.1	A short introduction to metaheuristics	100
7.2	General algorithm of evolution strategies	100
7.2.1	Marriage	102
7.2.2	Recombination	102
7.2.3	Mutation	104
7.2.4	Repair	105
7.2.5	Selection	105
7.3	Parameter tuning	105
7.4	Multi-objective optimization and PISA	106
7.4.1	PISA Structure	106
7.5	Optimization of multi-physic model of a gearless drive	109
7.5.1	Object Parameter	109
7.5.2	Determination of fitness value	109
7.5.3	Natural frequency penalty function	111
7.5.4	Stator & rotor currents	112
7.6	Minimization of mass usage in gearless drive construction - single objective optimization	112
7.7	Minimization of mass usage and losses in gearless drive construction	114
7.8	Comparison of original and optimized gearless drive	116
8	Conclusion & future aspects	124
8.1	Conclusions and general comments	124
8.2	Future aspects	126
	References	128

A	Appendix	137
A.1	Data	137
A.2	Verification of Fortran code for FD thermal model	138

Nomenclature

i	Index $i \in [x, y, z]$ axis of rotation, [-]	μ_d	Dynamic viscosity, [(N·s)/m ²]
\sim	Mutated parameter, [-]	μ_p	Permeability, [H/m]
α	Thermal diffusivity, [m ² /s]	μ_s	Dynamic viscosity at the heat transfer boundary surface temperature, [(N·s)/m ²]
α_u	Slot angle, [Rad]	μ_0	Permeability of free space, [H/m]
α_z	Phasor angle, [Rad]	∇	Del operator, [-]
α_k	Kinetic energy coefficient, [-]	ν	Kinematic viscosity, [m ² /s]
α_L	Thermal linear expansion coefficient [1/°C]	Ω	Rotational speed, [Hz]
α_{ref}	Temperature coefficient of resistivity, [1/°C]	ω	Frequency, [Hz]
\bar{V}	Mean velocity, [m/s]	ρ	Number of individuals for reproduction, [-]
β	angle between object vectors, [-]	ρ_d	Density, [kg/m ³]
ΔL	Change in length [m]	ρ_{air}	Density of dry air at altitude h_{alt} , [kg/m ³]
ΔT	Change in temperature [°C]	ρ_{ele}	Element density, [kg/m ³]
δ	Kronecker's delta, [-]	ρ_{ref}	Electrical resistivity, [$\Omega \cdot m$]
ϵ_0	Permittivity of free space, [F/m]	σ	Standard deviation, [-]
λ	Number of offspring individuals, [-]	τ	Learning factor, [-]
A	Magnetic vector potential, [Wb/m]	τ_0	Learning factor, [-]
B	Magnetic flux density, [T]	a	Individual parameter vector, [-]
F	Electromagnetic force, [N]	F	Fitness value vector, [-]
f	Lorentz force, [N]	r	Recombinant, [-]
H	Magnetic field strength, [A/m]	s	Strategy parameter vector, [-]
S	Maxwell stress tensor, [N/m ²]	y	Object parameter vector, [-]
S_i	Maxwell stress tensor component, [N/m ²]	g	Generation number, [-]
T	Torque tensor, [Nm]	\vec{n}	Unit vector normal to the surface, [-]
t	Torque, [Nm]	\vec{r}	Vector from origin of torque to current position, [m]
\mathcal{N}	Random number from the standard normal distribution, [-]	$\vec{i}, \vec{j}, \vec{k}$	Unit vectors, [-]
\mathcal{E}_i	Marriage population, [-]	*	Base winding, [-]
\mathfrak{F}	Function, [-]	A	Area, [m ²]
\mathfrak{P}_o	Offspring population, [-]	A_r	Copper cross section area of parallel strands (rotor), [m ²]
\mathfrak{P}_p	Parent population, [-]	A_s	Copper cross section area of parallel strands (stator), [m ²]
μ	Number of parent individuals, [-]	$A_{Coil,r}$	Cross-section area of the coil packs in one rotor pole [m ²]
μ_0	Reference viscosity at reference temperature T_0 , [(N·s)/m ²]	$A_{Coil,s}$	Cross-section area of one coil pack in the stator [m ²]
		$A_{Cu,r}$	Cross-section area of the copper part of one rotor pole [m ²]

$A_{Cu,s}$	Cross-section area of the copper part of one stator coil pack [m ²]	h_l	Major loss, [Nm/kg]
$A_{Fe,r}$	Cross-section area of the iron part of one rotor pole [m ²]	i	Iteration number, [-]
$A_{Fe,s}$	Cross-section area of the iron part of the stator [m ²]	I_{exc}	Excitation current (DC), [A]
A_{wire}	Cross section area of wire, [m ²]	I_{ph}	Phase current (peak), [A]
B	B-field, [T]	J	Electric current density, [A/m ²]
B_i	Magnetic flux density component, [T]	K	Loss coefficient, [-]
C	Sutherland's constant, [-]	k_f	Fluid thermal conductivity, [W/(m·K)]
c	Proportionality factor, [-]	k_{Cu}	Thermal conductivity of copper, [W/(m·K)]
C_e	Eddy current loss coefficient, [W/(kg·T ² ·Hz)]	$k_{eq,rx}$	Equivalent thermal conductivity in x-dir. of rotor coil pack [W/(m·K)]
C_h	Hysteresis loss coefficient, [W/(kg·T ² ·Hz)]	$k_{eq,ry}$	Equivalent thermal conductivity in y-dir. of rotor coil pack [W/(m·K)]
C_p	Specific heat capacity of air at constant pressure, [J/(kg·K)]	$k_{eq,sx}$	Equivalent thermal conductivity in x-dir. of stator coil pack [W/(m·K)]
C_{Cu}	Specific heat capacity of copper [J/(kg·K)]	$k_{eq,sy}$	Equivalent thermal conductivity in y-dir. of stator coil pack [W/(m·K)]
C_{Fe}	Specific heat capacity of carbon steel [J/(kg·K)]	k_{ins}	Thermal conductivity of insulation [W/(m·K)]
C_{ins}	Specific heat capacity of insulation [J/(kg·K)] (glass fiber 66% glass, 33% epoxy)	K_{SC}	Loss coefficient, sudden contraction, [-]
C_{M400}	Thermal conductivity of M400-50A steel [W/(m·K)]	K_{SE}	Loss coefficient, sudden expansion, [-]
$C_{s,ele}$	Element stacking factor, [-]	L	Length, [m]
D	Diameter, [m]	L_e	Equivalent length, [m]
d	Diameter, [m]	$L_{active,r}$	Active coil length (rotor), [m]
E	Electric field strength, [V/m]	$L_{active,s}$	Active coil length (stator), [m]
e	Roughness, [m]	L_{con}	Connection of coil bars at the ends, [m]
ele	Element number, [-]	L_{Cu}	Length of copper [m]
F	Residuals, [-]	$L_{end,r}$	End windings (rotor), [m]
f	Friction coefficient, [-]	$L_{end,s}$	End windings (stator), [m]
F_i	Electromagnetic force component, [N]	L_{ins}	Length of insulation [m]
F_i	Individual i's fitness value, [-]	L_{jump}	Jump of coil bars between slots, [m]
g	Gravitational acceleration, [m/s ²]	L_{motor}	Axial length of the motor [m]
h	Heat transfer coefficient, [W/(m ² ·K)]	L_{twist}	Twist of copper strand in active length, [m]
h_{alt}	Altitude, [m]	L_{wire}	Wire length, [m]
h_{lm}	Minor loss, [Nm/kg]	$Loss_{Cu,s}$	Copper loss in stator, [W]
h_{lT}	Total energy loss, [Nm/kg]	M	Molar mass of dry air, [kg/mol]
		m	Harmonic number, [-]
		m_p	Number of phases, [-]

n	Number of elements, [-]	Re	Reynolds number, [-]
n_d	Fractional slot winding divider, [-]	s_i	Individual i's strategy parameters, [-]
n_{poles}	Number of poles [-]	t	Layers in the voltage phasor diagram, [-]
Nu	Nusselt number, [-]	T_0	Sea level standard temperature, [K]
P	Wetted perimeter, [m]	T_s	Heat transfer boundary surface temperature, [°C]
p	Pressure, [Pa]	T_{air}	Absolute temperature of air, [K]
p_0	Sea level standard atmospheric pressure, [Pa]	T_{ini}	Initial temperature after the cooler [°C]
p_p	Number of pole pair, [-]	T_{lap}	Temperature lapse rate, [K/m]
p_{alt}	Pressure at altitude, [Pa]	T_{wire}	Wire temperature, [°C]
$P_{Fe,total}$	Total iron losses, [W]	V	Volume, [m ³]
Pr	Prandtl number, [-]	$V_{Cu,r}$	Volume of rotor copper [m ³]
Q	Volume flow, [m ³ /s]	$V_{Cu,s}$	Volume of stator copper [m ³]
q	Correction parameter, [-]	V_{ele}	Element volume, [m ³]
Q_s	Number of slots, [-]	$V_{Fe,r}$	Volume of rotor iron [m ³]
q_s	Slots per pole and phase, [-]	$V_{Fe,s}$	Volume of stator iron [m ³]
R	Universal gas constant, [J/(mol·K)]	x	Function variables, [-]
r_i	i component of vector from origin of torque to current position, [-]	y_i	Individual i's object parameters, [-]
R_{ref}	Reference resistance, [Ω]	z	Vertical distance, [m]
$R_{wire,r}$	Wire resistance (rotor), [Ω]		
$R_{wire,s}$	Wire resistance (stator), [Ω]		
R_{wire}	Wire resistance, [Ω]		

Chapter 1

Introduction

1.1 State of the art

All electric motors generate heat due to losses in windings and iron core which, if not predicted correct, could have fatal consequences for the operation of the device. This is increasingly important for large and very expensive motors like gearless mill drives in mineral mining mills, Nieto and Ahrens (2007), Boughey et al. (2000), Hamdani (2000), which is also very costly in downtimes and therefore require high reliability. It is of common practice in thermal modeling of motors to use the lumped thermal method, Nerg et al. (2008), Galea et al. (2012), Mellor et al. (1991), Staton et al. (2003), Bracikowski et al. (2012), however, if higher level of details is desired one needs to move to more refined methods like finite difference Drubel and Runge (2004), Baehr and Stephan (2011) and/or finite element method Li et al. (2012), Galea et al. (2012), Srinivas and Arumugam (2001), Mezani et al. (2001). These types of methods can give a highly accurate and clear view of the temperature distribution within the motor, if the convection coefficient has been determined with a high accuracy which is one of the major hurdles in heat transfer simulations. This convection coefficient is highly dependent on the fluid properties, channel geometry and the channel flow rate and can only be determined through experiments. Several empirical equations, Incropera et al. (2006), Kreith (2000), Stephan et al. (2010) have, however, been formulated which are especially optimized for different channel geometries and parameter ranges. Before the convection coefficient can be determined, knowledge of the flow is needed. If high level of detail is desired, numerical CFD can be used for predicting the flow as in Jungreuthmayer et al. (2011), however, these 3D simulations are very computationally expensive and less suited for iterative optimization. Another and fast way of determine the flow is as described in Fox et al. (2004) by the use of Bernoulli's energy equation where the pressure losses from the different channel segments can be summed up. These losses are split into what is called major and minor losses, where the major losses are head losses in straight channel with constant cross section and minor losses are head losses due to inlet/outlet condition, fittings, valves, bends and other devices which create a resistance in the fluid flow. These head losses can again only be determined through experiments, but as before some empirical equations and constants for common components can be found in the literature, Stephan et al. (2010), White (1998). The electromagnetic losses in the motor are what is generating the heat and consist of two main types of losses. The core losses which are generated by eddy current and hysteresis in the iron parts as the magnetic field oscillates and the resistance losses as current flow through the coils. The core losses can be determined through a series of static finite element simulations as described in Meeker (2009), Dlala (2009), Bertotti (1988), Chen and Pillay (2002), Zhao et al. (2011) and the resistance losses can be found when the resistance and

the current are known, Bouheraoua et al. (2012). The electromagnetic forces and heat expansions can then be applied to a structural model where it is customary to model the structural part of a gearless mill drive by the use of the finite element method as in EAnD (2000), EAnD (1999), Meimaris and Boughey (2001), Dreher et al. (2004). This can be accomplished by the use of many different mesh element types or combination of these which can be more or less suited for modeling the different cases. According to Benzley et al. (1995) it is shown that an all hexahedron finite element mesh is superior to an all tetrahedral finite element mesh for stress, deformation and natural frequency estimation. Based on this investigation it is preferable to keep the structural mesh of the mill drive in an all hexahedron mesh. Many different types of optimization algorithms can be used in the optimization of a gearless mill drive, where one of them is with the use of metaheuristic optimization. One of these metaheuristic algorithms is called Evolution Strategies and has proven to give good results in a previous optimization of a PM motor, Andersen and Santos (2012). This optimization algorithm does not guarantee that the optimal solution is ever found, but it will find a good solution. One of the benefits of using this algorithm is that it can optimize several parameters at the same time, where none of these have to be in the same physical area, as long as the solution can be given a fitness value explaining the goodness of the solution. Another benefit of using this metaheuristic algorithm is that it is very easy to implement into any previous made model.

1.2 Goals and main originality of this work

A computational multi-physics tool is created to aid gearless drive design, taking into consideration electromagnetism, fluid mechanics, mass and heat transfer, which has been closely linked to the flexible structural behavior of stator and rotor (solid mechanics model). The different models are validated against data and results presented in selected literatures. The global multi-physics model is afterwards used in a single and multi-objective optimization process with the goal of minimizing the mass and losses in the drive.

The presented model, roughly illustrated in Fig.1.1, is a completely integrated multi-physics model incorporating electromagnetic losses, forces, torques, cooling flow, mass transfer, fluid characteristics, temperature, heat transfer, structural deformation, stresses and natural frequencies. Grinbaum (2012) and Bermudez (2012), used for comparison of the flow and thermal submodels, only use partly interconnected models. The model in Grinbaum (2012) only include one cooling channel for the rotor and one for the stator with constant fluid properties and it is based on a lumped model looking only at one cross-section of the drive. The model in Bermudez (2012) is based on several lumped models at different cross-section positions and also uses constant fluid properties and losses found by Grinbaum (2012). The presented electromagnetic submodel is a numerical model which predict the core losses with higher accuracy than Grinbaum (2012) as it takes all the losses for the desired number of harmonics into account and not just the losses due to the fundamental frequency as in Grinbaum (2012). The integrated electromagnetic-flow-thermal model is therefore an improvement of the previously used models of a gearless

mill drives as it predict the losses with higher accuracy and the intermediate results are iteratively updated between the submodels for a more precise determination of the different parameters. This has also been presented in Andersen et al. (2012c) and is one of the original contributions to the modeling of gearless drives. As finite element models can be very time consuming to solve, especially when used in an iterative process, it is also important to be able to minimize the computation time by making simplifications to the models. It has therefore been examined how this can be performed without losing significant accuracy in the final results and has been described in the thesis and in Andersen et al. (2012c) and Andersen et al. (2012b). The structural model is a finite element model created in Fortran using GMSH as a mesh generator and MATLAB solver to solve the large system of linear equations. The forces, torques and heat expansion found in the other submodels are automatically added to the structural model when the model is run, where Casado (2012) used for comparison, do not include the heat expansion and the forces and torques have to be added manually making it impossible to make a fully automated global optimization using the model in Casado (2012). However, this is possible and has been done for the presented completely integrated multi-physics model. The work performed in this thesis therefore gives a theoretical contribution to the application of metaheuristics in a global optimization process of gearless mill drives, more specifically with the use of evolution strategies. The use of evolution strategies has also been proven to be applicable in the

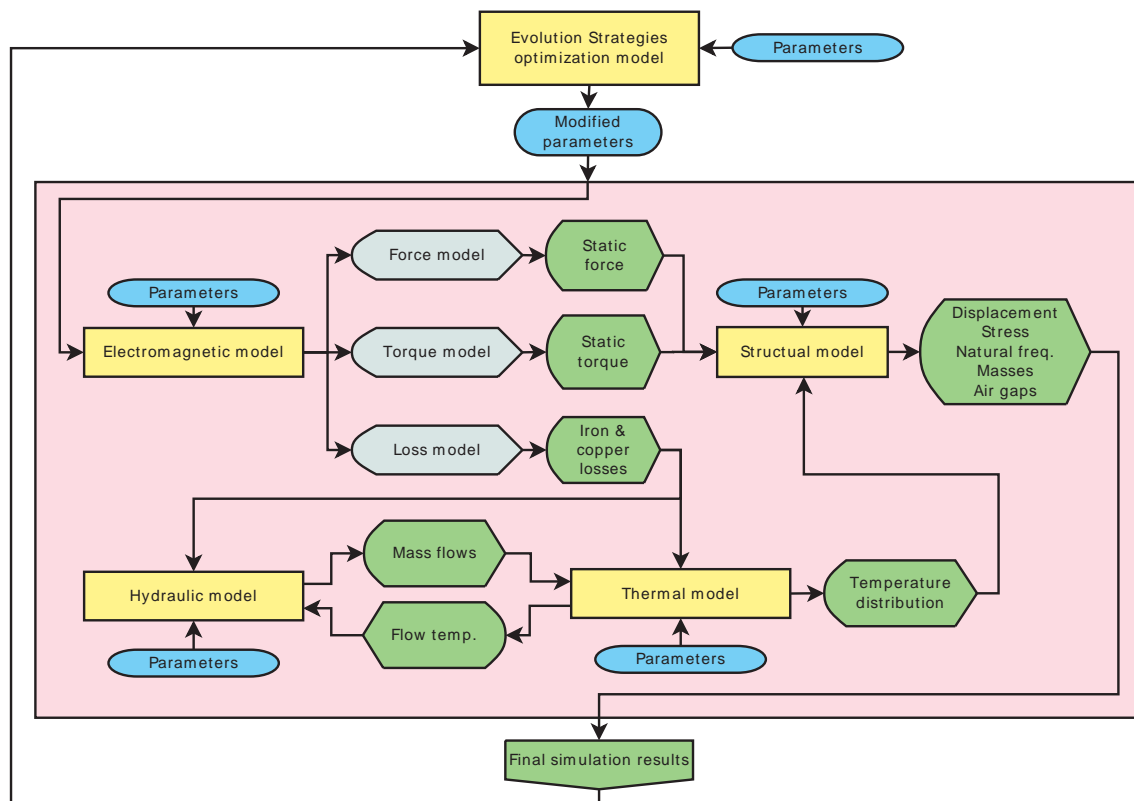


Figure 1.1 Rough overall description of the global multi-physics model of the gearless mill drive

optimization of PM motors as shown in Andersen and Santos (2012) which is an other original contribution as this also has not been performed before on a complete PM motor.

Verification of the different models are important but has only been done against other mathematical models. To truly verify the models, experimental validation are essential as it has been shown in Andersen et al. (2012a) who model and experimentally verify the analysis of a rotor levitated by passive cylinder-magnet bearings which is one of the original contributions.

1.3 Structure of this work

This thesis is split up in chapters each corresponding to the different physical disciplines of the multi-physics model of the gearless mill drive. At the start of each section the basic theory of the specific physical area is explained followed by the results from the presented model and finally the results are verified against data received from ABB Switzerland Ltd.

Chapter 2 gives an introduction to the main components of a gearless drive and describe how a gearless drive work.

Chapter 3 describe the electromagnetic part of the gearless drive beginning with the theory, then model description and finally verification. The main goal of the electromagnetic model are to estimate losses, forces and torques of the drive under different conditions which are used in the structural part and the optimization part of the global model.

Chapter 4 describe how the air cooling flow of a gearless drive can be modeled. The chapter starts by presenting the used theory, then how the cooling flow model was created and finally the model is verified against results from an external source. The main goals of the flow model are estimations of air flow rate and the pressure drop through the cooling channels in the drive. These parameter values are needed in the thermal model and for estimating the electric power loss in the cooling system.

Chapter 5 describe the thermal model of the gearless drive using two different methods (FEM and FD). Initially the theory is explained followed by the model description and finally a verification of the model against results from an external source is performed. The main results from this model are the maximum coil temperature which must not exceed a certain value, the average core temperature which is used for estimating the heat expansion for the structural part of the global model and the heat flux entering the cooling flow which is used in the cooling flow model.

Chapter 6 describe the structural model of the frame and the rotor of the gearless drive. The chapter starts by explaining the theory used for building the FEM code to model the structural part of the drive. Then the modeling of the different elements in the model are described followed by a verification against an external source. The main results of the structural model of the drive are the mass, rotor/stator air gap distortion, deformation, stresses and natural frequencies of the drive which are used for validating a solution in the

optimization part of the global model.

Chapter 7 describe the two optimizations performed on the drive in an attempt to minimize the masses and losses. The chapter starts by presenting the theory behind the optimization algorithm used followed by a description on how the algorithm have been implemented for both the single- and multi-objective optimization. Finally the results are presented and the optimized drives are compared against the drive with the original dimensions.

Chapter 8 summarize the main results and conclusion of the thesis and suggest possible future research directions.

Chapter 2 Gearless mill drives

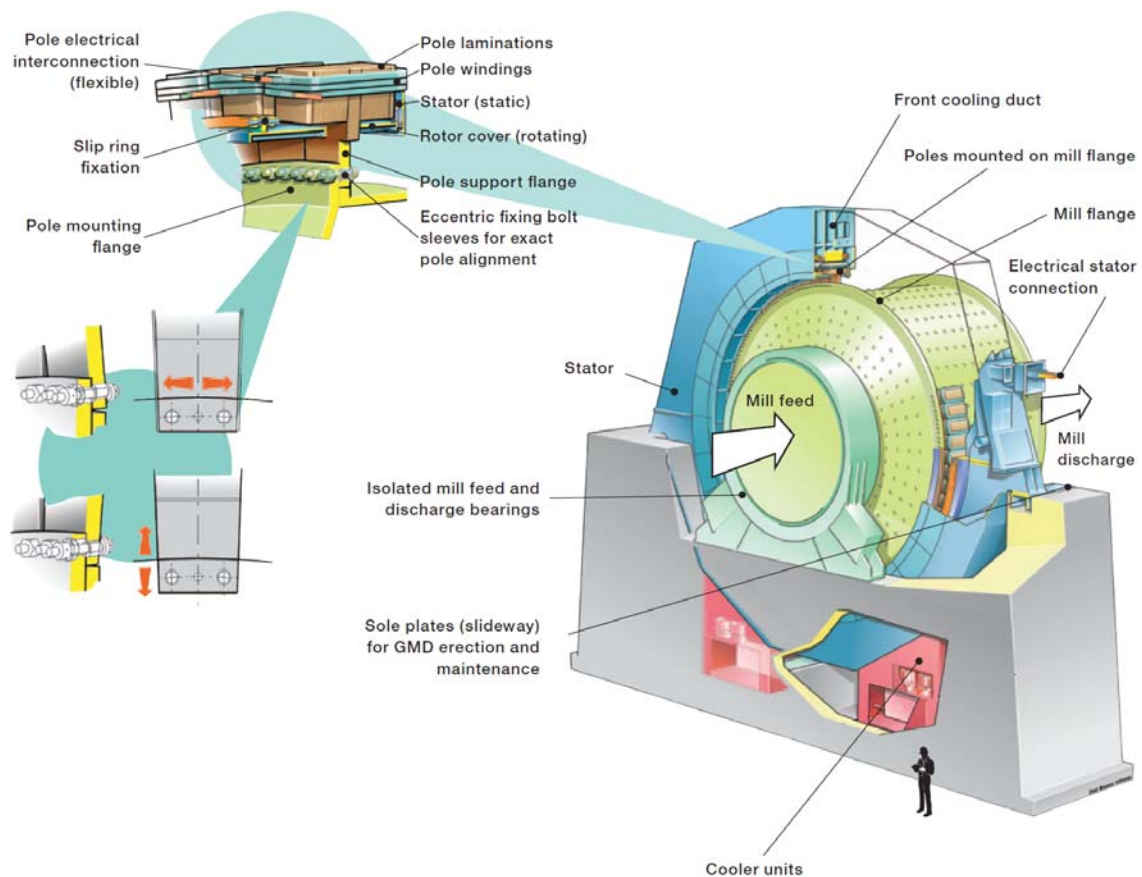
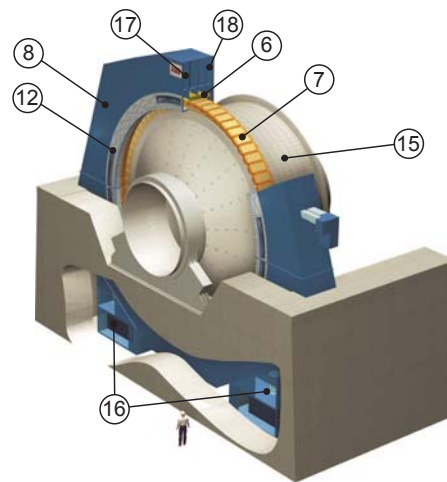
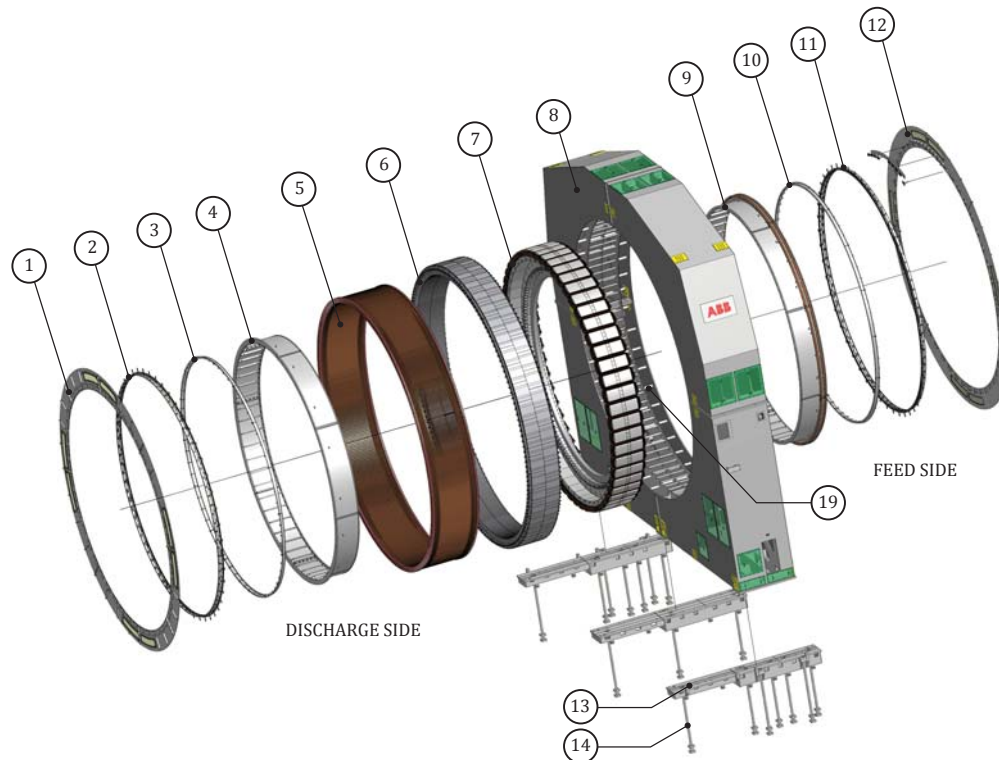


Figure 2.1 Explanation of components of a pedestal mounted SAG mill, ABB Switzerland Ltd. (2009)

The following sections will briefly describe the main components of a mill used in the mining industry to give an overall understanding of how such machines are built and work, Fig. 2.1 and Fig. 2.2. There are several types of mills where the most commonly used in the mineral mining industry can be split up in three groups: ball mills, Autogenous Grinding (AG) mills and Semi-Autogenous Grinding (SAG) mills. AG and SAG mills usually have a large mill drum diameter (up to 40ft~12.2m 28MW, ABB Communications (2011)) compared to their length and are mainly used in a first stage grinding process with large rocks. The ball mill has a smaller diameter (up to 28ft~8.5m 22MW, ABB Communications (2011)) than the AG and SAG mill, but is usually several times longer than their diameter and are mainly used in a second stage grinding process with



(a) Drawing of a SAG mill



(b) Exploded view of a gearless drive

Figure 2.2 (1) Stator cover, (2) Sealing system, (3) Sealing protection cover, (4) Rotor cover, (5) Stator winding, (6) Stator core, (7) Rotor poles, (8) Stator frame (with holding plates and key bars), (9) Rotor cover with slip rings, (10) Sealing protection cover, (11) Sealing system, (12) Stator cover with brush holder, (13) Sole plate, (14) Anchor bolts, (15) Mill drum, (16) Fan and coolers, (17) Inlet side chamber, (18) Outlet side chamber, (19) Frame stiffeners.

smaller rocks. Both the SAG and the ball mill are partially filled with balls of steel or stone to improve the grinding process where as the AG mill rely entirely on the rocks grinding themselves when they tumble around inside the drum. All of these mills can be fitted either with ring motor or with ring gears where the trend is moving towards the use of gearless drives due to smaller maintenance requirements and due to the structural integrity of geared drives when torque requirements increase. All of the mills can come as pedestal mounted Fig. 2.1 or foot mounted Fig. 2.2 and are just a question of how the frame is attached to the concrete foundation. The drive which is modeled in this thesis is a foot mounted gearless ball mill and the following will refer to such a mill drive if not otherwise stated.

Balloon ① - ④ and ⑨ - ⑫ in Fig. 2.2 are sealing and covers to keep external dust out of the frame and for creating a closed cooling system. ⑤ is the stator windings consisting of a lot of copper bars which are fitted into slits in the stator core ⑥ consisting of laminated steel sheets. Balloon ⑨ and ⑫ also include the slip ring and brushes which powers the coils in the rotor poles ⑦. The frame ⑧ consist of mainly steel plates and some stiffener tubes ⑰ and has two main purposes which are to hold the stator and to create a closed cooling system. The frame is fixed on the sole plates ⑬ which again are bolted firmly to the concrete foundation by the anchor bolts ⑭. Cooling fans and coolers ⑯ are placed at both bottom corners of the frame forcing cooling air up the inlet side chamber ⑰ through the stator and rotor cooling channels and down the outlet chamber ⑱.

2.1 Mill drum

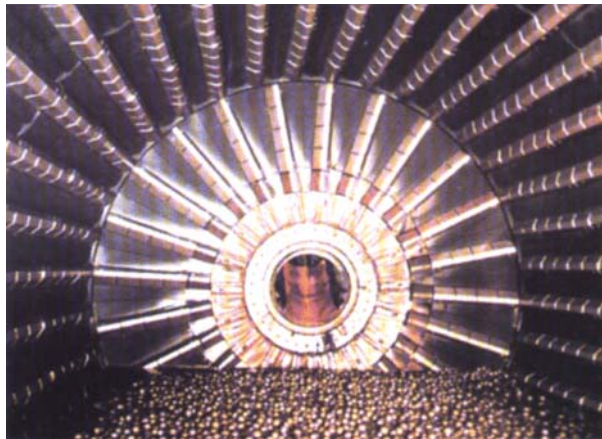
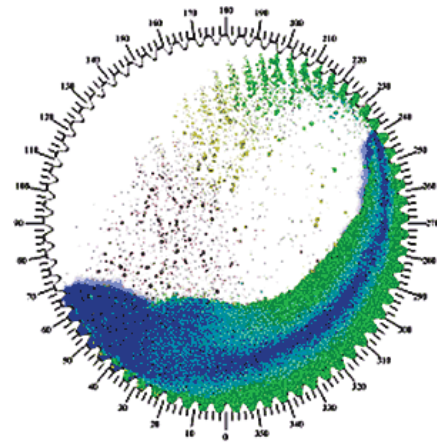
The mill drum is more or less like a very large drum from a washing machine with a feed and discharge hole in either end of the drum. This drum is supported at the feed and discharge trunnions by two large hydrostatic bearings. The teller shaped end plates called the head extend a bit further than the diameter of the cylindrical part of the drum to form the mill flange for the rotor pole attachment. Liners are screwed onto the inside of the heads and cylinder to protect the mill from wear as the rock and balls tumble around inside the drum. The liners are screwed onto the cylinder and heads to make the maintenance easier as these liners will be worn down in time and will have to be replaced. Figure 2.3(a) show the inside of a SAG mill with rock load and Fig. 2.3(b) show how the rock will tumble around inside the drum under optimal conditions.

2.2 Rotor pole

The rotor poles, Fig. 2.4, are more or less just very large electromagnets with copper coils feed with a DC current ($I_{DC} = 490$ A) to create a constant magnetic field. Each rotor pole weighs approximately 2 tons and the modeled drive has 60 of these poles which is fare

¹<http://www.infomine.com/minesite/minesite.asp?site=bingham>

²http://ffden-2.phys.uaf.edu/211_fall2002.web.dir/keith_palchikoff/sag_physics_2.html

(a) Inside a SAG mill, Bingham Canyon¹(b) DEM software simulated SAG charge²*Figure 2.3* Inside view of a mill drum.

from that of a common synchronous motor. The poles consist of a middle plate which is used for attaching the poles to the mill flange. Profile cut St.42 steel are stacked on each side of this middle plate to the desired length of the pole. Press plates are added at the end of each stack and bolts are run through the whole length of the pole pressing the entire pole firmly together. Copper coils are then wound around the pole in three groups creating two air gaps between the coil packs for the cooling of the coils. The two upper coil packs consist of 3 x 18 square copper strands wrapped in insulation where the lower coil pack only consist of 3 x 17 square copper strands. The bushings used for the fixation of the poles are eccentric to ease the alignment of the poles on the mill flange.

2.3 Frame

The frame consists of several steel plates with some internal stiffeners, Fig. 2.5. The frame have four main functions which are to form a rigid connection to the concrete foundation, to fixate the stator, to form chambers, to guide the cooling flow and as housing for the cooling system. The frame consists of 3 internal plates which are the ones holding the stator in place and form the internal walls of the chamber for the cooling flow. On each side of these internal plates are the end plates which form the outside walls of the chambers for the cooling flow. Side and bottom plates are added around these vertical plates fixating the plates and closing the cooling flow chambers. Just behind the stator a series of equally spaced stiffener tubes are placed in a circle around the stator and connected to all the vertical plates. The frame, including the stator, are manufactured in four quarters where the final assembly is performed at the plant due to transportation of such a large structure.

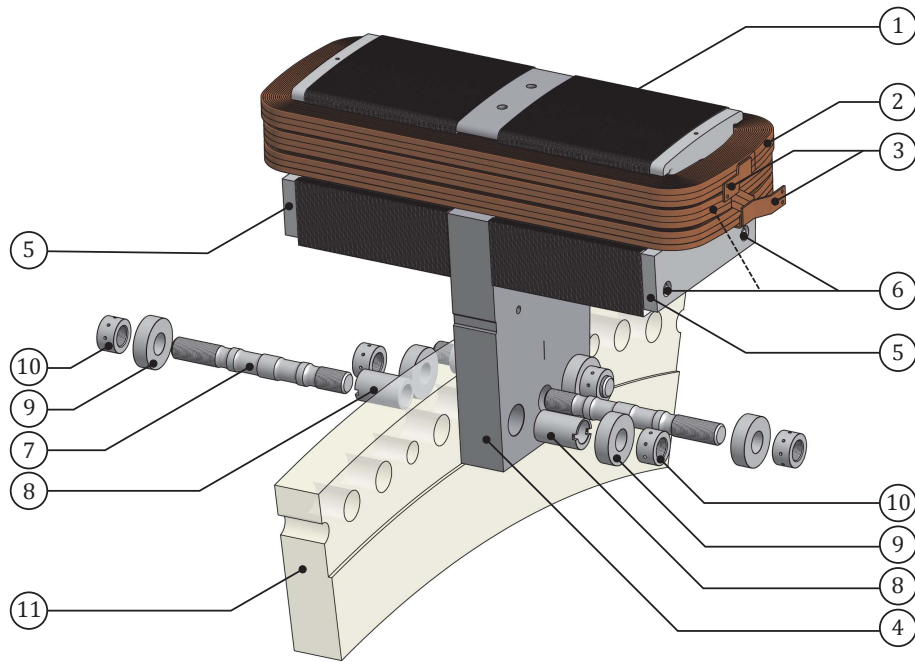


Figure 2.4 Rotor pole, ① Core (Segments), ② Winding, ③ Connections, ④ Middle Pole Plate, ⑤ Press Plate, ⑥ Bolts (1 hid), ⑦ Fixation Bolt, ⑧ Eccentric Bushings (2 Positions), ⑨ Washer, ⑩ Round Nut, ⑪ Mill Flange

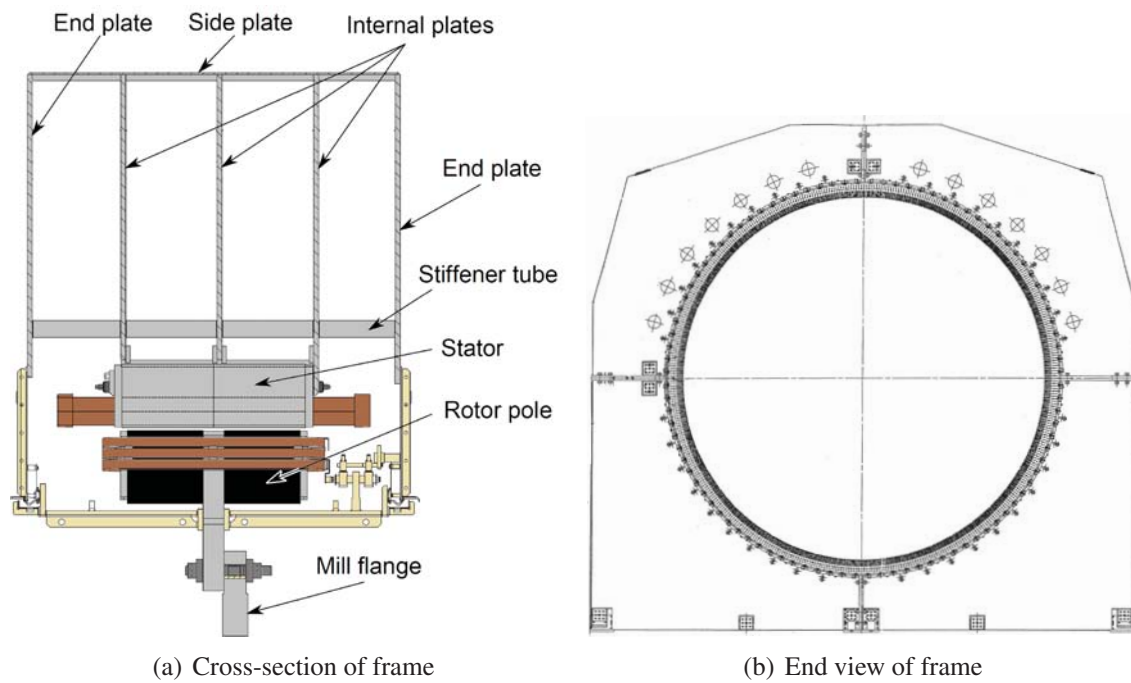


Figure 2.5 Explanation of frame components

2.4 Stator

The stator consists of several thousands of profile cut 0.5 mm thick electric steel sheets like the one shown in Fig. 2.6. These sheets overlap each other and are fixated by the keybars which are slid into the slot at the outer diameter of the sheets. In the core back two rows of holes are cut, which will form the cooling channels and holes for bolting the sheets together. On the inner diameter of the sheet a series of square slots are cut, which are used for the two stator coil bars which are to be added to each slot to form the stator windings. In each stator finger (material between square slots) three holes are cut along the finger. These holes will form the cooling channels needed for cooling the stator coils. Small cuts into the end of the stator fingers form grooves where a fiberglass composite strip can be slid in, locking the copper bars firmly inside the slots. Due to the high currents in the copper bars ($I_{RMS} = 2480 \text{ A}$) the end windings which protrudes about half a meter out from the stator will have to be tied together to prevent them attract each other which can be seen in Fig. 3.4(a). The stator is attached to the frame by the use of the mentioned keybars, which are bolted to the 3 internal plates mentioned in the previous section forming a small air gap between the stator and the frame to compensate for some of the heat expansion, Fig. 2.5(a). Furthermore, bolts are run through the entire stator and through one of the 3 internal plates.

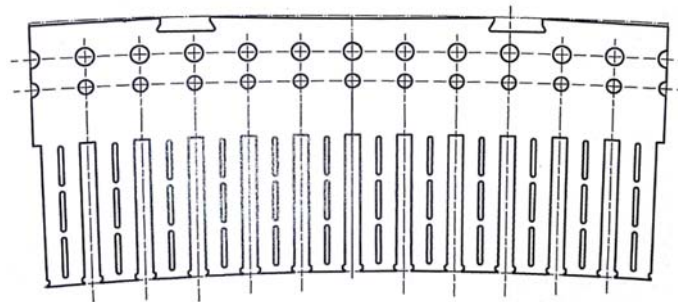


Figure 2.6 Stator sheet

2.5 Fan and cooling system

The cooling system consists of several coolers and cooling fans located inside the frame at each bottom corner. The path of the cooling flow is illustrated in Fig. 2.7 for a pedestal mounted GMD, however, the principle is the same for a foot mounted GMD which is the one modeled. The warm air is sucked through the coolers and pas the cooling fans before it is send up through the large chamber in the frame. From this chamber the air is pressed through the mentioned cooling channels and the air gap between the poles and stator and between the poles themself. The warm cooling air then exits into the large chamber at the other side of the frame where it is sucked through the cooler again. Due to the fact that the cooling fans are placed on the cold side of the coolers, the cooling air will initially be

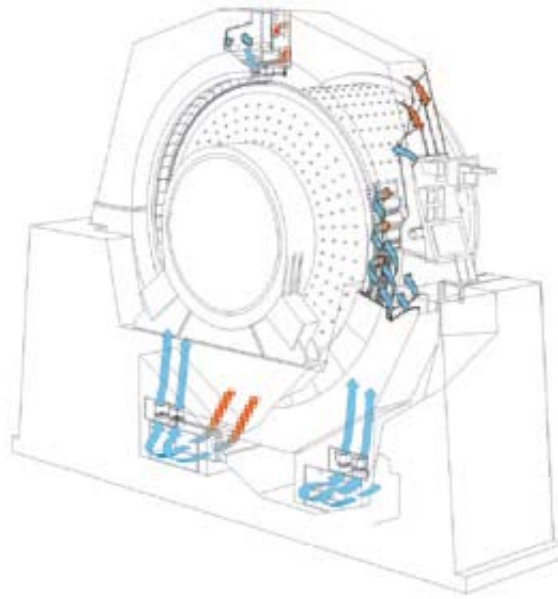


Figure 2.7 Gearless mill drive cooling system, ABB Switzerland Ltd. (2009)

heated due to losses in the cooling system before it is sent up in the frame chamber. This initial heating of the cooling air cannot be neglected as the losses of the cooling system are relatively large.

Chapter 3

Electromagnetic forces, torque and losses in gearless drives - Electromagnetic model

The electromagnetic part of a motor is the heart of the complete unit as it is the component which produces the torque specified by the customer. It is therefore also this part which usually is the first to be dimensioned in a design phase. However, the produced torque is only one of many parameters which can be obtained from the electromagnetic model and are needed for an optimal design. There are a lot of parameters which need to be determined in the design of a motor as for example the type of winding of the stator which if chosen correctly can minimize the harmonics in the motor and thereby reducing the losses and torque ripples as shown in EL-Refaie and Shah (2011) for an induction motor. Another example is the type of motor used which for example could be induction motor, Li et al. (2010), permanent magnet motor, Rahideh and Korakianitis (2012), Wu et al. (2012) or DC excited synchronous motor as the one simulated.

The three most important results from the electromagnetic model needed in the further design of a complete motor are the torque, the pole radial magnetic pull and the losses from the copper windings and core material. The torque and the pole radial magnetic pull are needed in the structural calculations for dimensioning the frame which support the stator and rotor as a too low stiffness would result in a critical reduction of the rotor/stator air gap. The electromagnetic induced losses in the core material and the losses in the copper windings as current flows through the coils are needed in the thermal model as heat generation. These electromagnetic models can be created as both analytical and numerical models. If high level of details of the magnetic flux within the iron core is needed or the core geometry is complex it is of common practice to use a 2D finite element model as presented by Cundev and Cerovsky (2007) for a salient poles synchronous motor and by Arumugam et al. (1985) for a switched reluctance motor.

This chapter starts by explaining the basic theory of electromagnetism and how to estimate forces and torques in a finite element magnetostatic model followed by a description on how the winding diagram for the simulated drive can be found. As the drive has a lot of poles which result in a relatively large model, it will be described how it is possible to reduce the model without losing any significant accuracy in the results achieved. Results from the full and the reduced models will be compared against each other and results achieved at ABB to demonstrate the validity and limitations of the reduced model. Finally, it will be described how the core and resistive losses in the drive can be found through a series of magnetostatic simulations which will be verified against values received from ABB. All finite element magnetostatic simulations in this thesis are performed with the program "Finite Element Method Magnetic" and will in subsequent sections be referred to as FEMM.

3.1 Basic equation

Magnetostatic problems are problems in which the fields are time-invariant. In this case, the field strength \mathbf{H} and flux density \mathbf{B} must obey Eq. 3.1 and 3.2:

$$\nabla \times \mathbf{H} = \mathbf{J} \quad (3.1)$$

$$\nabla \cdot \mathbf{B} = 0 \quad (3.2)$$

The relationship between \mathbf{B} and \mathbf{H} is given in Eq. 3.3 where the proportionality constant μ_p is the permeability of the material:

$$\mathbf{B} = \mu_p \mathbf{H} \quad (3.3)$$

In cases where the material is nonlinear, the permeability, μ_p is a function of \mathbf{B} and is given by:

$$\mu_p = \frac{\mathbf{B}}{\mathbf{H}(\mathbf{B})} \quad (3.4)$$

The software program FEMM goes about finding a field that satisfies Eq. 3.1-3.3 via a magnetic vector potential approach. Flux density is written in terms of the vector potential, \mathbf{A} , as:

$$\mathbf{B} = \nabla \times \mathbf{A} \quad (3.5)$$

This definition of \mathbf{B} always satisfies Eq. 3.2 and Eq. 3.1 can be rewritten as:

$$\nabla \times \left(\frac{1}{\mu_p(\mathbf{B})} \nabla \times \mathbf{A} \right) = \mathbf{J} \quad (3.6)$$

For a linear isotropic material (and assuming the Coulomb gauge, $\nabla \cdot \mathbf{A} = 0$), Eq. 3.6 reduces to:

$$-\frac{1}{\mu_p} \nabla^2 \mathbf{A} = \mathbf{J} \quad (3.7)$$

FEMM retains the form of Eq. 3.6, so that magnetostatic problems with a nonlinear B-H relationship can be solved. In the general 3-D case, \mathbf{A} is a vector with three components. However, in the 2-D planar and axisymmetric cases, two of these three components are zero, leaving just the component in the "out of the paper" direction. The advantage of using the vector potential formulation is that all the conditions to be satisfied have been combined into a single equation. If \mathbf{A} is found, \mathbf{B} and \mathbf{H} can then be deduced by differentiating \mathbf{A} .

For calculating the forces, one can use Maxwell's stress tensor which is particularly suited for this purpose, as the integral depends only on the field distribution outside the object in question. For this reason, it is not necessary to know the exact current density distributions within complex anisotropic or nonlinear materials. From the theory of electromagnetism the Lorentz force and Ampere's law are expressed respectively by Eq. 3.8 and Eq. 3.9.

$$\mathbf{f} = \mathbf{J} \times \mathbf{B} \quad (3.8)$$

$$\nabla \times \mathbf{B} = \mu_0 \mathbf{J} \quad (3.9)$$

Inserting Eq. 3.9 into Eq. 3.8 and integrating over the volume of the object, an expression for the force on the object expressed solely by the B-field is achieved.

$$\mathbf{F} = \frac{1}{\mu_0} \iiint (\nabla \times \mathbf{B}) \times \mathbf{B} \, dV \quad (3.10)$$

Expanding the curl and the cross product, the x, y and z component of Eq. 3.10 is

$$F_x = \frac{1}{\mu_0} \iiint \left(B_z \frac{\partial B_x}{\partial z} - B_z \frac{\partial B_z}{\partial x} - B_y \frac{\partial B_y}{\partial x} + B_y \frac{\partial B_x}{\partial y} \right) dV \quad (3.11)$$

$$F_y = \frac{1}{\mu_0} \iiint \left(B_x \frac{\partial B_y}{\partial x} - B_x \frac{\partial B_x}{\partial y} - B_z \frac{\partial B_z}{\partial y} + B_z \frac{\partial B_y}{\partial z} \right) dV \quad (3.12)$$

$$F_z = \frac{1}{\mu_0} \iiint \left(B_y \frac{\partial B_z}{\partial y} - B_y \frac{\partial B_y}{\partial z} - B_x \frac{\partial B_x}{\partial z} + B_x \frac{\partial B_z}{\partial x} \right) dV \quad (3.13)$$

Introducing Maxwell's stress tensor, Eq. 3.14, where E is the electric field, B is the magnetic field, ϵ_0 is the vacuum permittivity and μ_0 is the vacuum permeability.

$$\mathbf{S}_{ij} = \epsilon_0 \left(E_i E_j - \frac{1}{2} \delta_{ij} E^2 \right) + \frac{1}{\mu_0} \left(B_i B_j - \frac{1}{2} \delta_{ij} B^2 \right) \quad (3.14)$$

If the field is only magnetic, which is largely true in motors, some of the terms cancel out resulting in Eq. 3.15:

$$\mathbf{S}_{ij} \cong \frac{1}{\mu_0} \left(B_i B_j - \frac{1}{2} \delta_{ij} B^2 \right) \quad (3.15)$$

Expanding this for the x, y and z directions result in Eq. 3.16 to Eq. 3.18:

$$\mathbf{S}_x = \frac{1}{\mu_0} \left[\left(B_x^2 - \frac{B_x^2 + B_y^2 + B_z^2}{2} \right) \vec{i} + B_x B_y \vec{j} + B_x B_z \vec{k} \right] \quad (3.16)$$

$$\mathbf{S}_y = \frac{1}{\mu_0} \left[B_y B_x \vec{i} + \left(B_y^2 - \frac{B_x^2 + B_y^2 + B_z^2}{2} \right) \vec{j} + B_y B_z \vec{k} \right] \quad (3.17)$$

$$\mathbf{S}_z = \frac{1}{\mu_0} \left[B_z B_x \vec{i} + B_z B_y \vec{j} + \left(B_z^2 - \frac{B_x^2 + B_y^2 + B_z^2}{2} \right) \vec{k} \right] \quad (3.18)$$

Now taking the divergence of vector Eq. 3.16 to Eq. 3.18 results in Eq. 3.19 to Eq. 3.21

$$\begin{aligned} \nabla \cdot \mathbf{S}_x &= \frac{1}{\mu_0} \left[B_x \left(\frac{\partial B_x}{\partial x} + \frac{\partial B_y}{\partial y} + \frac{\partial B_z}{\partial z} \right) \right. \\ &\quad \left. - B_y \frac{\partial B_y}{\partial x} - B_z \frac{\partial B_z}{\partial x} + B_y \frac{\partial B_x}{\partial y} + B_z \frac{\partial B_x}{\partial z} \right] \end{aligned} \quad (3.19)$$

$$\begin{aligned} \nabla \cdot \mathbf{S}_y &= \frac{1}{\mu_0} \left[B_y \left(\frac{\partial B_x}{\partial x} + \frac{\partial B_y}{\partial y} + \frac{\partial B_z}{\partial z} \right) \right. \\ &\quad \left. - B_x \frac{\partial B_x}{\partial y} - B_z \frac{\partial B_z}{\partial y} + B_x \frac{\partial B_y}{\partial x} + B_z \frac{\partial B_y}{\partial z} \right] \end{aligned} \quad (3.20)$$

$$\begin{aligned} \nabla \cdot \mathbf{S}_z &= \frac{1}{\mu_0} \left[B_z \left(\frac{\partial B_x}{\partial x} + \frac{\partial B_y}{\partial y} + \frac{\partial B_z}{\partial z} \right) \right. \\ &\quad \left. - B_x \frac{\partial B_x}{\partial z} - B_y \frac{\partial B_y}{\partial z} + B_x \frac{\partial B_z}{\partial x} + B_y \frac{\partial B_z}{\partial y} \right] \end{aligned} \quad (3.21)$$

According to Eq. 3.2 the term $\left(\frac{\partial B_x}{\partial x} + \frac{\partial B_y}{\partial y} + \frac{\partial B_z}{\partial z} \right)$ is equal to zero and the first part of the right hand side can be canceled. The remaining right hand side expressions are similar to the ones in Eq. 3.11, 3.12 and 3.13. The force in the x, y and z direction on the object can therefore be expressed as:

$$F_x = \iiint \nabla \cdot \mathbf{S}_x dV \quad (3.22)$$

$$F_y = \iiint \nabla \cdot \mathbf{S}_y dV \quad (3.23)$$

$$F_z = \iiint \nabla \cdot \mathbf{S}_z dV \quad (3.24)$$

Using the divergence theorem to convert the volume integral to a surface integral one achieves:

$$F_x = \iint \mathbf{S}_x \cdot \vec{\mathbf{n}} dA \quad (3.25)$$

$$F_y = \iint \mathbf{S}_y \cdot \vec{\mathbf{n}} dA \quad (3.26)$$

$$F_z = \iint \mathbf{S}_z \cdot \vec{\mathbf{n}} dA \quad (3.27)$$

where $\vec{\mathbf{n}}$ is the unit vector normal to the surface. In a general 3D FE case this normal vector can be expressed as:

$$\vec{\mathbf{n}} = \frac{(\mathbf{p}_2 - \mathbf{p}_1)}{|\mathbf{p}_2 - \mathbf{p}_1|} \times \frac{(\mathbf{p}_3 - \mathbf{p}_1)}{|\mathbf{p}_3 - \mathbf{p}_1|} \quad (3.28)$$

when looking at a triangular segment as shown in Fig. 3.1(a). \mathbf{p}_1 to \mathbf{p}_3 in Eq. 3.28 are vectors and marked by arrows in the figure pointing from the reference system to the

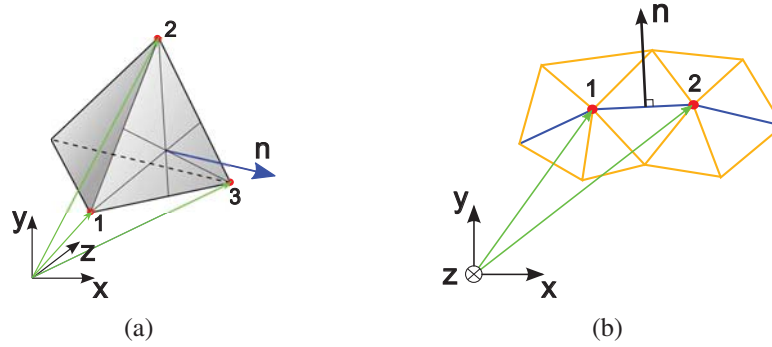


Figure 3.1 (a) General case unit vector, (b) FEMM unit vector

corner points of the triangle marked by dots. FEMM, however, is a 2D solver and assume no variation of the B-field in the "out the paper" direction and the depth into the paper Δz is constant. In this case, the normal vector is as shown in Fig. 3.1(b) where the contour between the two dots defines the edge of the surface. In this case, the normal vector can, according to Fig. 3.1(b), be found as:

$$\vec{n} = \vec{n}_z \times \frac{(\mathbf{p}_1 - \mathbf{p}_2)}{|\mathbf{p}_1 - \mathbf{p}_2|} \quad (3.29)$$

where \vec{n}_z is a unit vector pointing in the z-direction. It is now possible to write a general force law expressed as:

$$\mathbf{F} = \iint \mathbf{S} \cdot \vec{n} dA \quad (3.30)$$

The quantity \mathbf{S} is the Maxwell stress tensor for magnetostatic fields

$$\mathbf{S} = \frac{1}{\mu_0} \begin{bmatrix} B_x^2 - B^2/2 & B_x B_y & B_x B_z \\ B_y B_x & B_y^2 - B^2/2 & B_y B_z \\ B_z B_x & B_z B_y & B_z^2 - B^2/2 \end{bmatrix} \quad (3.31)$$

where $B^2 = B_x^2 + B_y^2 + B_z^2$.

The torque on a differential element can be expressed as:

$$d\mathbf{t} = \vec{\mathbf{r}} \times d\mathbf{F} \quad (3.32)$$

where $\vec{\mathbf{r}}$ is a vector pointing from the origin of torque to the current position

$$\vec{\mathbf{r}} = \begin{Bmatrix} r_x \\ r_y \\ r_z \end{Bmatrix} = \begin{Bmatrix} x - x_t \\ y - y_t \\ z - z_t \end{Bmatrix} \quad (3.33)$$

Inserting Eq. 3.30 into this, results in:

$$\mathbf{t} = \iint \vec{\mathbf{r}} \times (\mathbf{S} \cdot \vec{n}) dA \quad (3.34)$$

Expanding the cross product, a torque tensor \mathbf{T} can be found, which satisfy Eq. 3.35 and is a function of the stress tensor Eq. 3.31 and the components of the vector from the torque origin Eq. 3.33:

$$\mathbf{t} = \iint \mathbf{T} \cdot \vec{\mathbf{n}} dA \quad (3.35)$$

$$\mathbf{T} = \begin{bmatrix} (r_y S_{31} - r_z S_{21}) & (r_y S_{32} - r_z S_{22}) & (r_y S_{33} - r_z S_{23}) \\ (r_z S_{11} - r_x S_{31}) & (r_z S_{12} - r_x S_{32}) & (r_z S_{13} - r_x S_{33}) \\ (r_x S_{21} - r_y S_{11}) & (r_x S_{22} - r_y S_{12}) & (r_x S_{23} - r_y S_{13}) \end{bmatrix} \quad (3.36)$$

Further information on Maxwell's stress tensor can be found in Humphries (2010); Jr. (2010); Bastos and Sadowski (2003).

3.2 Rotor and stator windings

The following explains how the winding configuration for the FEMM calculation of the simulated drive is found. It will only be described how this can be performed for the specific drive and will refer to Pyrhönen et al. (2008) for other drive configurations.

The winding design of the simulated drive is a double-layer winding which means that there are two copper coil bars in each stator slot. The main parameters of the drive are:

- Number of slots: $Q_s = 504$
- Number of pole pair: $p_p = 30$
- Number of phases: $m_p = 3$

This result in the following number of slots per pole and phase:

$$q_s = \frac{Q_s}{2p_p m_p} = 2 + \frac{4}{5} \quad (3.37)$$

As $q_s \notin \mathbb{N}$ means that the winding is a fractional slot winding in this case with the divider $n_d = 5$. The conditions of symmetry (Table 2.6, Pyrhönen et al. (2008)) $p_p/n_d = 30/5 = 6 \in \mathbb{N}$ and $n_d/m_p = 5/3 \notin \mathbb{N}$ are met. According to Table 2.7, Pyrhönen et al. (2008), if n_d is an odd number $n_d = 5 \in \mathbb{N}_{odd}$, a first-grade fractional slot winding is to be created. The parameters of the voltage phasor diagram of such a winding are:

- Number of layers in the voltage phasor diagram for the base winding $t^* = 1$
- Number of pole pairs in the base winding $p_p^* = n_d = 5$
- Number of slots in the base winding $Q_s^* = Q_s \cdot n_d/p_p = 84$
- Number of radii $Q'_s = Q_s^*/t^* = 84$
- Slot angle $\alpha_u = 2 \cdot \pi \cdot p^*/Q_s^* = 0.374$
- Phasor angle $\alpha_z = 2 \cdot \pi \cdot t^*/Q_s^* = 0.0748$
- Number of phasors skipped in the numbering $(p_p^*/t^*) - 1 = 4$

Since $t^* = 1$ the number of radii Q'_s is the same as the number of phasors Q_s^* and we obtain $Q_s^*/m_p = 84/3 = 28$ phasors for each phase which are then divided into negative $Z-$ and positive $Z+$ phasors. The number of phasors per phase in the first-grade base winding is $Q_s^*/m_p = Q_s/m_p t \in \mathbb{N}_{even}$. In normal cases, there are no zone variation and the phasors are evenly divided into positive and negative phasors. For the specific case, the number of phasors of both types are therefore 14, $Z- = Z+ = 14$. By employing a normal zone order $-U, +V, -W, +U, -V, +W$ it is possible to divide the voltage phasor diagram into zones with 14 phasors in each, Fig. 3.2.

When the voltage phasor diagram is ready, the bottom layer of the winding is set. The positions of the coil sides in the top layer are defined when an appropriate coil span is selected. For fractional slot windings, it is not possible to construct a full-pitch winding, because q_s is not a member of \mathbb{N} . For the winding in question, the full-pitch coil span y_Q of a full-pitch winding would be y slot pitches

$$y = y_Q = m_p \cdot q_s = 3 \cdot 2.8 = 8.4 \notin \mathbb{N} \quad (3.38)$$

This is not possible in practice because the step has, of course, to be an integer number of slot pitches. The double pitch has to be an integer, here defined as $y_1 + y_2$, and the difference between $y_1 + y_2$ and $2 \cdot y$ has to be less than 0.5. Either y_1 or y_2 has to be equal to $\beta_{optimal} \cdot y = 5/6 \cdot 8.4 \approx 7$. One can now choose one of the two cases: $y_1 < y$ or $y_1 > y$. In the case of the specific drives winding it is chosen that $y_1 < y$. This results in:

$$y_1 + y_2 = 2 \cdot y \quad (3.39)$$

$$7 + y_2 = 2 \cdot 8.4 \Rightarrow y_2 = 10 \quad (3.40)$$

Double-layer fractional slot windings are thus short-pitched windings. When constructing a two-layer fractional slot winding, there are two coil sides in each slot. Hence, there are as many coils as slots in the winding. Initially the -U-phase bottom coil side is located in slot 9 to match the numbering used in the simulated drive. The other coil side is placed according to the coil span of $y = 10$ at a distance of 10 slots in the upper part of slot 19. Similarly, coils run from 10 to 20. The coils to be formed in the base winding are listed in Tab. 3.1 and are repeated 6 times to fill out the 504 slots of the stator. A complete winding diagram can be seen in Fig. 3.3 and Fig. 3.4 show pictures of the windings at a plant with a similar drive.

3.3 Full and reduced finite element motor model

As the full magnetostatic model of the simulated drive seen in Fig. 3.5(a) is relatively large due to the large number of poles, it is desirable to find a way to reduce it without losing accuracy in the final results. The most obvious reduction will be to only model the part of the drive corresponding to the base winding found in Sec. 3.2 consisting of 10 poles (5 pole pairs) by applying symmetric boundary conditions at the end of the section. However, looking closer at the winding diagram Fig. 3.3, it can be seen that it is possible

+U	-U	+V	-V	+W	-W
18 - 28	9 - 19	12 - 22	21 - 31	23 - 33	15 - 25
19 - 29	10 - 20	13 - 23	22 - 32	24 - 34	16 - 26
20 - 30	11 - 21	14 - 24	37 - 47	25 - 35	17 - 27
35 - 45	26 - 36	29 - 39	38 - 48	40 - 50	32 - 42
36 - 46	27 - 37	30 - 40	39 - 49	41 - 51	33 - 43
51 - 61	28 - 38	31 - 41	54 - 64	42 - 52	34 - 44
52 - 62	43 - 53	46 - 56	55 - 65	57 - 67	49 - 59
53 - 63	44 - 54	47 - 57	56 - 66	58 - 68	50 - 60
68 - 78	45 - 55	48 - 58	71 - 81	59 - 69	65 - 75
69 - 79	60 - 70	63 - 73	72 - 82	74 - 84	66 - 76
70 - 80	61 - 71	64 - 74	73 - 83	75 - 85	67 - 77
85 - 95	62 - 72	79 - 89	88 - 98	76 - 86	82 - 92
86 - 96	77 - 87	80 - 90	89 - 99	91 - 101	83 - 93
87 - 97	78 - 88	81 - 91	90 - 100	92 - 102	84 - 94

Table 3.1 Base winding table

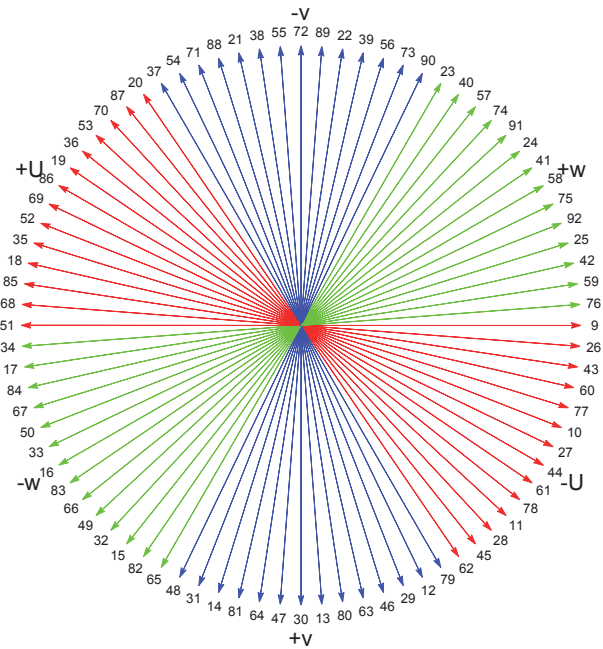


Figure 3.2 Phasor diagram

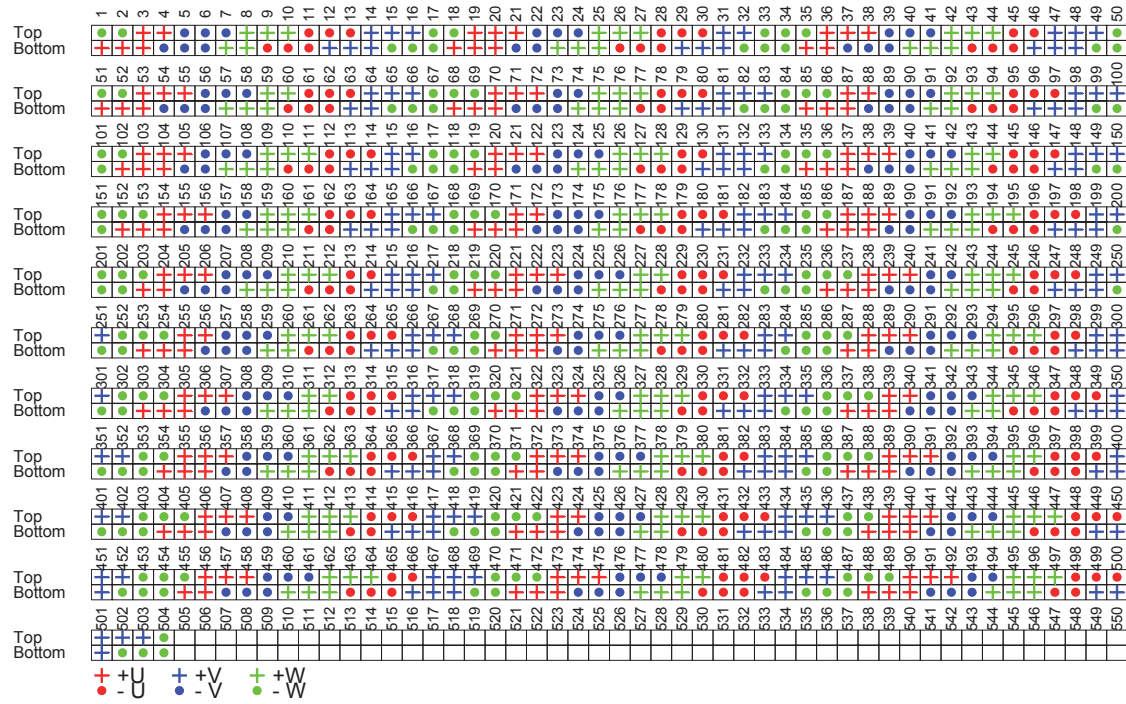


Figure 3.3 Winding diagram



(a) End windings (approximately one pole)



(b) Section of stator with windings

Figure 3.4 Stator windings from a similar drive as the one simulated

to reduce the model even further by modeling only half of the base winding, as the second part of the base winding is just a repetition of the first half with opposite signs. It is thereby possible to simulate the full drive with 60 poles by only modeling 5 poles with anti-symmetric boundary conditions at the ends of the section. To handle different rotor angles the reduced model is split into two sub-models consisting of the rotor including half of the air gap and the stator including the other half of the air gap. The rotor sub-model can now be rotated to the desired angle and an anti-symmetric boundary condition applied to the newly formed air gap boundary. Figure 3.5(b) shows the reduced model of the drive where the red, blue and green lines indicate the anti-symmetry boundary conditions. It is obvious that this simplification does not reduce the accuracy of the final results, as it is just an exploitation of symmetry in the drive configuration and has reduced the model size by a factor of 12 compared to the full model. The last statement is, however, only correct as long as the rotor is not placed at an eccentricity compared to the stator. But as will be shown in Sec. 3.4.2 the loss in accuracy by also using the reduced model for cases with an eccentric rotor is minimal and can for the overall picture be accepted to be sufficient accurate.

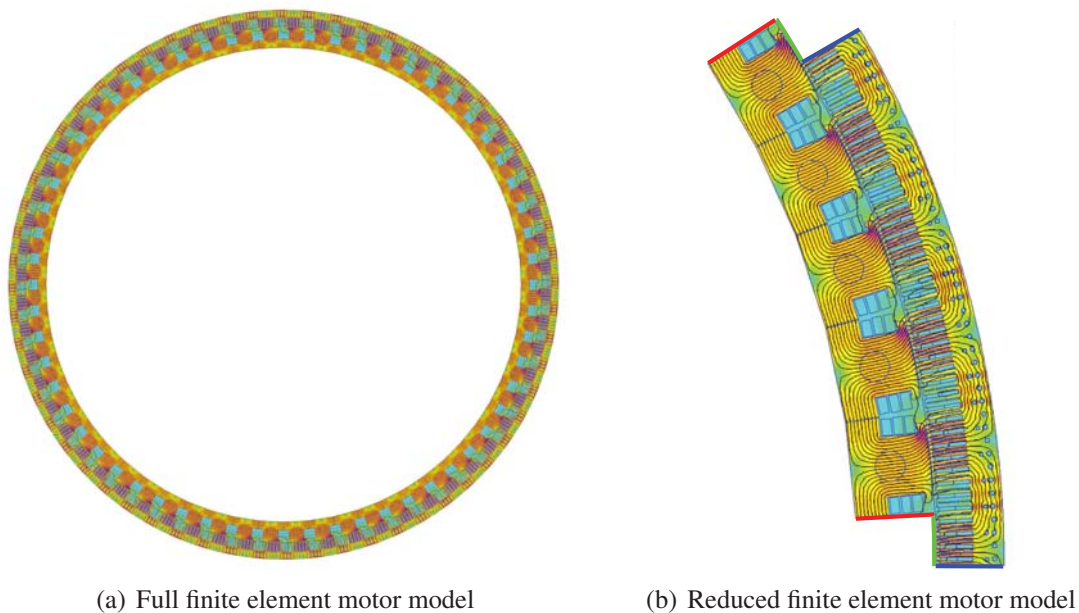


Figure 3.5 Full and reduced FEMM magnetostatic models

3.4 Estimation of force and torque

3.4.1 Zero torque phase angle

A series of magnetostatic calculations are performed for finding the phase angle at which the stator currents will produce the maximum rotor torque. This is done by keeping the rotor fixed while the phase angle is rotated. The rotor torque is estimated and recorded for

each phase angle as described in Sec. 3.1, with a build-in function in FEMM. Figure 3.6 shows the found torque/phase angle relationship, where the blue line with dots represent, the finite element results. A spline is drawn through the finite element results (red curve) to smoothen the curve and thereby get a more accurate determination of the phase angle which produce the maximum torque. The remaining simulations in this thesis use the phase angle which produce the maximum torque if not otherwise stated.

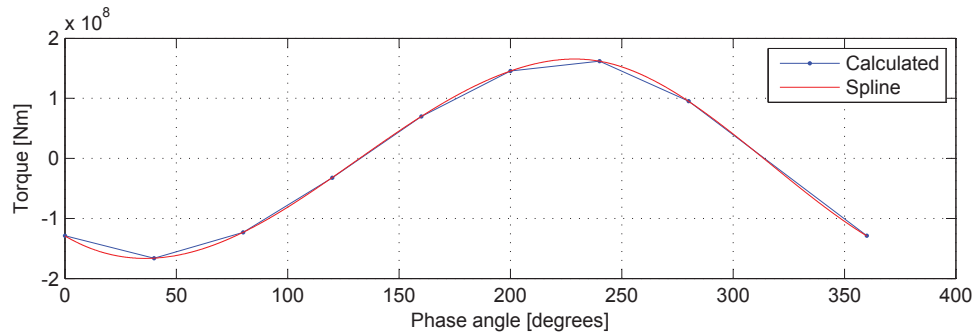


Figure 3.6 Rotor torque vs. phase angle (Constant rotor angle at 0°)

3.4.2 Torque & magnetic pull

Several magnetostatic simulations are made to examine the validity of the reduced model described in Sec. 3.3 when the rotor is placed at an eccentricity compared to the stator. The way the eccentricity is introduced for the reduced model is to shift the rotor sub-model in the direction of the 3rd pole and calculate the resulting magnetic pull due to air gap size for that pole. Assuming a linear relationship between the produced magnetic pull and the air gap size, it is possible to determine the magnetic pull of the individual poles by finding the air gap at the different poles due to the eccentricity. Figure 3.7(a) shows the magnetic pull found by the full and the reduced model for 5 different load cases when the rotor has no eccentricity. As expected, the magnetic pull for all the poles in the reduced model has the same value equal to the magnetic pull for the 3rd pole in the full model, as the force is found for the 3rd pole in the reduced model. However, as can be seen from the full model, the magnetic pull is not constant for the different poles even though the air gap is the same for all the poles. This difference in magnetic pull from one pole to another can be explained by the number of slots per pole in the stator which is a fraction and result in different stator surface area per pole area. This area will change as the rotor rotate creating a pulsating magnetic pull, when looking at one specific pole. In other words, the magnetic pull for a pole depend slightly on the angular position of the rotor. However, the difference between the maximum and minimum magnetic pull within the different load cases are relatively small making the reduced model acceptable for zero eccentricities. Figure 3.7(b) shows the same load cases but now with a rotor eccentricity of 6 mm in the direction of pole 1. Before continuing, it should be mentioned that the drive will never in reality reach this eccentricity as an automated security system will have shut

down the drive before this happens. From the figure it can be seen that the magnetic pull for the full model again is pulsation from pole to pole due to the same reason as before, but otherwise following an offset sinus curve nicely corresponding to the change in air gap due to eccentricity of the rotor. The results of the reduced model of course also follow an offset sinus curve, as it is based solely on a linear relationship between magnetic pull and the air gap and correspond nicely with the results found by the full model. It has been shown that the reduced model can be used for cases with and without rotor eccentricities assuming a linear relationship between magnetic pull and the air gap. Figure 3.7(c) shows this linear relationship for the 5 simulated cases. The reason for this linear relationship can be explained by the fact that the drive is running in a saturated state and is therefore less sensitive to changes in air gap as the magnetic flux in the core material remain almost constant. Another interesting fact which can be concluded from the two figures, Fig. 3.7(a) and 3.7(b), is that the produced torque is almost independent of the rotor eccentricity. Due to the fact that a linear relationship between the magnetic pull and the air gap can be assumed, it is possible to find an equivalent spring stiffness for modeling the change in stator/pole forces due to change in air gap. Table 3.2 shows the spring stiffnesses for the 5 cases. These equivalent spring stiffnesses for changes in force will later on, together with the static forces, be used in the structural model for calculation of both deformation and natural frequencies.

Stiffness [kN/m]	Torque [kNm]
-8216.66	~52
-8258.99	~4785
-8176.50	~9013
-8134.07	~12076
-8518.47	~13601

Table 3.2 Equivalent stiffness per pole

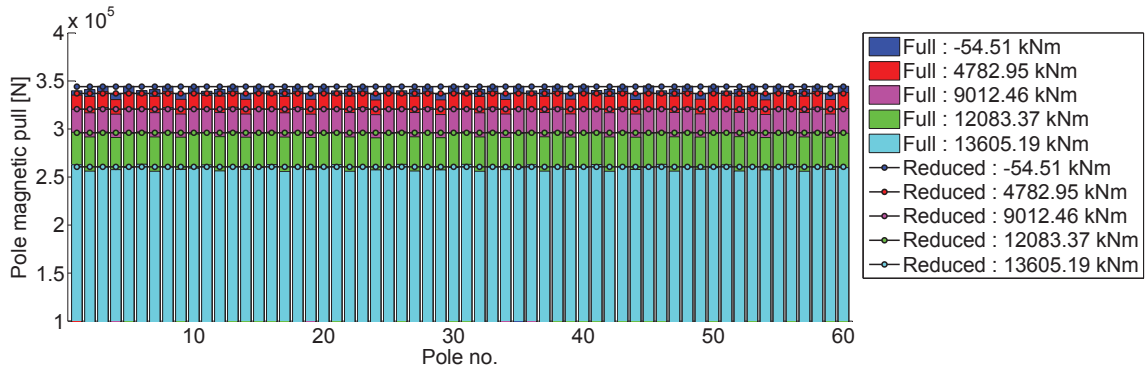
3.4.3 Verification of force & torque model

For validation of the presented force and torque model, ABB has provided their results, as this is the only possible validation of the model due to the fact that the drive is not yet in operation and therefore no measurements are available at the time. Table 3.3 shows the results provided by ABB together with the results from the presented model. As it is

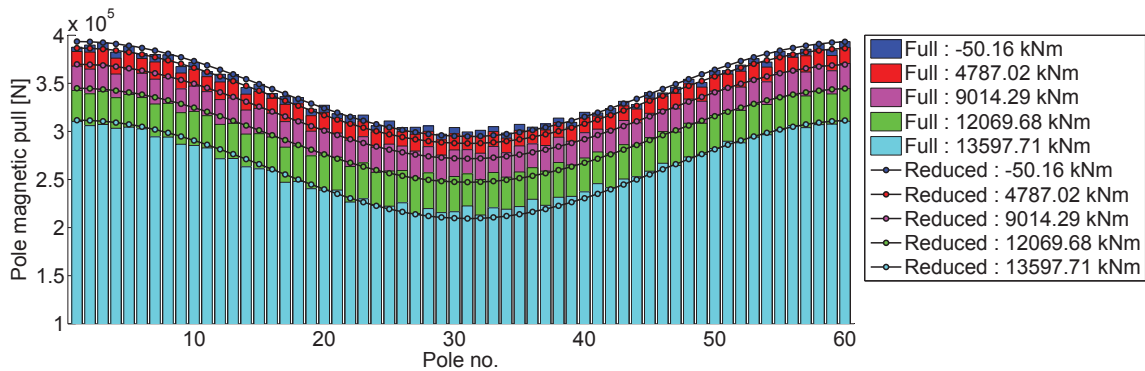
Reduced FEMM model		ABB results		Deviation	
Force [N]	Torque [Nm]	Force [N]	Torque [Nm]	Force [%]	Torque [%]
$259.9 \cdot 10^3$	$13.6 \cdot 10^6$	$249 \cdot 10^3$	$13.3 \cdot 10^6$	4.4	2.3

Table 3.3 Comparison of force and torque (@ max. torque zero eccentricity)

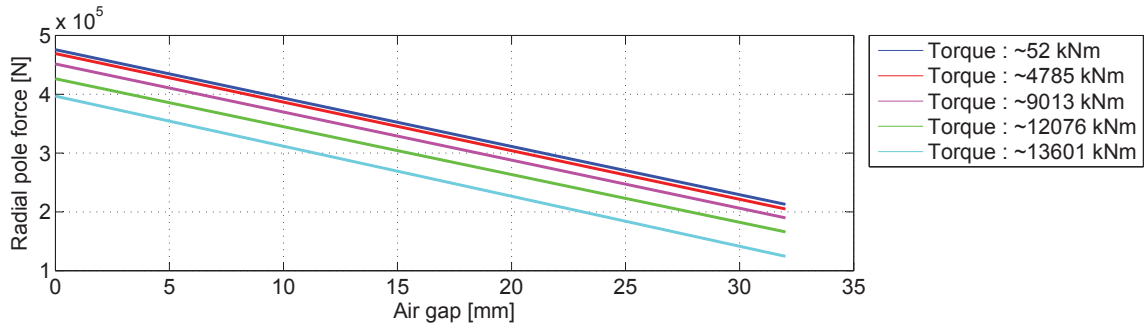
known that the results from ABB are found solely by analytical equations, whereas the results from the reduced model are found by finite elements which have a more detailed knowledge of the flux densities, a deviation of only 4.4% is assumed to be an acceptable deviation.



(a) Magnetic pull, 0.0 mm eccentricity



(b) Magnetic pull, 6.0 mm eccentricity



(c) Magnetic pull per pole as a function of air gap size

Figure 3.7 Magnetic pull per pole

3.5 Core and coil resistive losses

The global loss model consists of two types of losses, the core losses and the resistance losses. The core losses are losses in the iron part due to oscillation of the magnetic B-field within the material and the resistance losses are losses in the coils as current passes through them.

3.5.1 Eddy current & hysteresis losses

There are two major types of core losses in electrical machines. One is due to eddy currents and the other is due to hysteresis. The eddy currents are currents that are induced in the electric conducting core material when it is exposed to a varying magnetic field. These currents causes resistive losses in the core material which can be minimized either by increasing the resistance in the material and/or laminating the core material. Hysteresis loss in the core material is the energy expended to magnetize and demagnetize the core as it will resist to becoming magnetized. The losses in the material in one cycle of a applied field is proportional to the area inside the hysteresis loop formed by the B-H curve for the core material in question. One way of determine these losses is described in the following based on the procedure described in Meeker (2009), Dlala (2009), Bertotti (1988) and Chen and Pillay (2002). Through a series of static FEM calculations applied to the principle of separation of losses, it is possible to estimate the core losses. This principle is commonly used in estimation of losses in motors and transformers and state that it is possible to treat the different losses separately by assuming that the average losses in a material can be split up into hysteresis losses and eddy current losses. The hysteresis losses are defined as the oscillation frequency of the B-field in the material times the square of the peak value of the B-field times a loss coefficient times the mass, Eq.3.41. The equation for the eddy current losses looks almost the same, however, it is not just a function of the frequency, but of the square of the oscillation frequency, Eq.3.42. The two loss coefficients C_h and C_e , for hysteresis and eddy current losses respectively, are based on material loss curves provided by the material manufacture and will be determined in Sec.3.5.2.

$$P_h = C_h \cdot \omega \cdot B^2 \cdot \rho \cdot V \quad (3.41)$$

$$P_e = C_e \cdot \omega^2 \cdot B^2 \cdot \rho \cdot V \quad (3.42)$$

With the equation for hysteresis and eddy current losses, it is possible to estimate the total losses in a material experiencing a sinusoidal induced B-field with the oscillation frequency ω and peak value B by the use of Eq.3.43:

$$P_{loss} = P_h + P_e = (C_h \cdot \omega + C_e \cdot \omega^2) B^2 \cdot \rho \cdot V \quad (3.43)$$

This equation is only valid for sinusoidal B-field with a constant oscillation frequency and amplitude. However, in most cases the material is not just exposed to one frequency, but several frequencies at the same time. By creating a series of magneto static simulations Andersen et al. (2012b), where the rotor is rotated at least one pole pitch and the B-field in the centroid of every finite element cell is recorded for each step, it is possible to extract the amplitude of the B-field of each harmonic frequency in each cell by applying Fast Fourier Transformation, Fig. 3.8(b). If the rotor is rotated only one pole pitch the vector containing the B-field for the FFT has to be extended to cover 2 pole pitches by adding a copy of the calculated value with a sign change for the stator as the B-field in the stator for the next pole pitch would be the same as the first, but with opposite sign. The rotor will, however, experience the same B-field for the second pole pitch which therefore has

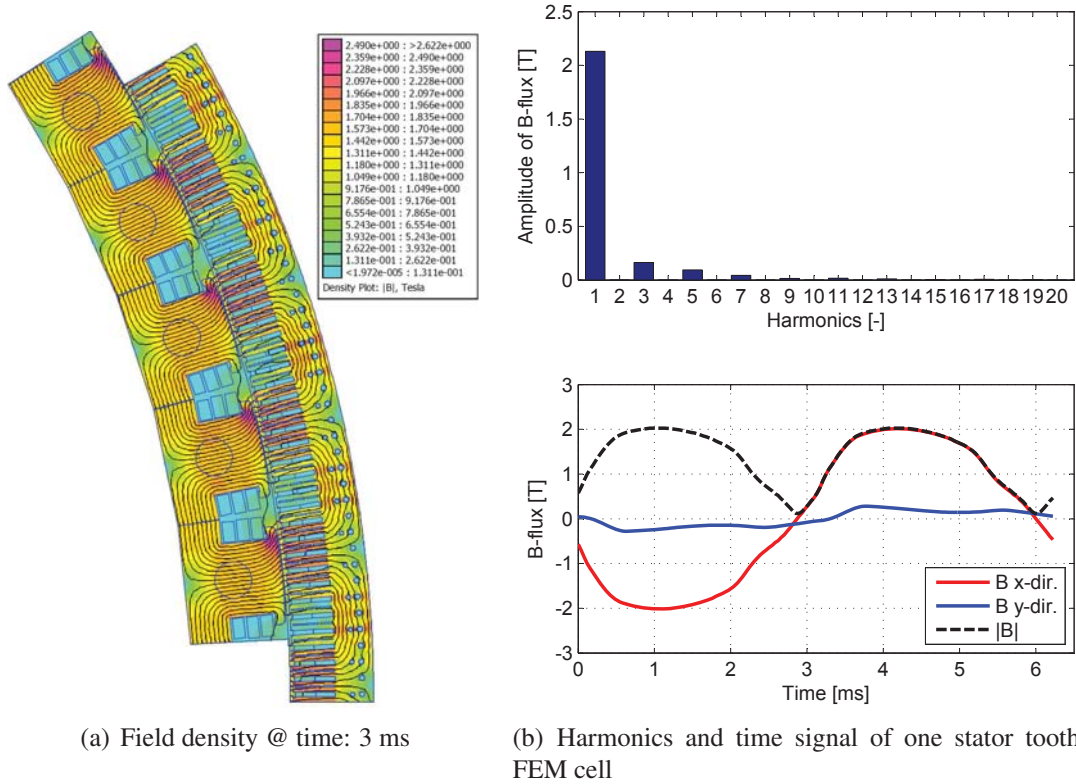


Figure 3.8 B-field in the center of a finite element cell in the stator tooth at rated currents, speed and torque.

to be added without a sign change. The square of the amplitude of each harmonic at the centroid of each element cell can now be found by the use of Eq. 3.44, 3.45 and 3.46:

$$\mathbf{B}_{x,\text{fft}} = |\text{fft}([\mathbf{B}_x; \pm\mathbf{B}_x])| \cdot \frac{2}{2 \cdot n_{\text{step}}} \quad (3.44)$$

$$\mathbf{B}_{y,\text{fft}} = |\text{fft}([\mathbf{B}_y; \pm\mathbf{B}_y])| \cdot \frac{2}{2 \cdot n_{\text{step}}} \quad (3.45)$$

$$\mathbf{B}^2 = \mathbf{B}_{x,\text{fft}} \circ \mathbf{B}_{x,\text{fft}} + \mathbf{B}_{y,\text{fft}} \circ \mathbf{B}_{y,\text{fft}} \quad (3.46)$$

where \mathbf{B}_x and \mathbf{B}_y are matrices containing the B-field for every element cell and steps for the x and y direction respectively. The corresponding frequency associated with each of the harmonic can be found by Eq. 3.47 where the last half of the entries are zeroed out as not to count each harmonic twice, as the upper half of the FFT is just a mirror of the lower half.

$$\omega = \frac{n_{\text{poles}}}{2} \cdot \Omega_{\text{base}} \cdot \omega_m \circ \omega_m \quad (3.47)$$

where

$$\omega_m = [0, 1, 2, \dots, n_{\text{step}}, 0, \dots, 0]_{1 \times 2 \cdot n_{\text{step}}} \quad (3.48)$$

With the use of Eq. 3.43 for each of the above found frequencies and corresponding amplitude of each finite element cell, it is possible by summation to find the total iron

loss, Eq. 3.49.

$$P_{Fe,total} = \frac{(\mathbf{C}_h \circ \boldsymbol{\omega} + \mathbf{C}_e \circ \boldsymbol{\omega} \circ \boldsymbol{\omega}) \cdot \mathbf{B}^2 \cdot (\boldsymbol{\rho}_{ele} \circ \mathbf{V}_{ele})^T}{C_{s,ele}} \cdot \frac{n_{poles}}{n_{polepair}} \quad (3.49)$$

where $\boldsymbol{\rho}_{ele}$ and \mathbf{V}_{ele} are vectors containing the density and volume of every element cell. The $C_{s,ele}$ in Eq. 3.49 is the element stacking factor and is introduced in the equation to take the reduced iron volume into account. The last fraction in Eq. 3.49 is to be added if the FEM model is a reduced model as the one shown in Fig. 3.8(a) where n_{poles} in this case is equal to 5. A flow diagram of the loss calculation procedure is shown in Fig. 3.9.

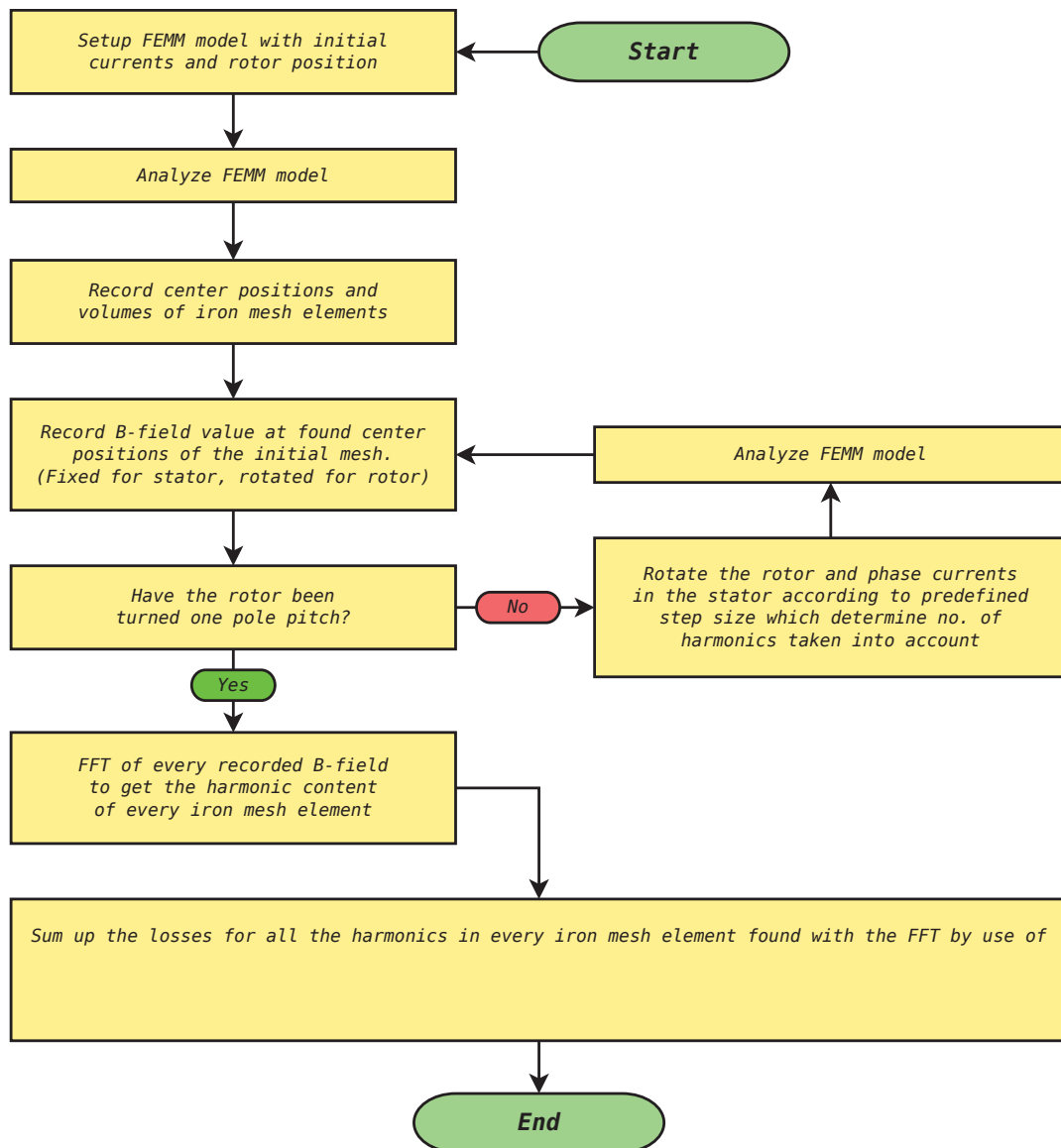


Figure 3.9 Flow diagram of the core loss calculation procedure

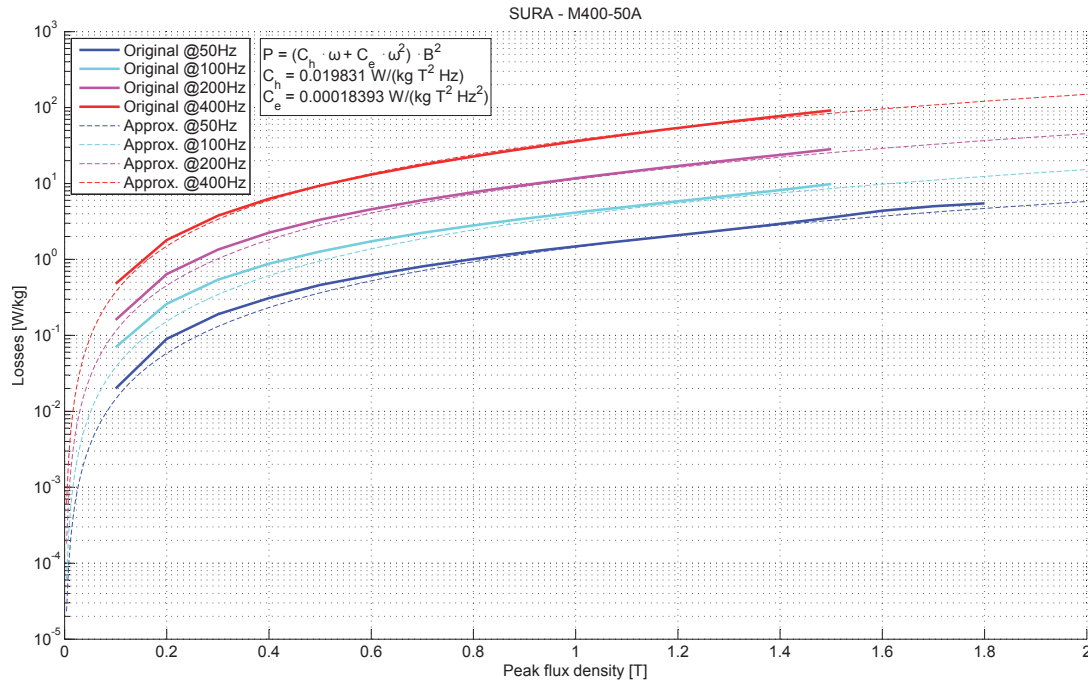


Figure 3.10 SURA - M400-50A Loss Curve Surahammars Bruks AB (2009)

3.5.2 Determination of hysteresis & eddy current loss coefficients

Before the losses can be determined by Eq. 3.49 the two loss coefficients C_h and C_e has to be estimated. This can be done with the help of the loss curves provided by the manufacturer/distributor of the core material. As an example, the loss curves for electric steel SURA M400-50A which is used for the stator core can be seen as the full bold curves in Fig. 3.10. These curves show the losses in W/kg in this case for four different sinusoidal oscillations frequencies of the B-field. By using Eq. 3.43 as an approximation polynomial, one can achieve the loss coefficients as the values which best fit the manufacture provided curves. In this case, the loss coefficients have been found to $C_h = 0.019831$ W/(kg·T²·Hz) and $C_e = 0.00018393$ W/(kg·T²·Hz²) and the approximation polynomial with these values are indicated by the dotted curves in Fig. 3.10).

3.5.3 Copper resistive losses

The majority of losses in an electrical motor originate from the resistive losses in the copper coils of the stator and the rotor. For this, the resistance of the coils has to be determined initially. The resistance of a material with a constant cross section area is proportional to the length and can be found by Eq. 3.50 where ρ_{ref} is the proportionality constant called electrical resistivity.

$$R_{ref} = \rho_{ref} \cdot \frac{L_{wire}}{A_{wire}} \quad (3.50)$$

The subscript “ref” refers to the reference temperature T_{ref} at which the resistance R_{ref} is found. This reference temperature is in the literature usually 20°C. As the coil temperature in the motor most likely is much higher than this, the resistance of the copper has to be corrected for this increase in temperature. If the temperature change is not too large, this can be accomplished by the use of Eq. 3.51 where α_{ref} is an empirical constant found called the temperature coefficient of resistance. As Eq. 3.51 is a linear approximation, it is important that α_{ref} has been found for the same reference temperature as R_{ref} has been calculated, respecting the Taylor approximation of $R_{wire}(T)$ around $T = T_{ref}$.

$$R_{wire} = R_{ref} \cdot (1 + \alpha_{ref} \cdot (T_{wire} - T_{ref})) \quad (3.51)$$

Once the temperatures of the copper coils are found the resistive losses can be found by Eq. 3.52 and Eq. 3.53 for stator and rotor coils respectively.

$$Loss_{Cu,s} = R_{wire,s} \cdot \left(\frac{I_{ph}}{\sqrt{2}} \right)^2 \quad (3.52)$$

$$Loss_{Cu,r} = R_{wire,r} \cdot I_{exc}^2 \quad (3.53)$$

The reason for the $\sqrt{2}$ in Eq. 3.52 is that I_{ph} is the peak phase current which needs to be the RMS current before it is squared according to Veltman et al. (2007).

3.5.4 Verification of loss models

The estimation of the coil length for calculating the resistance losses consists of several different length contributions to the most obvious active coil length. These contributions come from the twisting of the copper strands in the active part of the stator, connection between upper and lower coil segments, jump between slots in the stator and finally the end windings. The found lengths and cross section areas of the coils are listed in Tab. 3.4 and are the values used in the following calculations. To evaluate the presented loss model, a simulation is made with rated currents, speed and torques of the gearless drive while assuming that the copper coils are kept at a constant temperature of 75°C. Similar calculation has been carried out by Grinbaum (2012) using the same assumptions, but based on analytical equations. Results from Grinbaum (2012) can be seen in Tab. 3.5 and results from the finite element model can be seen in Tab. 3.6. Before a comparison can be made, it is important to note that the loss model used in Grinbaum (2012) only takes the first harmonic into account, when estimating the losses where the finite element model can estimate as many harmonics as the machine precision allows. For this reason, two simulations are made to estimate the losses coming only from the fundamental frequency and losses coming from the first 80 harmonics. Both results are listed in Tab. 3.6. As can be seen, there is a significant increase in the estimated core losses when using the first 80 harmonics as basis for the calculation compared to only the fundamental frequency. However, in order to allow a comparison between the different loss calculation

Parameter		Value	Description
L_{twist}	[mm]	25.0	Twist of copper strand in active length (stator per bar)
L_{con}	[mm]	120.0	Connection of coil bars at the ends (stator per bar)
L_{jump}	[mm]	72.12	Jump of coil bars between slots (stator per bar)
$L_{end,s}$	[mm]	1173.0	End windings (stator per bar)
$L_{active,s}$	[mm]	1250	Active coil length (stator per bar)
A_s	[m ²]	$9.8658 \cdot 10^{-4}$	Copper cross section area of parallel strands (stator)
$L_{end,r}$	[mm]	3313	End windings (rotor all poles)
$L_{active,r}$	[m]	7950	Active coil length (rotor all poles)
A_r	[m ²]	$245.85 \cdot 10^{-6}$	Copper cross section area of parallel strands (rotor)

Table 3.4 Electromagnetic losses - Data of length and cross section areas of copper coils

Stator			Rotor		
Yoke	[kW]	19.1	Pitch	[kW]	4.9
Teeth	[kW]	20.6	Pitch SC	[kW]	3.8
Teeth SC	[kW]	1.8			
Coil DC	[kW]	328.7	Field windings	[kW]	229.2
Coil AC	[kW]	4.4			
Total Fe losses	[kW]	41.5	Total Fe losses	[kW]	8.7
Total Cu losses	[kW]	333.1	Total Cu losses	[kW]	229.2

Table 3.5 Electromagnetic losses - Losses at 75°C calculated by Grinbaum Grinbaum (2012) using only the 1st harmonic.

Parameter	Value
Rotor core loss	[W] 536.42
Rotor core loss (only 1 st harmonic taken into account)	[W] 0.00
Stator core loss	[kW] 48.80
Stator core loss (only 1 st harmonic taken into account)	[kW] 41.86
Total core loss	[kW] 49.27
Loss/core volume (rotor)	[W/m ³] 41.15
Loss/core volume (stator)	[W/m ³] 4251.14
Stator resistance loss @ 75 °C (incl. end windings)	[kW] 347.72
Stator resistance loss in active part @ 75 °C	[kW] 167.92
Stator resistance loss/coil pack volume @ 75 °C	[kW/m ³] 77.1
Rotor resistance loss @ 75 °C (incl. end windings)	[kW] 230.54
Rotor resistance loss in active part @ 75 °C	[kW] 162.72
Rotor resistance loss/coil pack volume @ 75 °C	[kW/m ³] 76.8
Average torque	[MNm] 13.61
Mechanical power	[MW] 15.96

Table 3.6 Electromagnetic losses - Results from the FEMM loss calculation using the first 80 harmonics at rated current, speed and torque based on Andersen et al. (2012b).

approaches, namely presented in Grinbaum (2012) and in this work, only the fundamental frequency will be initially considered. Table 3.7 lists the results from the finite element model and the results from Grinbaum (2012) both considering only the fundamental frequency. Good agreement for stator core losses, rotor and stator resistance losses can be seen in Tab. 3.7 with only minor deviations, except for rotor core losses. However, as the rotor core is not experiencing a B-field with the fundamental frequency, it is obvious that the losses for this will be zero. The reason for this is that the only oscillation of the B-field in the rotor core comes from the rotor passing the slots and the fractional stator windings where the stator is experiencing the fundamental frequency due to the pulsating phase currents in the stator. However, taking the first 80 harmonics into account, it is seen that the total losses are not zero even though the losses are small, as the B-field is almost

Parameter		Value FEM	Value Grinbaum (2012)	Deviation
Rotor core loss (only 1 st harmonic)	[kW]	0.0	8.7	∞
Stator core loss (only 1 st harmonic)	[kW]	41.9	41.5	0.95%
Rotor resistance loss @ 75 °C	[kW]	230.5	229.2	0.6%
Stator resistance loss @ 75 °C	[kW]	347.7	333.1	4.2%

Table 3.7 Electromagnetic losses - Comparison of loss results, Grinbaum (2012).

constant within the rotor core material and only small oscillations occur at the top of the pole shoes. All in all, the finite element model has been verified against analytical results and proved to give similar results under similar assumptions.

Chapter 4

Estimation of cooling flows in gearless drives - Flow model

To be able to predict the temperatures within a motor an accurate determination of the cooling air flow is needed. This can be achieved in many different ways both numerical and analytical. If it is desired to get a detailed determination of the flow in complex structures CFD can be used as in Srinivas and Arumugam (2005) who model a switched reluctance motor in 3D. However, these 3D models can be quite computational expensive. A more fast and a more commonly used method is by the use of a lumped model adding up the losses for the different components of the flow system. This method has proven in several instances to be sufficient accurate for modeling the cooling flow in electric motors as for example shown in Traxler-Samek et al. (2008) and Traxler-Samek et al. (2010) who model a hydro-generator. The articles also show that these flow calculations should be closely connected with the electromagnetic and thermal model as these has an influence on each other.

This section will explain the theory behind the hydraulic calculation needed for determining the pressure losses in the cooling channels which later will be used in combination with the thermal model to determine the properties of the cooling flow. Furthermore, it will be possible to use the results to find a suitable cooling system for the drive.

4.1 Energy equation - Bernoulli's equation

The energy equation, Fox et al. (2004), also called Bernoulli's equation named after Daniel Bernoulli who first proposed it, can be written as:

$$\left(\frac{p_1}{\rho_d} + \alpha_{k,1} \frac{\bar{V}_1^2}{2} + gz_1 \right) - \left(\frac{p_2}{\rho_d} + \alpha_{k,2} \frac{\bar{V}_2^2}{2} + gz_2 \right) = h_{l_T} = \sum h_l + \sum h_{l_m} \quad (4.1)$$

The two first terms in brackets on the left hand side represent each the mechanical energy at a specific cross sections of a pipe and the terms on the right hand side represent the irreversible losses between two cross-sections due to heat generation and heat transfer losses. This equation can be used for calculating the pressure losses between two cross-sections of a pipe with constant cross section area. Assuming that $\alpha_{k,1} \cdot \frac{\bar{V}_1^2}{2} = \alpha_{k,2} \cdot \frac{\bar{V}_2^2}{2}$ and neglecting the effect of the gravitation, $z_1 = z_2$ the equation can be simplified to:

$$\frac{p_1}{\rho_d} - \frac{p_2}{\rho_d} = h_{l_T} = \sum h_l + \sum h_{l_m} \quad (4.2)$$

These assumptions will be used throughout the entire thesis. As indicated in the equation the total energy loss, h_{l_T} , can be split up as the sum of minor losses, h_{l_m} , plus the sum of major losses, h_l . The next sections will explain how these losses can be determined.

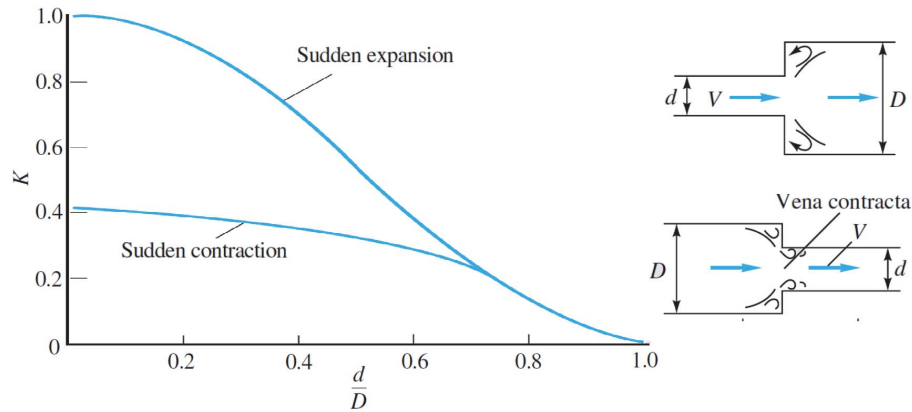


Figure 4.1 Loss coefficient for expansion and contraction, White (1998)

4.2 Head losses

Head losses can, as explained, be divided into minor losses and major losses. Minor losses consist of losses due to inlet and outlet conditions, sudden expansion and contraction of pipes, bends in pipes, valves and fittings. These losses are usually small compared to the total loss in systems consisting of long pipes with constant cross section areas, hence the name minor losses. Major losses, which are usually the dominant losses, are due to viscous friction between the pipe and the fluid, which generate heat which is stored in the fluid and/or dissipated through the pipe walls.

4.2.1 Minor losses

The minor losses can be defined in two ways, either by the loss coefficient or an equivalent length as shown in Eq.4.3

$$h_{lm} = K \frac{\bar{V}^2}{2} = f \frac{L_e}{D} \frac{\bar{V}^2}{2} \quad (4.3)$$

where K is the loss coefficient and L_e is the equivalent pipe length which results in equivalent losses. These constants can only be determined experimentally and are shown in Fig. 4.1 (Eq. 4.4) and Fig. 4.2 (Eq. 4.5) for pipe enlargement and contraction and Fig.4.3 for pipe bends. Loss coefficient for other fittings, valves and so on can be found in Fox et al. (2004) and White (1998).

$$K_{SE} = \left(1 - \frac{d^2}{D^2}\right)^2 \quad (4.4)$$

$$K_{SC} \approx 0.42 \left(1 - \frac{d^2}{D^2}\right)^2 \quad (4.5)$$

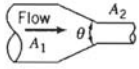
	Included Angle, θ , Degrees							
	A_2/A_1	10	15–40	50–60	90	120	150	180
	0.50	0.05	0.05	0.06	0.12	0.18	0.24	0.26
	0.25	0.05	0.04	0.07	0.17	0.27	0.35	0.41
	0.10	0.05	0.05	0.08	0.19	0.29	0.37	0.43

Figure 4.2 Loss coefficient for gradual contractions, Fox et al. (2004)

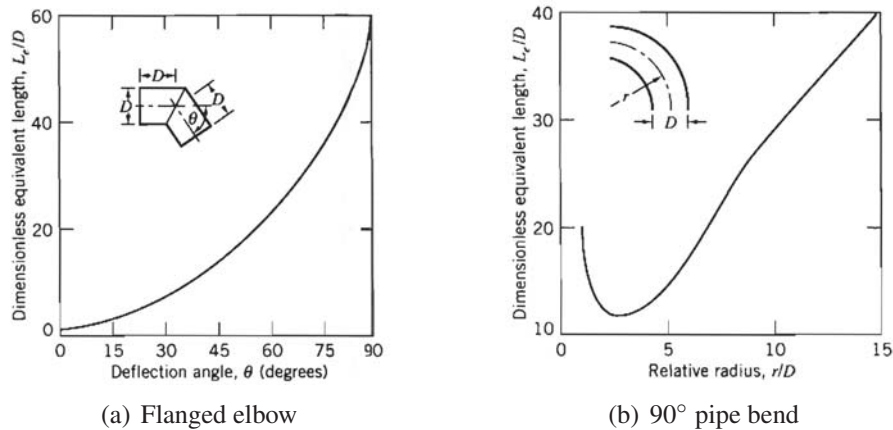


Figure 4.3 Equivalent length for pipe bends, Fox et al. (2004)

4.2.2 Major losses

Major losses are losses due to viscous friction between a fluid and its boundaries, which generate heat that is stored in the fluid itself and/or dissipated through its boundaries. The major losses are dependent on the length/diameter ratio of the pipe, the mean velocity of the flow and the friction factor which tell something about the friction between the fluid and the inner surface of the pipe. For a fully developed flow in a round pipe, the major loss can be determined by:

$$h_l = f \frac{L}{D} \frac{\bar{V}^2}{2} \quad (4.6)$$

4.3 Reynolds number

Before it is possible to determine the friction factor, the Reynolds number for the fluid has to be found. The Reynolds number, named after its inventor Osborne Reynolds, is a number that can, among other things, be used for determining if a fluid is in the laminar or turbulent regime. It is a measure of the ratio of inertial forces to viscous forces and is defined as:

$$Re = \frac{\rho_d \cdot \bar{V} \cdot D}{\mu_d} \quad (4.7)$$

4.4 Friction factor

There are two ways of determining the Darcy-Weisbach friction factor, either by the use of the Moody's diagram Fig. 4.4 or by the use of Darcy-Weisbach equation, Eq. 4.8, for the laminar regime and Colebrooks equation, Eq. 4.9 for the turbulent regime. Before the friction factor can be determined, the Reynolds number has to be known, as explained above, to determine if the flow is in the laminar or turbulent regime.

4.4.1 Laminar flow

When the Reynolds number for a fluid flow is below 2300, the flow is in the laminar regime. In this regime, the friction factor is easily determined as it is a linear function of the Reynolds number and is defined as:

$$f = \frac{64}{Re} \quad (4.8)$$

4.4.2 Turbulent flow

When the Reynolds number for a fluid flow is above 2300, the flow is in the tubular regime. The friction factor is not linear dependent on the Reynolds number anymore, but is a function of the diameter and roughness of the pipe walls as well. The equation for determining the friction factor for the turbulent regime is defined as:

$$\frac{1}{f^{0.5}} = -2.0 \cdot \text{Log} \left(\frac{e/D}{3.7} + \frac{2.51}{Re \cdot f^{0.5}} \right) \quad (4.9)$$

This equation can not be solved analytically and has to be solved iteratively.

4.4.3 Moody's diagram

The Moody's diagram shown in Fig. 4.4 is a diagram showing the friction factor curves for pipes with different Reynolds numbers and relative roughness. The Moody's diagram can be reproduced with the use of Eq. 4.8 and Eq. 4.9. A small table of common relative roughness can be found in the bottom left corner of Fig. 4.4.

4.5 Volume flow

The volume flow for a pipe with constant cross section area and mean velocity can be calculated by Eq. 4.10. If the volume flow is given, it is a simple matter to calculate the mean velocity which is needed for the above heat transfer calculations by isolating \bar{V} .

$$Q = \int_A \bar{V} \cdot d\bar{A} = \pi \frac{D^2}{4} \bar{V} \Rightarrow \bar{V} = \frac{4Q}{\pi D^2} \quad (4.10)$$

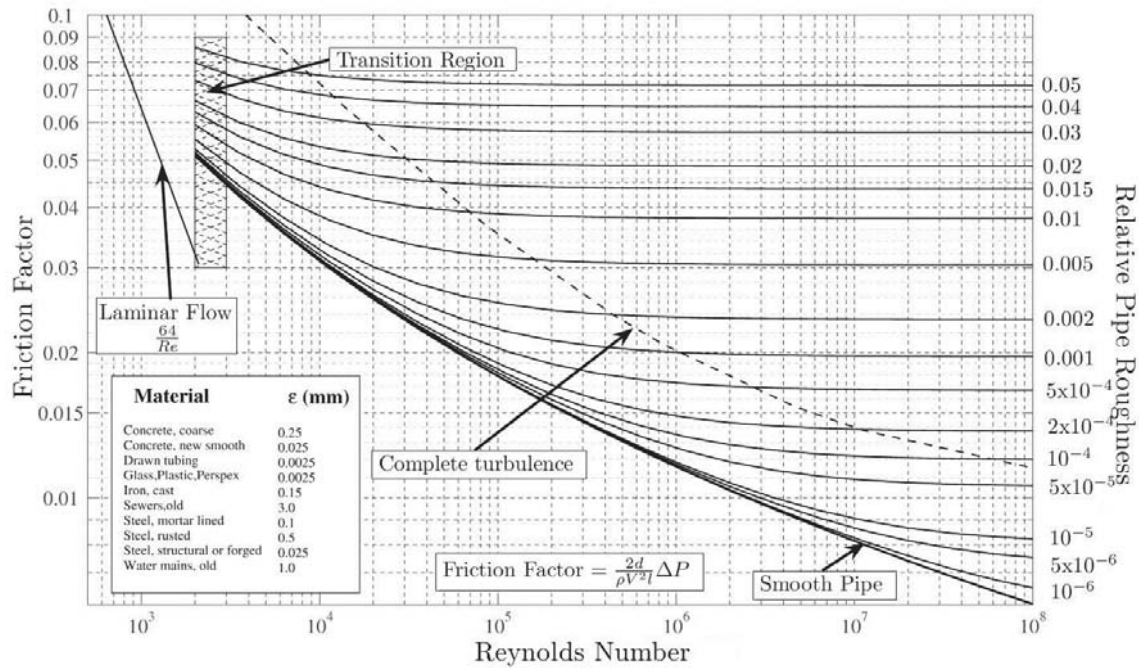


Figure 4.4 Moody diagram

4.6 Non-circular channels and hydraulic diameter

All the above theory and equations explain how it is possible to calculate flow and pressure losses in circular pipes. As this is far from the only type of channels used for fluids, there is a need for estimating an equivalent diameter for other geometries. This diameter is called the hydraulic diameter and is defined as, White (1998):

$$D_h = \frac{4A}{P} \tag{4.11}$$

where A is the cross section area and P is the wetted perimeter of the channel. For a rectangular channel the hydraulic diameter would therefore be:

$$D_h = \frac{4 \cdot h \cdot w}{2 \cdot (h + w)} \tag{4.12}$$

where h is the height and w is the width of the channel. The above equation will, according to Fox et al. (2004), give results with acceptable accuracy for a height/width ratio of approximately $1/4 \leq h/w \leq 4$. Beyond this ratio and for irregular shaped channels experimental values must be used.

Channel no.	1	2	3	4	5	6
a, width [mm]	28.1	137.5	428.0	94.0	94.0	2.5
b, height [mm]	193.0	72.0	18.0	11.0	11.0	180.0
D, diameter [mm]	-	-	-	-	-	-
L, length [mm]	1250.0	1250.0	1250.0	1250.0	1250.0	1250.0
e, roughness [mm]	0.3	0.3	0.3	0.3	0.3	0.3
No. of channels	60	60	60	120	120	60
Channel no.	7	8	9	10	11	
a, width [mm]	-	-	6.0	6.0	6.0	
b, height [mm]	-	-	52.0	52.0	52.0	
D, diameter [mm]	23.5	19.5	-	-	-	
L, length [mm]	1250.0	1250.0	1250.0	1250.0	1250.0	
e, roughness [mm]	0.3	0.3	0.3	0.3	0.3	
No. of channels	504	252	504	504	504	

Table 4.1 Fluid flow model - Channel dimensions

Parameter	Value	Description
H_{alt}	4100	Altitude [m]
$C_{s,ele}$	0.97	Lamination stacking factor
$A_{Fe,r}$	$179.90 \cdot 10^{-3}$	Cross-section area of the iron part of one rotor pole [m ²]
$A_{Fe,s}$	9.6548	Cross-section area of the iron part of the stator [m ²]
$A_{Cu,r}$	$26.060 \cdot 10^{-3}$	Cross-section area of the copper part of one rotor pole [m ²]
$A_{Cu,s}$	$0.9866 \cdot 10^{-3}$	Cross-section area of the copper part of one stator coil pack [m ²]
$A_{Coil,r}$	$28.254 \cdot 10^{-3}$	Cross-section area of the coil packs in one rotor pole [m ²]
$A_{Coil,s}$	$1.728 \cdot 10^{-3}$	Cross-section area of one coil pack in the stator
L_{motor}	1.250	Axial length of the motor [m]
T_{ini}	36.4	Initial temperature after the cooler [°C]
n_{poles}	60	Number of poles [-]
Q_s	504	Number of slots [-]

Table 4.2 General parameters

4.7 Cooling channel geometry model

Figure 4.5(a) shows a section of the rotor and the stator of the electric motor which is analyzed and Fig. 4.5(b) shows a close-up of approximately one stator tooth including coils. The green rectangles and circles indicate the cooling flow channels which are used in the calculations. Even though not all of the channels are rectangles, it is assumed to only have minor effect on the accuracy as long as the cross section area of the channels and the perimeter are comparable. Each of the channels is numbered according to the number in the blue circle beside the channels. It is this number that has been referred to in Tab. 4.1 which shows the dimensions used for the channels. Every subsequent content will use this numbering of the channels for both the flow and heat calculation. Table 4.1 also shows how many parallel channels there are of the different channels based on the number of poles and number of slots of the motor which can be found in Tab. 4.2. It is assumed that the system only consists of two nodes, one at each end of the motor. All the channels are connected to these two nodes resulting in a pressure drop between the nodes. To counteract this pressure drop, a fan has been connected between the nodes as well. A diagram of the system can be seen in Fig. 4.6. The justification for the assumed two node model is that the chambers in each side of the frame is much larger than the described cooling channels which result in considerable lower flow velocities and pressure losses in these chambers.

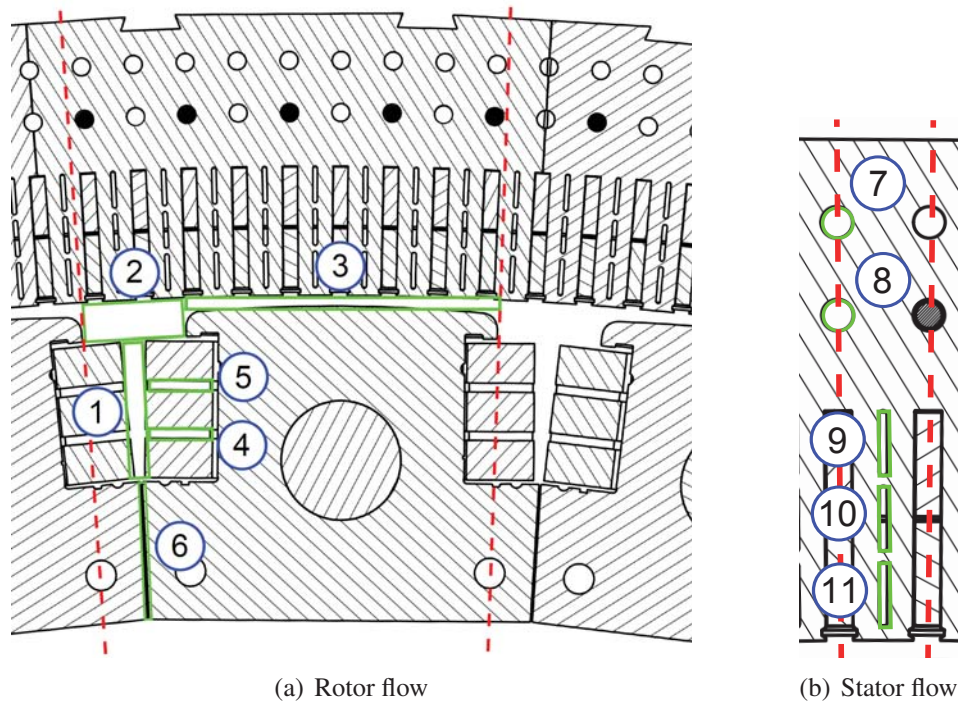


Figure 4.5 Flow channels through motor

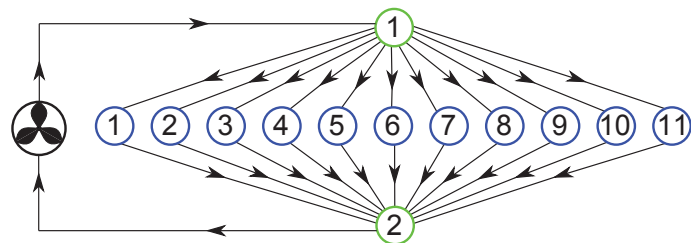


Figure 4.6 Flow diagram for motor cooling

4.8 Mathematical model

Newton-Raphsons method is used for solving the hydraulic system of equations as these cannot be solved analytically. In this case, there are 11 functions for the channels of the form:

$$\tilde{\mathfrak{F}}_{1-11} = \frac{8 \cdot Q^2}{\pi^2 \cdot D_h^4} \left(f \frac{L}{D_h} + K_{SE} + K_{SC} \right) - \frac{p_1 - p_2}{\rho_d} = 0 \quad (4.13)$$

which are based on Bernoulli's energy equation, Eq. 4.1. Furthermore there is 1 function for the fan which says that the flow through the fan must be equal to the sum of flow through the cooling channels:

$$\tilde{\mathfrak{F}}_{12} = Q_{tot} - \sum_{i=1}^{11} Q_i \cdot N_{O_{channels,i}} = 0 \quad (4.14)$$

By assuming that the total flow through the fan is known, it is possible to set up a vector \mathbf{x} containing all the unknown parameters which here are the 11 volume flows, Q_{1-11} , and the differential pressure between node 1 and node 2, Δp :

Unknown: $\mathbf{x} = \{Q_1, Q_2, Q_3, Q_4, Q_5, Q_6, Q_7, Q_8, Q_9, Q_{10}, Q_{11}, \Delta p\}^T$

By making some initial guesses for the unknowns, it is possible iteratively to get closer to the correct value by the use of Eq. 4.15:

$$\mathbf{J} \cdot \mathbf{q} = -\mathbf{F} \quad (4.15)$$

\mathbf{J} is the Jacobian matrix which is defined as the partial derivatives of the functions, $\tilde{\mathfrak{F}}_{1-12}(\mathbf{x})$, with respect to the unknown parameters and \mathbf{F} is a vector containing the function values calculated with the initial guessed values. In matrix form, this will look as shown in Eq. 4.16 where n is the number of functions, in this case $n = 12$.

$$\begin{bmatrix} \frac{\partial \tilde{\mathfrak{F}}_1(\mathbf{x})}{\partial x_1} & \frac{\partial \tilde{\mathfrak{F}}_1(\mathbf{x})}{\partial x_2} & \dots & \frac{\partial \tilde{\mathfrak{F}}_1(\mathbf{x})}{\partial x_n} \\ \frac{\partial \tilde{\mathfrak{F}}_2(\mathbf{x})}{\partial x_1} & \frac{\partial \tilde{\mathfrak{F}}_2(\mathbf{x})}{\partial x_2} & \dots & \frac{\partial \tilde{\mathfrak{F}}_2(\mathbf{x})}{\partial x_n} \\ \vdots & \vdots & \ddots & \vdots \\ \frac{\partial \tilde{\mathfrak{F}}_n(\mathbf{x})}{\partial x_1} & \frac{\partial \tilde{\mathfrak{F}}_n(\mathbf{x})}{\partial x_2} & \dots & \frac{\partial \tilde{\mathfrak{F}}_n(\mathbf{x})}{\partial x_n} \end{bmatrix} \cdot \begin{Bmatrix} q_1 \\ q_2 \\ \vdots \\ q_n \end{Bmatrix} = - \begin{Bmatrix} F_1 \\ F_2 \\ \vdots \\ F_n \end{Bmatrix} \quad (4.16)$$

Solving this for the \mathbf{q} vector, it is possible to get values which are closer to the correct values by adding the \mathbf{q} vector to the \mathbf{x} vector consisting of the current values for the unknown.

$$\mathbf{x}_{i+1} = \mathbf{x}_i + \mathbf{q}_i \quad (4.17)$$

The new values for the unknown can then be used for another iteration until the absolute value of the \mathbf{q} vector falls below a certain predefined limit determining the precision of the results in the \mathbf{x} vector.

As the friction coefficient f in Eq. 4.13 has to be determined iteratively it is not possible

to form the Jacobian matrix analytically which is therefore done numerical with a $dx = 10^{-10}$. On the other hand, the equation for the fan can be solved analytically and the Jacobian matrix for the fan is therefore also made analytically. However, a problem in the iteration can arise, as the function of the friction coefficient f is discontinuous, as it jumps between the laminar and turbulent regime. For this reason, it has been necessary to introduce a transition region to make the function continuous. This transition region is set to be between Reynolds numbers of 2300 to 3300 and the friction coefficient in this range is defined as:

$$f = \left(1 - \frac{Re - 2300}{1000}\right) \cdot f_{laminar} + \frac{Re - 2300}{1000} \cdot f_{turbulent} \quad (4.18)$$

4.9 Fan/cooler losses

As the fans and coolers are placed inside the frame, the losses from these components will contribute to the heating of the air and can therefore not be neglected in neither the flow nor the thermal calculations which will be described in the next section. Initially, these losses will, however, be kept constant at a value of $Loss_{fan} = 106.3$ kW due to verification against results received from ABB. However, as the fan/cooler losses obviously increase as the produced flow increases, it would be wrong to maintain a constant loss. These losses will also later be part of a multi objective optimization for minimizing masses and losses, which is another reason why it can not be kept constant. As the design of the fan/cooling system is out of the scope of this thesis and no loss curves have been available it is just assumed that there is a linear relationship between the produced flow and the fan losses. The fan loss of 106.3 kW should according to ABB come from a fan/cooler system which could cool the coils to 90°C. Several simulations of the final global model have been performed to find the cooling flow which would achieve this goal, $Q \approx 53$ m³/s. Drawing a straight line from (0 m³/s, 0 kW) through (53 m³/s, 106.3 kW) would result in this linear relationship, Fig. 4.7, which is used in the global optimization

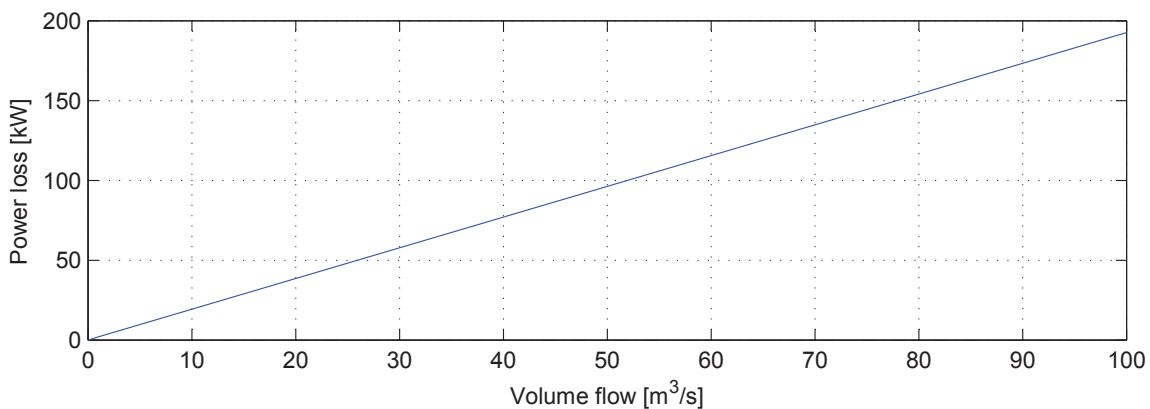


Figure 4.7 Fan losses as a function of volume flow

Channel number	Hydraulic diameter [m]	flow rate [m ³ /s]	Mean vel. [m/s]	Pressure drop [Pa]
1	0.0491	4.89	15.04	170.0
1 Bermudez (2012)	0.0634	5.77	15.98	170.0
<i>Deviation</i>	22.6%	15.3%	5.9%	0.0%
2	0.0945	9.19	16.84	170.0
3	0.0346	7.70	14.18	170.0
2+3 Bermudez (2012)	0.0585	16.03	15.72	170.0
<i>Deviation</i>		5.4%	1.3%	0.0%
4+5	0.0197	2.72	10.96	170.0
4+5 Bermudez (2012)	0.0208	2.68	11.08	170.0
<i>Deviation</i>	5.3%	1.5%	1.1%	0.0%
6	0.0049	0.06	2.94	170.0
6 Bermudez (2012)	-	-	-	170.0
7	0.0235	2.56	11.70	170.0
7 Bermudez (2012)	0.0235	2.56	11.73	170.0
<i>Deviation</i>	0.00%	0.0%	0.3%	0.0%
8	0.0195	0.81	10.77	170.0
8 Bermudez (2012)	0.0195	0.81	10.76	170.0
<i>Deviation</i>	0.00%	0.0%	0.1%	0.0%
9+10+11	0.0108	3.68	7.80	170.0
9+10+11 Bermudez (2012)	0.0110	3.58	7.78	170.0
<i>Deviation</i>	1.8%	2.8%	2.6%	0.0%

Table 4.3 Fluid flow model - Results and comparison to Bermudez (2012), (same input).

model, Sec. 7. If the assumption of the linear relationship is far from the truth, it is a simple matter at a later point to exchange this relationship in the model with a more correct one.

4.10 Verification of flow model

Before any comparisons are made for verification of the flow model, it has to be mentioned that not all of the channels fulfill the criteria for the height/width ratio stated for the use of Eq. 4.12. However, in lack of any better determination of the hydraulic diameter, it has been chosen to use Eq. 4.12 anyway, keeping in mind that this is a possible course of error. Even though the limit for Eq. 4.12 has been exceeded, the results seem reasonable based on for example the flow in channel 6, Tab. 4.3. This channel is a very narrow channel compared with the other channels and, as expected, it also has a much smaller flow than the other channels. For validation of the fluid flow model, preliminary results have been received from ABB Bermudez (2012) using the same input values for both models, Tab. 4.4. These results are listed in Tab. 4.3 where the channel numbers refer to the numbering in Fig. 4.5. It has to be mentioned that these results are only for verification purposes and do not reflect the results of the final flow for the drive. The results show a deviation of the fluid flow rate of less than 3%, except for channel 1 and 2+3 which have a deviation of 15.3% and 5.4%. However, adding up the flow rate in these channels and comparing the total flow rate for these channels result in a deviation of 0.1%, which could indicate a different split-up of the air gap at the rotor. The large deviation in the hydraulic diameter for channel 1 also backup this theory. Accepting this as the cause of deviation, there is

Parameter		Value
Rotor core loss	[W]	536.42
Stator core loss	[kW]	48.80
Stator resistance loss @ 75 °C (incl. end windings)	[kW]	347.72
Rotor resistance loss @ 75 °C (incl. end windings)	[kW]	230.54
Altitude of drive	[m]	4100
Axial length of the motor	[m]	1.250
Initial temperature after the cooler	[°C]	36.4
Final differential pressure	[Pa]	170

Table 4.4 Input values used in flow model comparison

a relatively good agreement in all the cases. The reason for the lack of comparison of channel 6 in Tab. 4.3 is due to the fact that this channel has been neglected by ABB in their model.

Chapter 5

Determination of heat distribution in gearless mill drives - Thermal model

Accurate determination of the temperature distribution in electric motors is very important as this will have an impact on many different areas in the motor. For example, when the temperature increases, the resistance losses and needed cooling flow will also increase and so will the thermal expansion of the different motor parts which again has an impact on other areas. Several different methods of determine the temperature distribution are possible where the most common one are the lumped thermal model Boglietti et al. (2008), Boglietti et al. (2003), Trigeol et al. (2006), Chin and Staton (2004). If higher detailed knowledge of the temperature distribution within complex parts are needed two other methods can be used namely the finite difference method Drubel and Runge (2004) and the more commonly used finite element method Chin and Staton (2004), Boglietti et al. (2009), Minghui and Weiguo (2010). Each of these methods have their advantages and disadvantages. The advantage of the lumped thermal model is that it is extremely fast in estimating the temperatures within the different motor parts. However, it less suited for complex geometries where the other two mentioned methods are superior. The finite difference and the finite element methods are more computational expensive, however, it is still manageable with todays computers if they are kept in 2D. As a last check one could redo the final motor design in a 3D finite element model as has been done in Komeza et al. (2010) for a three-phase induction motor, however, this will be to time consuming to do in the initial design phase as several iterations might be needed.

This section will derive and present the thermal models which are used for the determination of the temperature distribution in the rotor and stator of the ring motor in question. Two different models are made for modeling the heat distribution in the gearless drive. The first assume that it is sufficient to look only at a cross section in the center of the gearless drive, assuming that the cooling flow temperature can be kept constant at an elevated temperature compared to the outlet temperature of the cooler, equivalent to that half of the losses are transferred into the fluid. Furthermore, the coil losses used are assumed to be constant in the axial direction and are calculated at an assumed 90°C copper temperature. The second model is more refined, as it is sliced in several pieces in the axial direction as shown for the pole in Fig. 5.1. The cooling flow temperature in the different channels are constantly updated by the heat flux transfered to the fluid from the previous cross section slice. Furthermore, the coil losses are updated iteratively according to the coil temperature of the current slice. The cooling flow temperature of the first slice is determined as the temperature of the flow from the cooler, where the losses from the end windings are added. The temperatures of the end winding are assumed to be the same as the winding temperature of the first slice, which again is found iteratively. The mass

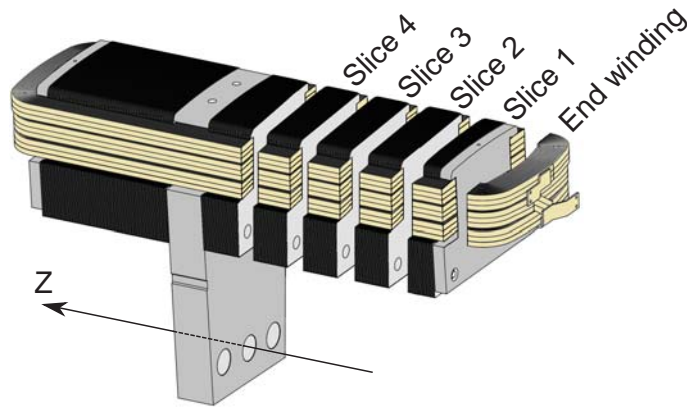


Figure 5.1 Sliced rotor pole in axial direction

flow for both models is determined with air properties equivalent to the air properties in the different channels in the center of the drive, which is the same for all the channels in the center slice model and different for the different channels in the multi sliced model. If the initial guesses of these air properties are not within an acceptable error the whole model is run again with updated air properties from the previous calculation. A flow diagram of the calculation procedure for the multi sliced model can be seen in Fig. 5.2. The center slice model is simulated with both the explicit finite difference method and the finite element method, where the multi sliced model is only modeled with the finite element method due to the time consuming explicit finite difference method. The explicit finite difference model is programmed in Fortran and the finite element models is created in the program FEMM. The following will briefly describe the models with major focus put on the finite difference model as it is programmed completely in Fortran, whereas the finite element model is created with the commercial software FEMM. An in depth explanation of the finite difference method can be found in Incropera et al. (2006), however, a short description is in place.

5.1 Finite difference thermal calculations

The energy balance equation state that the energy that enters a control volume, plus the energy that is generated in the control volume must equal the energy stored in the control volume. This can be written as:

$$\dot{E}_{in} + \dot{E}_{gen} = \dot{E}_{st} \quad (5.1)$$

where energy that leaves the control volume is added as negative energy flow. The energy that enters/leaves the control volume could be due to conduction between the control volume and the neighbor material through the control volume's sides. Another source of energy leaving/entering the control volume is through convection between the control volume's sides and a heating/cooling fluid.

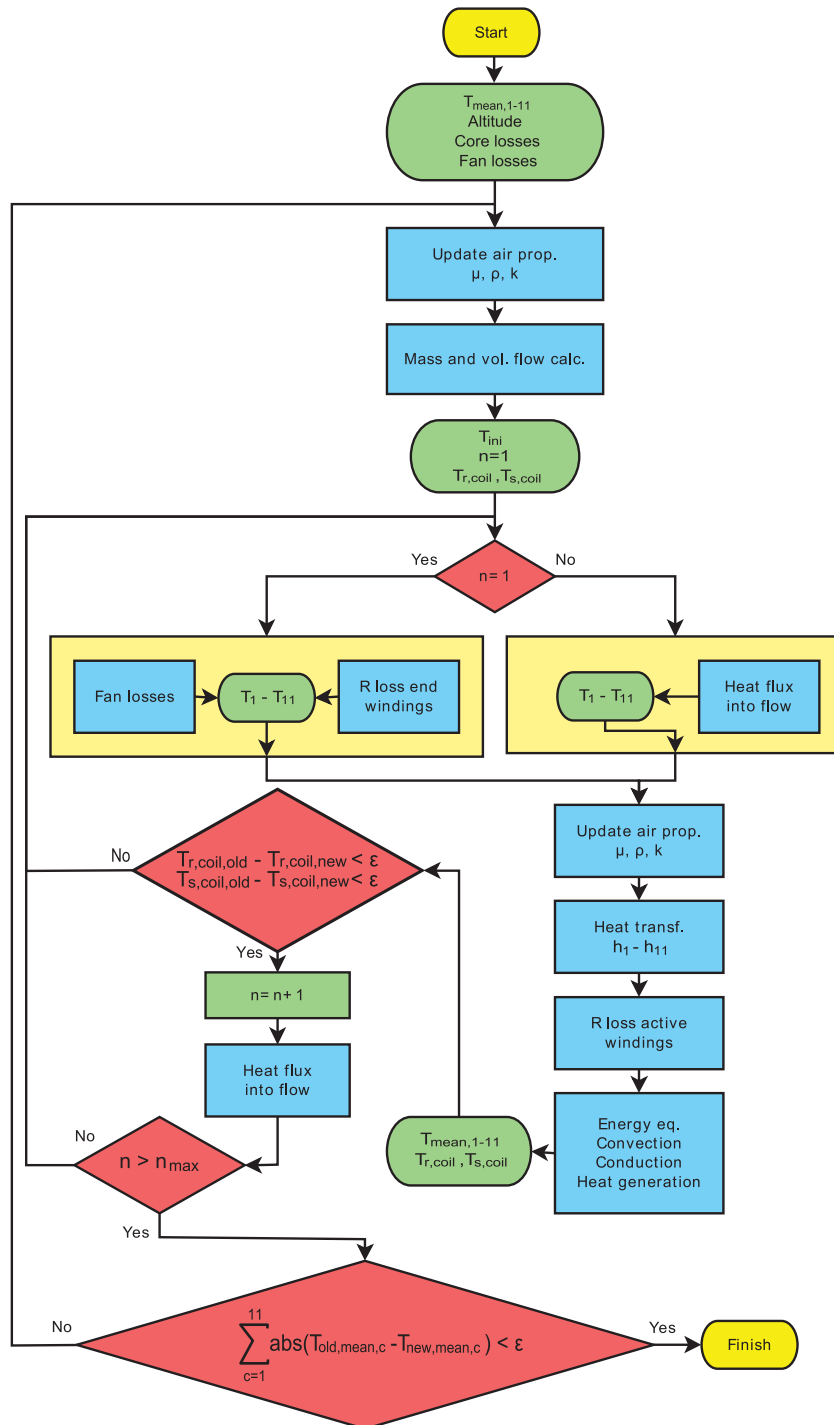


Figure 5.2 Flow diagram for iterative flow and temperature calculations

When solving for the nodal temperature, $T_{m,n}$, there are 4 general situations which are illustrated in Fig. 5.3. In case a) the node is an internal node where only heat generation in the control volume indicated by the colored box and conduction between neighbor control volumes can occur.

The energy flow done by conduction can be found by:

$$\begin{aligned}
 q_{cond} = & \underbrace{L \cdot \Delta y \frac{k_{m+1,n}}{\Delta x} (T_{m+1,n}^t - T_{m,n}^t)}_{\text{Conduction with node}_{m+1,n}} + \underbrace{L \cdot \Delta x \frac{k_{m,n-1}}{\Delta y} (T_{m,n-1}^t - T_{m,n}^t)}_{\text{Conduction with node}_{m,n-1}} \\
 & + \underbrace{L \cdot \Delta y \frac{k_{m-1,n}}{\Delta x} (T_{m-1,n}^t - T_{m,n}^t)}_{\text{Conduction with node}_{m-1,n}} + \underbrace{L \cdot \Delta x \frac{k_{m,n+1}}{\Delta y} (T_{m,n+1}^t - T_{m,n}^t)}_{\text{Conduction with node}_{m,n+1}} \quad (5.2)
 \end{aligned}$$

where the 4 terms on the RHS are conduction through the control volume's 4 edges.

The term for the energy generation, if there is any, is just the volumetric energy rate multiplied by the volume of the control volume as shown in Eq. 5.3.

$$q_{gen} = \dot{q} \cdot L \cdot \Delta x \cdot \Delta y \quad (5.3)$$

The stored energy in the control volume can be expressed as the density multiplied by the heat capacity multiplied by the volume multiplied by the time derivative of the temperature as shown in Eq. 5.4

$$q_{st} = \rho_{solid} \cdot C_{solid} \cdot L \cdot \Delta x \cdot \Delta y \frac{T_{m,n}^{t+dt} - T_{m,n}^t}{dt} \quad (5.4)$$

In case b), c) and d) in Fig. 5.3 some of the control volume has been removed compared with case a) where convection has been added. Due to the smaller control volume Eq. 5.2, 5.3 and 5.4 have to be corrected for this reduction. As an example, the conduction in the $(m+1, n)$ and $(m, n-1)$ directions of case b), under the assumption that $\Delta x = \Delta y$, would only be half of that of case a), as the area has been reduced to half in these two directions. For the heat generation in case b), again under the assumption that $\Delta x = \Delta y$, would be reduced to 3/4 of that of case a), as the volume has been reduced to 3/4.

The convective energy from a fluid at constant temperature where $\Delta x = \Delta y$ can be determined by:

$$q_{conv} = h \cdot L \cdot \Delta x (T_{conv} - T_{m,n}^t) \quad (5.5)$$

This expression for the convective energy is independent of being in case b), c) or d) as long as $\Delta x = \Delta y$. This is due to the fact that the convective area is the same for the three different cases.

Combining Eq. 5.1 to Eq. 5.5 and rearranging, it is possible to determine the temperature at time $t + dt$ when the temperature distribution at time t is known.

$$T_{m,n}^{t+dt} = \frac{(q_{cond} + q_{conv} + q_{gen}) \cdot dt}{\rho_{solid} \cdot C_{solid} \cdot L \cdot \Delta x \cdot \Delta y} + T_{m,n}^t \quad (5.6)$$

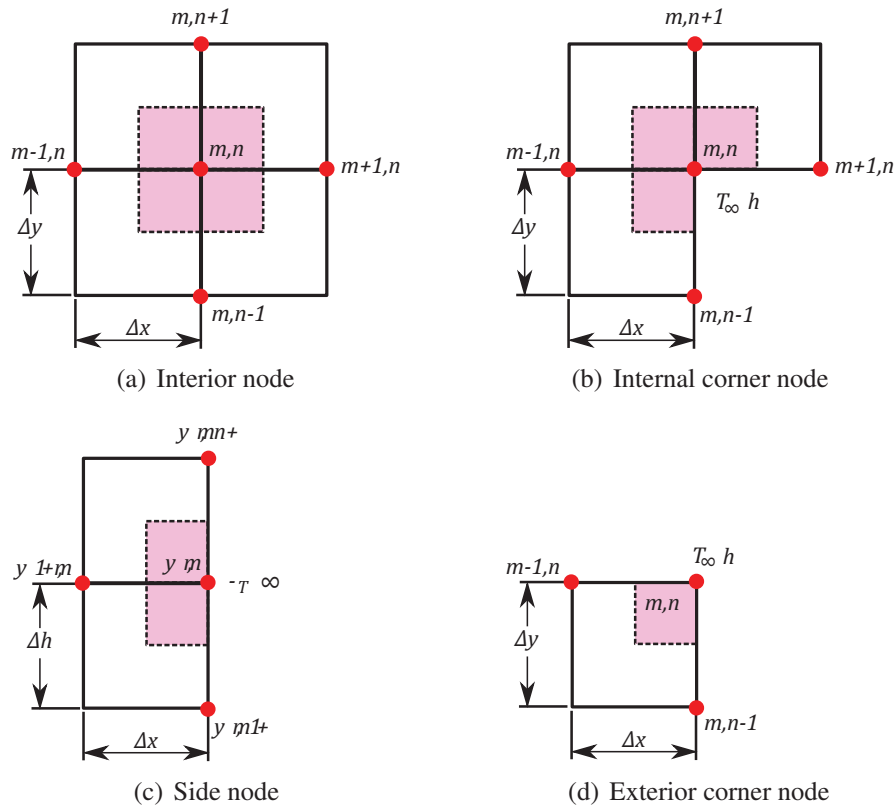


Figure 5.3 Finite difference cases

For modeling an adiabatic or symmetry line boundary condition the expression for the conduction Eq. 5.2 has to be corrected. This is most easily done by adding this boundary effect to the thermal conductivity constant of the solid. If looking at case d) as an example and assuming that the convection surface has been perfectly insulated. This will result in $k_{m+1,n} = k_{m,n+1} = 0$, as no convection occurs in these direction and $k_{m-1,n} = k_{m,n-1} = k_{solid}/2$ as only half of the conductive area is available under the assumption that $\Delta x = \Delta y$. The generated and stored energy, Eq. 5.3 and Eq. 5.4, has of course to be corrected as well according to the volume of the control volume.

In cases where two different materials meet in a control volume, the thermal conductivity in the direction of the boundary between the two materials has to be changed to $k_{equivalent} = (k_{solid,1} + k_{solid,2})/2$.

5.2 Forced convection

To be able to calculate the convection between a fluid and a solid, the heat transfer coefficient h has to be determined. This is normally done by the use of empirical equations and

is defined by:

$$h = \frac{k_f}{D_h} \cdot Nu \quad (5.7)$$

There are many different empirical equations for determining the Nusselt number, Nu , which is especially optimized for different geometries and parameter ranges. This thesis will, however, only focus on the determination of the Nusselt numbers for forced convection in internal duct flows.

For internal turbulent flow Kreith (2000) suggests that the Nusselt number is to be found by the empirical equation:

$$Nu = \frac{(f/2) \cdot (Re - 1000) \cdot Pr}{1 + 12.7 \cdot (f/2)^{0.5} \cdot (Pr^{2/3} - 1)} \cdot \left(1 + \left(\frac{D}{L}\right)^{2/3}\right) \cdot \left(\frac{T_f}{T_s}\right)^{0.45} \quad (5.8)$$

which is valid for the following ranges:

$$0.6 \leq Pr \leq 2000, 2300 \leq Re \leq 10^6, 0 \leq \frac{D}{L} \leq 1$$

and f is defined as:

$$f = (1.58 \cdot \ln(Re) - 3.28)^{-2} \quad (5.9)$$

The Prandtl number, Pr , can be found by Eq. 5.12.

For internal laminar flow Incropera et al. (2006) suggest that the Nusselt number is to be found by the empirical equation:

$$Nu = 1.86 \cdot \left(\frac{Re \cdot Pr}{(L/D)}\right)^{1/3} \cdot \left(\frac{\mu_d}{\mu_s}\right)^{0.14} \quad (5.10)$$

which is valid for the following ranges:

$$0.6 \leq Pr \leq 5, Re \leq 2300, 0.0044 \leq \frac{\mu_d}{\mu_s} \leq 9.75, Nu \geq 3.66$$

In the case that the Nusselt number found by Eq. 5.10 falls below $Nu = 3.66$, Incropera et al. (2006) suggest that Eq. 5.11 is to be used instead.

$$Nu = 3.66 + \frac{0.0668 \cdot (D/L) \cdot Re \cdot Pr}{1 + 0.04 \cdot ((D/L) \cdot Re \cdot Pr)^{2/3}} \quad (5.11)$$

which is valid for the following ranges:

$$Re \leq 2300, Nu < 3.66$$

The Prandtl number used above to find the Nusselt number is another dimensionless number frequently used in heat calculation and is defined as the ratio of momentum and thermal diffusivity:

$$Pr = \frac{\nu}{\alpha} = \frac{C_p \cdot \mu_d}{k_f} \quad (5.12)$$

5.3 Heat transfer in the solid parts

The schematics of the motor for the heat transfer analysis is shown in Fig. 5.4 with the dimensions listed in Tab. 5.1. The different colors indicate the different material where gray is iron, M400-50A for the stator and St.42 for the rotor. The yellow color is the insulation material and the brownish color is the copper/coil packs. The red lines on the edges of the solids indicate surfaces which have convection with the cooling flow found in previous section. The blue lines indicate adiabatic boundary conditions which are either a symmetry line or a surface which is considered to have no heat flux passing through it. The stator section is modeled with parallel symmetry lines at the sides, which are acceptable assumptions as the radius of the rotor is large and the error in connection with this assumption will therefore be minimal. The coils in the rotor and stator do not just consist of copper, but of copper bars wrapped in one or several layers of insulation. Figure 5.5 show the schematics of the coil packs for the stator and rotor. The different layers of insulation are assumed to be made of the same material (glass fiber composite, 66% glass fiber, 33% epoxy). Looking at Fig. 5.5(b) it can be seen that each copper bar in the rotor coil pack is wrapped in 0.105 mm of insulation. By taking the sum of the insulation length and dividing it by the sum of length per conductivity of the different materials, one can

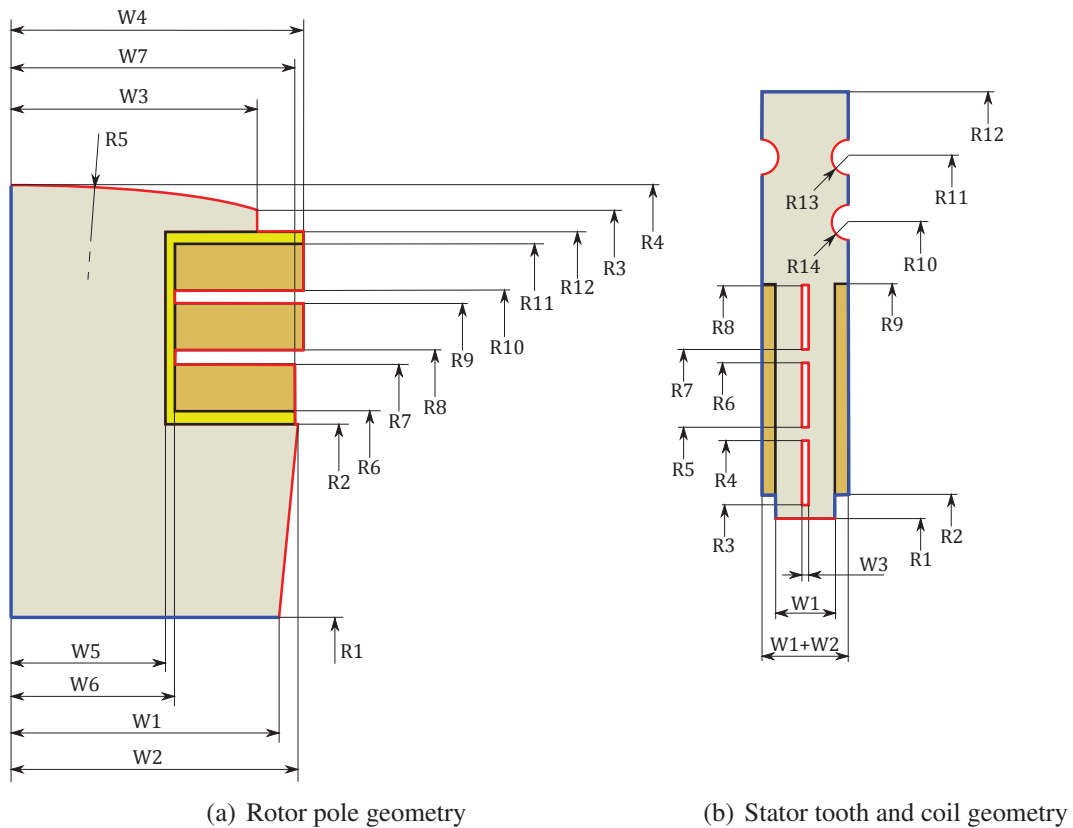


Figure 5.4 Stator and rotor geometry

Parameter	Stator [m]	Rotor [m]	Parameter	Stator [m]	Rotor [m]
R1	5.400	4.955	R12	5.750	5.372
R2	5.415	5.135	R13	0.012	-
R3	5.410	5.328	R14	0.010	-
R4	5.462	5.384	W1	$4.830 \cdot 10^{-2}$	0.2584
R5	5.470	1.870	W2	$1.970 \cdot 10^{-2}$	0.2679
R6	5.522	5.145	W3	$6.000 \cdot 10^{-3}$	0.2140
R7	5.530	5.196	W4	-	0.2605
R8	5.582	5.207	W5	-	0.1620
R9	5.585	5.258	W6	-	0.1665
R10	5.659	5.269	W7	-	0.2553
R11	5.700	5.320			

Table 5.1 Rotor and stator dimensions cf. Fig. 5.4

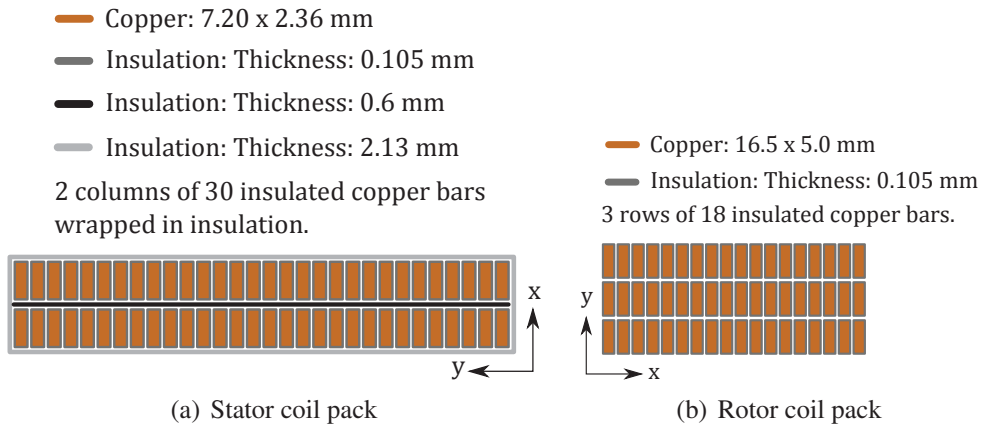


Figure 5.5 Rotor & stator coil packs

achieve an equivalent conductivity. For the x and y direction of the rotor copper pack this can be found as:

x-direction:

$$\begin{aligned}
 k_{eq,rx} &= \frac{L_{ins} + L_{Cu}}{L_{ins}/k_{ins} + L_{Cu}/k_{Cu}} \\
 &= \frac{18 \cdot 2 \cdot 0.105 \cdot 10^{-3} + 18 \cdot 5.0 \cdot 10^{-3}}{\frac{18 \cdot 2 \cdot 0.105 \cdot 10^{-3}}{0.3} + \frac{18 \cdot 5.0 \cdot 10^{-3}}{393}} = 7.6539 \text{ W/(m}\cdot\text{K)} \quad (5.13)
 \end{aligned}$$

y-direction:

$$\begin{aligned}
 k_{eq,ry} &= \frac{L_{ins} + L_{Cu}}{L_{ins}/k_{ins} + L_{Cu}/k_{Cu}} \\
 &= \frac{3 \cdot 2 \cdot 0.105 \cdot 10^{-3} + 3 \cdot 16.5 \cdot 10^{-3}}{\frac{3 \cdot 2 \cdot 0.105 \cdot 10^{-3}}{0.3} + \frac{3 \cdot 16.5 \cdot 10^{-3}}{393}} = 23.565 \text{ W/(m}\cdot\text{K)} \quad (5.14)
 \end{aligned}$$

In a similar way, this can be done for the stator pack Fig. 5.5(a). In the x direction this will, however, just be done starting from the copper bar of one of the columns and to the outer surface of the insulation, as no conduction will occur through the center due to

symmetry. The equivalent conductivity for the stator coil packs are found to:

x-direction:

$$\begin{aligned} k_{eq,sx} &= \frac{L_{ins} + L_{Cu}}{L_{ins}/k_{ins} + L_{Cu}/k_{Cu}} \\ &= \frac{2.13 \cdot 10^{-3} + 0.105 \cdot 10^{-3} + 7.20 \cdot 10^{-3}}{\frac{2.13 \cdot 10^{-3} + 0.105 \cdot 10^{-3}}{0.3} + \frac{7.20 \cdot 10^{-3}}{393}} = 1.2633 \text{ W/(m}\cdot\text{K)} \end{aligned} \quad (5.15)$$

y-direction:

$$\begin{aligned} k_{eq,sy} &= \frac{L_{ins} + L_{Cu}}{L_{ins}/k_{ins} + L_{Cu}/k_{Cu}} \\ &= \frac{2 \cdot 2.13 \cdot 10^{-3} + 30 \cdot 2 \cdot 0.105 \cdot 10^{-3} + 30 \cdot 2.36 \cdot 10^{-3}}{\frac{2 \cdot 2.13 \cdot 10^{-3} + 30 \cdot 2 \cdot 0.105 \cdot 10^{-3}}{0.3} + \frac{30 \cdot 2.36 \cdot 10^{-3}}{393}} = 2.2996 \text{ W/(m}\cdot\text{K)} \end{aligned} \quad (5.16)$$

5.4 Losses in the solid parts

As the heat from the copper losses is generated in the copper of the coil packs which have a smaller volume than that of the coil packs, due to the insulation, it is necessary to estimate an equivalent heat generation per volume of the coil pack. Initially the losses per volume of pure copper will be found, which then will be multiplied by the ratio of pure copper volume per coil pack volume, to achieve the equivalent heat generation per volume. The heat generation in the iron part is simpler, as it is just the iron losses per iron volume. The heat generation per volume for the different parts can be found as:

Rotor:

Volume of pure copper per rotor pole:

$$V_{Cu,r} = m_{Cu,r} / \rho_{Cu} \quad (5.17)$$

Loss per volume in pure rotor copper:

$$\frac{Loss_{Cu,r}}{V_{Cu,r}} = \frac{Loss_{Cu,r} / n_{poles}}{V_{Cu,r}} \quad (5.18)$$

Ratio of copper/coil pack:

$$R_{Cu/coil,r} = A_{Cu,r} / A_{Coil,r} \quad (5.19)$$

Loss per volume in rotor coil pack:

$$\frac{Loss_{Coil,r}}{V_{Coil,r}} = \frac{Loss_{Cu,r}}{V_{Cu,r}} \cdot R_{Cu/coil,r} \quad (5.20)$$

Volume of iron in rotor poles:

$$V_{Fe,r} = A_{Fe,r} \cdot L_{motor} \cdot n_{poles} \quad (5.21)$$

Loss per volume in rotor iron:

$$\frac{Loss_{Fe,r}}{V_{Fe,r}} \quad (5.22)$$

Stator:

Volume of pure copper in stator:

$$V_{Cu,s} = m_{Cu,s} / \rho_{Cu} \quad (5.23)$$

Loss per volume in pure stator copper:

$$\frac{Loss_{Cu,s}}{V_{Cu,s}} \quad (5.24)$$

Ratio of copper/coil pack:

$$R_{Cu/coil,s} = A_{Cu,s} / A_{Coil,s} \quad (5.25)$$

Loss per volume in stator coil pack:

$$\frac{Loss_{Coil,s}}{V_{Coil,s}} \quad (5.26)$$

Volume of iron in stator:

$$V_{Fe,s} = A_{Fe,s} \cdot L_{motor} \quad (5.27)$$

Loss per volume in rotor iron:

$$\frac{Loss_{Fe,s}}{V_{Fe,s}} \quad (5.28)$$

5.5 Dependency of fluid characteristics on temperatures and altitude changes

As the properties of air changes at different temperatures and pressures, which has a significant influence on the flow and heat transfer results, it is of utmost importance that these are estimated as precise as possible. As all calculations are made in 2D, the most correct air temperature to use for the calculations must be the average air temperature in the center of the motor. By using the found losses in the iron, copper and fan together with the initial temperature after the cooler, it is possible to estimate the temperature in the center of the motor by assuming that half of the copper and iron losses are at that point transferred to the fluid. The losses of the fan have to be added to these losses as the fan is

placed after the cooler and therefore contribute to the increase in temperature. The center temperature can be found as:

$$T_{mid} = \frac{Loss_{fan} + (Loss_{Fe,s} + Loss_{Fe,r} + Loss_{Cu,s} + Loss_{Cu,r})/2}{\dot{m} \cdot C_p} + T_{ini} \quad (5.29)$$

This equation has to be solved iteratively as the center air temperature is dependent on the mass flow and specific heat capacity which again is dependent on the center air temperature. As air pressure decrease with the altitude the pressure has to be determined with the help of Eq. 5.30 and the altitude from Tab. 4.2.

$$p_{alt} = p_0 \cdot \left(1 - \frac{T_{lap} \cdot h_{alt}}{T_0}\right)^{\frac{g \cdot M}{R \cdot T_{lap}}} \quad (5.30)$$

It is now possible to calculate the remaining needed properties by the use of Eq. 5.31 to 5.34:

$$\rho_{air} = p_{alt} \cdot \frac{M}{R \cdot (273.15 + T_{mid})} \quad (5.31)$$

$$\mu_d = \mu_0 \frac{T_0 + C}{(273.15 + T_{mid}) + C} \left(\frac{273.15 + T_{mid}}{T_0}\right)^{3/2} \quad (5.32)$$

$$C_p = 4.44 \cdot 10^{-7} \cdot (273.15 + T_{mid})^3 - 3.33 \cdot 10^{-5} \cdot (273.15 + T_{mid})^2 - 6.99 \cdot 10^{-2} \cdot (273.15 + T_{mid}) + 1.02 \cdot 10^3 \quad (5.33)$$

$$k_f = 7.6686 \cdot 10^{-5} \cdot (273.15 + T_{mid}) + 3.0438 \cdot 10^{-3} \quad (5.34)$$

Figure 5.6 and 5.7 show the air properties dependency on the temperature and have been added to give a quick overview of their trends.

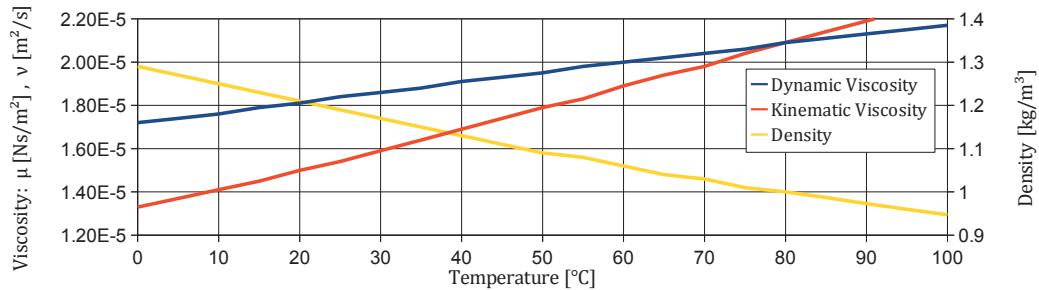


Figure 5.6 Properties of air at atmospheric pressure

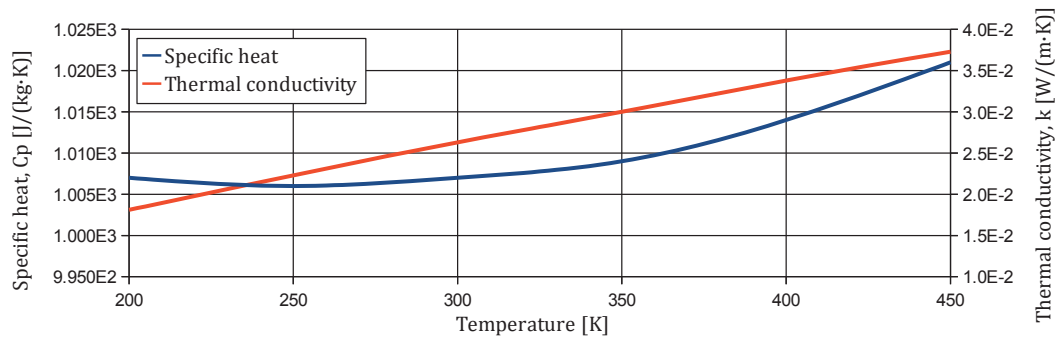


Figure 5.7 Properties of air at atmospheric pressure

5.6 System parameters

Table 4.2 shows the general parameters which are used in the calculations and are mainly values to determine the heat generation and cooling air properties. Table 5.2 shows the material parameters used for the materials in the rotor and stator and Tab. 4.1 shows the channel dimensions and number of channels for the flow calculation. These parameters have been kept constant throughout the entire calculation.

Parameter	Value	Description
k_{Cu}	393	Thermal conductivity of copper [W/(m·K)]
ρ_{Cu}	8933	Density of copper [kg/m ³]
C_{Cu}	397	Specific heat capacity of copper, [J/(kg·K)]
k_{ins}	0.3	Thermal conductivity of insulation [W/(m·K)] (glass fiber 66% glass, 33% epoxy)
k_{Fe}	56.7	Thermal conductivity of carbon steel [W/(m·K)]
ρ_{Fe}	7854	Density of carbon steel [kg/m ³]
C_{Fe}	487	Specific heat capacity of carbon steel [J/(kg·K)]
k_{M400}	26.0	Thermal conductivity of M400-50A steel [W/(m·K)]
ρ_{M400}	7800	Density of M400-50A steel [kg/m ³]
C_{M400}	487	Specific heat capacity of M400-50A steel [J/(kg·K)]

Table 5.2 Material parameters

5.7 Heat expansion

As it is common knowledge that steel expand as it is heated up, this can not be neglected as it has an influence on the air gap in the drive. The thermal linear expansion can be expressed as shown in Eq. 5.35 where the thermal linear expansion coefficient α_L for steel is $\alpha_L = 13 \cdot 10^{-6} \frac{1}{^\circ\text{C}}$. Is only the stator and the rotor which is at an elevated temperature and the frame and the mill drum remain at almost room temperature, Fig. 5.8.

The stator can only expand slightly in the radial direction corresponding to the build in initial gap between the stator and the vertical frame plates surrounding the stator, Sec. 2.4. As the outer diameter of the stator then becomes restricted by the cold frame plates,

it will instead begin to expand inward again and in the circumferential direction where a build in gap between the four quarters of the stator begins to decrease. If the stator for some reason get hotter than estimated and the mentioned gaps decrease to zero, the stator which is build of sheet metal will begin to bugle in the circumferential direction. This has been experienced at a few plants. As the stator initially expand in an outward radial direction until it reaches the frame plate after which it starts to expand inward again, it is assumed that the resulting change in stator inner diameter remain zero, thereby neglecting the impact of the stator heat expansion on the rotor/stator air gap. Under this assumption, it is only the heat expansion of the rotor core which will have an impact on the rotor/stator air gap.

The temperature increase ΔT used in the simulations is the average rotor core temperature of the final slice in the thermal model, as this is the warmest section of the pole core. The thermal expansion is subtracted from the original rotor/stator air gap which has an influence on the forces between the poles and the stator, Sec. 3.4.2 which again has an influence on the air gap. The change in rotor/stator air gap is also used for the more obvious check to examine if the minimum air gap has been exceeded. If the assumption that it is only the heat expansion of the rotor core which has an influence on the rotor/stator air gap, does not hold, it will at least give the worst case scenario and predict the absolute minimum air gap, thereby not harming the drive.

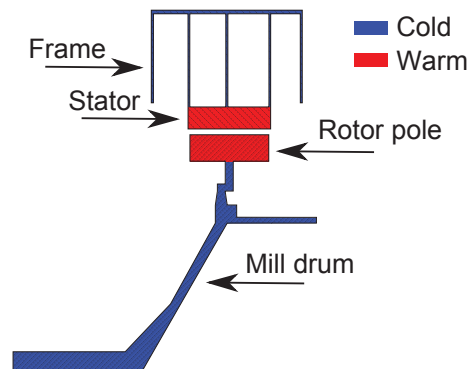


Figure 5.8 Cross-section of mill drive

$$\Delta L = L\alpha_L\Delta T \quad (5.35)$$

5.8 Verification of thermal models

For the center slice thermal model four different grid sizes are used for the finite difference model, two for the stator and two for the rotor. The grid sizes are chosen as to best represent the geometry of the different parts with the coarsest grid possible. To examine the accuracy of the results with the coarse grid, an extra simulation is carried out with a

		$\Delta x = 2.5$ [mm]	$\Delta x = 1.25$ [mm]	Dev. [%]	FEMM	Dev. [%]
Cu rotor max.	[°C]	113.8	113.4	0.4	114.3	0.4
Cu rotor min.	[°C]	103.9	102.7	1.2	102.4	1.5
Fe rotor max.	[°C]	87.7	87.2	0.6	87.7	0.0
Fe rotor min.	[°C]	83.8	85.0	1.4	84.3	0.6
		$\Delta x = 2.0$ [mm]	$\Delta x = 1.0$ [mm]	Dev. [%]	FEMM	Dev. [%]
Cu stator max.	[°C]	94.6	95.5	2.0	96.4	1.9
Cu stator min.	[°C]	89.2	90.0	0.9	91.3	2.3
Fe stator max.	[°C]	91.5	92.3	0.9	93.2	1.8
Fe stator min.	[°C]	86.9	87.7	0.9	87.9	1.1

Table 5.3 Rotor and stator max. and min. temperatures, Center slice model

twice as fine grid. The entire grid used is of equal side length, $\Delta x = \Delta y$. The following grid sizes are used for the stator and the rotor:

$$\begin{aligned}
 \text{Stator} & : \quad \Delta x = \Delta y = 2.00 \text{ mm} \\
 & \quad \Delta x = \Delta y = 1.00 \text{ mm} \\
 \text{Rotor} & : \quad \Delta x = \Delta y = 2.50 \text{ mm} \\
 & \quad \Delta x = \Delta y = 1.25 \text{ mm}
 \end{aligned}$$

Figure 5.9 shows the results of the converged steady-state temperature of the rotor and stator achieved with the finite difference method together with results from the finite element model. Figure 5.9(a) is for the coarse grid, Fig. 5.9(b) is for the fine grid and Fig. 5.9(c) is for the finite element model. As a proof of convergence of the finite difference model the coldest and warmest part of the copper and iron are plotted in Fig. 5.10. Here it can be seen that the steady-state has been reached after approximately 30 simulated hours and it converges toward the finite element results. As it is difficult to read the exact temperatures from Fig. 5.9, the coldest and warmest temperatures are listed in Tab. 5.3. Furthermore, the deviation between the achieved temperature values for the fine and coarse grid and between the FD and FEM model are added to the table. It can be seen that the increase in refinement does not make a large change in the found temperatures, only a deviation of approximately 1.5%. However, looking at the increase in computational time spend per iteration and the maximum possible time step Δt shown in Tab. 5.4, it is not worth the effort, as other part of the calculations are connected with higher errors. One obvious reason for the deviation in the stator temperature for the two different grid sizes is that the cooling channels in the tooth for the coarse grid is actually modeled with a width of 8 mm, due to the size and placement of the grid, where it is modeled as 6 mm in the fine grid case which are the actual width of the cooling channels. This increase in modeled cooling channel width will of course increase the surface area for the convection slightly and thereby decrease the temperature in the solid parts. From Tab. 5.3 it must be concluded that the three models produce results with almost same accuracy. To validate the results obtained by using the three models, comparisons are done with results and data presented by Grinbaum (2012) under almost the same conditions as the one used in the simulations. Table 5.5 shows these results together with the ones found by the FEMM model. As can be seen, there is only minor deviation between the temperature results. It must therefore, with a high probability, be concluded that the models produce similar

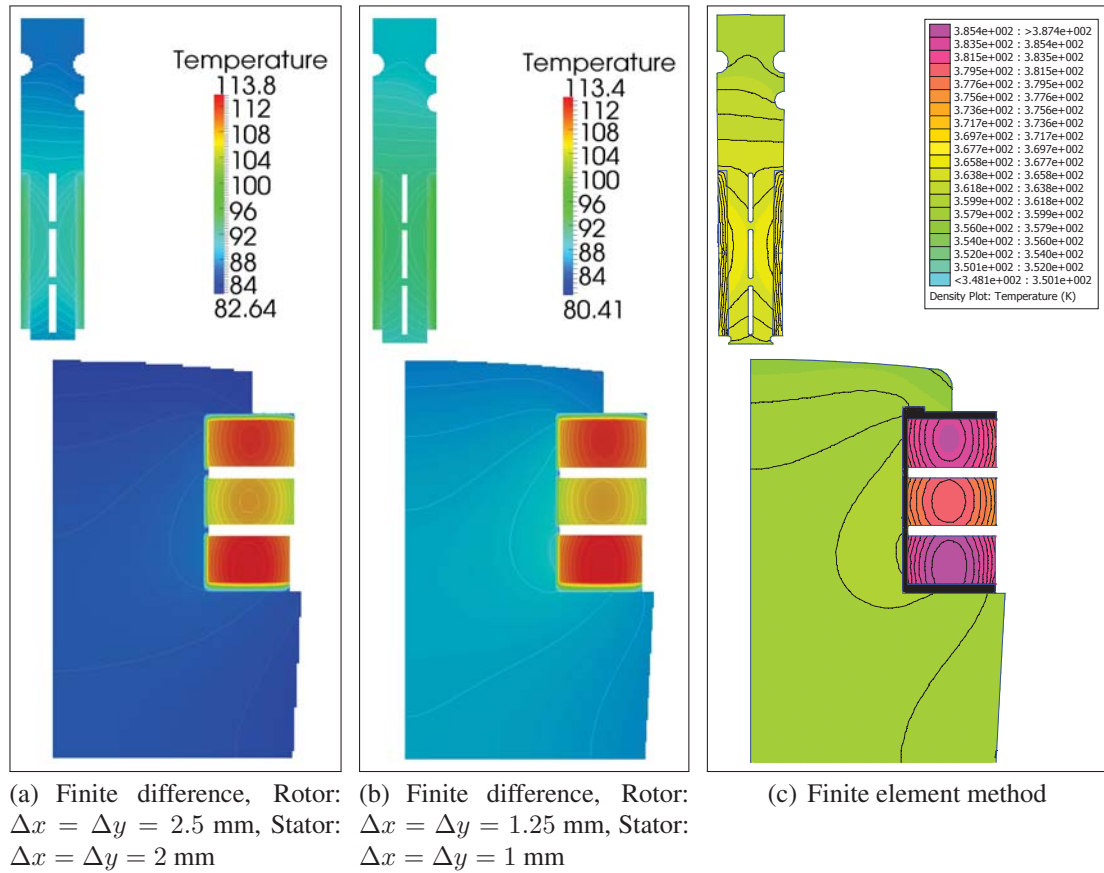


Figure 5.9 Finite difference Steady-State and finite element temperatures of rotor and stator, Center slice model

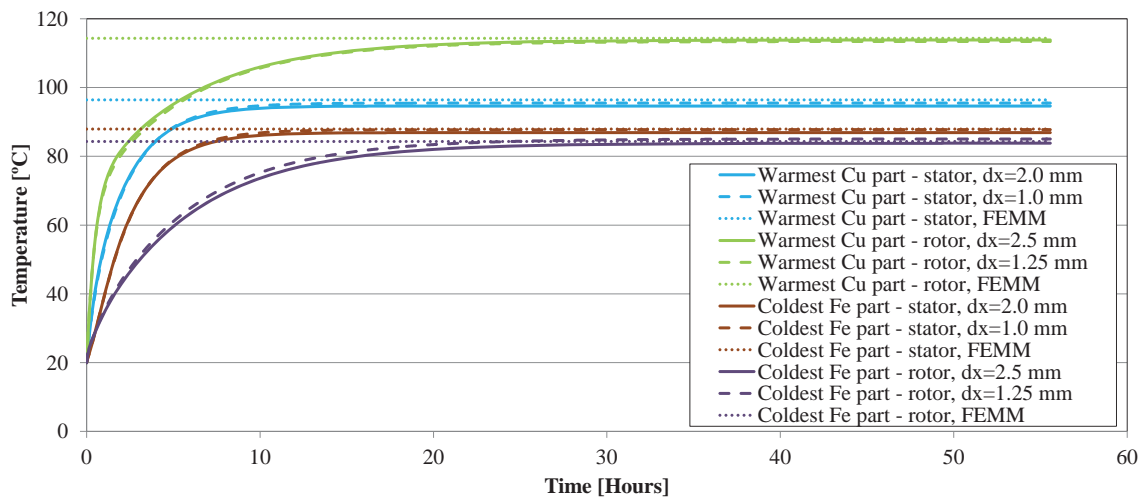


Figure 5.10 Maximum and minimum temperatures in stator and rotor poles, Center slice model

	Δx [mm]	Max. Δt [ms]	CPU time/step [ms]	Steady-state CPU time [h]
Rotor	1.25	20	10.25	15.375
Stator	1.00	20	3.16	4.740
Rotor	2.50	100	2.49	0.747
Stator	2.00	100	0.78	0.234

Table 5.4 Finite difference model computation time, Intel core I5 CPU M450@2.4GHz, OS Windows 7 64-bit, Steady-state @ 30 simulated hours

	FEMM	Grinbaum (2012)	Deviation	Deviation
Rotor max.	109.1 °C	109.5 °C	0.4 °C	0.4%
Stator max.	104.7 °C	104.9 °C	0.2 °C	0.2%
Volume flow	31.4 m ³ /s	32.9 m ³ /s	1.5 m ³ /s	4.6%
Loss/coil vol. stator	96891 W/m ³	96891 W/m ³	0.0 W/m ³	0.0%
Loss/vol. stator iron	5729 W/m ³	5729 W/m ³	0.0 W/m ³	0.0%
Loss/coil vol. rotor	70657 W/m ³	70657 W/m ³	0.0 W/m ³	0.0%
Loss/vol. rotor iron	621 W/m ³	621 W/m ³	0.0 W/m ³	0.0%

Table 5.5 Temperature comparison with data and results provided by Grinbaum (2012), Center slice model

results under the same assumptions. The multi-sliced model which updates cooling flows and copper losses due to the increasing temperatures in the axial direction is only modeled by FEMM. This is due to the fact that it is highly time consuming to run the explicit finite difference model, as many iterations have to be performed. As a comparison between the computational time for one slice the two finite difference models take 20 hours and 1 hour respectively, where the FEM model takes approximately 1 second to compute 1 slice. The multi sliced model consists of 40 slices evenly distributed over the total length of the gearless drive. Figure 5.11 shows the temperature distribution of the center and the two end slices found by the FEMM model. Figure 5.12 shows the cooling flow temperatures in the different channels. From this, it is obvious that the center slice model is too simple, as the temperature difference between the two end slices is 31.1°C for the highest part. Furthermore, the highest temperature is 30.0°C warmer than what was found by the first model. For validating the multi sliced model, comparisons with data and results obtained in Bermudez (2012) using the same input as the present model are carried out and presented in Tab. 5.6. The difference between the results could, among other things, be explained by the fact that Bermudez (2012) uses Dittus-Boelters equation for calculating the Nusselt number which is for smooth channels with a Reynolds number above 10,000 and is therefore less suited for these cases. Furthermore, there is a difference in the mass flow at the same differential pressure, which could be explained by the fact that the author

	FEMM	Bermudez (2012)	Deviation	Deviation
Rotor max.	144.3 °C	147.7 °C	3.4 °C	2.3%
Stator max.	127.5 °C	123.8 °C	3.7 °C	3.0%
Mass flow	20.45 kg/s	19.55 kg/s	0.90 kg/s	4.6%
Vol. flow	31.60 m ³ /s	31.43 m ³ /s	0.17 m ³ /s	0.5%
Pressure loss	170.0 Pa	170.0 Pa	0.0 Pa	0.0%

Table 5.6 Temperature comparison of multi sliced model against Bermudez (2012) results, (same inputs)

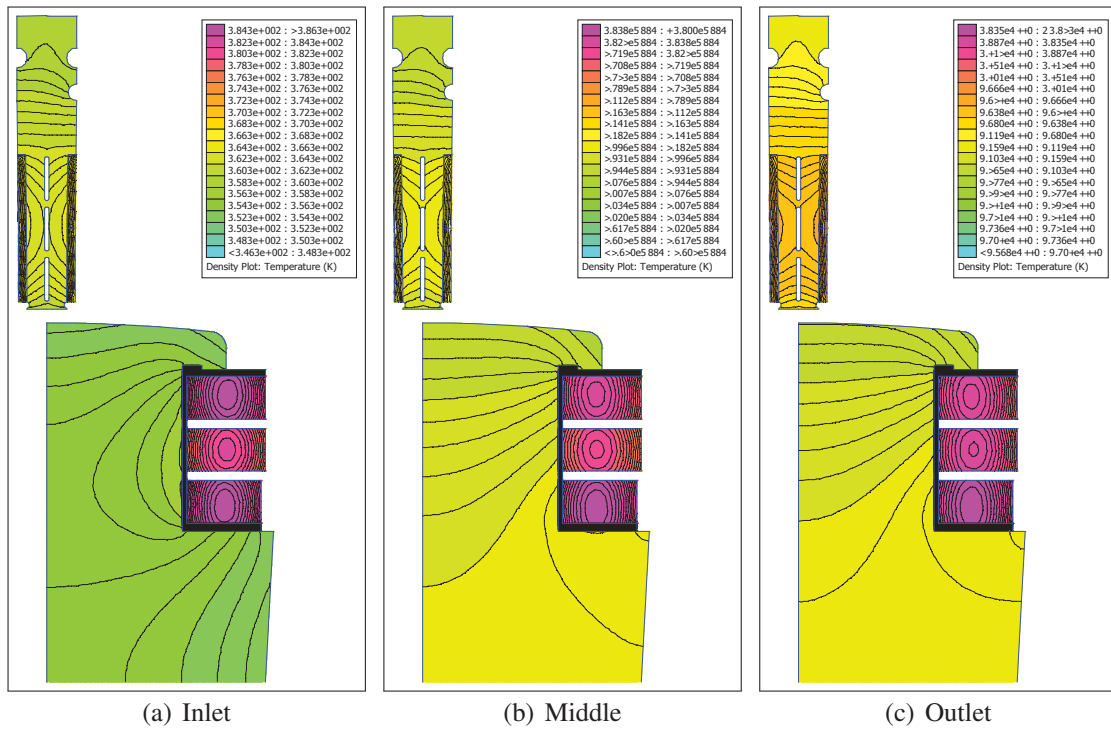


Figure 5.11 Temperature distribution with updated copper resistance losses, Multi sliced model

of Bermudez (2012) assumes that the air properties in the channels are the same for all the channels. Moreover, small discrepancies in the geometry used for the flow calculation are also verified. For further verification of the FORTRAN code see Appendix A.2.

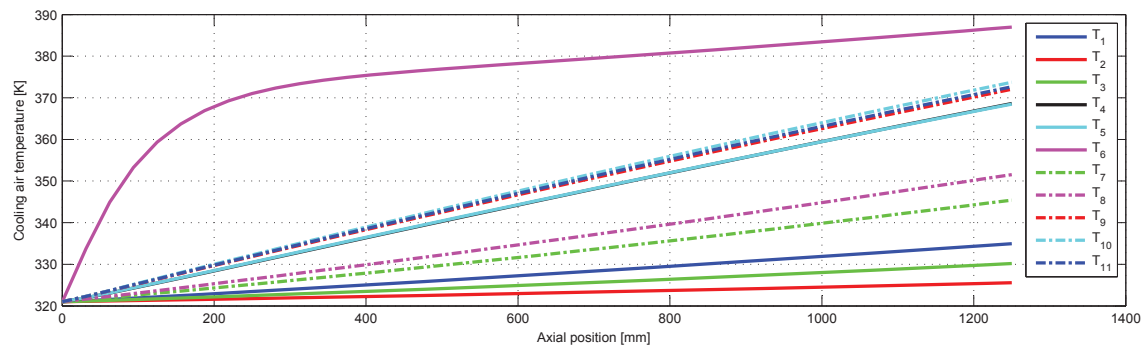


Figure 5.12 Cooling air temperatures, Temperature updated copper resistance losses, Multi sliced model

5.9 Effects of neglecting the axial heat flux

It is assumed in all the models that no axial heat flux is present in the solid parts of the drive. The only axial heat transfer occurring is in the cooling fluid, as heat is transferred

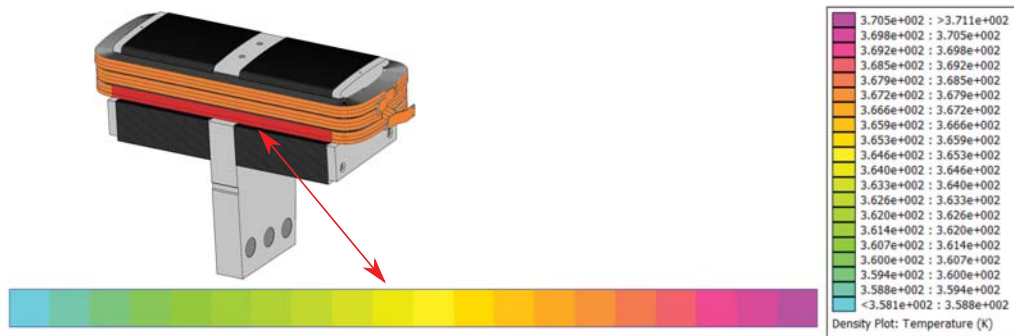


Figure 5.13 FEM of rotor coil pack in axial direction (z-dir.) to examine heat flux along copper strands

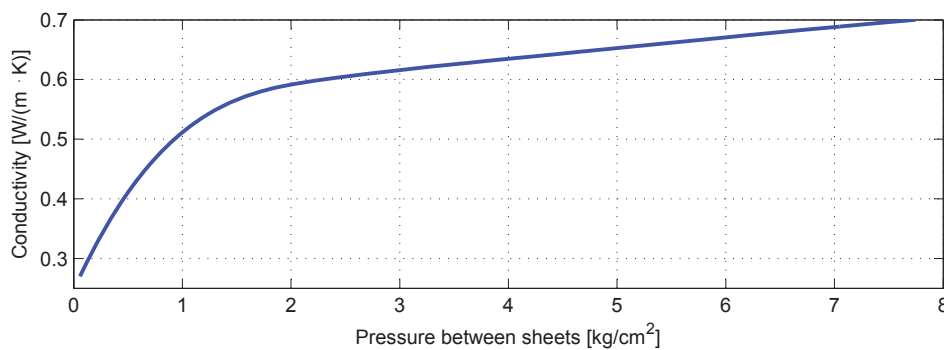


Figure 5.14 Conductivity coefficient normal to Si-steel sheet surface, Filippov (1974)

from the solids to the fluid through the walls of the cooling channels. To investigate the error in connection with this assumption, a simulation has been carried out where the axial heat flux of the warmest coil has been found (bottom rotor coil), Fig. 5.11. The axial heat flux for this coil is found to be 41.6 W which is approximately 8.6% of the total loss in that coil segment. However, as the maximum allowed coil temperature at ABB is 90°C a simulation has been made where the flow has been changed to achieve this goal. This simulation show that as the flow increase the temperature difference between the cold and hot end decreases and thereby the error due to the neglect of axial flux also decreases. The new simulation shown in Fig. 5.13 now results in an axial heat flux of 17 W which is approximately 2.6% of the total loss in that coil segment. The axial heat flux in the core material is much smaller than in the copper coils, as this is laminated steel sheets. Figure 5.14 show the conductivity coefficient in a direction perpendicular to the sheet plan as a function of the compression pressure, Filippov (1974). According to ABB, the compression pressure used in their drives is approximately 1.5 kg/cm² ~ 147.1 kPa, which results in a conductivity coefficient of approximately 0.5658 W/(m·K). The conductivity coefficient parallel to the sheets plan is 26 W/(m·K) which is 46 times larger than the conductivity perpendicular to the sheet plan. The error due to this assumption will, however, only overestimate the temperature rise in the gearless drive and will therefore not predict lower temperatures which could be fatal for the operation and lifespan of the drive.

Chapter 6

Structural investigations of gearless drives - Structural model

When modeling large devices like a gearless mill drive it is important also to include a structural investigation as it otherwise could have catastrophic and high economic consequences. Even though a structural calculation has been performed it is no guarantee that no problem will occur as was experienced at Cadia Hill gold mine in Australia which had severe vibration problems in their gearless mill drive, Meimaris et al. (2001). Vibrations investigation is only one of the important examinations which has to be performed. Deformation of the structure due to forces and torque between rotor and stator is another and highly important factor as it can seriously distort the relatively small air gap between the rotor and stator and if not determined correctly could be the reason for a complete destruction of the entire unit. Another important thing to investigate is that none of the parts of the gearless drive experience stresses beyond the yielding stress.

The natural frequencies and their corresponding mode shapes can for simple structures be found analytically as described in Blevins (1979) which for example shows it for a solid ring. However, for more complex devices as the gearless mill drive which cannot be assumed to behave as one of these simple structural cases one needs to move to more refined methods as the finite element method. A 3D FEM model is also the most commonly used in the structural modeling of gearless mill drives, Dreher et al. (2004), Warner (2006) and several books have been written on the subject, Bathe (1982), Bhatti (2005), Cook et al. (2002). The benefit of using FEM in the structural calculation of a gearless drive is that the FEM model can use the same structural mesh to estimate all the above mentioned main results and thereby saving setup time. Furthermore it is highly suited for modeling complex geometries.

The structural model of the mill is a 3D FEM programmed entirely in Fortran using 20 nodes hexahedron isoparametric elements. For this reason, the section will start by presenting the basic equations needed for building a finite element model using hexahedron elements followed by an explanation for the choice of using this type of element. Finally, the results of the structural model will be presented and compared against results received from ABB. These results are deformation, Von Mises stress, air gap distortion, eigenvalues and their corresponding mode shapes.

6.1 Hexahedron 20 nodes isoparametric

This subsection describes in detail how the hexahedron 20 nodes element shown in Fig.6.1 is modeled. Basically what needs to be solved is a system of linear equations as the one shown in Eq. 6.1 which is the equation of motion. For the static displacement case the first

part of the equation of motion is neglected as the accelerations are zero and the equation reduces to Eq. 6.2. For the determination of the eigenvalues the forces in the equation of motion are zero and what needs to be solve is Eq. 6.3.

$$[\mathbf{M}] \{\mathbf{a}\} + [\mathbf{K}] \{\mathbf{d}\} = \{\mathbf{R}\} \quad (6.1)$$

$$[\mathbf{K}] \{\mathbf{d}\} = \{\mathbf{R}\} \quad (6.2)$$

$$-[\mathbf{K}] \{\mathbf{d}\} = \lambda [\mathbf{M}] \{\mathbf{d}\} \quad (6.3)$$

The following subsections will describe how the stiffness matrix \mathbf{K} , the mass matrix \mathbf{M} and the force reaction vector \mathbf{R} can be determined.

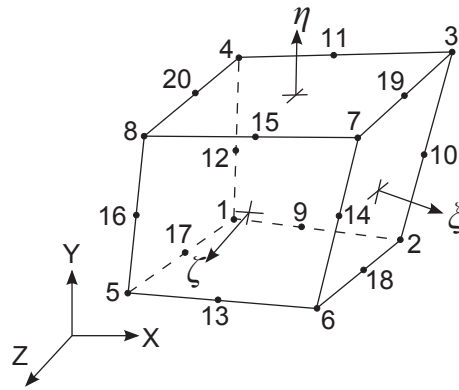


Figure 6.1 Isoparametric 20 nodes hexahedron cell

6.1.1 Element stiffness matrix

The element stiffness matrix can be found by the volume integral in Eq.6.4:

$$[\mathbf{k}_e] = \int_{-1}^1 \int_{-1}^1 \int_{-1}^1 [\mathbf{B}]^T [\mathbf{C}] [\mathbf{B}] J d\xi d\eta d\zeta \quad (6.4)$$

where \mathbf{B} is the strain-displacement relationship matrix, \mathbf{C} is the constitutive matrix and J is the determinant of the Jacobian matrix \mathbf{J} . This element stiffness matrix \mathbf{k}_e can then later be assembled into the global stiffness matrix \mathbf{K} corresponding to the location of the specific degree of freedom.

Initially the 20 shape functions are found, Sec.6.1.2, together with their derivative with respect to ξ , η and ζ , Sec.6.1.3, 6.1.4 and 6.1.5, which are used to form the Jacobian and the strain-displacement relationship matrix. Then the Jacobian matrix and its inverse are assembled and the determinant calculated, Sec.6.1.6. The strain-displacement relationship matrix \mathbf{B} can now be assembled, 6.1.7 and the constitutive matrix \mathbf{C} can be found by derivation of Hooke's law in 3D and is shown in Sec.6.1.8 for both a isotropic as well as for a anisotropic material.

6.1.2 Shape functions

As the hexahedron 20 nodes element consists of 20 nodes, it must have 20 shape functions which are listed in Eq. 6.5 - 6.24:

$$N_1 = \frac{1}{8} (1 - \xi) (1 - \eta) (1 - \zeta) (-\xi - \eta - \zeta - 2) \quad (6.5)$$

$$N_2 = \frac{1}{8} (1 + \xi) (1 - \eta) (1 - \zeta) (+\xi - \eta - \zeta - 2) \quad (6.6)$$

$$N_3 = \frac{1}{8} (1 + \xi) (1 + \eta) (1 - \zeta) (+\xi + \eta - \zeta - 2) \quad (6.7)$$

$$N_4 = \frac{1}{8} (1 - \xi) (1 + \eta) (1 - \zeta) (-\xi + \eta - \zeta - 2) \quad (6.8)$$

$$N_5 = \frac{1}{8} (1 - \xi) (1 - \eta) (1 + \zeta) (-\xi - \eta + \zeta - 2) \quad (6.9)$$

$$N_6 = \frac{1}{8} (1 + \xi) (1 - \eta) (1 + \zeta) (+\xi - \eta + \zeta - 2) \quad (6.10)$$

$$N_7 = \frac{1}{8} (1 + \xi) (1 + \eta) (1 + \zeta) (+\xi + \eta + \zeta - 2) \quad (6.11)$$

$$N_8 = \frac{1}{8} (1 - \xi) (1 + \eta) (1 + \zeta) (-\xi + \eta + \zeta - 2) \quad (6.12)$$

$$N_9 = \frac{1}{4} (1 - \xi^2) (1 - \eta) (1 - \zeta) \quad (6.13)$$

$$N_{10} = \frac{1}{4} (1 - \eta^2) (1 + \xi) (1 - \zeta) \quad (6.14)$$

$$N_{11} = \frac{1}{4} (1 - \xi^2) (1 + \eta) (1 - \zeta) \quad (6.15)$$

$$N_{12} = \frac{1}{4} (1 - \eta^2) (1 - \xi) (1 - \zeta) \quad (6.16)$$

$$N_{13} = \frac{1}{4} (1 - \xi^2) (1 - \eta) (1 + \zeta) \quad (6.17)$$

$$N_{14} = \frac{1}{4} (1 - \eta^2) (1 + \xi) (1 + \zeta) \quad (6.18)$$

$$N_{15} = \frac{1}{4} (1 - \xi^2) (1 + \eta) (1 + \zeta) \quad (6.19)$$

$$N_{16} = \frac{1}{4} (1 - \eta^2) (1 - \xi) (1 + \zeta) \quad (6.20)$$

$$N_{17} = \frac{1}{4} (1 - \zeta^2) (1 - \xi) (1 - \eta) \quad (6.21)$$

$$N_{18} = \frac{1}{4} (1 - \zeta^2) (1 + \xi) (1 - \eta) \quad (6.22)$$

$$N_{19} = \frac{1}{4} (1 - \zeta^2) (1 + \xi) (1 + \eta) \quad (6.23)$$

$$N_{20} = \frac{1}{4} (1 - \zeta^2) (1 - \xi) (1 + \eta) \quad (6.24)$$

6.1.3 Derivative of shape functions with respect to ξ

To be able to form the Jacobian matrix the previously mentioned shape functions has be differentiated with respect to ξ , η and ζ and result in Eq. 6.25 - 6.84.

$$N_{1,\xi} = \frac{1}{8}(\zeta - 1)(\eta - 1)(\zeta + \eta + 2\xi + 1) \quad (6.25)$$

$$N_{2,\xi} = -\frac{1}{8}(\zeta - 1)(\eta - 1)(\zeta + \eta - 2\xi + 1) \quad (6.26)$$

$$N_{3,\xi} = \frac{1}{8}(\zeta - 1)(\eta + 1)(\zeta - \eta - 2\xi + 1) \quad (6.27)$$

$$N_{4,\xi} = -\frac{1}{8}(\zeta - 1)(\eta + 1)(\zeta - \eta + 2\xi + 1) \quad (6.28)$$

$$N_{5,\xi} = \frac{1}{8}(\zeta + 1)(\eta - 1)(\zeta - \eta - 2\xi - 1) \quad (6.29)$$

$$N_{6,\xi} = -\frac{1}{8}(\zeta + 1)(\eta - 1)(\zeta - \eta + 2\xi - 1) \quad (6.30)$$

$$N_{7,\xi} = \frac{1}{8}(\zeta + 1)(\eta + 1)(\zeta + \eta + 2\xi - 1) \quad (6.31)$$

$$N_{8,\xi} = -\frac{1}{8}(\zeta + 1)(\eta + 1)(\zeta + \eta - 2\xi - 1) \quad (6.32)$$

$$N_{9,\xi} = -\frac{1}{2}(\zeta - 1)(\eta - 1)\xi \quad (6.33)$$

$$N_{10,\xi} = \frac{1}{4}(\zeta - 1)(\eta^2 - 1) \quad (6.34)$$

$$N_{11,\xi} = \frac{1}{2}(\zeta - 1)(\eta + 1)\xi \quad (6.35)$$

$$N_{12,\xi} = -\frac{1}{4}(\zeta - 1)(\eta^2 - 1) \quad (6.36)$$

$$N_{13,\xi} = \frac{1}{2}(\zeta + 1)(\eta - 1)\xi \quad (6.37)$$

$$N_{14,\xi} = -\frac{1}{4}(\zeta + 1)(\eta^2 - 1) \quad (6.38)$$

$$N_{15,\xi} = -\frac{1}{2}(\zeta + 1)(\eta + 1)\xi \quad (6.39)$$

$$N_{16,\xi} = \frac{1}{4}(\zeta + 1)(\eta^2 - 1) \quad (6.40)$$

$$N_{17,\xi} = -\frac{1}{4}(\zeta^2 - 1)(\eta - 1) \quad (6.41)$$

$$N_{18,\xi} = \frac{1}{4}(\zeta^2 - 1)(\eta - 1) \quad (6.42)$$

$$N_{19,\xi} = -\frac{1}{4}(\zeta^2 - 1)(\eta + 1) \quad (6.43)$$

$$N_{20,\xi} = \frac{1}{4}(\zeta^2 - 1)(\eta + 1) \quad (6.44)$$

6.1.4 Derivative of shape functions with respect to η

$$N_{1,\eta} = \frac{1}{8}(\zeta - 1)(\xi - 1)(\zeta + 2\eta + \xi + 1) \quad (6.45)$$

$$N_{2,\eta} = -\frac{1}{8}(\zeta - 1)(\xi + 1)(\zeta + 2\eta - \xi + 1) \quad (6.46)$$

$$N_{3,\eta} = \frac{1}{8}(\zeta - 1)(\xi + 1)(\zeta - 2\eta - \xi + 1) \quad (6.47)$$

$$N_{4,\eta} = -\frac{1}{8}(\zeta - 1)(\xi - 1)(\zeta - 2\eta + \xi + 1) \quad (6.48)$$

$$N_{5,\eta} = \frac{1}{8}(\zeta + 1)(\xi - 1)(\zeta - 2\eta - \xi - 1) \quad (6.49)$$

$$N_{6,\eta} = -\frac{1}{8}(\zeta + 1)(\xi + 1)(\zeta - 2\eta + \xi - 1) \quad (6.50)$$

$$N_{7,\eta} = \frac{1}{8}(\zeta + 1)(\xi + 1)(\zeta + 2\eta + \xi - 1) \quad (6.51)$$

$$N_{8,\eta} = -\frac{1}{8}(\zeta + 1)(\xi - 1)(\zeta + 2\eta - \xi - 1) \quad (6.52)$$

$$N_{9,\eta} = -\frac{1}{4}(\zeta - 1)(\xi^2 - 1) \quad (6.53)$$

$$N_{10,\eta} = \frac{1}{2}(\zeta - 1)\eta(\xi + 1) \quad (6.54)$$

$$N_{11,\eta} = \frac{1}{4}(\zeta - 1)(\xi^2 - 1) \quad (6.55)$$

$$N_{12,\eta} = -\frac{1}{2}(\zeta - 1)\eta(\xi - 1) \quad (6.56)$$

$$N_{13,\eta} = \frac{1}{4}(\zeta + 1)(\xi^2 - 1) \quad (6.57)$$

$$N_{14,\eta} = -\frac{1}{2}(\zeta + 1)\eta(\xi + 1) \quad (6.58)$$

$$N_{15,\eta} = -\frac{1}{4}(\zeta + 1)(\xi^2 - 1) \quad (6.59)$$

$$N_{16,\eta} = \frac{1}{2}(\zeta + 1)\eta(\xi - 1) \quad (6.60)$$

$$N_{17,\eta} = -\frac{1}{4}(\zeta^2 - 1)(\xi - 1) \quad (6.61)$$

$$N_{18,\eta} = \frac{1}{4}(\zeta^2 - 1)(\xi + 1) \quad (6.62)$$

$$N_{19,\eta} = -\frac{1}{4}(\zeta^2 - 1)(\xi + 1) \quad (6.63)$$

$$N_{20,\eta} = \frac{1}{4}(\zeta^2 - 1)(\xi - 1) \quad (6.64)$$

6.1.5 Derivative of shape functions with respect to ζ

$$N_{1,\zeta} = \frac{1}{8}(\eta - 1)(\xi - 1)(2\zeta + \eta + \xi + 1) \quad (6.65)$$

$$N_{2,\zeta} = -\frac{1}{8}(\eta - 1)(\xi + 1)(2\zeta + \eta - \xi + 1) \quad (6.66)$$

$$N_{3,\zeta} = -\frac{1}{8}(\eta + 1)(\xi + 1)(-2\zeta + \eta + \xi - 1) \quad (6.67)$$

$$N_{4,\zeta} = \frac{1}{8}(\eta + 1)(\xi - 1)(-2\zeta + \eta - \xi - 1) \quad (6.68)$$

$$N_{5,\zeta} = -\frac{1}{8}(\eta - 1)(\xi - 1)(-2\zeta + \eta + \xi + 1) \quad (6.69)$$

$$N_{6,\zeta} = \frac{1}{8}(\eta - 1)(\xi + 1)(-2\zeta + \eta - \xi + 1) \quad (6.70)$$

$$N_{7,\zeta} = \frac{1}{8}(\eta + 1)(\xi + 1)(2\zeta + \eta + \xi - 1) \quad (6.71)$$

$$N_{8,\zeta} = -\frac{1}{8}(\eta + 1)(\xi - 1)(2\zeta + \eta - \xi - 1) \quad (6.72)$$

$$N_{9,\zeta} = -\frac{1}{4}(\eta - 1)(\xi^2 - 1) \quad (6.73)$$

$$N_{10,\zeta} = \frac{1}{4}(\eta^2 - 1)(\xi + 1) \quad (6.74)$$

$$N_{11,\zeta} = \frac{1}{4}(\eta + 1)(\xi^2 - 1) \quad (6.75)$$

$$N_{12,\zeta} = -\frac{1}{4}(\eta^2 - 1)(\xi - 1) \quad (6.76)$$

$$N_{13,\zeta} = \frac{1}{4}(\eta - 1)(\xi^2 - 1) \quad (6.77)$$

$$N_{14,\zeta} = -\frac{1}{4}(\eta^2 - 1)(\xi + 1) \quad (6.78)$$

$$N_{15,\zeta} = -\frac{1}{4}(\eta + 1)(\xi^2 - 1) \quad (6.79)$$

$$N_{16,\zeta} = \frac{1}{4}(\eta^2 - 1)(\xi - 1) \quad (6.80)$$

$$N_{17,\zeta} = -\frac{1}{2}\zeta(\eta - 1)(\xi - 1) \quad (6.81)$$

$$N_{18,\zeta} = \frac{1}{2}\zeta(\eta - 1)(\xi + 1) \quad (6.82)$$

$$N_{19,\zeta} = -\frac{1}{2}\zeta(\eta + 1)(\xi + 1) \quad (6.83)$$

$$N_{20,\zeta} = \frac{1}{2}\zeta(\eta + 1)(\xi - 1) \quad (6.84)$$

6.1.6 Jacobian matrix

The Jacobian matrix and its inverse can now be formed as shown in Eq. 6.85 and Eq. 6.86 by the use of the above found derivatives of the shape functions:

$$[\mathbf{J}] = \begin{bmatrix} x_{,\xi} & y_{,\xi} & z_{,\xi} \\ x_{,\eta} & y_{,\eta} & z_{,\eta} \\ x_{,\zeta} & y_{,\zeta} & z_{,\zeta} \end{bmatrix} = \sum_i \begin{bmatrix} N_{i,\xi}x_i & N_{i,\xi}y_i & N_{i,\xi}z_i \\ N_{i,\eta}x_i & N_{i,\eta}y_i & N_{i,\eta}z_i \\ N_{i,\zeta}x_i & N_{i,\zeta}y_i & N_{i,\zeta}z_i \end{bmatrix} \quad (6.85)$$

$$\begin{Bmatrix} \phi_{,x} \\ \phi_{,y} \\ \phi_{,z} \end{Bmatrix} = \begin{bmatrix} \Gamma_{11} & \Gamma_{12} & \Gamma_{13} \\ \Gamma_{21} & \Gamma_{22} & \Gamma_{23} \\ \Gamma_{31} & \Gamma_{32} & \Gamma_{33} \end{bmatrix} \begin{Bmatrix} \phi_{,\xi} \\ \phi_{,\eta} \\ \phi_{,\zeta} \end{Bmatrix} \quad \text{where} \quad [\Gamma] = [\mathbf{J}]^{-1} \quad (6.86)$$

$$J = \det [\mathbf{J}] \quad (6.87)$$

6.1.7 Strain-displacement relationship

By the use of Eq. 6.88, Eq. 6.89 and Eq. 6.90 the strain-displacement relationship matrix \mathbf{B} can now be assembled as shown in Eq. 6.91.

$$\begin{Bmatrix} \epsilon_x \\ \epsilon_y \\ \epsilon_z \\ \gamma_{xy} \\ \gamma_{yz} \\ \gamma_{zx} \end{Bmatrix} = \underbrace{\begin{bmatrix} 1 & 0 & 0 & 0 & 0 & 0 & 0 & 0 & 0 \\ 0 & 0 & 0 & 0 & 1 & 0 & 0 & 0 & 0 \\ 0 & 0 & 0 & 0 & 0 & 0 & 0 & 0 & 1 \\ 0 & 1 & 0 & 1 & 0 & 0 & 0 & 0 & 0 \\ 0 & 0 & 0 & 0 & 0 & 1 & 0 & 1 & 0 \\ 0 & 0 & 1 & 0 & 0 & 0 & 1 & 0 & 0 \end{bmatrix}}_{\mathbf{L}} \begin{Bmatrix} u_{,x} \\ u_{,y} \\ u_{,z} \\ v_{,x} \\ v_{,y} \\ v_{,z} \\ w_{,x} \\ w_{,y} \\ w_{,z} \end{Bmatrix} \quad (6.88)$$

$$\begin{Bmatrix} u_{,x} \\ u_{,y} \\ u_{,z} \\ v_{,x} \\ v_{,y} \\ v_{,z} \\ w_{,x} \\ w_{,y} \\ w_{,z} \end{Bmatrix} = \underbrace{\begin{bmatrix} \Gamma_{11} & \Gamma_{12} & \Gamma_{13} & 0 & 0 & 0 & 0 & 0 & 0 \\ \Gamma_{21} & \Gamma_{22} & \Gamma_{23} & 0 & 0 & 0 & 0 & 0 & 0 \\ \Gamma_{31} & \Gamma_{32} & \Gamma_{33} & 0 & 0 & 0 & 0 & 0 & 0 \\ 0 & 0 & 0 & \Gamma_{11} & \Gamma_{12} & \Gamma_{13} & 0 & 0 & 0 \\ 0 & 0 & 0 & \Gamma_{21} & \Gamma_{22} & \Gamma_{23} & 0 & 0 & 0 \\ 0 & 0 & 0 & \Gamma_{31} & \Gamma_{32} & \Gamma_{33} & 0 & 0 & 0 \\ 0 & 0 & 0 & 0 & 0 & 0 & \Gamma_{11} & \Gamma_{12} & \Gamma_{13} \\ 0 & 0 & 0 & 0 & 0 & 0 & \Gamma_{21} & \Gamma_{22} & \Gamma_{23} \\ 0 & 0 & 0 & 0 & 0 & 0 & \Gamma_{31} & \Gamma_{32} & \Gamma_{33} \end{bmatrix}}_{\tilde{\Gamma}} \begin{Bmatrix} u_{,\xi} \\ u_{,\eta} \\ u_{,\zeta} \\ v_{,\xi} \\ v_{,\eta} \\ v_{,\zeta} \\ w_{,\xi} \\ w_{,\eta} \\ w_{,\zeta} \end{Bmatrix} \quad (6.89)$$

$$\begin{Bmatrix} u_{,\xi} \\ u_{,\eta} \\ u_{,\zeta} \\ v_{,\xi} \\ v_{,\eta} \\ v_{,\zeta} \\ w_{,\xi} \\ w_{,\eta} \\ w_{,\zeta} \end{Bmatrix} = \underbrace{\begin{bmatrix} N_{1,\xi} & 0 & 0 & N_{2,\xi} & 0 & 0 & \dots & N_{20,\xi} & 0 & 0 \\ N_{1,\eta} & 0 & 0 & N_{2,\eta} & 0 & 0 & \dots & N_{20,\eta} & 0 & 0 \\ N_{1,\zeta} & 0 & 0 & N_{2,\zeta} & 0 & 0 & \dots & N_{20,\zeta} & 0 & 0 \\ 0 & N_{1,\xi} & 0 & 0 & N_{2,\xi} & 0 & \dots & 0 & N_{20,\xi} & 0 \\ 0 & N_{1,\eta} & 0 & 0 & N_{2,\eta} & 0 & \dots & 0 & N_{20,\eta} & 0 \\ 0 & N_{1,\zeta} & 0 & 0 & N_{2,\zeta} & 0 & \dots & 0 & N_{20,\zeta} & 0 \\ 0 & 0 & N_{1,\xi} & 0 & 0 & N_{2,\xi} & \dots & 0 & 0 & N_{20,\xi} \\ 0 & 0 & N_{1,\eta} & 0 & 0 & N_{2,\eta} & \dots & 0 & 0 & N_{20,\eta} \\ 0 & 0 & N_{1,\zeta} & 0 & 0 & N_{2,\zeta} & \dots & 0 & 0 & N_{20,\zeta} \end{bmatrix}}_{\tilde{\mathbf{N}}} \{\mathbf{d}\} \quad (6.90)$$

$$\{\epsilon\} = \underbrace{[\mathbf{L}][\tilde{\Gamma}][\tilde{\mathbf{N}}]}_{\mathbf{B}} \{\mathbf{d}\} \quad (6.91)$$

6.1.8 Constitutive matrix

The appearance of the constitutive matrix depends on which type of material is used in the model. The materials used in this thesis are linear elastic isotropic materials and linear elastic orthotropic materials and the constitutive matrix for these types of materials are defined in Eq. 6.92 and Eq. 6.93 below.

Linear elastic isotropic material:

$$[\mathbf{C}] = \frac{E}{(1+\nu)(1-2\nu)} \begin{bmatrix} 1-\nu & \nu & \nu & 0 & 0 & 0 \\ \nu & 1-\nu & \nu & 0 & 0 & 0 \\ \nu & \nu & 1-\nu & 0 & 0 & 0 \\ 0 & 0 & 0 & (1-2\nu)/2 & 0 & 0 \\ 0 & 0 & 0 & 0 & (1-2\nu)/2 & 0 \\ 0 & 0 & 0 & 0 & 0 & (1-2\nu)/2 \end{bmatrix} \quad (6.92)$$

Linear elastic orthotropic material:

$$[\mathbf{C}] = \begin{bmatrix} C_{11} & C_{12} & C_{13} & 0 & 0 & 0 \\ C_{21} & C_{22} & C_{23} & 0 & 0 & 0 \\ C_{31} & C_{32} & C_{33} & 0 & 0 & 0 \\ 0 & 0 & 0 & C_{44} & 0 & 0 \\ 0 & 0 & 0 & 0 & C_{55} & 0 \\ 0 & 0 & 0 & 0 & 0 & C_{66} \end{bmatrix} \quad (6.93)$$

$$C_{11} = E_1 \left(1 - \frac{\nu_{23}^2 E_3}{E_2} \right) \gamma \quad (6.94)$$

$$C_{22} = E_2 \left(1 - \frac{\nu_{13}^2 E_3}{E_1} \right) \gamma \quad (6.95)$$

$$C_{33} = E_3 \left(1 - \frac{\nu_{12}^2 E_2}{E_1} \right) \gamma \quad (6.96)$$

$$C_{12} = E_1 \left(\frac{\nu_{12} E_2}{E_1} + \frac{\nu_{23} \nu_{13} E_3}{E_1} \right) \gamma \quad (6.97)$$

$$C_{21} = C_{12} \quad (6.98)$$

$$C_{13} = E_1 \left(\frac{\nu_{13} E_3}{E_1} + \frac{\nu_{12} \nu_{23} E_2 E_3}{E_1 E_2} \right) \gamma \quad (6.99)$$

$$C_{31} = C_{13} \quad (6.100)$$

$$C_{23} = E_2 \left(\frac{\nu_{23} E_3}{E_2} + \frac{\nu_{12} \nu_{13} E_3}{E_1} \right) \gamma \quad (6.101)$$

$$C_{32} = C_{23} \quad (6.102)$$

$$C_{44} = G_{23} \quad (6.103)$$

$$C_{55} = G_{13} \quad (6.104)$$

$$C_{66} = G_{12} \quad (6.105)$$

$$\gamma = \frac{1}{1 - \frac{\nu_{12}^2 E_2}{E_1} - \frac{\nu_{23}^2 E_3}{E_2} - \frac{\nu_{13}^2 E_3}{E_1} - \frac{2\nu_{12} \nu_{23} \nu_{13} E_2 E_3}{E_1 E_2}} \quad (6.106)$$

6.1.9 The principal stresses in three dimensions

The principal stress calculation in three dimensions are a bit more cumbersome than for two dimension cases, however, it is still manageable and can be expressed as:

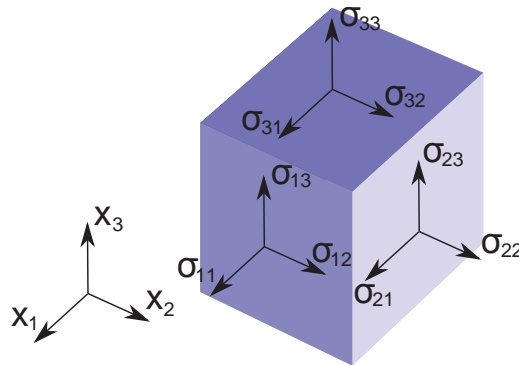


Figure 6.2 Stress in 3D

$$\sigma_1 = \frac{I_1}{3} + \frac{2}{3} \left(\sqrt{I_1^2 - 3I_2} \right) \text{Cos}(\phi) \quad (6.107)$$

$$\sigma_2 = \frac{I_1}{3} + \frac{2}{3} \left(\sqrt{I_1^2 - 3I_2} \right) \text{Cos} \left(\phi + \frac{2\pi}{3} \right) \quad (6.108)$$

$$\sigma_3 = \frac{I_1}{3} + \frac{2}{3} \left(\sqrt{I_1^2 - 3I_2} \right) \text{Cos} \left(\phi + \frac{4\pi}{3} \right) \quad (6.109)$$

where the angle ϕ and the stress invariants I_1 , I_2 and I_3 are given by:

$$\phi = \frac{1}{3} \text{Cos}^{-1} \left(\frac{2I_1^3 - 9I_1I_2 + 27I_3}{2(I_1^2 - 3I_2)^{3/2}} \right) \quad (6.110)$$

$$I_1 = \sigma_{11} + \sigma_{22} + \sigma_{33} \quad (6.111)$$

$$I_2 = \sigma_{11}\sigma_{22} + \sigma_{22}\sigma_{33} + \sigma_{33}\sigma_{11} - \sigma_{12}^2 - \sigma_{23}^2 - \sigma_{31}^2 \quad (6.112)$$

$$I_3 = \sigma_{11}\sigma_{22}\sigma_{33} - \sigma_{11}\sigma_{23}^2 - \sigma_{22}\sigma_{31}^2 - \sigma_{33}\sigma_{12}^2 + 2\sigma_{12}\sigma_{23}\sigma_{31} \quad (6.113)$$

6.1.10 Von Mises stress

From the theory it is known that the Von Mises stress is defined as in Eq. 6.114 and is used for validating if the material has exceeded its yield strength.

$$\sigma_v = \sqrt{\frac{1}{2} \{ (\sigma_1 - \sigma_2)^2 + (\sigma_2 - \sigma_3)^2 + (\sigma_3 - \sigma_1)^2 \}} \quad (6.114)$$

6.1.11 Surface traction

Surface traction on a solid hexahedron element can be converted to nodal loads. The theory below will explain how this is done for a surface load normal to the surface $\xi=1$. However, it is easily expanded to the other two directions in the plane. If $\mathbf{V} = x\mathbf{i} + y\mathbf{j} + z\mathbf{k}$

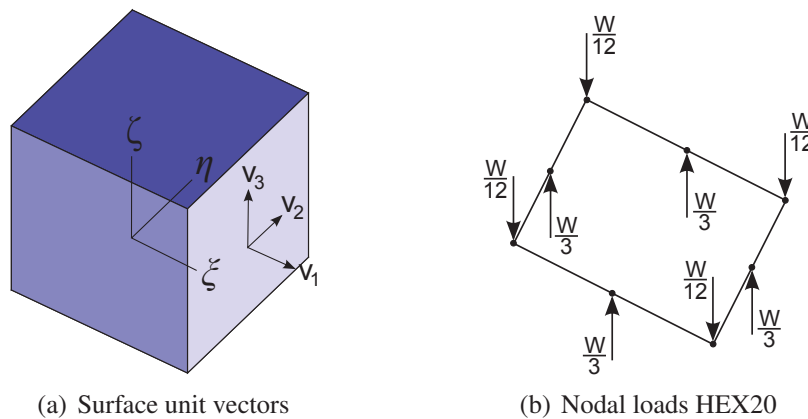


Figure 6.3 Surface traction on a hexahedron 20 nodes solid

is an arbitrary vector on the surface in Fig. 6.3(a) where \mathbf{i} , \mathbf{j} and \mathbf{k} are unit vectors in the

x , y and z direction, the vectors normal (\mathbf{V}_1) and tangential (\mathbf{V}_2 and \mathbf{V}_3) to the surface can be expressed as:

$$\mathbf{V}_1 = \frac{\partial \mathbf{V}}{\partial \xi} d\xi = (x_{,\xi} \mathbf{i} + y_{,\xi} \mathbf{j} + z_{,\xi} \mathbf{k}) d\xi = (J_{11} \mathbf{i} + J_{12} \mathbf{j} + J_{13} \mathbf{k}) d\xi \quad (6.115)$$

$$\mathbf{V}_2 = \frac{\partial \mathbf{V}}{\partial \eta} d\eta = (x_{,\eta} \mathbf{i} + y_{,\eta} \mathbf{j} + z_{,\eta} \mathbf{k}) d\eta = (J_{21} \mathbf{i} + J_{22} \mathbf{j} + J_{23} \mathbf{k}) d\eta \quad (6.116)$$

$$\mathbf{V}_3 = \frac{\partial \mathbf{V}}{\partial \zeta} d\zeta = (x_{,\zeta} \mathbf{i} + y_{,\zeta} \mathbf{j} + z_{,\zeta} \mathbf{k}) d\zeta = (J_{31} \mathbf{i} + J_{32} \mathbf{j} + J_{33} \mathbf{k}) d\zeta \quad (6.117)$$

The direction cosines l , m and n of a normal to the surface can now easily be found by the cross product:

$$l \mathbf{i} + m \mathbf{j} + n \mathbf{k} = \frac{\mathbf{V}_2 \times \mathbf{V}_3}{|\mathbf{V}_2 \times \mathbf{V}_3|} = \frac{\mathbf{V}_2 \times \mathbf{V}_3}{dS} \quad (6.118)$$

We now have $\{\Phi\} dS = \{l, m, n\}^T \sigma dS$ which inserted in the equation for the nodal load vector, Eq.6.119, result in Eq. 6.120 which can be integrated numerically. This will result in the surprising results shown in Fig. 6.3(b) where the nodal loads in the corners are actually pointing in the opposite direction of the surface load. The resulting force on the surface is divided between the nodes with the weights shown in the figure. To calculate the nodal forces for surface traction in the two other direction one only has to calculate the appropriate cosines for that direction by cross products of the vectors \mathbf{V}_1 , \mathbf{V}_2 and \mathbf{V}_3 .

$$\{r_e\} = \int [\mathbf{N}] \{\Phi\} dS \quad (6.119)$$

$$\begin{Bmatrix} r_{xi} \\ r_{yi} \\ r_{zi} \end{Bmatrix} = \int_{-1}^1 \int_{-1}^1 N_i \sigma \begin{Bmatrix} J_{22} J_{33} - J_{23} J_{32} \\ J_{23} J_{31} - J_{21} J_{33} \\ J_{21} J_{32} - J_{22} J_{31} \end{Bmatrix} d\eta d\zeta \quad (6.120)$$

6.1.12 Volume forces

As for the surface traction on a solid hexahedron element, the volume forces can also be converted to nodal loads. This can be achieved by the volume integral shown in Eq. 6.121.

$$\begin{Bmatrix} r_{xi} \\ r_{yi} \\ r_{zi} \end{Bmatrix} = \int_{-1}^1 \int_{-1}^1 \int_{-1}^1 N_i \mathbf{F} |\mathbf{J}| d\xi d\eta d\zeta \quad (6.121)$$

6.2 Performance of hexahedron 8 nodes and 20 nodes elements

This section will compare the performance of the hexahedron 8 nodes and 20 nodes elements which made the foundation for choosing the hexahedron 20 nodes elements for the structural model. Initially the elements performance are examined when considering computational time vs. error and degree of freedoms vs. error. The finite element model

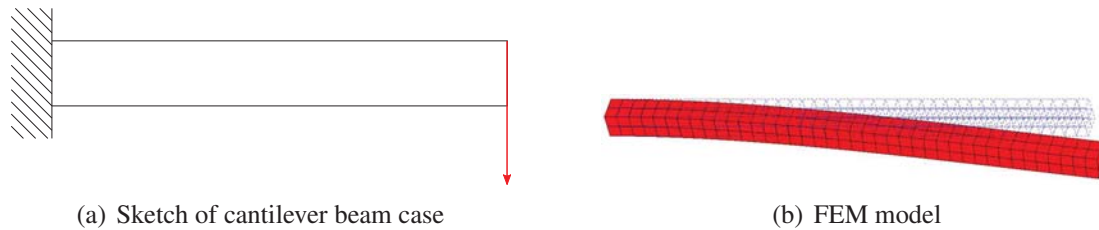


Figure 6.4 Bending cantilever beam test case

Element size	Dofs	Computational time [s]			Displacement		
		Assembly	Solving	Total	Numerical sol.	Analytical sol.	Relative error [%]
0.5000	1107	0.1720	0.1710	0.3430	2.80608	3.2000	12.31
0.3333	2928	0.6250	0.7350	1.3600	3.00742	3.2000	6.031
0.2500	6075	1.4690	2.2340	3.7030	3.08574	3.2000	3.752
0.1667	17787	4.9370	10.563	15.500	3.14485	3.2000	1.751
0.1250	39123	11.703	33.516	45.219	3.15273	3.2000	1.051

Table 6.1 Computational time and displacement - hexahedron 8 nodes

Element size	Dofs	Computational time [s]			Displacement		
		Assembly	Solving	Total	Numerical sol.	Analytical sol.	Relative error [%]
1.0000	744	0.047	0.812	0.859	3.17804	3.2000	0.686
0.5000	3663	0.514	4.493	6.007	3.191045	3.2000	0.280
0.3333	10200	1.233	14.913	8.047	3.192958	3.2000	0.220
0.2500	21975	2.558	42.47	45.02	3.19374	3.2000	0.197
0.1667	65919	8.080	192.2	200.2	3.19446	3.2000	0.173

Table 6.2 Computational time and displacement - hexahedon 20 nodes

used for these comparisons is a simple model of a cantilever shown in Fig. 6.4. The parameters used for this test case of a bending cantilever beam are $P = 0.0001$, $h = 1$, $b = 1$, $L = 20$, $E = 1$ and $\nu = 0.3$ where the element size has been varied. Table 6.1 and 6.2 show the computational time and displacement for each of the tested element sizes. Here we need to consider that the Poisson's ratio is set to 0.3 instead of 0 therefore the analytical solution in this case does not conform exactly to the actual displacement of the beam, however, the effect will be relatively small. From the table it can be seen that the hexahedron 20 nodes element shows a significantly increase in precision compared to the hexahedron 8 nodes element for the same number of degree of freedoms. Because of this characteristic of hexahedron 20 nodes element, it is possible to save solving time using 20 nodes elements instead of 8 nodes elements. A glance at Fig. 6.5 will reveal that the computational time decreased more than tenfold with the use of the 20 nodes elements compared to the 8 nodes elements to achieve the same accuracy. A final test is made to

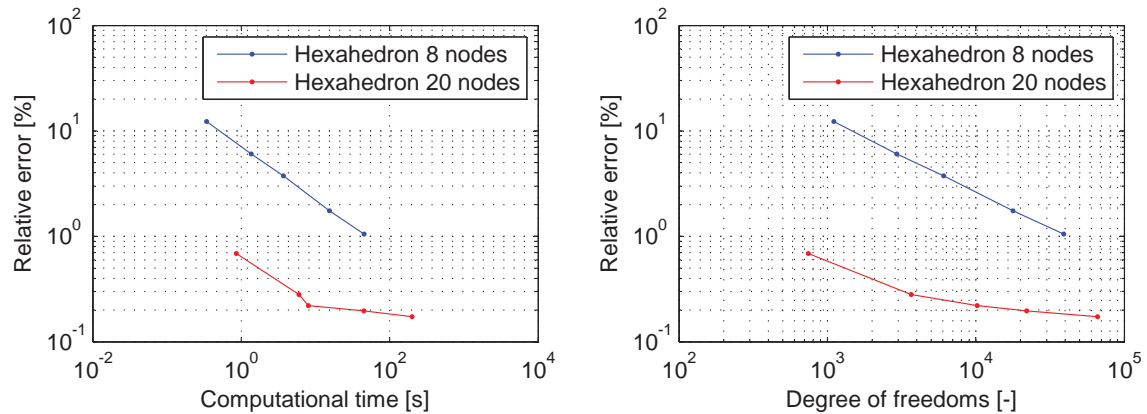


Figure 6.5 Comparison of hexahedron 8 nodes and hexahedron 20 nodes elements

examine the hexahedron 8 nodes and 20 nodes elements performance when looking at the determination of natural frequencies vs. degree of freedoms. The parameters used for this comparison are the same as in the previous case. Table 6.3 and 6.4 show the found natural frequencies for the different element discretization for the hexahedron 8 nodes and 20 nodes elements respectively. Figure 6.6 shows the natural frequencies from these tables plotted against the degree of freedoms. What can be seen from these plots are that the hexahedron 20 nodes elements has converged with the lowest number of freedoms tested where the hexahedron 8 nodes elements need a larger degree of freedoms to converge. It can also be seen that the hexahedron 8 nodes elements are inferior in determining the bending modes than the 20 nodes elements, as it can be seen that the 8 nodes elements quickly converted to the longitudinal mode (ω_8), but needed more degree of freedoms to converge for the bending modes (ω_1 to ω_6). An other thing which can be concluded from the plot with the 8 nodes elements is that one needs an increasingly finer discretization to determine increasingly higher modes. As a final conclusion, if one is modeling something to examine the bending modes, one should use the 20 nodes elements to decrease the number of elements needed. Due to the conclusions from these tests it is decided to

Element size	Dofs	ω_1	ω_2	ω_3	ω_4	ω_5	ω_6	ω_7	ω_8
		$\times 10^{-3}$	$\times 10^{-3}$	$\times 10^{-3}$	$\times 10^{-3}$	$\times 10^{-3}$	$\times 10^{-3}$	$\times 10^{-3}$	$\times 10^{-3}$
0.5000	1107	2.6874	2.6874	16.710	16.710	46.241	46.241	55.540	78.545
0.3333	2928	2.6029	2.6029	16.170	16.170	44.672	44.672	53.282	78.542
0.2500	6075	2.5727	2.5727	15.976	15.976	44.106	44.106	52.362	78.541
0.1666	17787	2.5509	2.5509	15.836	15.836	43.696	43.696	51.650	78.540
0.1250	39123	2.5432	2.5432	15.787	15.787	43.551	43.551	51.389	78.540

Table 6.3 Natural frequencies - hexahedron 8 nodes

Element size	Dofs	ω_1	ω_2	ω_3	ω_4	ω_5	ω_6	ω_7	ω_8
		$\times 10^{-3}$	$\times 10^{-3}$	$\times 10^{-3}$	$\times 10^{-3}$	$\times 10^{-3}$	$\times 10^{-3}$	$\times 10^{-3}$	$\times 10^{-3}$
0.5000	3663	2.5333	2.5333	15.725	15.725	43.375	43.375	51.261	78.540
0.3333	10200	2.5333	2.5333	15.723	15.723	43.367	43.367	51.082	78.540
0.2500	21795	2.5333	2.5333	15.723	15.723	43.365	43.365	51.054	78.540

Table 6.4 Natural frequencies - hexahedron 20 nodes

model the structural model of the mill with hexahedron 20 nodes elements.

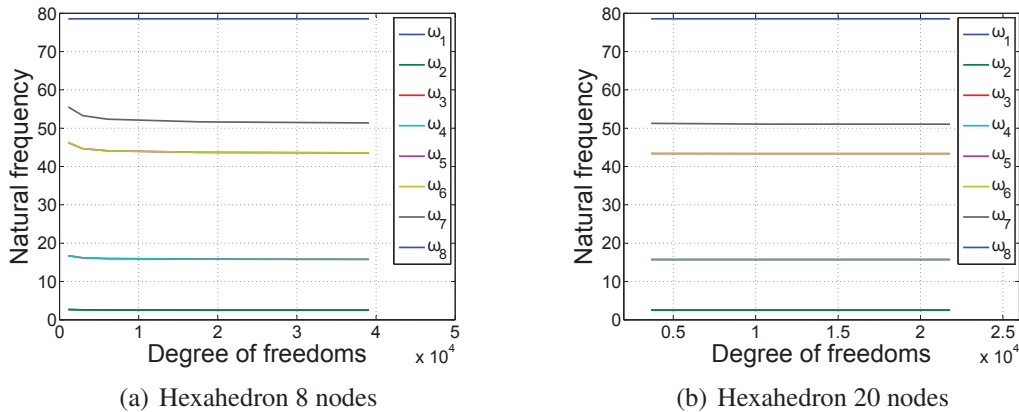


Figure 6.6 Natural frequencies vs. degree of freedoms

6.3 External programs

A couple of external programs are used in conjunctions with the Fortran finite element program. These programs are:

- GMSH, Geuzaine and Remacle (2010)
- ParaView, Kitware, Inc. (2011)
- MATLAB solvers

GMSH is a free 3D finite element mesh generator with a build-in CAD engine and post-processor. **GMSH** is used for generating the finite element mesh for the Fortran program

through script files. The program is capable of auto-generating mesh consisting of triangle, tetrahedron and pyramid elements and to some extent collapse these into hexahedron elements. However, as the finite element program is written for pure hexahedron mesh, the mesh is created completely manually through the mentioned script files.

ParaView is an open-source, multi-platform application designed to visualize data sets of varying sizes from small to very large. It is used for visualizing the results from the Fortran finite element program for the deformation, stress, strain and natural frequency mode shape results. The program even has the capability to animate the mode shapes for quick and better visualizing of the modes.

MATLAB solvers are used for solving the large system of equations created by the finite element program. The reason why MATLAB solvers are used is due to the failure to find an effective sparse matrix solver for Fortran. Due to the size of the problem, it is necessary to store the mass and stiffness matrices in sparse format which makes the use of full matrix solvers unsuitable. To speed up the data transfer between the Fortran and MATLAB the matrices are written as unstructured binary data dumps from the Fortran program. The MATLAB solvers solve both the linear system of equations for displacements and the eigenvalues and their corresponding eigenvectors.

6.4 Stator & frame

The model of the frame including stator is shown in Fig. 6.7. It consists of the following main items:

- Side, bottom and top plates (red)
- Feed side end plate (gray)
- Discharge side end plate (gray)
- 3 internal plates (blue)
- Frame stiffener tubes (not visible)
- Stator (green)

6.4.1 Frame model

The frame consists of 5 vertical plates in the axial direction, Fig. 6.8(a), 6.8(b), 6.8(c), 6.8(d) where the three internal plates are attached to the stator. The bottom and side plates, Fig. 6.8(e), keep these plates at a fixed distance between each other and further more create the closed chamfers for the cooling flow. The bottom half of the 5 vertical plates is a bit thicker than the upper half and therefore consists of two elements in the axial direction where the upper part only consist of one element. The cut outs in the three internal plates are for the cooling fans and coolers which are neglected in this model. The material for the plates are modeled as linear elastic isotropic material with the following material parameters: $E = 200 \cdot 10^9 \text{ N/m}^2$, $\rho = 7850 \text{ kg/m}^3$ and $\nu = 0.3$.

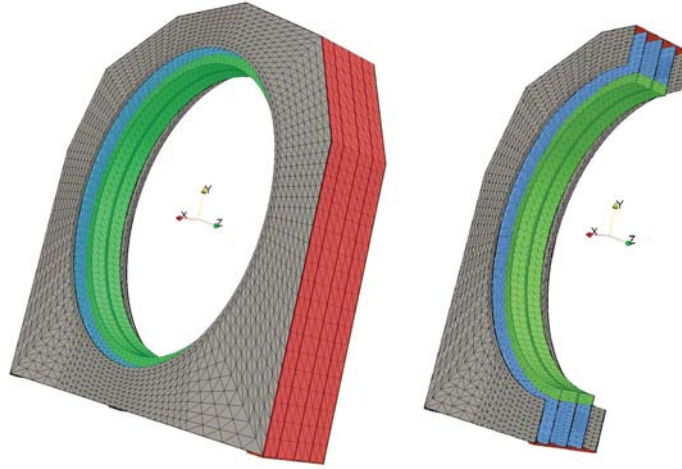


Figure 6.7 Frame with stator

6.4.2 Frame stiffener model

The stiffener tubes between the frame plates are modeled as springs to minimize the number of elements and to ease the modeling of the tubes, Fig. 2.2(b) (19). To estimate an equivalent spring stiffness of these tubes the two elementary beam cases in Fig. 6.9 are used. The displacement due to bending of a fixed-free cantilever beam with a force and a moment at the end, Fig. 6.9(a), can be expressed as shown in Eq. 6.122 where the inertia for a beam with a cross-section shown in Fig. 6.9(c) can be found by Eq. 6.123.

$$\delta(L) = \frac{PL^3}{12EI} \quad (6.122)$$

$$I = \frac{\pi}{64}(D^4 - d^4) \quad (6.123)$$

By inserting Eq. 6.123 into Eq. 6.122 and rearranging, an equivalent stiffness due to bending of one stiffener tube can be found to:

$$k_{x,eq} = k_{y,eq} = \frac{3E\pi(D^4 - d^4)}{16L^3} \quad (6.124)$$

In a similar fashion the displacement of a beam in tension/compression, Fig. 6.9(b), can be expressed as in Eq. 6.125 where the cross-section area in Fig. 6.9(c) can be found by Eq. 6.126.

$$\delta(L) = \frac{PL}{EA} \quad (6.125)$$

$$A = \frac{\pi}{4}(D^2 - d^2) \quad (6.126)$$

By inserting Eq. 6.126 into Eq. 6.125 and rearranging one can again find an equivalent stiffness this time for tension/compression of the stiffener tube:

$$k_{z,eq} = \frac{E\pi(D^2 - d^2)}{4L} \quad (6.127)$$

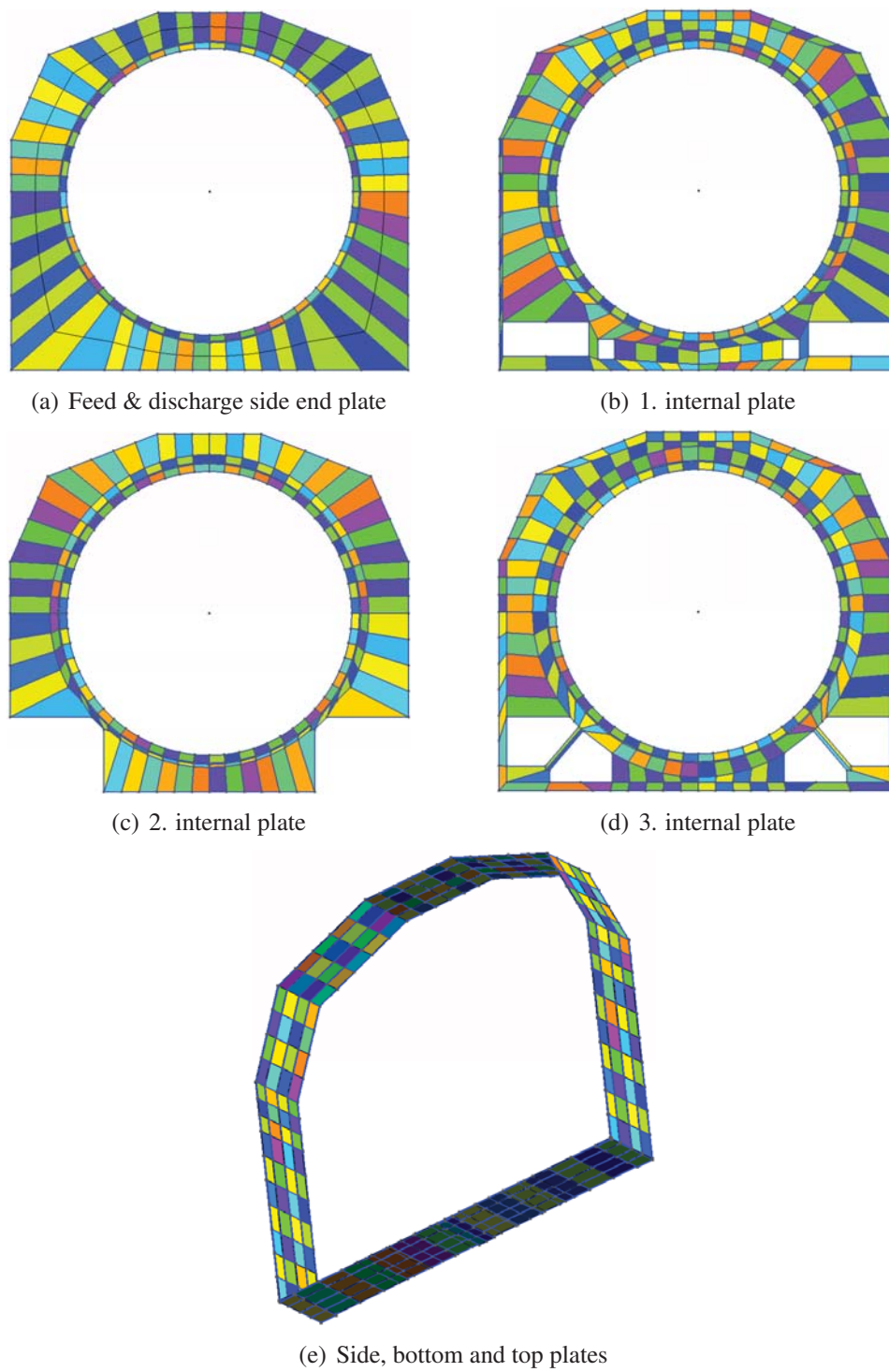


Figure 6.8 Frame plates mesh

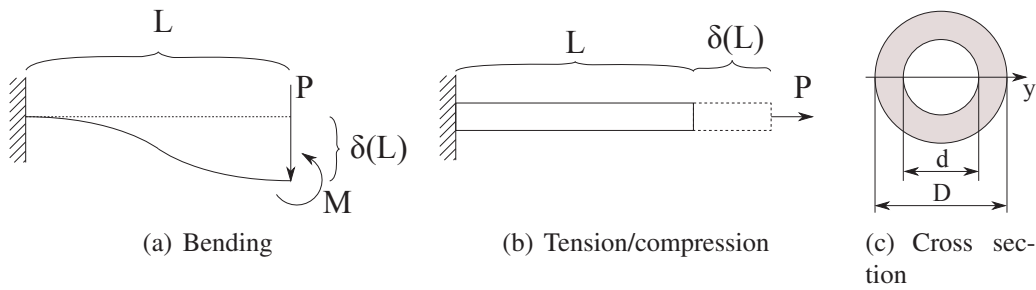


Figure 6.9 Elementary beam cases

Parameter	Value	Unit
D	0.100	m
d	0.080	m
L	0.530	m
E	$200 \cdot 10^9$	N/m ²
$k_{x,eq}, k_{y,eq}$	$46.72 \cdot 10^6$	N/m
$k_{z,eq}$	$1066.95 \cdot 10^6$	N/m

Table 6.5 Equivalent stiffness of one frame stiffener pipe

The parameter values and the found equivalent stiffnesses of one stiffener tube are listed in Tab. 6.5. As the stiffener tubes are closely spaced in a circle a bit larger than the stator outer diameter, it is assumed that the best way of applying these equivalent stiffnesses to the model are to distribute them evenly to two circles spaced with the distance of the diameter of the stiffener tubes, Fig. 6.10. In this way, the moment from the bending motion of the stiffener tubes is to some extent also taken into account. These distributed stiffnesses have been added to the stiffness matrix as both diagonal and off diagonal elements to take the relative movement of the different frame plates into account.

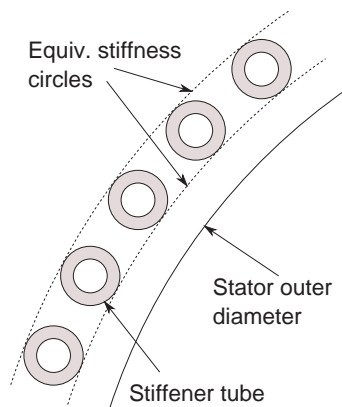


Figure 6.10 Circles for applying equivalent stiffness

6.4.3 Stator model

The stator is build up of M400-50A steel sheets with a thickness of 0.5 mm like the one shown in Fig. 6.11(a). These sheets are stacked on top of each other with an overlap to form the complete stator core. The slots are then filled with the copper bars to form the stator windings. As the stator is modeled as a solid ring, Fig. 6.11(b), but is actually build of sheets with copper bars, it can not be modeled as an linear elastic isotropic material. It is therefore modeled as a linear elastic orthotropic material with different radial and axial Young's modulus. According to ABB, the elasticity modulus in the axial direction is a factor 10 smaller than that of the radial direction. $E_{rad} = 100 \cdot 10^9 \text{ N/m}^2$, $E_{axial} = 10 \cdot 10^9 \text{ N/m}^2$. Due to the fact that the real stator consists of both steel with holes and copper, the density of the modeled stator is corrected to give an equivalent mass. This is done by splitting the stator in two parts. One consisting of the core back (iron with holes) and the other consisting of stator teeth (iron with holes) and the copper bars. The densities used for the two parts are: $\rho_{Fe} = 5588 \text{ kg/m}^3$, $\rho_{Fe-Cu} = 8389 \text{ kg/m}^3$. The stator is modeled as rigidly attached to the 3 internal plates described in Sec. 6.4.1. However, the stator is in fact attached to a lot of beams on the outer diameter which again are attached to the 3 internal plates. Furthermore, the stator is bolted to one of the internal plates. However, as the stator heats up the outer diameter of the stator will be pressed up against the 3 internal plates which make this simplification valid.

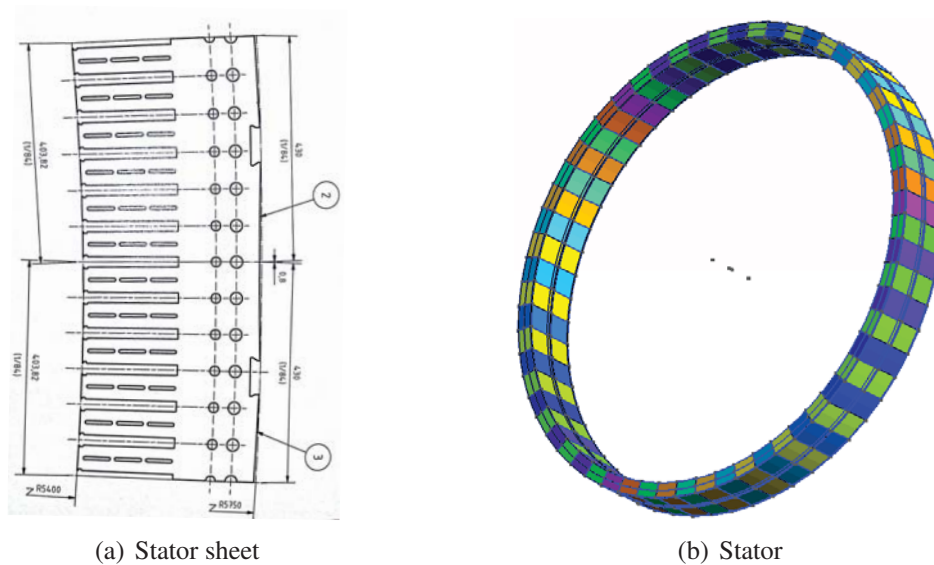


Figure 6.11 Stator mesh

6.5 Mill drum, rotor poles & bearings

The model of the mill drum, including poles, is shown in Fig. 6.12. It consists of the following main items:

- Feed head & trunnion (red)
- Discharge head & trunnion (blue)
- Cylinder (gray)
- Rotor poles (green)
- Feed cone liners (not visible)
- Discharge cone liners (not visible)
- Cylinder liners (not visible)

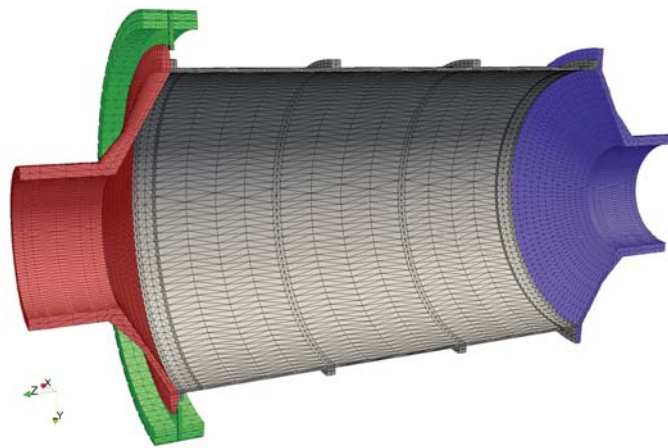


Figure 6.12 Mill drum with poles

6.5.1 Mill drum model

The mill drum consists of the feed/discharge head & trunnion shown in Fig. 6.13(a) and cylinder Fig. 6.13(b). As the rock load tumble around inside the drum, causing a lot of wear, the drum is fitted with replaceable liners which are a lot of plates bolted to the inside of the drum. These liners do not contribute significantly to the stiffness of the drum, however, the weight of them can not be neglected. The way that this additional mass is added to the model is by creating an equivalent density for both the feed/discharge head & trunnion and the cylinder. The following material parameters are used for the mill drum, Tab. 6.6 A drawing of the mill drum can be seen in Fig. A.1 in appendix.

Feed/discharge head & trunnion	Cylinder
$E = 172.5 \cdot 10^9 \text{ N/m}^2$	$E = 200 \cdot 10^9 \text{ N/m}^2$
$\rho = 10975 \text{ kg/m}^3$	$\rho = 21222 \text{ kg/m}^3$
$\nu = 0.275$	$\nu = 0.3$

Table 6.6 Mill drum material parameters

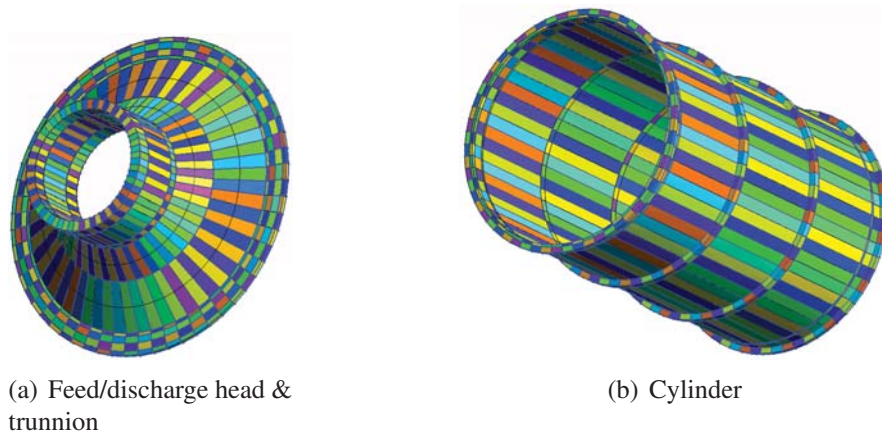


Figure 6.13 Mill drum model mesh

6.5.2 Rotor pole model

A rotor pole, Fig. 6.14(a), consists of a middle plate where several profile cut St.42 steel sheets are stacked on each side of the plate. A press plate is added at each end of the poles and bolts are run through the entire stack pressing it firmly together. The copper windings are then wrapped around the entire pole core. The end of the middle plate is bolted to the mill flange with 3 bolts. This is simplified to the model shown in Fig. 6.14(b) where the bottom element of the middle plate is completely fixed to the mill flange at all merging surface nodes. The density of the pole core is modified to take into account that density of copper is larger than steel. The material parameters used for modeling the pole are: $E = 200 \cdot 10^9 \text{ N/m}^2$, $\rho = 8613 \text{ kg/m}^3$ and $\nu = 0.3$.

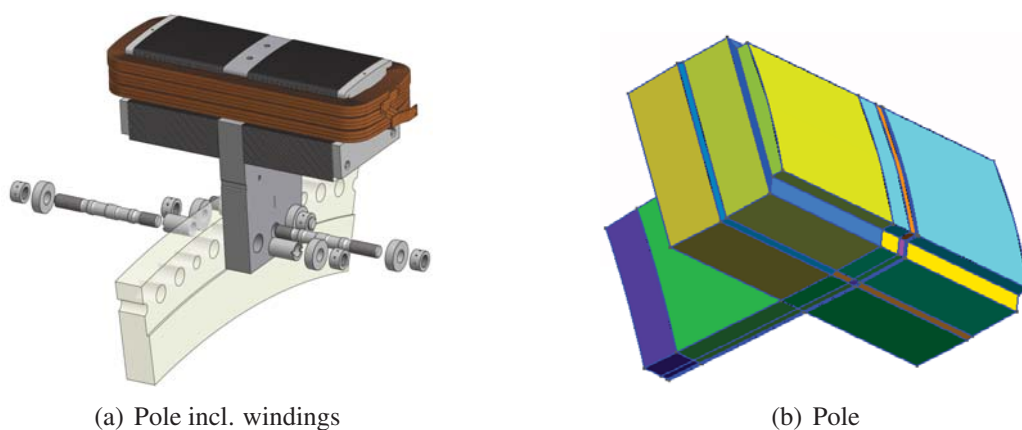


Figure 6.14 Pole mesh

6.5.3 Bearings

Two large hydrostatic bearings are wrapped around the trunnion at each end of the mill drum. The stiffness of these bearings are provided by ABB and listed in Tab. 6.7. These stiffnesses are added to the model with a sinusoidal distribution at the surface indicated in Fig. 6.15 as to obtain a gradually transition from the horizontal stiffness to the vertical stiffness. The surface stiffness is applied to the model in a similar way as the surface traction described in Sec. 6.1.11.

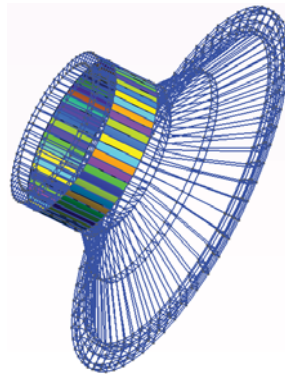


Figure 6.15 Bearing surface on the trunnion

Direction	Stiffness [N/m]	Damping [k-s/m]
Vertical	$1.9455 \cdot 10^{10}$	$817.89 \cdot 10^6$
Horizontal	$1.2010 \cdot 10^{10}$	$505.38 \cdot 10^6$

Table 6.7 Bearing stiffness includes all components from the oil film down to the bottom plate. Damping values are for the oil film only

6.6 Stator/rotor/frame forces and torque

The forces between the poles and the stator, estimated in Sec. 3.4, have for the static simulations been applied as distributed surface forces on top of the pole and on the inner surface of the stator as described in Sec. 6.1.11. In addition to these forces, springs with a negative stiffness have been applied between the pole and stator surfaces equivalent to the change in forces due to change in air gap. As shown in Sec. 3.4, the relationship between forces and air gap size is very linear, which makes it a good assumption to use linear springs for the change in forces due to displacement. These surface distributed spring stiffnesses have been added to the stiffness matrix as both diagonal and off diagonal elements to take the relative movement of the poles and stator into account and have been distributed in a similar fashion as the forces described in Sec. 6.1.11.

The static forces between the poles and the stator will not be taken into account when

estimating the natural frequencies and their corresponding mode shapes due to the way the natural frequencies are calculated, see Sec. 6.1 Eq. 6.3. However, the change of forces due to change in air gap are still applied as negative stiffness between the pole and stator as described above.

The forces from the rock charge inside the mill drum have been applied to the inside bottom half of the drum as downward acting distributed surface forces. As the majority of forces act on the lowest part of the drum, the forces have not been added evenly but with a sinusoidal distribution. Again, the distribution of the forces on the different elements have been done as described in Sec. 6.1.11.

As the whole mill is very large and extremely heavy, it would be wrong to neglect the effect of gravity. The mass of every finite element in the model has for this reason been calculated and the gravity forces have been distributed to the nodes of the elements as described in Sec. 6.1.12.

The torque has only been applied to the inner surface of the stator in the mill drive. There are two reasons for this. The first is that the exact distribution of the torque opposing the rotor pole torque, which comes from the rock load, is unknown as the exact distribution of the rock load is unknown. The second and more important reason is that an even slight difference between the values of the torque from the rotor poles and the torque from the rock load would result in the mill drum beginning to rotate and a static solution would not be possible. The torque has been applied to the inner surface of the stator as equivalent nodal forces which sum multiplied by the radius result in the produced torque. These equivalent forces are applied to the surface as described in Sec. 6.1.11.

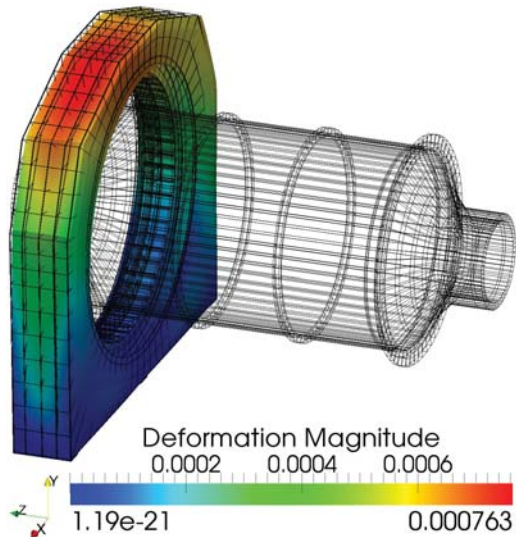
A list of the used forces, torque and spring constants are listed in Tab. 6.8.

Parameter	Value	Unit
Pole force, one pole no eccentricity	259.9	kN
Equivalent pole stiffness, one pole	-8518.5	kN/m
Rock charge	14.32	MN
Frame/stator gravity force	2.4	MN
Drum/pole gravity force incl. liners	12.3	MN
Torque	13.6	MNm

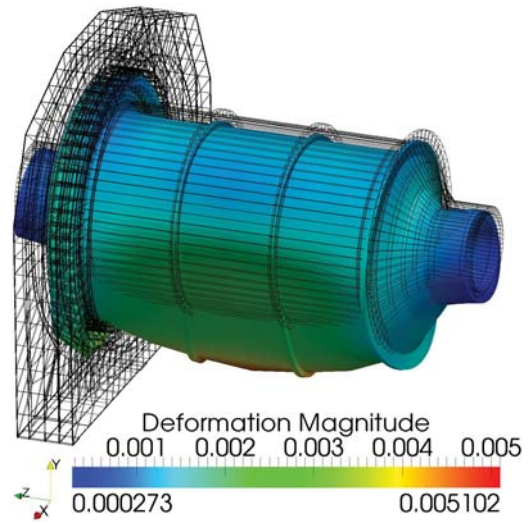
Table 6.8 Forces, torque and equivalent stiffnesses

6.7 Static deflection

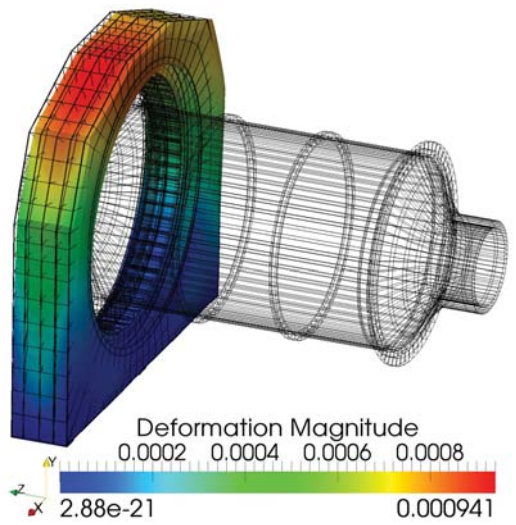
By using the model described above, it is possible to calculate the static deflection of the entire mill due to heat, torque and forces applied to it. Due to the different magnitude of deflection of the frame and the rotor, the results are split up in deflection of the frame and deflection of the rotor to clearly show the deformation of these two parts. The parts



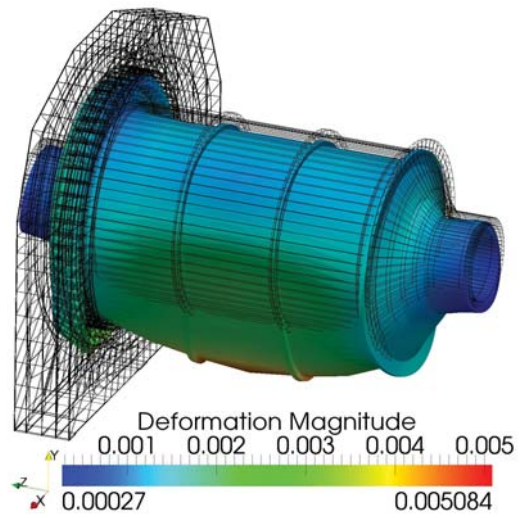
(a) Frame deformation [m], undeformed rotor eccentricity $(x,y)=(0,0)$ [mm]



(b) Drum deformation [m], undeformed rotor eccentricity $(x,y)=(0,0)$ [mm]

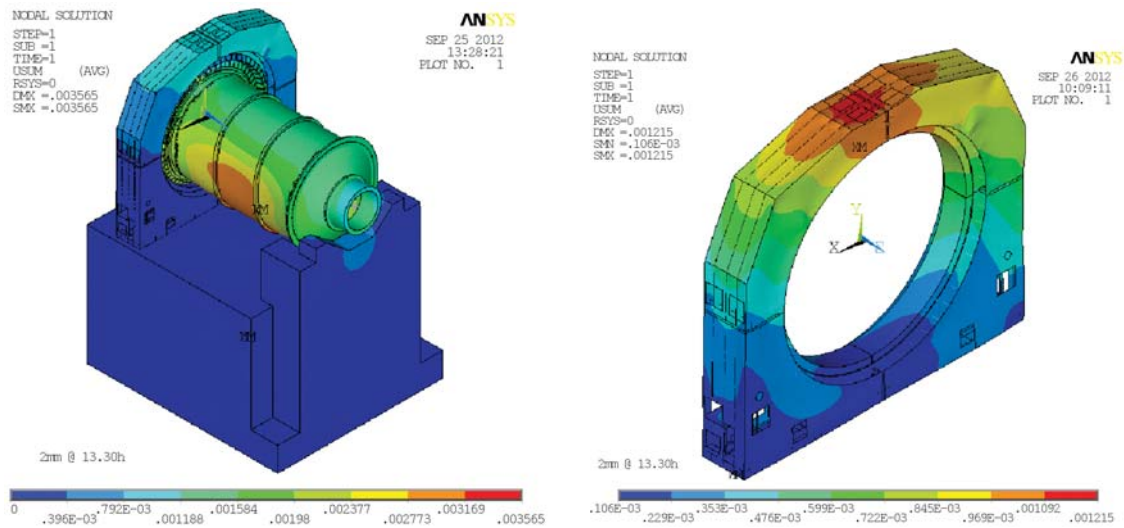


(c) Frame deformation [m], undeformed rotor eccentricity $(x,y)=(1.4142,1.4142)$ [mm]



(d) Drum deformation [m], undeformed rotor eccentricity $(x,y)=(1.4142,1.4142)$ [mm]

Figure 6.16 Deformation of the full structural model due to gravity, pole forces, torque, heat expansion and rock charge



(a) Mill drive deformation [m], undeformed rotor eccentricity (x,y)=(1.4142,1.4142) [mm] (b) Frame deformation [m], undeformed rotor eccentricity (x,y)=(1.4142,1.4142) [mm]

Figure 6.17 Deformation of the mill drive due to gravity, pole forces, torque and rock charge, Source: ABB Switzerland Ltd.

are, however, still completely interconnected through the forces and surface springs between the poles and the stator. Figure 6.16(a) shows the deformation of the frame when the undeformed rotor has zero eccentricity. The figure shows a maximum magnitude of deflection of approximately 0.763 mm in the top of the frame. The reason that the deformation is not completely symmetric around the center of the frame as could have been expected when dealing with a rotor eccentricity of zero, is due to the applied torque on the stator. Figure 6.16(b) shows the deflection of the mill drum and rotor poles which are highly dominated by the mass of the liners and forces from the rock charge inside the drum. As expected, the maximum deflection is in the center bottom part of the drum and has a maximum deflection magnitude of approximately 5.10 mm. Due to the bending of the drum, the poles are turned from their undeformed state which is most obvious in the lower part of the drive. This results in an air gap which is not the same for the entire pole surface of a specific pole and will be determined in Sec. 6.9. To examine the effect of an eccentric rotor on the deflection of the mill, a case is performed where the rotor eccentricity is set to 2 mm in a direction of 45° from the horizontal plane (x-axis). The results from this case are shown in Fig. 6.16(c) and 6.16(d) for the frame and drum respectively. Looking at the frame, Fig. 6.16(c), it is clear that the resulting force has increased the maximum magnitude of the deflection in the direction of the eccentricity. The magnitude of the deflection has increased to approximately 0.941 mm, as the air gap in the top of the drive has decreased and the pole forces have therefore increased, pulling the top of the frame in a downward direction. Looking at the drum, Fig. 6.16(d), it can be seen that the maximum magnitude of the deflection (5.08 mm) is only slightly smaller than that of the zero eccentricity case. ABB Switzerland Ltd. has provided their results of a similar

case as the one with the 2 mm eccentricity in a direction of 45° from the horizontal plane (x-axis). These results can be seen in Fig. 6.17(a) and Fig. 6.17(b) which shows the deformation of the complete drive and the frame alone, respectively. These results show a maximum deformation of the mill drum of 3.565 mm and a maximum deformation of the frame of 1.215 mm. A comparison of these results with the results from the Fortran model will show a relatively large deviation which will be further described and commented on in Sec. 6.13.

6.8 Static stress

The Von Mises stresses, Sec. 6.1.10, in the mill are calculated to make sure that the material does not yield due to gravity and forces between the poles and the stator. Figure 6.18 shows the resulting Von Mises stresses for the two cases examined in the previous section, Sec. 6.7. It can be seen from the figures that the stresses for the two cases are almost identical with slightly smaller stresses for the eccentric case. The highest stresses are mainly concentrated at the center bottom part of the drum and at the top where the mill flange meets the pole middle plate. However, as the maximum Von Mises stress for the two cases is $\sigma_{v,max} = 27.86 \text{ MN/m}^2$ and the yield strength for ordinary construction steel normally used for plates, bars and pipes is approximately $\sigma_y = 250 \text{ MN/m}^2$, no yielding will occur for the two cases as $\sigma_{v,max} \leq \sigma_y$. A similar check is performed later in the optimization of the drive to discard invalid solutions due to yielding of the material, Sec. 7. As for the deformation case, ABB has also provided stress results from their model with the eccentric mill drum which can be seen in Fig. 6.19. From this plot it can be seen that the maximum stress on the frame is located at the bottom of the side plate just as in the results from the Fortran program however the size of the stress is higher in the ABB model, approximately 25 MN/m^2 . A further discussion on this deviation are found in Sec. 6.13.

6.9 Rotor/stator air gap

The air gap between the rotor and stator is extremely critical for the operation of the drive and must for this reason be within some specific limits. The air gap is not identical at the different poles nor in the axial direction of a specific pole, as result of the heat expansion and the deformation of the entire structure. A model is therefore created in which to determine the air gap at the maximum and minimum z-values of each pole (feed side/discharge side), Fig. 6.20. Figure 6.21(a) shows the found air gap around the drive due to gravity, pole forces, torque, heat expansion and rock charge where the effect from the deformed rotor is clearly reflected, as the air gap in the feed end is not the same as in the discharge end and none of them are nice sinus shaped curves.

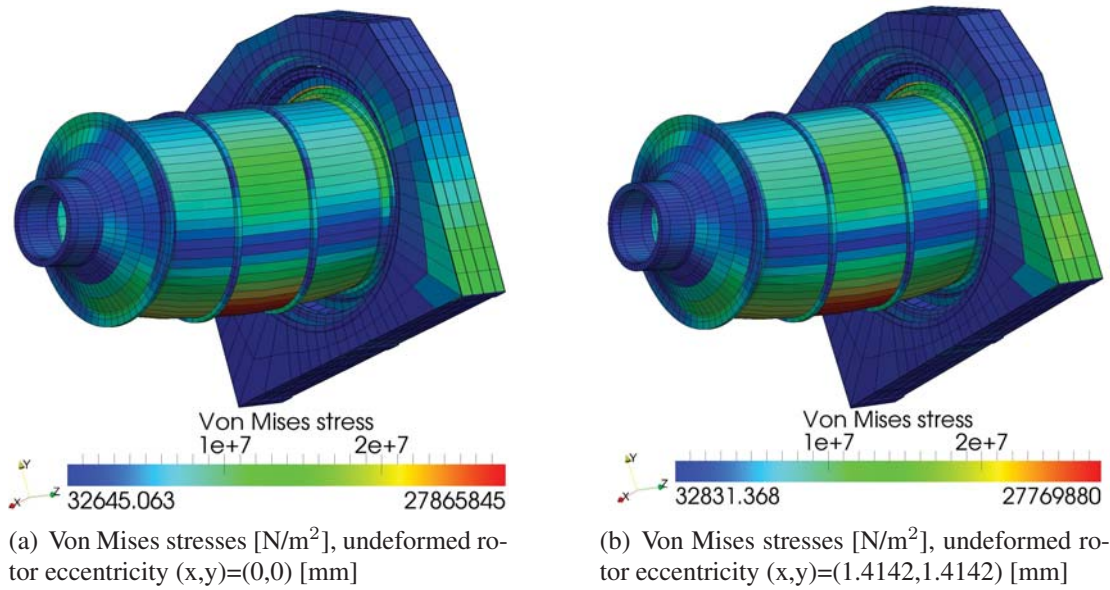


Figure 6.18 Stresses of the full structural model due to gravity, pole forces, torque, heat expansion and rock charge

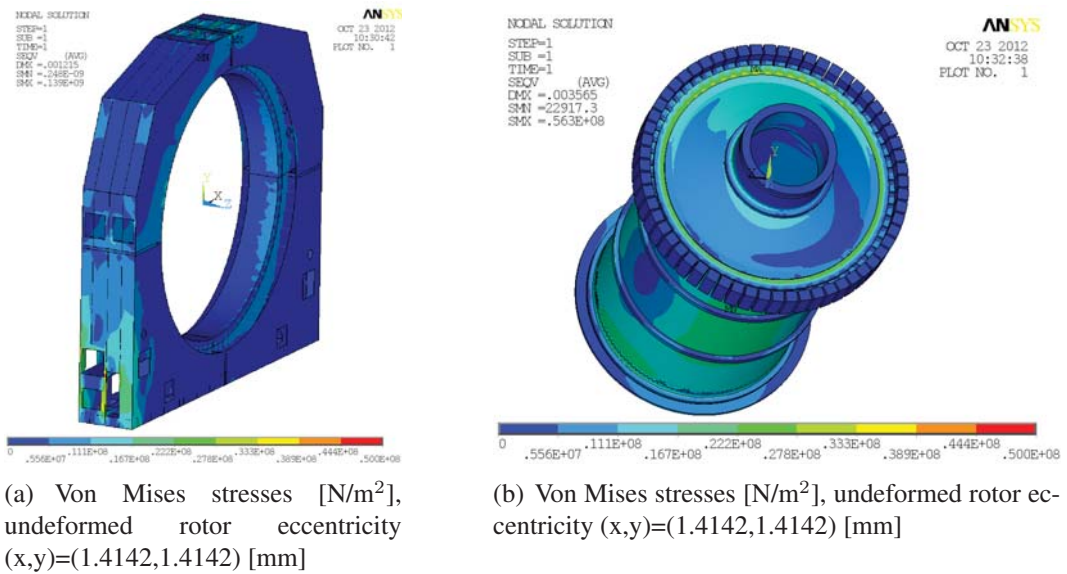


Figure 6.19 Stresses of the mill drive due to gravity, pole forces, torque and rock charge, Source: ABB Switzerland Ltd.

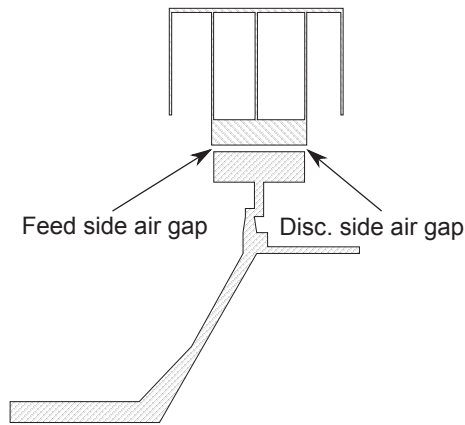
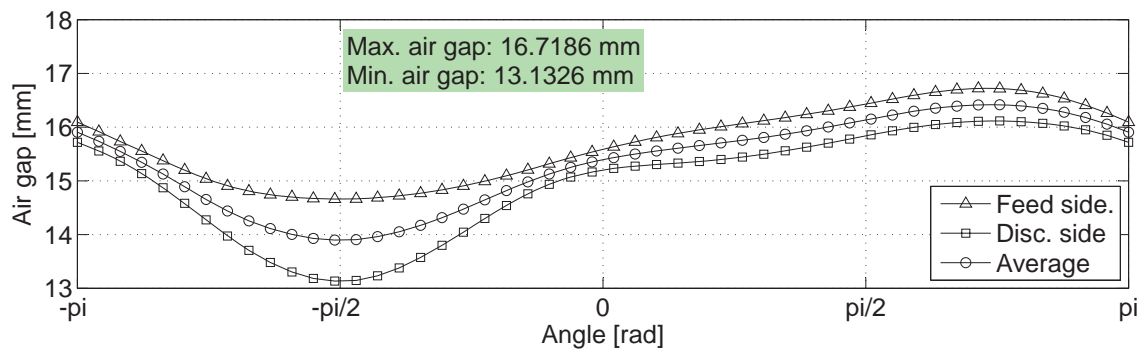
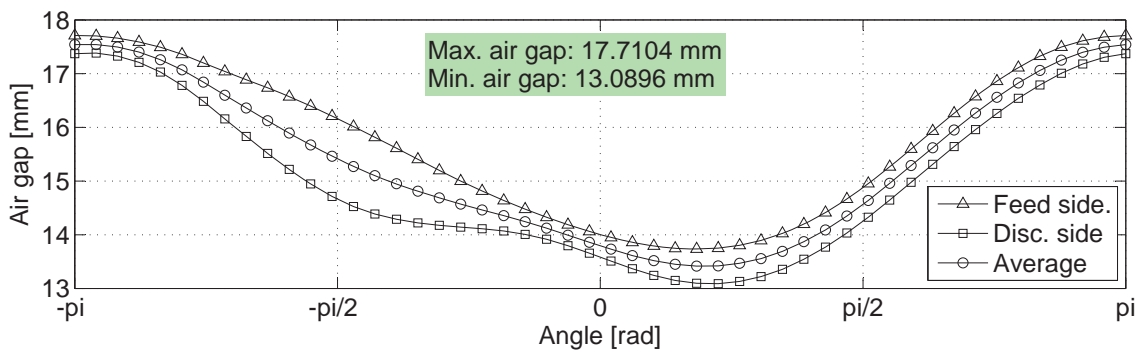


Figure 6.20 Explanation for air gap determination



(a) Undeformed rotor eccentricity (x,y)=(0,0) [mm], angle CCW from x-axis



(b) Undeformed rotor eccentricity (x,y)=(1.4142,1.4142) [mm], angle CCW from x-axis

Figure 6.21 Rotor/stator air gap due to gravity, pole forces, torque, heat expansion and rock charge

6.10 Natural frequencies & mode shapes

The natural frequencies of the mill drive are independent of the eccentricity of the rotor, as all the forces are set to zero due to the way the natural frequencies are calculated. For an undamped system with forces equal to zero (free vibration) Newton's second law states that the equation of motion can be expressed as:

$$\mathbf{M}\ddot{x} + \mathbf{K}x = 0 \quad (6.128)$$

This differential equation can be solved by assuming the following type of solution

$$x = X \cdot e^{i\omega t} \quad (6.129)$$

Inserting Eq. 6.129 in Eq. 6.128 and exploiting that $e^{i\omega t} \neq 0$ result in:

$$[\mathbf{K} - \omega^2\mathbf{M}] X = 0 \quad (6.130)$$

This is referred to as an eigenvalue problem and when solved will give the undamped natural frequencies. By inserting the found eigenvalues into the equation their corresponding eigenvectors can be found representing the mode shapes of the system. The only connection between the rotor poles and the stator are therefore the surface springs with the negative stiffnesses described in Sec. 3.4.2 and Sec. 6.6 and as these are linear springs the initial position of the rotor has no influence on the results. The reason for estimating the natural frequencies are to make sure that none of the “critical” natural frequencies match those of the potential excitation frequencies like mill speed, pole passing and power supply output. The word “critical” in this context should be understood as natural frequencies with mode shapes that seriously distort the air gap between the rotor and stator. Mode shapes where the majority of the vibrations come from the frame plates, for example, are not categorized as “critical”, as these do not directly have an influence on the operation of the mill drive. The way that this categorization of “critical” and “non-critical” natural frequencies are performed is by estimating the air gap between the rotor and stator created by plotting the normalized eigenvectors. If the maximum air gap exceed a value of 0.05 it is categorized as “critical” which has proved to give consistent and accurate evaluation of the modes. Figure 6.22 shows a couple of the “critical” modes of the frame alone, assuming that the rotor remains rigid and fixed. Similar mode shapes are supplied by ABB for comparison and are plotted in the figure next to the Fortran estimated modes. It is seen from the plots that the shape of the modes correspond relatively well between the ABB provided results and that of the Fortran program, however, their corresponding natural frequency differs significantly from each other. An explanation for these discrepancies are to be found in the boundary conditions between the stator and frame used for the Fortran and the ABB model respectively. In the Fortran model, the stator is rigidly attached to the frame plates, which is an acceptable assumption, as the heat expansion of the stator leads to a high pressure between the frame and the stator, as described in Sec. 5.7. In the ABB model, the stator is not pressed against the frame plates, as it is modeled in cold condition without heat expansion. The stator is instead

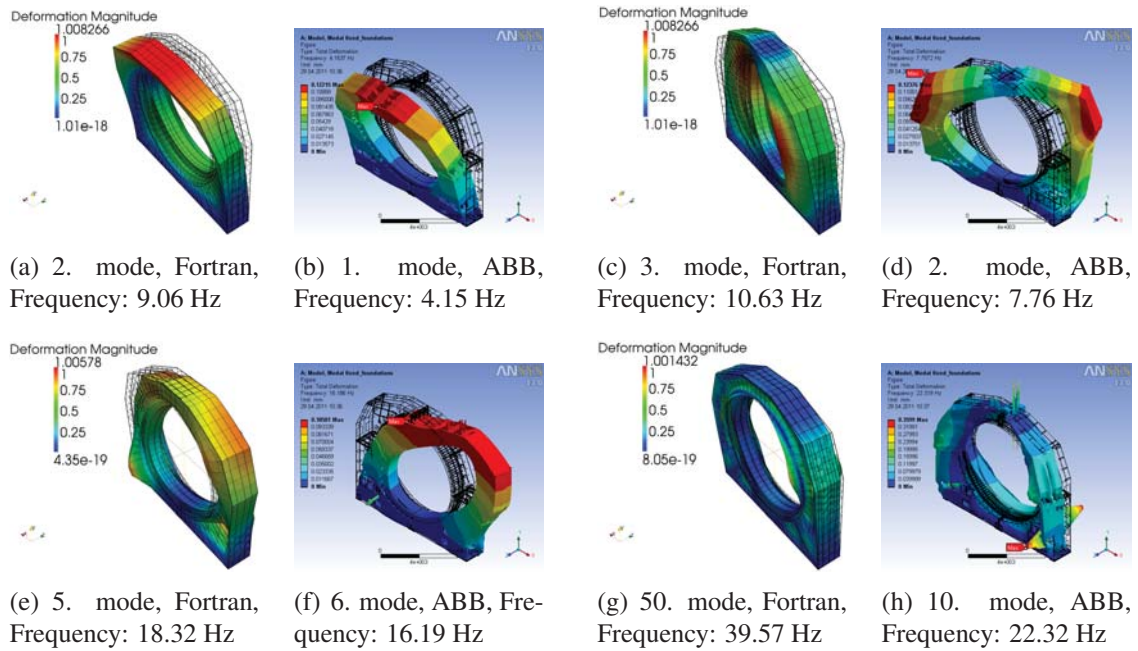


Figure 6.22 Comparison of mode shapes of the frame

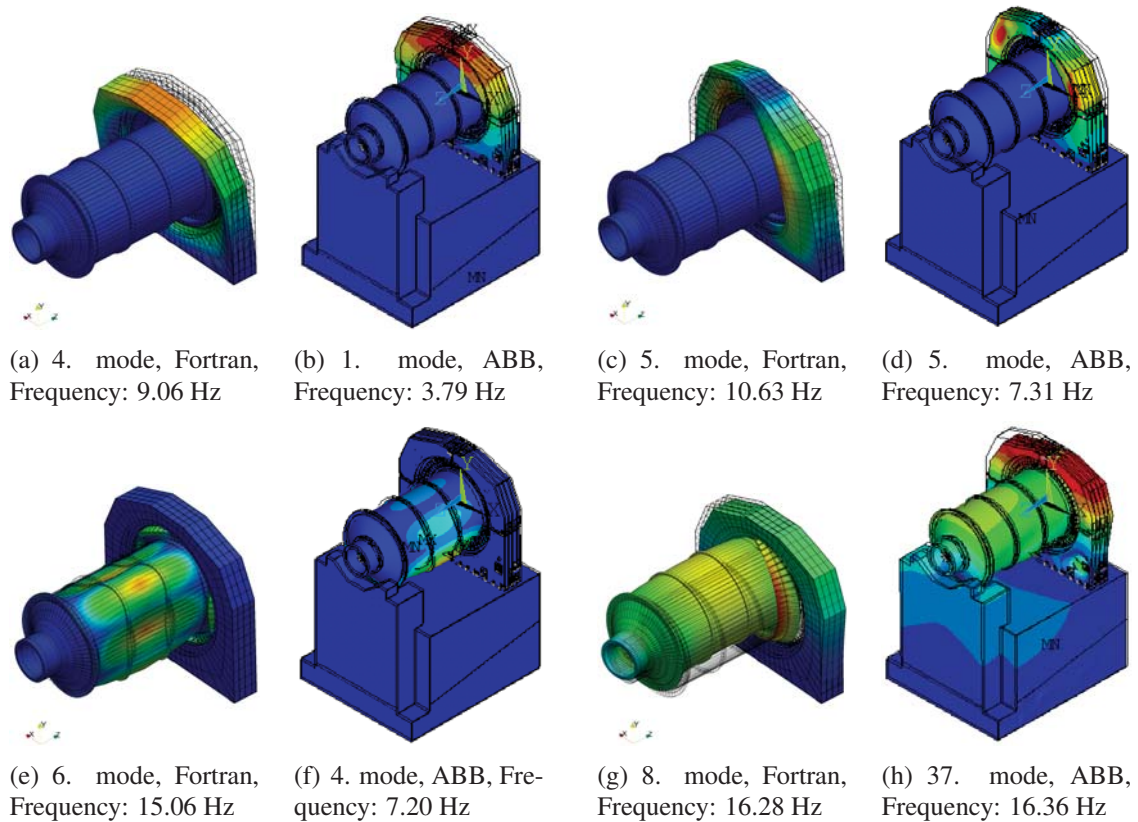


Figure 6.23 Comparison of mode shapes of the frame and mill drum

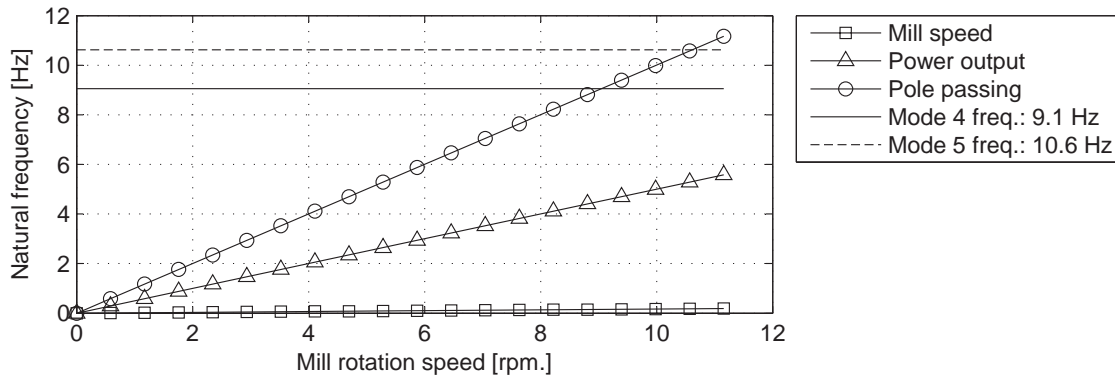


Figure 6.24 Critical speeds diagram

Source of excitation	Frequency [Hz]
Nominal mill speed	0.19
Nominal power supply output	5.60
Nominal mechanical pole passing	11.20

Table 6.9 Excitation frequencies

attached to a lot of beams on the outer diameter of the stator, which then again is attached to the 3 internal plates of the frame. As the ABB model of the drive is modeled in cold condition and the stator is not pressed against the 3 internal frame plates, this results in a smaller overall stiffness of the frame/stator model compared to the Fortran model. This corresponds well with the fact that the natural frequencies found by ABB in general are lower than those of the Fortran program found values, due to the smaller general stiffness of the ABB model. As the natural frequencies of the mill drive is unimportant if the mill is not in operation, it has been found to be more correct to model the drive in a hot condition and thereby with the stator rigidly attached to the frame. Figure 6.23 shows a couple of the “critical” modes of the complete coupled rotor-frame system. The results shown in the figure are again from the Fortran program and results received from ABB for comparison. It is seen from the plots that the shape of the modes again correspond relatively well between the ABB provided results and that of the Fortran program. However, their corresponding natural frequency again differs significantly from each other, as would be expected, as the frame alone had considerable deviations. The explanation for these discrepancies is the same as described for the frame alone. The major potential excitation frequencies of the drive are listed in Tab. 6.9 which has been provided by ABB. These potential excitation frequencies are visualized in Fig. 6.24 together with the “critical” natural frequencies that are close to any of these potential excitation frequencies within the operational speed range of the mill drive. Even though this plot has the appearance of a Campbell diagram it must not be mistaken for such a diagram, as the gyroscopic effects on the natural frequencies are neglected in this case. The diagram can, however, be used in a similar way as a Campbell diagram to find the critical speeds of the system. It can be seen that the system has two critical speeds at 9.1 Hz and 10.6 Hz respectively, due

to the pole passing frequency. However, as the damping of these natural frequencies are unknown, further examination has to be performed to determine if the damping of these natural frequencies are sufficiently high to safely run the mill at these speeds. This is, however, beyond the scope of this thesis.

6.11 On damping sources in mill drives

There are many types of damping in mills coming from different sources. The most easiest to obtain is the damping in the bearings as equations for the estimation of damping in oil lubricated bearings are well established. Another source is the material damping in the structure of the mill and a third source is the damping due to rock charge in the mill drum. The latter one is also the most difficult to determine as it depends on a lot of factors like rotational speed, size and density of the rocks, amount of water and steel balls added to the rock charge and the size of the rock load to name a few. Two Bachelor projects have examined the forces and damping in a downscaled model of a mill drum due to the charge inside the drum, Olsen (2011) and Christensen (2012). The outcome of these projects, regarding the damping, were that it was very difficult to determine the damping, however, it was clear that as the percentage of particles were increased an increase in damping was observed. Furthermore, it was observed that as the speed of the drum increase and the charge was centrifuged the damping of the system would decrease.

A way to apply structural damping to a system can be accomplished by the Rayleigh damping also called proportional damping. Rayleigh damping is based on a damping matrix that is proportional to the mass and stiffness matrices as shown in Eq. 6.131 where the proportionality constants α and β can be found by use of Eq. 6.132.

$$\mathbf{C} = \alpha\mathbf{M} + \beta\mathbf{K} \quad (6.131)$$

$$\xi_i = \frac{\alpha}{2\omega_{n_i}} + \frac{\beta\omega_{n_i}}{2} \quad i = 1, 2, \dots, n \quad (6.132)$$

By picking two natural frequencies and determine how fast each should be damp and apply this to Eq. 6.132 results in two equation with two unknowns. This can be solved giving the proportionality constants α and β . Figure 6.25 show the influence of the proportionality constants α and β on the damping factor

6.12 Simulating in time

If it is desired to model a start-up of the drive, a short-circuit in one of the rotor poles or any other time varying phenomena, the above described theory can be used in a iterative process with small time increments stepping through time. The following sections will explain how this can be performed and how it is possible to reduce the computational time by use of pseudo modal reduction although no analysis in time domain is performed in this work.

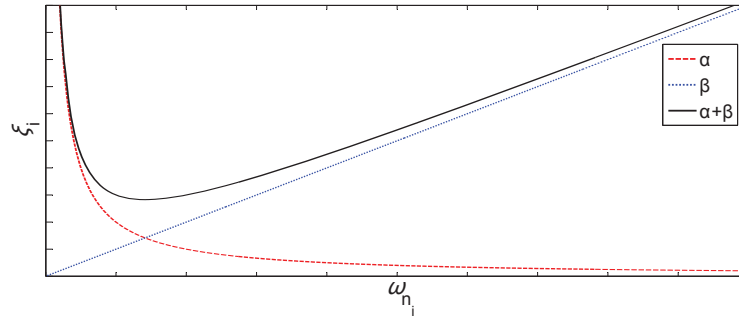


Figure 6.25 The influence of α and β on the damping factor

6.12.1 Equation of Motion

As described before, the equation of motion can be expressed as:

$$\mathbf{M}\ddot{x} + \mathbf{C}\dot{x} + \mathbf{K}x = \mathbf{F} \quad (6.133)$$

where \mathbf{M} is the mass matrix, \mathbf{C} is the damping matrix, \mathbf{K} is the stiffness matrix, \mathbf{F} is the force vector and \ddot{x} , \dot{x} and x are the acceleration, velocity and position vectors. The velocity \dot{x}_t and position x_t at time t can be determined by Eq. 6.134 and Eq. 6.135 together with the acceleration \ddot{x}_{t-1} , velocity \dot{x}_{t-1} and position x_{t-1} from previous time step. The observant reader might have noticed that the velocity used on the right hand side in Eq. 6.135 is for time t and not for time $t - 1$ as expected. This is, however, done on purpose and result in a better convergence. Inserting Eq. 6.134 and Eq. 6.135 into the equation of motion Eq. 6.136 together with the initial values of the acceleration, velocity and position at time $t-1$, one gets a linear system of equation in the form of $[\mathbf{A}] \{x\} = [\mathbf{B}]$ which can be solved for $\{x\}$ in this case the acceleration \ddot{x}_t .

$$\dot{x}_t = \dot{x}_{t-1} + \ddot{x}_{t-1}\Delta t \quad (6.134)$$

$$x_t = x_{t-1} + \dot{x}_t\Delta t \quad (6.135)$$

$$\mathbf{M}\ddot{x}_t = \mathbf{F}_t - \mathbf{C}\dot{x}_t - \mathbf{K}x_t \quad (6.136)$$

6.12.2 Pseudo modal reduction

Modeling in time can be highly time consuming as the maximum stable time step Δt_{max} decreases as the model's degree of freedom increase. To reduce the size of the model and increase the maximum stable Δt_{max} , the pseudo modal reduction can be applied. The following will explain how this can be performed and is a reduction method based on the modes of the natural frequencies which are significant for the specific case. Eq. 6.137 again shows the equation of motion where \mathbf{M} , \mathbf{C} and \mathbf{K} are the mass, damping and stiffness matrix, x is the displacement vector, \dot{x} and \ddot{x} are the 1st and 2nd derivative of the displacement vector respectively. This equation can be solved to get the natural frequencies ω_i and its corresponding eigenvectors ϕ_i

$$\mathbf{M}\ddot{x} + \mathbf{C}\dot{x} + \mathbf{K}x = 0 \quad \Rightarrow \quad \omega_i, \phi_i \quad (6.137)$$

It is now possible to transform the Cartesian coordinates to modal coordinates as illustrated in Eq. 6.138 and Eq. 6.139, using only eigenvectors up to the highest important mode and thereby reducing the system of equations. However, one has to be careful not to exclude important modes, as this will result in misleading results.

$$x(t) = \phi^* \cdot \eta(t) \quad (6.138)$$

$$\begin{Bmatrix} x_1(t) \\ x_2(t) \\ \vdots \\ x_n(t) \end{Bmatrix}_n = \begin{bmatrix} \phi_{1,1}^*(t) & \cdots & \phi_{1,m}^*(t) \\ \phi_{2,1}^*(t) & \cdots & \phi_{2,m}^*(t) \\ \vdots & \cdots & \vdots \\ \phi_{n,1}^*(t) & \cdots & \phi_{n,m}^*(t) \end{bmatrix}_{n \times m} \cdot \begin{Bmatrix} \eta_1(t) \\ \eta_2(t) \\ \vdots \\ \eta_m(t) \end{Bmatrix}_m \quad (6.139)$$

where n is the total degree of freedoms and m is the highest mode of interest.

The equation of motion now takes the form of Eq. 6.140 in modal coordinates.

$$\underbrace{\phi^{*T} M \phi^*}_{M_r} \ddot{\eta}(t) + \underbrace{\phi^{*T} C \phi^*}_{C_r} \dot{\eta}(t) + \underbrace{\phi^{*T} K \phi^*}_{K_r} \eta(t) = \phi^{*T} F \quad (6.140)$$

The transformation of the initial conditions to modal coordinates can be performed by use of Eq. 6.141 - 6.143:

$$\eta_0 = \phi^{*-1} \cdot x_0 \quad (6.141)$$

$$\dot{\eta}_0 = \phi^{*-1} \cdot \dot{x}_0 \quad (6.142)$$

$$\ddot{\eta}_0 = \phi^{*-1} \cdot \ddot{x}_0 \quad (6.143)$$

The numerical integration in modal coordinates can now be performed with the use of Eq. 6.144 - 6.146 in a similar way as for the integration in time domain.

$$\dot{\eta}_{(t+1)} = \dot{\eta}_{(t)} + \ddot{\eta}_{(t)} \Delta t \quad (6.144)$$

$$\eta_{(t+1)} = \eta_{(t)} + \dot{\eta}_{(t+1)} \Delta t \quad (6.145)$$

$$\ddot{\eta}_{(t+1)} = M_r^{-1} (\phi^{*T} F - C_r \dot{\eta}_{(t+1)} - K_r \eta_{(t+1)}) \quad (6.146)$$

The transformation from modal coordinates and back to Cartesian coordinates can be accomplished by the use of Eq. 6.147.

$$x_{(t+1)} = \phi^* \cdot \eta_{(t+1)} \quad (6.147)$$

6.13 Verification of structural model

This section will compare the results of the presented Fortran structural finite element model of the gearless mill drive with results from ABB's finite element model. Table 6.10 and Tab. 6.11 compare the masses of the different parts of the mill. As the drum is manufactured outside ABB regime, the manufacture reported masses have been added to

the table with the drum parts as well. From this table it can be seen that the masses found by the Fortran and ABB correspond very well with each other with a maximum deviation of only 1.1%. However, comparing with the manufacture provided masses the deviation is a lot larger. But as no information is available on how these masses are obtained or if it is just an estimate, no further conclusions can be drawn from this. Looking at Tab. 6.11 for the masses of the frame and stator it can be seen that significant higher deviations are achieved with a difference of nearly 10%. Some of this can be explained by the fact that the masses of the stiffener tubes were neglected in the Fortran model, as these tubes have just been added as spring stiffness's. However, this can not explain the large difference alone, as the total mass of these tubes only amount to approximately 2.5 tons, where the difference in mass of the frame is approximately 14 tons. A possible reason for the larger mass of the stator in the ABB model could be that they have forgot to compensate for the lack of material from the cooling channels, which would overestimate the mass by approximately 7.6 tons, where the deviation is approximately 12.2 tons. Another option, that may apply to both the stator and the frame, is that the supplied densities of the material do not comply with the used values in the ABB model and/or the dimensions on the drawings might not be up to date. It might as well be a combination of the above mentioned possibilities, however, the main cause of it has unfortunately not been determined yet. Table 6.12 show the stresses and deformations achieved by the Fortran and the ABB

Rotor part	Manufacture Weight [kg]	ABB FEM Weight [kg]	Fortran FEM Weight [kg]	Diff. Fortan vs.	
				Man.	ABB
Feed head & trunnion	119415	129146	129413	+8.4 %	+0.2 %
Disch. head & trunnion	121058	130758	129413	+6.9 %	-1.0 %
Cylinder	260936	262294	261369	+0.2 %	-0.3 %
Rotor	130568	156011	155715	+19.3 %	-0.2 %
Feed cone liners	68585	68585	67852	-1.1 %	-1.1 %
Disch. cone liners	68585	68585	67852	-1.1 %	-1.1 %
Cylinder liners	445228	445228	445226	-0.0 %	-0.0 %

Table 6.10 Comparison of masses of mill drum

Part	ABB FEM Weight [kg]	Fortran FEM Weight [kg]	Diff. Fortan vs. ABB
Frame	141089	127051	-9.9%
Stator	127500	115225	-9.6%

Table 6.11 Comparison of masses of frame and stator

model. What can be seen is that even higher deviations between the results are achieved. As also explained in Sec. 6.10 an explanation for these discrepancies are to be found in the boundary conditions between the stator and frame used for the Fortran and the ABB model respectively, together with the above mentioned reason for the mass difference. In the Fortran model the stator is rigidly attached to the frame plates which is an acceptable assumption as the heat expansion of the stator leads to a high pressure between the frame and the stator as described in Sec. 5.7. In the model by ABB the stator is not pressed

against the frame plates as it is modeled in cold condition without heat expansion. The stator is instead attached to a lot of beams on the outer diameter of the stator which then again is attached to the 3 internal plates of the frame. As the ABB model of the drive is modeled in cold condition and the stator is not pressed against the 3 internal frame plates result in a smaller overall stiffness of the frame/stator model compared to the Fortran model. This correspond well with the smaller displacement of the frame in the Fortran model compared with the ABB model, -22.5%. The discrepancies of the rotor displacement can be explained by the fact that ABB has added a no rotation boundary condition on the lower half part of the bearing surface restricting this surface in rotating due to the bending of the rotor. By doing this an artificial moment is added to these two surfaces to comply with this boundary condition which tries to counteract the bending of the rotor resulting in a decrease in deflection. In the Fortran FEM model the bearing surfaces have no such boundary conditions as the bearing stiffness have been applied as nodal springs to each node at the surface allowing the surface to rotate along with the bending of the drum. An additional reason for the discrepancies of the rotor deflection is that ABB has added the mass of the rock load as a constant distributed mass on the lower part of the drum where the rock load in the Fortran model has been applied with a sinusoidal distribution on the lower half of the drum assuming a higher rock mass in the center than at the sides. This higher mass will of course result in higher forces in the bottom part of the drum where the magnitude of deformation already is highest increasing it even further. The stresses in Tab. 6.12 also deviates a lot due to the same reasons as the ones described for the deformations. However, the highest stresses in the frame are located in the same area in the two different models.

	ABB FEM		Fortran FEM		Diff. Fortan vs. ABB	Rotor eccentricity [mm]
	Frame	Rotor	Frame	Rotor		
Max. deformation [mm]	1.215	3.565	0.941	5.084	-22.5% / +42.7%	(x,y)=(1.41,1.41)
Max. stress [MN/m ²]	≈35	≈33	17.45	27.77	-50.1% / -15.8%	(x,y)=(1.41,1.41)

Table 6.12 Comparison of deformation and stress in frame and rotor

Figure 6.26 shows a comparison of the air gap distortion estimated by the Fortran and the ABB model where the air gap from the Fortran model is the average air gap per pole and the air gap from the ABB model is found at the center of each pole. As can be seen from the figure the shape and the values of the air gap found by the two models are highly comparable with a deviation of the minimum and maximum air gap of 0.9% and 1.2% respectively, Tab. 6.13. From this it can be concluded that the air gap distortion is not that sensitive to the maximum deformation of the complete mill explained above where there were a deviation of up to 42.7% between the results of the two models. This is true even though the Fortran model has taken the heat expansion of the poles into account where the ABB model does not.

Comparing the natural frequencies of the modes shown in Fig. 6.23, which values are listed in Tab. 6.14, it can be seen that these deviates a lot which is also described in Sec. 6.10. The reason for these discrepancies is the same as explained above for the

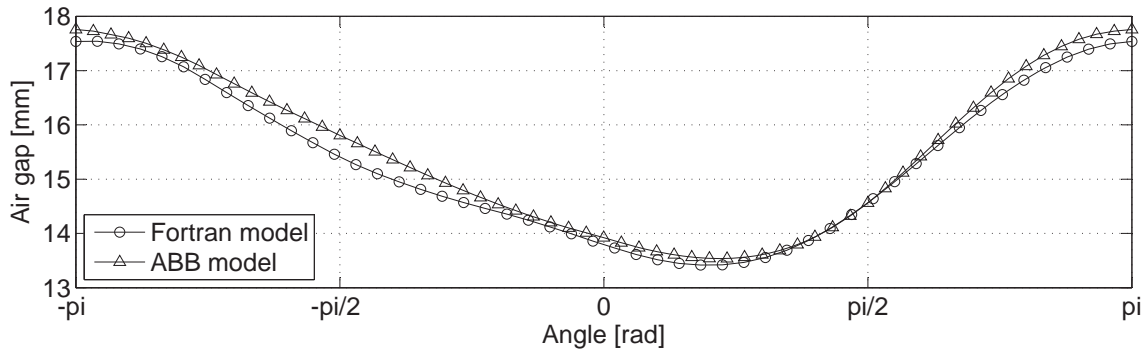


Figure 6.26 Comparison of Fortran and ABB estimated air gap distortion, rotor eccentricity: $(x,y)=(1.41,1.41)$, angle CCW from x-axis

	ABB FEM	Fortran FEM (Avg.)	Diff. Fortan vs. ABB	Rotor eccentricity [mm]
Max. air gap [mm]	17.76	17.54	-1.2%	$(x,y)=(1.41,1.41)$
Min. air gap [mm]	13.54	13.42	-0.9%	$(x,y)=(1.41,1.41)$

Table 6.13 Comparison of air gap between stator and rotor

deformation and stresses and is mainly due to the used boundary conditions in the two models.

Mode shape	ABB FEM Freq. [Hz]	Fortran FEM Freq. [Hz]	Diff. Fortan vs. ABB
Fig. 6.23(a) & 6.23(b)	3.79	9.06	58.2 %
Fig. 6.23(c) & 6.23(d)	7.31	10.62	31.2 %
Fig. 6.23(e) & 6.23(f)	7.20	15.06	52.2 %
Fig. 6.23(g) & 6.23(h)	16.36	16.28	0.5 %

Table 6.14 Comparison of natural frequencies

As explained above the two structural models do not produce exactly the same results due to the way they have been modeled. The most important result from the structural model, namely the air gap distortion, is, however, highly comparable despite the different approaches and assumptions made in the two models. The approach in the Fortran model has been to reduce the model as much as possible to decrease the computation time making it suitable for an iterative optimization process, where the ABB model include every little hole and bolt in the gearless drive. The two models nor use the same assumptions for the boundary conditions for the mill drum bearings, the applied rock load or the stator attachment and the Fortran model include the heat expansion where the ABB model do not. It is therefore not entirely fair to make this comparison as the results are expected to deviate but in lack of better results for comparison this has been performed anyway. It is at the current time impossible to determine which of the models produce the most accurate results as this would require experimental test on the drive. This has, however, not been possible as the mill drive is not yet in operation and will have to be performed at

a later time to justify the assumptions used. In the case that the structural model has to be modified after experimental test results have been received would not have any influence on the structure of the global multi-physics model as this will remain unaltered justifying the use of the presented model in this thesis.

Chapter 7

Metaheuristic optimization of multi-physics model of a gearless drive

7.1 A short introduction to metaheuristics

Metaheuristics is used in combinatorial optimization in discrete and real search space by iteratively trying to improve the current best solution. There have been several proposed metaheuristic algorithms throughout time, which can be used in optimization applications with some of the most commonly known being “hill climber”, “TABU” Glover (1989), Glover (1990), “simulated annealing” Suman and Kumar (2006), “ant colony optimization” Dorigo and Blum (2005), “genetic algorithm” Johnson and Rahmat-Samii (1997), and “evolution strategies” Schwefel and Beyer (2002), Andersen and Santos (2012), to name a few. Metaheuristics, however, does not guarantee that the optimal solutions are ever found but there is a good possibility that a near optimal solution will be determined. Evolution strategies ES used in this thesis were first proposed by Rechenberg and Schwefel in the mid-1960s for numerical optimization. It has since evolved from a simple (1+1) evolution strategy to a more complex $(\mu/\rho \dagger \lambda)$ with more complex internal routines. One of the benefits of ES is that it is extremely easy to run on parallel computers to decrease the time it takes to evaluate the population of individuals. Several papers describe the use of evolutionary algorithms in the quest for optimization of PM motors where Jolly et al. (2005) optimize the rotor of a PM motor using genetic algorithms and Bochnia et al. (1999) optimize an in-wheel motor using ES. ES has also been used by Chung and Kim (1997) for the optimization of the pole shapes in a BLDC motor for reducing cogging torque. The present work will concentrate on a more global holistic approach. As one usually is not just interested in the optimization of one single parameter like Jolly et al. (2005), Bochnia et al. (1999), Chung and Kim (1997) and a separate optimization of several parameters might not give a clear picture of the optimal combination of the parameters, a Multi-objective Optimization has to be performed. This can be accomplished by combining ES and PISA where PISA is a group of programs which can be used for solving such multi-objective search problems with conflicting goals. The following will explain the $(\mu/\rho \dagger \lambda)$ -ES which is used for optimizing the gearless mill drive together with a short description of the structure of PISA which has been used in combination with ES.

7.2 General algorithm of evolution strategies

In Fig. 7.1 a general pseudo code for Evolution Strategies (ES) is shown. This section will briefly explain each line of the code and the following sections will give a more

```

Procedure  $(\mu/\rho \ddagger \lambda)$ -ES
1 Begin
2    $g = 0$ 
3   initialize( $\mathfrak{P}_p^{(0)} = \{(\mathbf{y}_m^{(0)}, \mathbf{s}_m^{(0)}, \mathbf{F}(\mathbf{y}_m^{(0)})) , m = 1, \dots, \mu\}$ )
4   Repeat
5     For  $i = 1$  to  $\lambda$ 
6        $\mathfrak{E}_i = \text{marriage}(\mathfrak{P}_p^{(g)}, \rho)$ 
7        $s_i = s_{\text{recombination}}(\mathfrak{E}_i)$ 
8        $y_i = y_{\text{recombination}}(\mathfrak{E}_i)$ 
9        $\tilde{s}_i = s_{\text{mutation}}(s_i)$ 
10       $\tilde{y}_i = y_{\text{mutation}}(y_i, \tilde{s}_i)$ 
11       $\tilde{y}_i = \text{repair}_{\text{discrete}}(\tilde{y}_i)$ 
12       $\tilde{F}_i = F(\tilde{y}_i)$ 
13     End
14      $\mathfrak{P}_o^{(g)} = \{(\tilde{y}_i, \tilde{s}_i, \tilde{F}_i) , i = 1, \dots, \lambda\}$ 
15     Case Selection type of
16        $(\mu, \lambda) : \mathfrak{P}_p^{(g+1)} = \text{selection}(\mathfrak{P}_o^{(g)}, \mu)$ 
17        $(\mu + \lambda) : \mathfrak{P}_p^{(g+1)} = \text{selection}(\mathfrak{P}_o^{(g)}, \mathfrak{P}_p^{(g)}, \mu)$ 
18     End
19      $g = g + 1$ 
20   Until Termination condition
21 End

```

Figure 7.1 General pseudo code of $(\mu/\rho \ddagger \lambda)$ -ES

thorough explanation of the different parts of the ES algorithm based on Schwefel and Beyer (2002).

In line #2 the generation counter is initialized for generation zero. In line #3 the initial population is created which consists of μ individuals \mathbf{a}_m each consisting of an object vector \mathbf{y}_m , a strategy vector \mathbf{s}_m and a fitness vector $\mathbf{F}(\mathbf{y}_m)$. $\mathbf{a}_m = [\mathbf{y}_m, \mathbf{s}_m, \mathbf{F}(\mathbf{y}_m)]$. Lines #4-20 is the main loop of the algorithm which runs continuously until termination condition is reached, in our case until we run out of the allocated time for solving the problem. Lines #5-13 is the loop which generates offspring individuals who might enter the next generation of parents. The loop will run λ times for each generation producing λ new offspring. In line #6 the marriage procedure is executed which picks ρ individuals from the parent population for reproduction of offspring. Lines #7 and #8 recombine the object and strategy parameters of the ρ parents to form one new offspring individual. In lines #9 and #10 the strategy and object parameters of the newly formed offspring individual is mutated. In line #11 the object parameters are corrected for the discrete space variables. Finally, in line #12 the new offspring individual is completed by the addition of its fitness value. Line #14 collects the offspring created to form the offspring

population. In lines #15-18 the selection procedure is performed. There are two standard types of selection, a “;” and a “+” selection. This selection procedure decides which of the offspring individuals get to enter the new parent population of the next generation if any at all. Finally, in line #19 the generations counter increase by one and then jump to line #5, if the termination condition, as said before, has not been reached.

7.2.1 Marriage

In contrast to Evolutionary Algorithm with an elitist approach where the marriage process is made by choosing the best individuals of the parent population for reproduction, the marriage process in Evolution Strategies is made by selecting ρ individuals completely randomly from the parent population. As this does not improve the solution by itself, it is obvious that this part of the algorithm is not the main driving force in evolution strategies. The marriage process is the first part of the algorithm which is performed in the main loop, line 6 in Fig. 7.1.

7.2.2 Recombination

The idea behind recombination is that when parents with good genetic material are combined, they will also generate offspring with good genetic material. According to Schwefel and Beyer (2002), there is still an ongoing debate about the usefulness of recombination, however, recombination of the strategy parameters has been shown to be mandatory for this mechanism to work according to Bäck and Schwefel (1993). Due to this fact, the recombination will be performed on both the object and strategy parameters. A special case of the recombination is when $\rho = 1$ as the individual will be recombined with itself. In other words, an exact copy of the individual. In this case the recombination routine can be skipped.

There are two standard methods of recombination:

- Discrete recombination
- Intermediate recombination

According to Bäck and Schwefel (1993), Eiben and Schippers (1998), Bäck and Hoffmeister (1994) it has been shown that good results have been achieved when using intermediate recombination on strategy parameters and discrete recombination on object variables. We will follow this advice.

Recombination of Strategy Parameter

As mentioned above, intermediate recombination has proved to give a good result when applied to the strategy parameters which are parameters used for determine the size of the mutation of the object parameters. The vector with the strategy parameters is initially set as the normal standard deviation for each object parameter of the initial population of solutions. The intermediate recombination of the strategy parameters is performed first

by randomly selecting ρ parents from the entire population of μ individuals, which is performed by the “marriage” routine as described previously. It then calculates the centre of mass of the ρ selected parent vectors $\mathbf{a}_m = \{a_{m,1}, \dots, a_{m,N}\}$ for each strategy parameter as written in Eq. 7.1 and depicted at the bottom in Fig. 7.2.

$$\mathbf{r}_k = \frac{1}{\rho} \sum_{m=1}^{\rho} \mathbf{a}_{m,k} \quad (7.1)$$

The recombination of the strategy parameters can be performed before or after the recombination of the object parameters. In the pseudo code in Fig. 7.1 it is placed before the recombination of the object parameters at line 7.

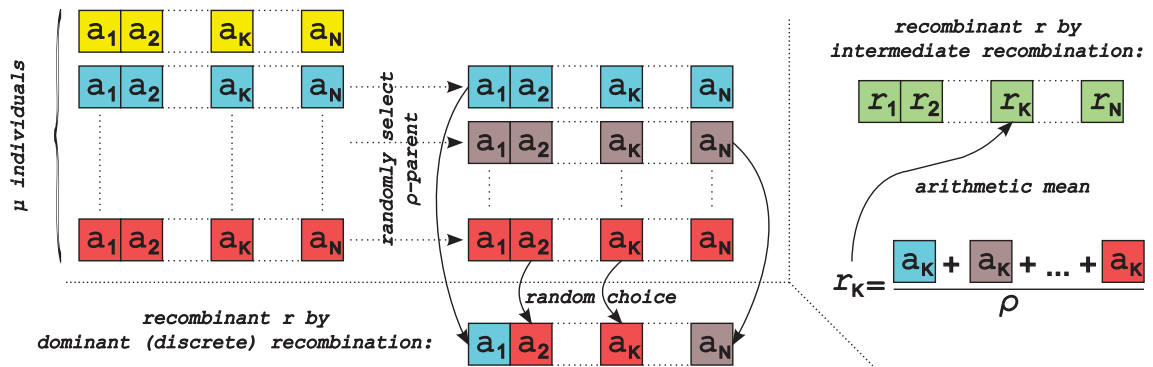


Figure 7.2 Standard μ/ρ recombination

Recombination of Object Parameter

As mentioned above, discrete recombination, also called dominant recombination, has proved to give a good result when applied to the object variables. The Discrete recombination is performed first by randomly selecting ρ parents from the entire population of μ individuals which again is performed by the “marriage” routine. The routine then randomly selects the object parameters from the ρ individuals for each object parameter until a completely new individual is created. This is written in Eq. 7.2 and depicted at the top of Fig. 7.2.

$$\mathbf{r}_k = (\mathbf{a}_{m_k})_k, \quad m_k = \text{Random}\{1, \dots, \rho\} \quad (7.2)$$

The recombination of the object parameters is performed in line 8 in Fig. 7.1, but as mentioned before, it can also be performed before recombination of the strategy parameters. If for some reason the intermediate recombination was chosen on the object parameters instead of discrete recombination, one should remember that this routine creates values in real space. A correction of the parameters has then to be performed, if some or all of the parameters are in discrete space. This correction could be a simple rounding of the parameter values.

7.2.3 Mutation

Mutation of the object and strategy parameters takes place in lines 9 and 10 in Fig. 7.1 and is usually the primary source of generic variation. There is currently (2002) no design methodology for the mutation operators, but some rules have been proposed by H. G. Beyer.

- Reachability
- Unbiasedness
- Scalability

Reachability: It should be possible from a random state to reach any other state within a finite number of mutations or generations.

Unbiasedness: The variation operators should only explore the information of the object space and not use any information about the individuals' fitness values. Thereby no individual is preferred over another. This leads, in a natural manner, to the principle of maximum entropy and the standard normal distribution.

Scalability: The mutation strength should be tunable to be able to adapt to the properties of the fitness landscape.

Mutation of Object Parameter

Schwefel and Beyer (2002) propose a standard mutation operator for mutating the object parameters in a real valued search space which reads:

Given a vector $\mathbf{s} = \sigma = \{\sigma_1, \dots, \sigma_N\}$ as the strategy parameter the principle of maximum entropy yields:

$$\tilde{\mathbf{y}} = \mathbf{y} + \mathbf{z} \quad (7.3)$$

with
$$\mathbf{z} = \{\sigma_1 \cdot \mathcal{N}_1(0, 1), \dots, \sigma_N \cdot \mathcal{N}_N(0, 1)\} \quad (7.4)$$

where $\mathcal{N}_i(0, 1)$ is a random number from the standard normal distribution.

Mutation of Strategy Parameter

For mutating the strategy parameters $\mathbf{s} = \sigma = \{\sigma_1, \dots, \sigma_N\}$ in Eq. 7.5 H. P. Schwefel suggests using an extended log-normal rule which reads:

$$\tilde{\sigma} = e^{\tau_0 \cdot \mathcal{N}(0,1)} \cdot \{\sigma_1 \cdot e^{\tau \cdot \mathcal{N}_1(0,1)}, \dots, \sigma_N \cdot e^{\tau \cdot \mathcal{N}_N(0,1)}\} \quad (7.5)$$

with

$$\tau_0 = \frac{c}{\sqrt{2N}} \quad (7.6)$$

$$\tau = \frac{c}{\sqrt{2\sqrt{N}}} \quad (7.7)$$

where $\mathcal{N}_i(0, 1)$ is a random number from the standard normal distribution and c is a proportionality factor for the learning factors τ_0 and τ .

7.2.4 Repair

As the above described procedure produces real value object parameters, an extra procedure has to be introduced when working with discrete parameters or a mixture of discrete and real value parameters. This procedure is inserted just before the evaluation by the fitness function in line 11 in Fig. 7.1. The procedure consists of a simple rounding of the real value to an integer at instances where the parameter is in discrete space. Furthermore, this repair procedure makes sure that the object parameters do not exceed their predefined upper and lower boundaries by moving values outside back onto the boundaries they exceeded. This is not a standard routine in ES, but it has to be introduced in the case where the object parameter values are a mixture of real and integer values.

7.2.5 Selection

The selection routine is the routine which drives the population to better regions by use of the individuals' fitness information. There are two standard types of selection methods in ES which is denoted $(\mu/\rho, \lambda)$ and $(\mu/\rho + \lambda)$. The “,”-sign and the “+”-sign in the notation tells something about how the selection pool for selecting the next generation parent population is created. In the “,” notation the selection pool is made up of only the λ offspring individuals and the current parent population is discarded even in the case of that population containing better solutions. This selection method of course requires that $\lambda > \mu$ as we want to keep a constant size of the parent population. In the “+” notation the selecting pool is made up of both the λ offspring and the μ parents of the current generation.

The actual selection is done simply by selection the μ individuals with the highest fitness value (maximizing) from the selection pool to form the next generation parent population and discarding the remaining solutions. The selection is performed just after the offspring has been created, line 16 for the “,” selection and line 17 for the “+” selection in Fig. 7.1. Both types of selection method have their advantages in specific applications. According to Schwefel and Beyer (2002) the “,” selection performs well on unbounded \mathbb{R}^N search spaces where the “+” selection should be chosen in the case of finite search space. As the problem at hand is defined in finite search space the “+” selection has been chosen as the selection method for this problem.

7.3 Parameter tuning

Parameter tuning of the algorithm is normally performed to insure an efficient and fast convergence toward the optimal solution. The ES algorithm explained above consists of

Parameter	Description
μ	Size of the parent population
ρ	No. of parent involved in the procreation of one offspring
λ	Size of offspring population
$\mathbf{s} = \sigma = (\sigma_1, \dots, \sigma_N)$	Mutation strength
c	Constant for the learning parameters τ and τ_0

Table 7.1 Endogenous and Exogenous Parameters

the endogenous and exogenous parameters listed in table 7.1 below. The exogenous parameters are parameters which remain constant throughout the entire run of the algorithm and are μ , ρ , λ and c . The endogenous parameters are parameters which continuously change and try to adapt to the current situation. These parameters are the standard deviations (mutation strength) \mathbf{s} . It is the exogenous parameters which are used for tuning of the algorithm by running several simulations with various parameter values and seeing which perform the best. This tuning can be a cumbersome task which takes a long time to perform, however, there are some guide lines for some of the parameters. According to Bäck and Schwefel (1993) the constant c for the learning factors τ and τ_0 has for example achieved good results when set to 1. However, as each fitness value in this problem take on average approximately 15 minutes to calculate, the evolution strategies algorithm in this thesis is not tuned for the exogenous parameters. The reason for neglecting the tuning of the algorithm is in view of the extensive amount of time needed for the tuning, which is assumed to far exceed the time needed for running a untuned algorithm. The performance of the algorithm can therefore, with a high probability, be increased dramatically and would be recommended if it should be used again and again. The exogenous parameters used in this thesis are: $\mu = 6$, $\rho = 4$, $\lambda = 1$ and $c = 1$.

7.4 Multi-objective optimization and PISA

For solving the multi-objective optimization problem, the previously described ES algorithm has been used in conjunction with a free software package called PISA. PISA is a group of programs for solving multi-objective search problems with conflicting goals and is developed and maintained at ETH TIK Zürich, Switzerland.

7.4.1 PISA Structure

The PISA structure operates with two main algorithms. One is called the variator and the other called the selector. These two algorithms run parallel with each other and communicate through ASCII files as symbolized in Fig. 7.3. The variator is the algorithm that is creating new offspring and calculates their respective fitness values. The fitness value together with an individual id number is then passed to the selector through the ASCII files. The selector then selects which of the individuals has to form the new parent population solely based on the evaluation of their fitness values. The ids of these individuals are then sent back to the variator. The variator then generates new offspring and their fitness values are again sent back to the selector. This ping-pong between the variator

and selector continues until some stopping criteria have been met. This could be time or number of generation. There are 6 common communication files which are used in the PISA structure for communication between the variator and selector:

- **CFG:** config file containing the size of the problem, μ , ρ , λ and dimension
- **INI:** file with the initial population fitness values and ids written by the variator
- **STA:** status file which is used to synchronize the variator and selector
- **SEL:** file with the next parent population ids written by the selector
- **VAR:** file with new offspring's fitness values and id's written by the variator
- **ARC:** archive file with solutions

For further information on the PISA structure visit their homepage¹ or see Bleuler et al. (2003).

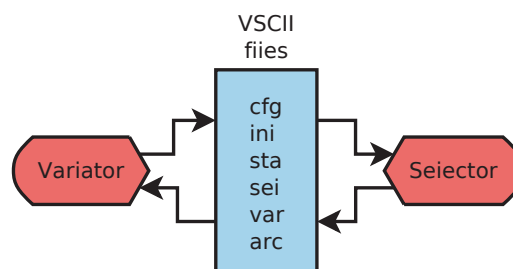


Figure 7.3 PISA structure

Variator

The variator is the algorithm in charge of generating new offspring through variation of selected individuals. In this thesis it is a modified version of a (6/4+1)-ES explained above. Two modifications have been made to the algorithm. The first is that it has been set up to communicate with the selector through the previously described communication files and the previously used selector has been removed. Secondly, an extra fitness parameter has been added as to optimize for both mass and losses.

Selector

The general function of the selector is to select promising individuals from the population, who through variation is expected to create new individuals which are able to find the Pareto front. A solution is called Pareto optimal when it is not possible to improve one objective without deteriorating at least one of the others. A set of Pareto optimal solutions constitute the Pareto front. The goal in multi-objective optimization is therefore to find this Pareto front, sometimes also called the Pareto frontier. Several different types of

¹<http://www.tik.ee.ethz.ch/pisa/>

selectors are available in the PISA environment and can be interchanged in the model with minimal effort. The following selectors are implemented in the model, but only the IBEA selector is used based on previous experience, Andersen and Santos (2012). The parameters for the different selectors have not been changed from their initial values and may be altered to improve their performance. However, this is deemed to be out of scope of this thesis and may be performed in future work with the model.

- **SPAM** - Set Preference Algorithm for multi-objective Optimization, Zitzler et al. (2009)
- **SEMO2** - Simple Evolutionary multi-objective Optimizer, Laumanns et al. (2002b)
- **IBEA** - Indicator Based Evolutionary Algorithm, Zitzler and Künzli (2004)
- **HypE** - Hypervolume Estimation Algorithm for multi-objective Optimization, Bader (2011)
- **SHV** - Sampling-based HyperVolume-oriented algorithm, Bader et al. (2008)
- **FEMO** - Fair Evolutionary Multiobjective Optimizer, Laumanns et al. (2002c)
- **SPEA2** - Strength Pareto Evolutionary Algorithm 2, Grandy (1997) and Zitzler et al. (2002)
- **NSGA2** - Nondominated Sorting Genetic Algorithm 2, Deb et al. (2000)
- **EPSMOEA** - Epsilon MOEA, Laumanns et al. (2002a), Rudolph and Agapie (2000), Deb et al. (2003)
- **MSOPS** - Multiple Single Objective Pareto Sampling, Hughes (2003), Hughes (2005)

7.5 Optimization of multi-physic model of a gearless drive

This section will explain how the optimization of the mill drive is performed, which is done as both single- and multi-objective optimization. The single objective optimization tries to minimize the mass usage in the mill, as this is somehow an expression for the cost of the mill. The lower the mass the cheaper the mill is to produce. In the long run, this is, however, not the only thing which will have economical consequences, as losses in the drive are wasted energy resulting in wasted money. The multi-objective optimization is therefore an attempt to minimize the mass of the mill and at the same time minimize the total loss of the drive.

7.5.1 Object Parameter

In the optimization process of minimizing the mass and losses of the mill, 8 object parameters are used. The first 6 object parameters are the thickness of the frame plates in the xy-plane as indicated in Fig. 7.4(a) where the bottom half of the frame has thicker plates than the top half. The 7th object parameter is the thickness of the plates on the side and the top of the frame, as indicated in Fig. 7.4(b). Object parameter 8 is the length of the rotor and stator. The length between the end plates in the feed and discharge end and the plates next to them is kept constant as the stator and rotor length increase/decrease. The distance between the three inner plates, where the stator is attached, change according to the stator length, while keeping the original ratio between them constant. The object parameters are limited to the value ranges shown in Tab. 7.2.

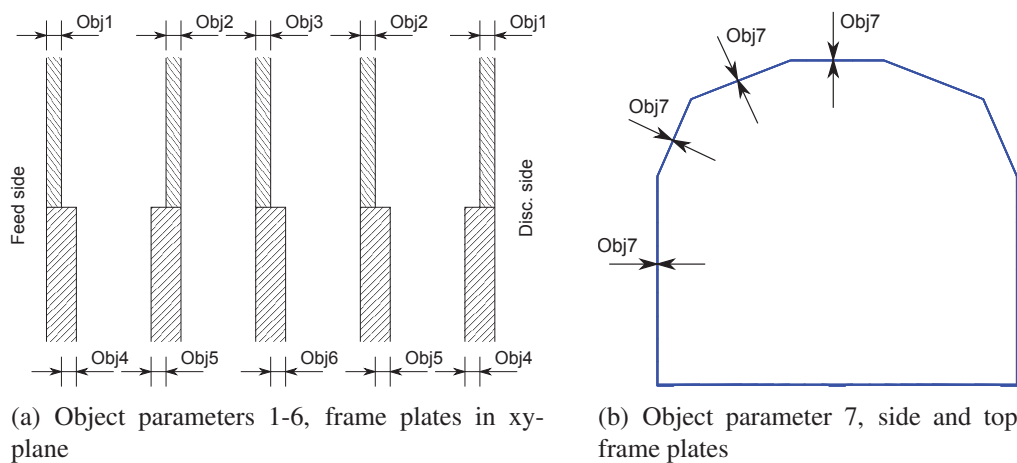


Figure 7.4 Description of object parameters

7.5.2 Determination of fitness value

The fitness values for the single and multi-objective optimization performed in this thesis are the mass and the mass and losses respectively. Figure 7.5 shows a flow diagram of the

Object parameter	lower limit	Upper limit
Obj1, [mm]	1.0	20.0
Obj2, [mm]	1.0	20.0
Obj3, [mm]	1.0	20.0
Obj4, [mm]	1.0	20.0
Obj5, [mm]	1.0	20.0
Obj6, [mm]	1.0	20.0
Obj7, [mm]	1.0	20.0
Obj8, [mm]	1100.0	1400.0

Table 7.2 Object parameter ranges

procedure for how these fitness values have been found for each optimization individual. To save computation time, the first thing that is done is to check if the mass is larger than the largest mass in the parent population, as there is no need to continue the rest of the simulations, as the solution will be discarded anyway. This can, however, only be done this way for the single objective optimization and only if the “+” selector has been used. For the multi-objective optimization, this check is neglected. Again to save computation time, it is checked if the current phase angle which produce zero torque has been found previously, Sec. 3.4.1, as this is the same in all the cases and is not dependent on the rotor/stator length. It therefore only needs to be run once. Next, the stator and rotor currents are found to produce the desired torque, as this change as the rotor/stator length changes, Sec. 7.5.4. These currents are then used in all subsequent magnetostatic and thermal models where initially the core losses, as described in Sec. 3.5.1, are found and used in the thermal model as heat sources. An initial guess of the needed cooling flow is send to the thermal model, Sec. 5, which calculates the temperatures of the core, the coil and the cooling flow, where the flow temperatures for each iteration are sent to the flow model, Sec. 4, which updates the fluid properties for the next iteration. Furthermore, the thermal model sends the coil temperatures for each slice of the thermal model to the resistance model Sec. 3.5.3, which updates the resistance losses in the coils according to its current temperature. Once the thermal model has converged a check of the coil temperature is performed to make sure that it does not exceed the maximum temperature. If the coil temperatures are too high, the flow is changed accordingly to decrease the temperature and the thermal model is then run again with the new flow. If the coil temperatures are within $\pm 5^{\circ}\text{C}$ of the maximum temperature of 90°C , the average core temperature is used in the heat expansion model, Sec. 5.7, to find the decrease in air gap due to the thermal expansion of the rotor poles. The distributed force coming from the rock load inside the mill drum is then found, Sec. 6.6, which is later to be used in the structural model. The forces between the pole and stator are then found, Sec. 6.6, taking into account the decreased air gap due to the thermal expansion and potential misalignment of the rotor. The pole/stator force model furthermore estimate the spring stiffness between the pole and stator, to take into account the change in force due to change in air gap from the undeformed situation. These forces are then send to the structural model, Sec. 6, which calculates the displacement, the stresses and natural frequencies of the complete mill. A

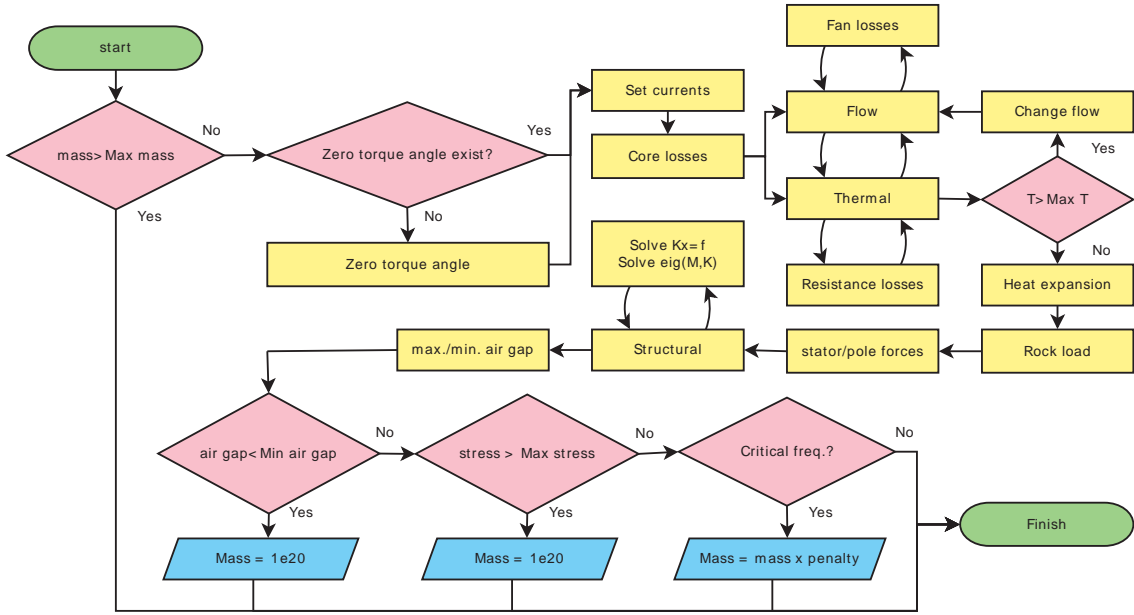


Figure 7.5 Flow diagram of fitness value determination

series of checks are then performed to evaluate if the solution is a valid solution. Initially the air gap is checked to see if it is larger than the minimum allowed air gap. If the air gap is smaller than the minimum allowed air gap, the mass is set to $1e20$ which means that the solution is discarded. The stresses are checked in a similar way as the air gap, setting the mass to $1e20$ if stresses are higher than the maximum allowed stress. The final check is the natural frequencies where the mass is penalized if the natural frequencies of the mill are within $\pm 1\text{Hz}$ of any possible excitation frequencies. The outputs of the fitness function are the found mass and total losses.

7.5.3 Natural frequency penalty function

If one of the found eigenfrequency f_{eig} , are within the frequency span f_{span} , around one of the possible excitation frequencies f_{exc} , the penalty factor $f_{penalty}$ can be found by Eq. 7.8 where the parameter $max_{penalty}$ determines the maximum penalty value.

$$f_{penalty} = 1 + \frac{f_{span} - |f_{eig} - f_{excite}|}{f_{span}} \cdot max_{penalty} \quad (7.8)$$

Everywhere else the penalty factor is set to one. This penalty factor can then be used to find the solution fitness value by multiplying it with the mass of the specific simulation case. By doing this, the cases with eigenfrequencies within the frequency span are penalized driving the solutions away from the critical eigenfrequencies, but in a smooth manner compared to just setting the fitness value to a high value. It is expected that this will result in a faster convergence toward the optimal solution. It has to be mentioned

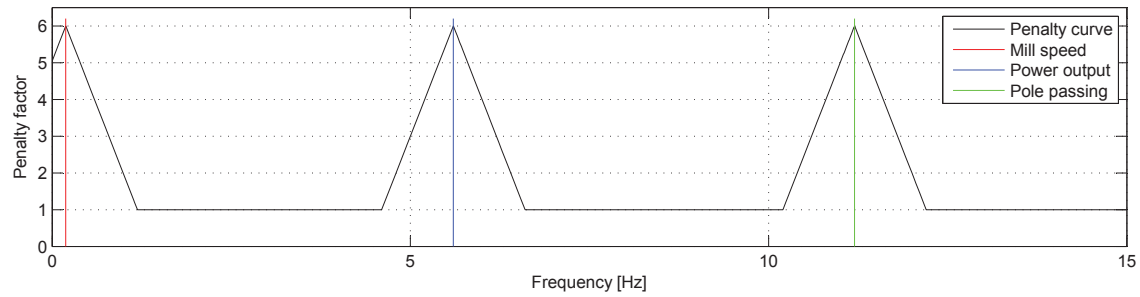


Figure 7.6 Penalty factor function with a penalty of 5 and a frequency span of ± 1 Hz around possible excitation frequencies

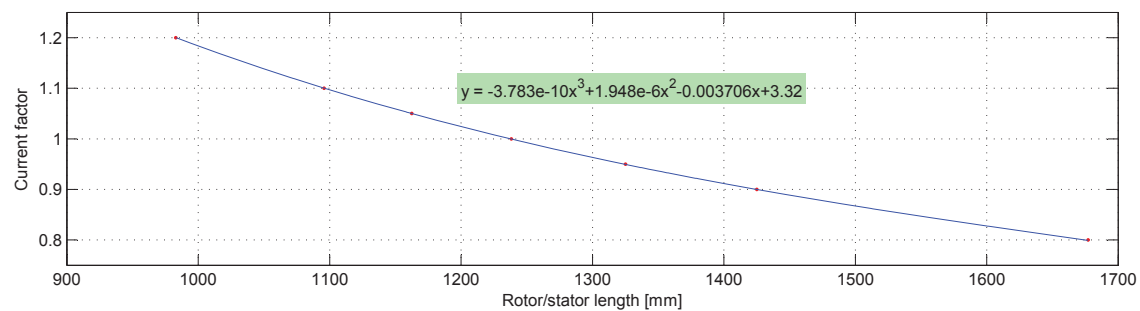


Figure 7.7 Current factor

that this penalty is only applied if the found eigenfrequencies are close to any possible excitation frequencies at rated speed, as the mill is expected to always run at that speed.

7.5.4 Stator & rotor currents

As the change in rotor and stator length will result in a change in produced torque, the current in the windings is corrected as to produce the desired torque value. This correction is done by multiplying the rotor and stator currents with a current factor. The relationship between this current factor and the length is nonlinear due to saturation in the stator and rotor core material. Several simulations have therefore been performed to find the correlation between the length and the needed current factor to produce the desired torque which can be seen in Fig. 7.7.

7.6 Minimization of mass usage in gearless drive construction - single objective optimization

This section and Sec. 7.8 will show the results of the single objective optimization of the gearless drive which attempts just to minimize the mass usage for constructing the drive. Figure 7.8 show plots from the single objective optimization using the (6/4+1)-ES algorithm with a termination criteria of 2500 generations. The plot in the top left

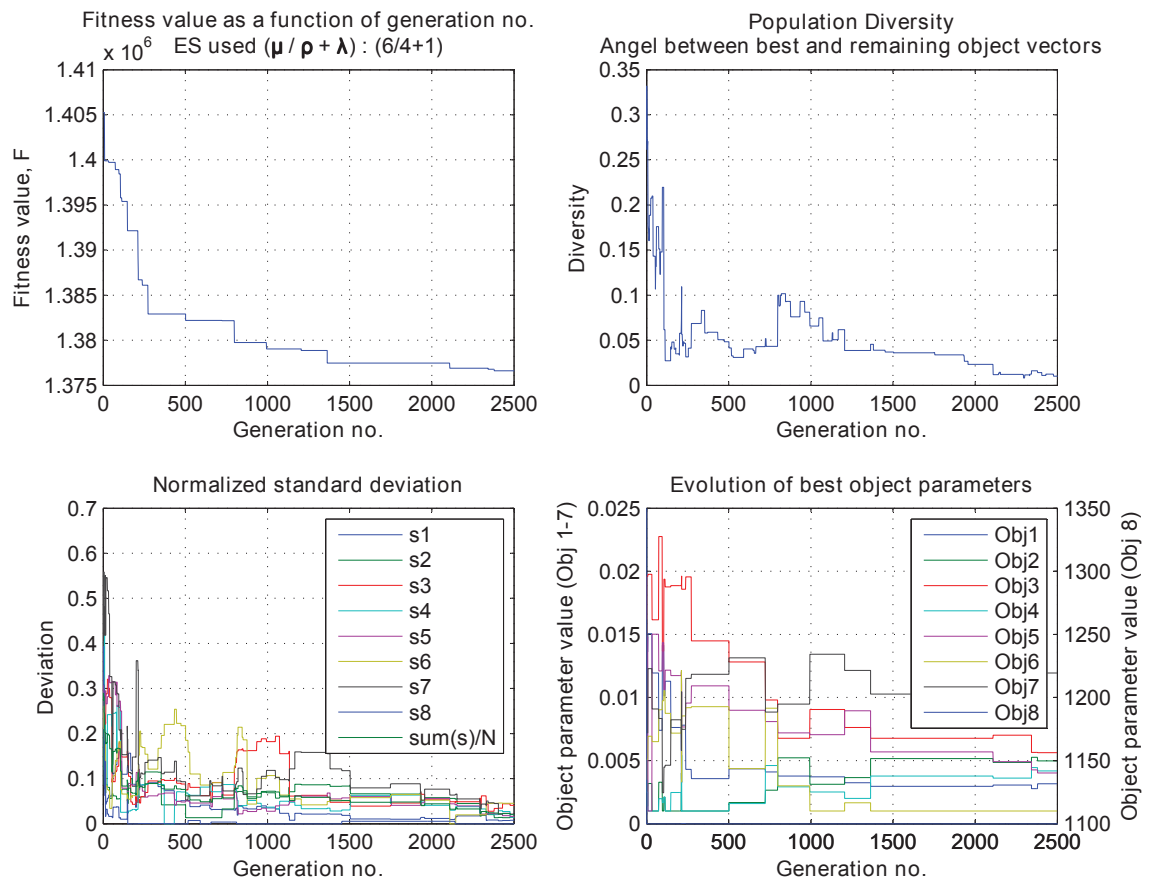


Figure 7.8 Single objective optimization - Evolution Strategy ($\mu/\rho + \lambda$): (6/4+1), Rotor eccentricity: $(x, y) = (1.4142, 1.4142)$

corner of Fig. 7.8 shows the fitness value which in this case is the mass as a function of the generation number. It can be seen that initially it converts fast toward a lower mass and then it slows down, as it gets closer to an optimal solution which is expected. This tendency can also to some extent be seen in the plot of the normalized standard deviation of the 8 object parameters together with the mean sum, lower left plot. From this plot, it is also obvious that not all the object parameters of the population have completely converged. However, the deviation is relatively small indicating that the solutions are very similar. Another indicator for the convergent is the one shown in upper right plot in Fig. 7.8. It shows the comparison of the angel between the current best object vector and the remaining object vectors calculated by Eq. 7.9.

$$\cos(\beta) = \left(\frac{\mathbf{y}_i \cdot \mathbf{y}_j}{\|\mathbf{y}_i\| \cdot \|\mathbf{y}_j\|} \right) \quad (7.9)$$

This value tells something about how similar the solutions in the population are to the current best solution. The reason for introducing this second convergent indicator is to make sure that the current best solution is not just a stroke of luck as this indicator will

have a high value if the current best solution differs much from the rest, even if the rest of the solutions are similar and the standard deviation is low. As for the normalized standard deviation, it is also obvious from the population diversity plot that not all the individuals in the population have the same object parameters as this would then have been zero. The last plot in lower right corner of Fig. 7.8 shows how the object parameters for the best solution in the population evolve as generations increase. By looking at the plots, it is obvious that the drive is optimized considerable with the objective of minimizing the mass, as the mass of the original drive is approximately 125 tons heavier. The final single objective optimized solution is shown in Sec. 7.8 where it is compared with the solution for the original drive with dimensions from ABB and the multi-objective optimized drive which will be explained in the following section.

7.7 Minimization of mass usage and losses in gearless drive construction

The previous section showed the optimization of only the mass of the gearless mill drive. As will be shown in Sec. 7.8, this minimization of just the mass resulted in a shorter stator and rotor. To be able to maintain the needed torque, the currents were therefore increased, resulting in an increase in resistance, core and fan losses. As this is not a feasible solution in a real life application, this section and Sec. 7.8 will show the results of a multi-objective optimization of the gearless drive, which attempt to minimize both the mass usage for constructing the drive and the total losses in the drive. The next six figures Fig. 7.9(a) - Fig. 7.9(f) show plots of all the individuals (dots) at different number of generations for the (6/4+1)-ES algorithm with the use of the IBEA selector, Sec. 7.4.1. The found Pareto front at the different generations have been added to each plot by a solid red line connecting the Pareto optimal solutions. Figure 7.9(a) shows a plot of the initial population consisting of six individuals as $\mu = 6$. It can be seen that some of the individuals have created invalid solutions or at least their fitness values have been penalized as the mass fitness value for these individuals are very high. The Pareto optimal solution for generation zero, indicated by the red line, gives very little knowledge of the optimal solutions as these individuals have been randomly generated. Looking at the next couple of plots showing the individuals and Pareto front as the number of generation increase, it can be seen that one quickly get an idea of how the Pareto front will end up looking. However, knowing the shape of the final Pareto front will only tell something about what can be expected and not how the solution would look like, as one needs a Pareto optimal solution for this. This can only be achieved by letting the optimization algorithm run for a longer period of time until it is decided that there is a sufficient number of Pareto optimal solutions to be able to make a qualified determination of the best mass/loss ratio for the current optimization case. Once it is determined to end the optimization algorithm, in this case after 3000 generations, it is up to the decision makers to determine the best ratio between the mass and losses which best fit their needs. Looking at Fig. 7.9(f) which shows all the individuals at the final generation, a good ratio between mass and losses can

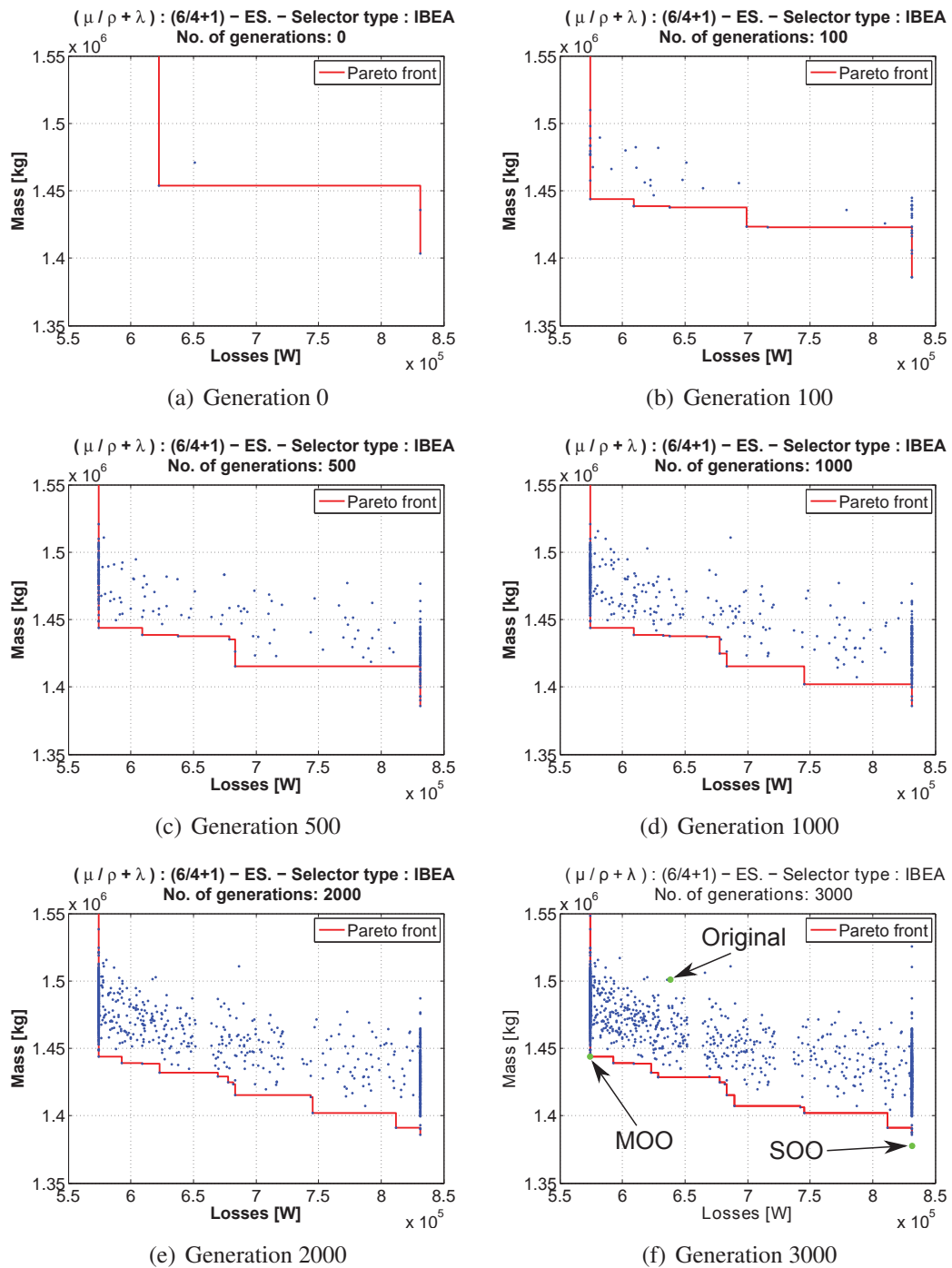


Figure 7.9 Multi-objective optimization - Evolution Strategy ($\mu/\rho + \lambda$): (6/4+1), Selector: IBEA, Rotor eccentricity: $(x, y) = (1.4142, 1.4142)$

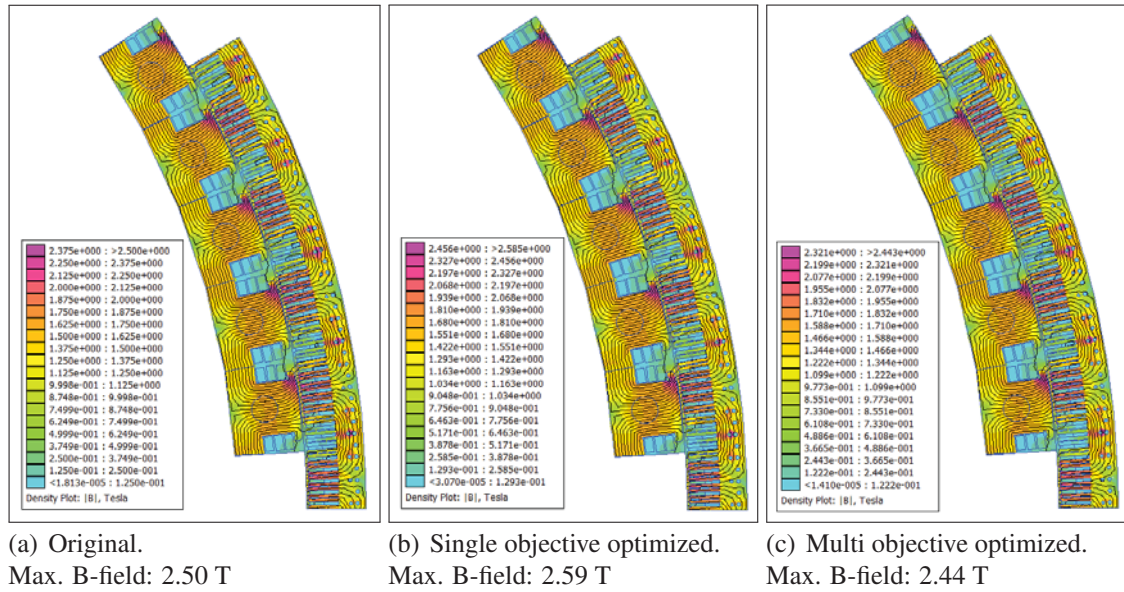


Figure 7.10 Magnetic B-field comparison of the original and optimized gearless drive

be obtained in the corner where the mass drops almost vertical at almost constant losses and turns in an almost horizontal direction where the mass stays almost constant as the losses increase. A solution in this area is chosen for comparison and is indicated by the black arrow (MOO). As an extra information the solutions for the original (Original) and the single objective (SOO) case have been indicated as well. The chosen multi-objective optimized solution is shown in the next section, Sec. 7.8, where it is compared against the solution for the original drive with dimensions from ABB and the single objective optimized drive.

7.8 Comparison of original and optimized gearless drive

This section will compare and comment on the final multi-physics models of the original single objective optimized and the multi objective optimized drive. All the following comparisons have been made with a rotor eccentricity of $(x, y) = (1.4142, 1.4142)$ and a cooling flow resulting in a maximum coil temperature of $90 \pm 5^\circ\text{C}$. The currents applied in all the models correspond to a rated torque production of 13.6 MNm. The following figures show some of the results from the different physical areas of the multi-physics model of the drive and Tab 7.3 shows a summary of the main results from the three cases. Figure 7.10 shows the magnetic flux densities at a rotor angle of 3.75° for the three cases. Even though the three subfigures look identical, the color legend next to them indicate a slight difference in the magnitude of the B-field. An explanation for this is found since the three different cases have three different rotor/stator lengths and to maintain the desired torque, the currents are corrected to achieve this which of course results in different magnitudes of the B-fields. The maximum value of the B-field in the

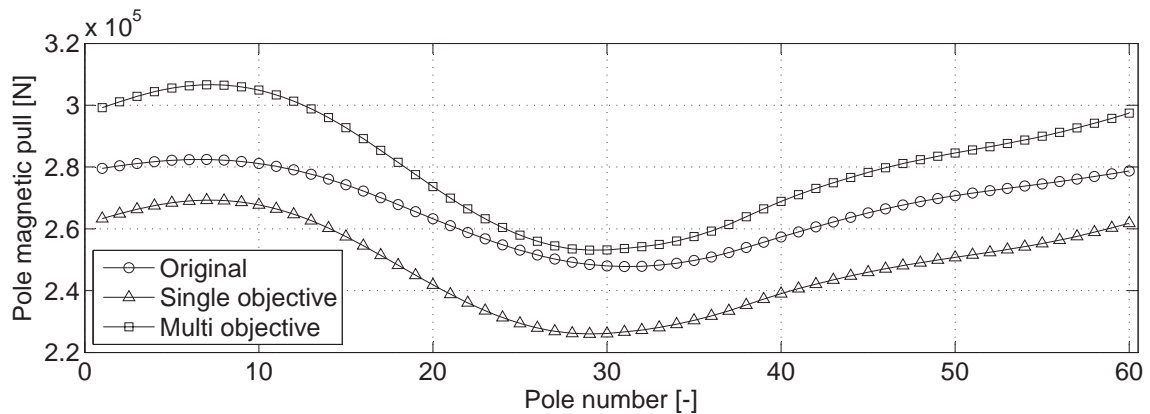


Figure 7.11 Pole magnetic pull comparison of the original and optimized gearless drive

three cases is listed in Tab 7.3 and it can be seen that all of them are operating in a saturated state as the maximum B-field is well above 2 Tesla and the core materials begin to get saturated at approximately 1.5 Tesla. Figure 7.11 shows the radial pole magnetic pull for the three cases, which is a combination of the static forces from an eccentric undeformed rotor and the forces due to air gap distortion resulting from the deformation of the rotor, stator and frame and heat expansion. The forces due to the air gap distortion in the figure have been calculated from the average air gap at the different poles. However, this is not exactly the force applied to the stator and poles as the air gap at a pole also change in the axial direction and the forces in the models have been applied according to this actual air gap. It can be seen that the shape of the curves showing the magnetic pull for the three cases looks very similar, however, the forces experienced by the different poles differ significantly and are not sinusoidal shaped which also was expected when dealing with an eccentric rotor. The reason for this is the before mentioned air gap distortion which is dependent on the forces between the rotor and stator and the structural stiffness of the structure, which will be shown further down in this section. Comparing only the curves for the two optimized cases, it can be seen that it is almost just a DC offset. This is due to the fact that the deformation shape for these two cases are almost identical where the original deformation shape differs from the optimized cases which will be shown later. The maximum forces for the three cases are listed in Tab. 7.3.

Figure 7.12 and Fig. 7.13 show a comparison of the final slice of the stator and rotor from the thermal model and the temperature change of the cooling flow in the different channels respectively. Looking first at the temperature distribution in the stator and rotor from the three cases, it can be seen that they are almost identical as a result of that the cooling flow has been altered as to achieve a maximum temperature of $90 \pm 5^\circ\text{C}$, as explained in the start of this section. The small temperature discrepancies between the cases are mainly due to the $\pm 5^\circ\text{C}$ tolerance in the maximum temperature. From the figures it can be seen that the rotor copper windings are significantly hotter than the rest of the drive for all of the three cases, $15 - 20^\circ\text{C}$ warmer than the rest of the drive. In the future it would therefore be a good idea to come up with a different cooling concept at the rotor

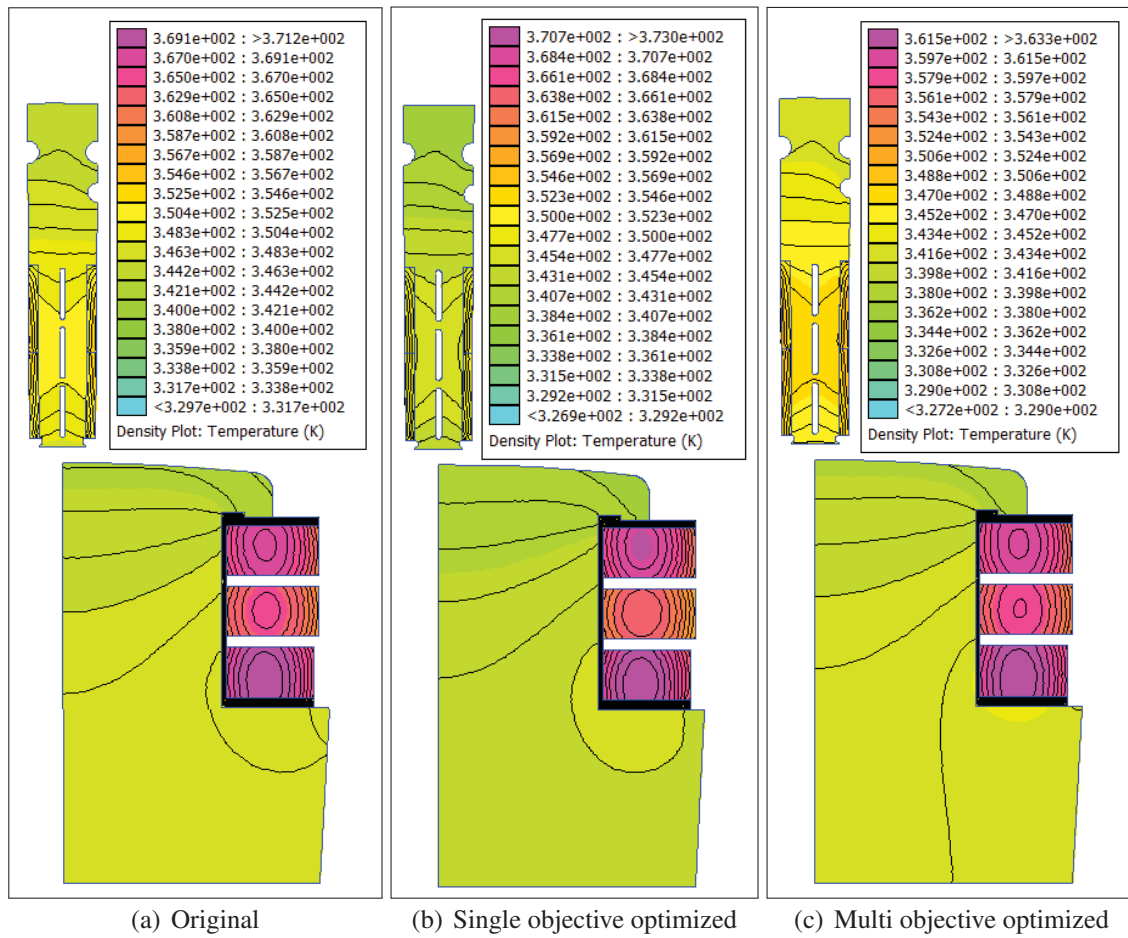


Figure 7.12 Temperature comparison of the warmest slice of the original and optimized gearless drive

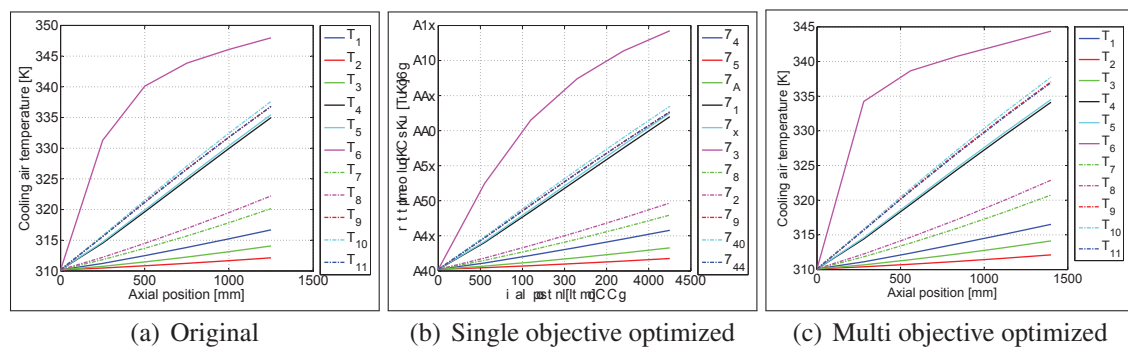


Figure 7.13 Cooling flow temperature comparison of the original and optimized gearless drive

coils, which could decrease the temperature and thereby reduce the needed cooling flow. The average core and coils temperatures for the three cases are listed in Tab. 7.3. Figure 7.13 shows the cooling air temperature in the different channels as a function of the axial

position. The temperature increase of the air is highly dependent on the mass flow in the channels and is almost linear dependent on the axial position in these three cases. However, looking at T_6 for channel 6, Sec. 4.7, which is the narrow channel between the pole core backs, it can be seen that this curve is far from linear which is due to the low mass flow in the channel and as the temperature of the flow increases, less heat flux enters the cooling air flow from the pole core. As the mass flow increase the curve will become more and more linear which can be seen when comparing T_6 curves from the single objective optimized and the multi objective optimized drive where the curve for the single objective optimized case is more linear as the flow in this case is higher than for the other cases. The cooling volume flow and pressure drop are listed in Tab. 7.3.

Figure 7.14 and Fig. 7.15 show the deformation and Von Mises stress results for the three cases coming from the structural model. Looking initially at Fig. 7.14 for the deformation, it is obvious that the rotor is placed at an eccentricity as the entire frame is pulled in the opposite direction of the eccentricity due to the increased magnetic pull in the eccentricity direction. This is the same for all the cases, however, it is mainly the center part of the frame that deforms for the original case, where it is more even for the two other cases. This is due to the fact that the original case has thick end plates which makes the end plates stiffer than for the two other cases with relatively thin end plates. The original frame is also generally stiffer than the two other cases, as these have been optimized for mass minimization which will decrease the overall stiffness if this is achieved only by decreasing plate thicknesses. This can clearly be seen in the maximum deformation of the frame indicated in the color legend and in Tab. 7.3. The deformation of the mill drum remain almost the same for the three cases as nothing has been changed on it, except the pole magnetic pull which clearly has little effect on the deformation. The main reason for the deformation of the mill drum comes for the gravity forces from the rock charge and the liners inside the drum, as these are extremely high and is the reason for the high deformation in the bottom of the drum. The maximum deformation of the mill drum is also listed in Tab. 7.3.

The Von Mises stress results are used to make sure that no part of the mill is yielding and is shown in Fig. 7.15 for the three cases. It is evident from these plots that the maximum stresses indicated in the color legend are way below the yielding stress for all the three cases as it is approximately $\sigma_y = 250 \text{ MN/m}^2$. However, the location and magnitude of the maximum Von Mises stress differs significantly between the original and the optimized cases. For the original case the maximum stress is located in the bottom of the mill drum. For the two optimized cases it is located at the side of the frame. The reason for the shift of maximum stress location is to be found in which the optimized frame is optimized for minimal mass usage, this has resulted in thinner frame plates than the original frame. The maximum stresses in the frame have also increased significantly, up to approximately 300% in the two optimized cases due to the thinner frame plates, however, as stated before, these values are still well below the yielding stress. As the mill drum has not changed geometry, except the length of the poles, and the loads applied to it are almost the same, the Von Mises stresses of the drum will also remain almost the same for the three cases. The maximum Von Mises stresses of the mill drum with rotor

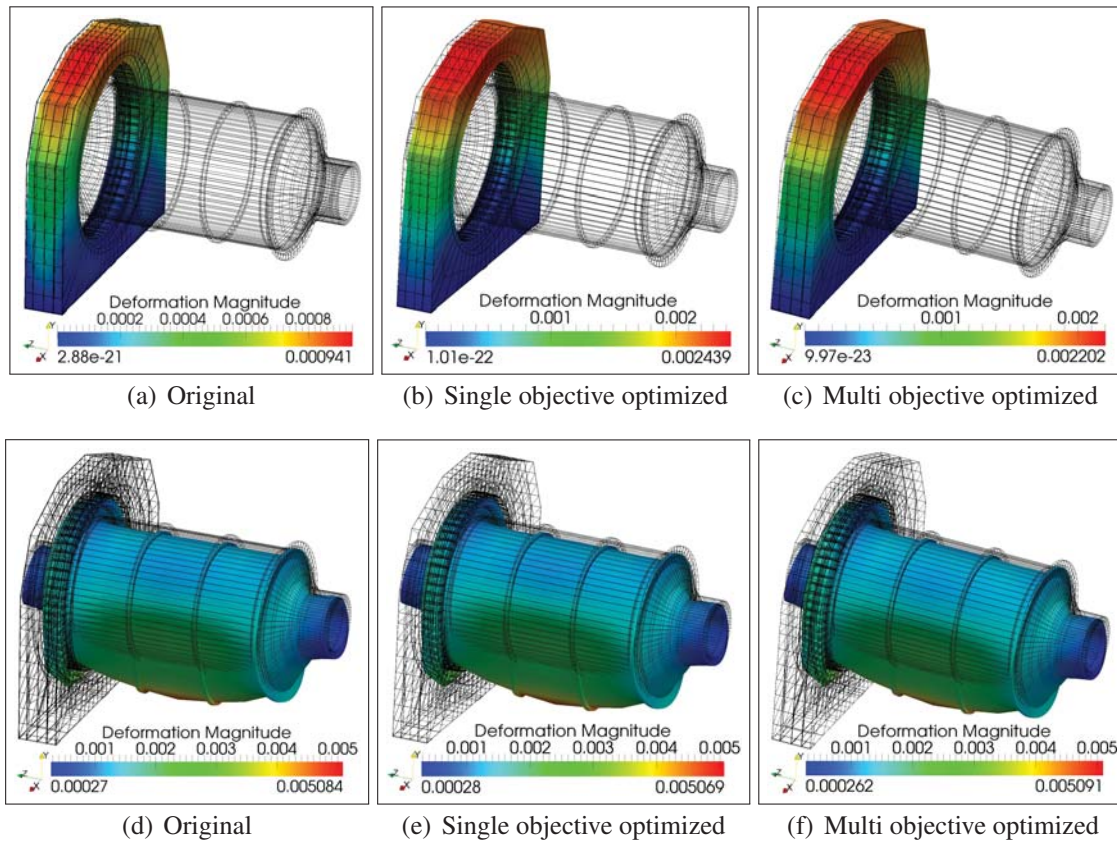


Figure 7.14 Deformation comparison of original and optimized gearless drive

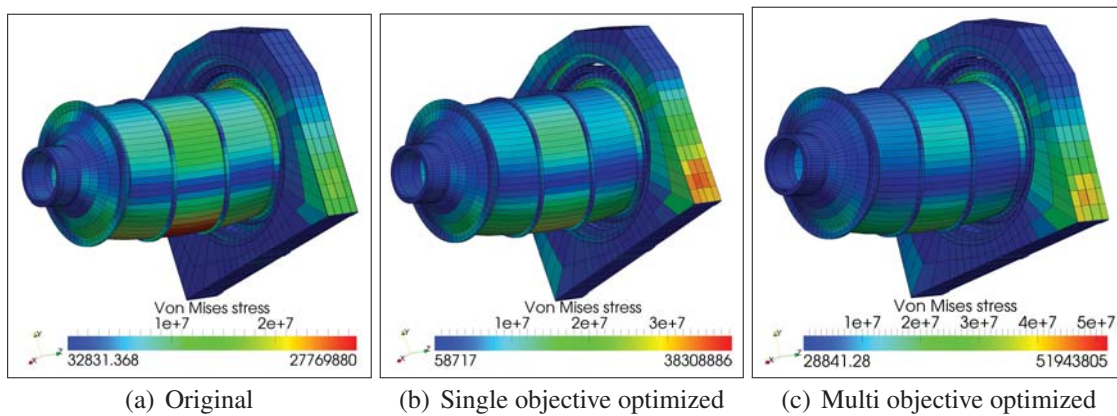


Figure 7.15 Stress comparison of original and optimized gearless drive

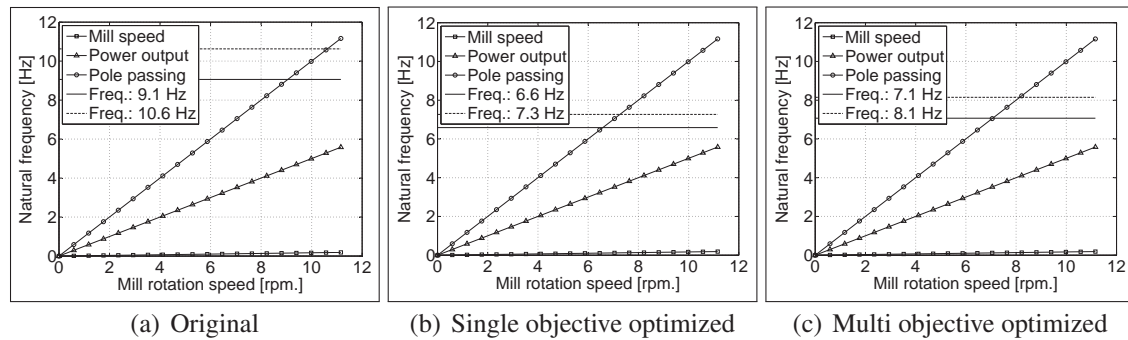


Figure 7.16 Natural frequencies comparison of original and optimized gearless drive

poles and the frame with the stator are listed in Tab. 7.3.

The next figures, Fig. 7.16 and Fig. 7.17, show the comparison of the natural frequencies and their corresponding mode shapes for the three cases. Looking initially at Fig. 7.16(a) of the natural frequencies for the original case, it can be seen that this actually fails the criteria set forth that the natural frequency should be at least 1 Hz from any potential excitation frequencies at rated speeds. As the damping of this natural frequency is unknown, it might still be safe to run the mill at this speed, if the damping is sufficiently high, but as the model does not include material damping, all “critical” frequencies are deemed unsafe. Looking at the two other plots in Fig. 7.16 for the optimized cases, it can be seen that these fulfill the criteria of the 1 Hz separation margin to the potential excitation frequencies at rated speeds. Figure 7.17 shows the mode shapes corresponding to these natural frequencies. It is obvious from these plots that all these modes distort the air gap between the poles and the stator, making these modes “critical” modes. The first “critical” mode of the three cases have a oscillation of the top of the frame in the axial direction where the single objective optimized case has high vibration amplitudes of the end plates due to the thin nature of these plates compared to the two other cases. The second “critical” mode of the the three case have a twisting oscillation of the frame around a vertical axis through the center of the frame where the single objective optimized case again has high vibration amplitudes of the end plates due to the thin nature of these plates. The found “critical” frequencies are listed in Tab 7.3.

The final figure, Fig. 7.18, shows the air gap distortion due to rotor eccentricity, heat expansion and deformation for the three cases. They are used for checking if the minimum air gap has been exceeded, as it would have catastrophic consequences if the rotor hit the stator under operation. Furthermore, the air gap has an impact on the produced pole magnetic pull as shown above. Each plot consists of 3 curves which indicate the air gap at each axial extremities of the poles and an average air gap at the poles. It is this average air gap which is used for the magnetic pull figures above where the effect of the air gap distortion is obvious. The limit of the minimum air gap of 12 mm is clearly indicated in the two optimized cases as these have a minimum air gap very close to this value where the original case which did not have this limit has a larger margin to this limit. The maximum and minimum air gap for the three cases are listed in Tab. 7.3.

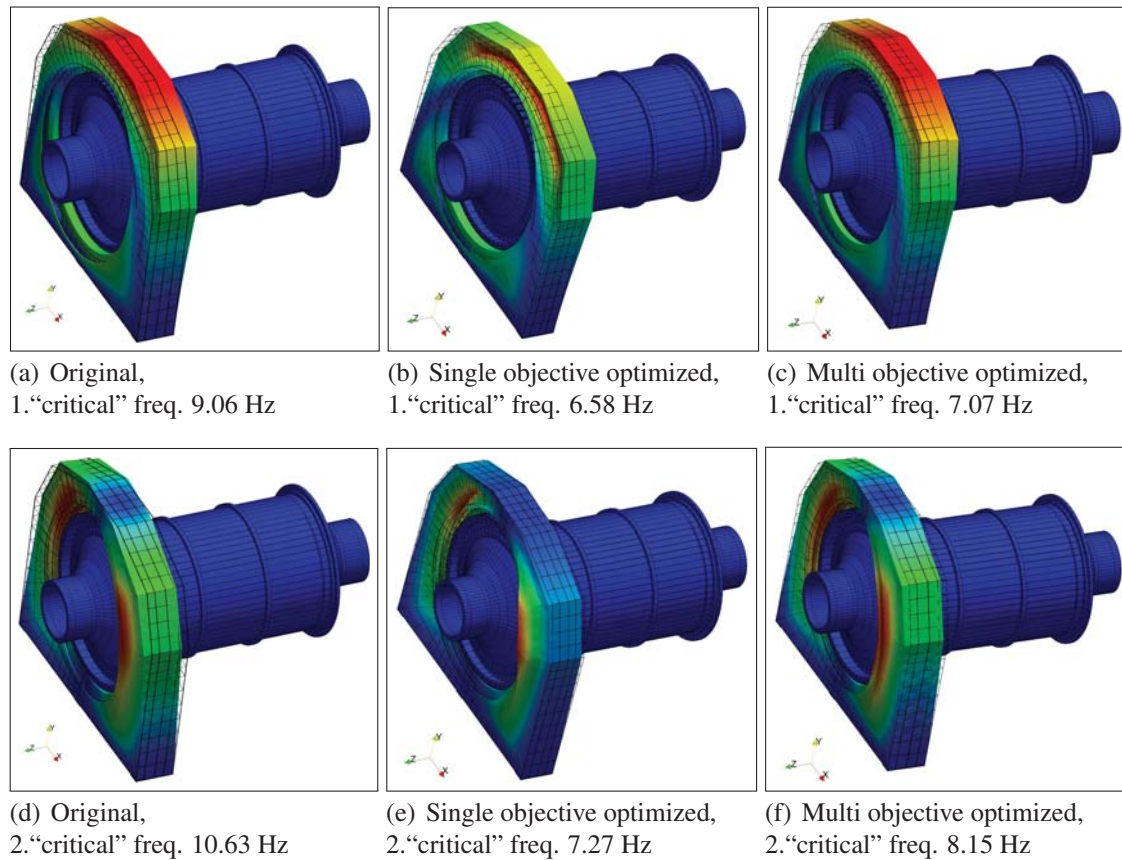


Figure 7.17 Mode shapes of original and optimized gearless drive

The main results of these simulations are of course the mass and the losses in the drive where the above shown results are only a means to estimate this and to make sure that none of the described limits have been exceeded. The found masses and losses of the three examined cases are listed in Tab. 7.3 together with a percentage deviation between the two optimized cases and the original case. Look initially at the mass optimized case, it has clearly achieved its goal, as the mass has been decreased by 8.8% compared to the original case. However, as this mass minimization has been performed without any restriction of the produced losses, these have increased significantly, 30.3%, which would be completely unacceptable in a real life situation. Looking at the multi-objective optimization which also minimize the losses, it is clear that this has also met its goal, as the mass has been decreased by 4.0% and at the same time, the losses have been decreased by 9.9% compared to the original case. However, looking at the object parameters achieved which are mainly frame plate thicknesses, it is obvious that no one would construct such a large device with plates with a thickness of 1 mm. However, this was the limit set forth to make sure that none of the elements in the finite element model would end up with a zero thickness and thereby it was possible to maintain the same general mesh structure for all the simulations. The object parameters with a value of 1 mm just indicate that these plates play no significant role in the solution for the specific case and can be removed if desired.

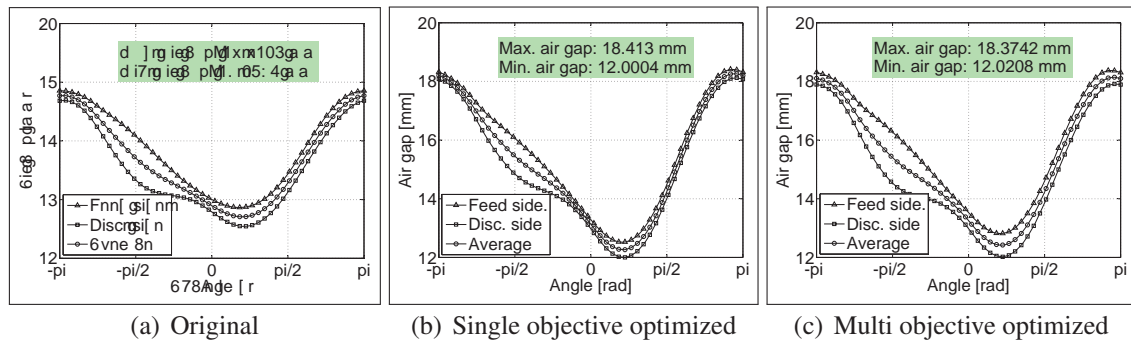


Figure 7.18 Air gap distortion comparison of original and optimized gearless drive

However, it has to be mentioned that none of the cases simulated have any axial forces which could affect the results. However, this requires that the magnetic forces are calculated with a 3D finite element program which clearly would increase the computational time significantly, but could be done in future work with the model.

	Original	Single objective	Multi objective
Max. deformation, Rotor [mm]	5.084	5.069	5.091
Max. deformation, Frame [mm]	0.941	2.439	2.202
Max. stress, Rotor [MN/m ²]	27.77	27.71	27.80
Max. stress, Frame [MN/m ²]	17.45	38.31	51.94
1. "critical" mode [Hz]	9.06	6.58	7.07
2. "critical" mode [Hz]	10.63	7.27	8.15
Max. air gap [mm]	17.71	18.41	18.37
Min. air gap [mm]	13.09	12.00	12.02
Total losses [kW]	638.01	831.55 (+30.3%)	574.57 (-9.9%)
Total mass [T]	1503.67	1376.61 (-8.8%)	1443.97 (-4.0%)
Cooling volume flow [m ³ /s]	50.00	64.96	50.00
Cooling pressure drop [Pa]	438.64	689.36	459.29
Avg. stator core temperature [°C]	74.96	70.62	72.28
Avg. rotor core temperature [°C]	73.69	71.12	69.14
Avg. stator coil temperature [°C]	78.73	75.09	75.52
Avg. rotor coil temperature [°C]	93.54	94.33	86.38
Max. magnetic B-field [Tesla]	2.500	2.585	2.443
Max. pole magnetic pull [kN]	282.4	269.3	306.6
Object parameter 1 [mm]	15	3.17	1.00
Object parameter 2 [mm]	25	4.99	2.33
Object parameter 3 [mm]	30	5.63	20.00
Object parameter 4 [mm]	20	4.18	1.00
Object parameter 5 [mm]	5	4.03	10.37
Object parameter 6 [mm]	5	1.00	5.87
Object parameter 7 [mm]	15	11.93	12.31
Object parameter 8 [mm]	1272	1100	1400

Table 7.3 Summary of results

Chapter 8

Conclusion & future aspects

8.1 Conclusions and general comments

ABB Switzerland Ltd. had a request for a multi-physics tool which could be used as an aid in the design process of their gearless mill drives. What has been proposed is a multi-physics model for one of ABB's gearless drives designs combining the three main physical branches: electromagnetics, heat and mass transfer and structural calculations. To further enhance the model as a design tool an optimization algorithm has been wrapped around the global model, in this case for minimizing the mass and losses but can easily be changed for other optimization parameters if desired.

The electromagnetic part of the model is created in FEMM through Lua scripts and estimates the pole magnetic pull, torque and core losses as its main output. As the drive consist of many poles (60) and many stator slots (504) there was a need for reducing the model to decrease the computation time and storage needs without losing accuracy in the final results. It has been shown that by applying symmetry and anti-symmetry boundary conditions at specific location in the model the full model of the drive could be reduced by over 90% without any loss in accuracy as long as the rotor was placed in the center of the stator without any eccentricity. However an investigation has shown that there is a highly linear relationship between the rotor-stator air gap and the magnetic pull for a pole which make it possible to simulate any eccentricity based solely on the present air gap at the specific poles. This makes the reduced model applicable to cases with rotor eccentricities as well. However some errors have been introduced if this was to be used in a time simulation as the force and torque ripple effect from the pole passing the stator slots has been neglected. These ripple effects are however relatively small and has no effect on the static case. If it is desired to take these effects into account in a time simulation with an eccentric rotor the full drive would have to be modeled. The torque of the drive is on the other hand almost independent on the eccentricity of the rotor making the reduced model sufficient for estimating it. Both the pole magnetic pull and torque have been compared with external results and have shown good agreement between the results with deviations of 4.4% and 2.3% for the force and torque respectively. The core losses of the drive have been found through a series of magnetostatic calculations where the magnetic flux densities were recorded for different rotor positions. By use of FFT the harmonic content of these flux densities could then be extracted and used for estimation of the losses from each of these harmonics and finally summed up under the assumption that the principle of separation of losses could be applied. These losses have been compared with external results for the first harmonic and shown a deviation of less than 1%. The used model is however an improvement as it is not just limited to the losses from the first harmonic as the model from the external source but can include as many harmonics as the machine

precision allow.

A lumped model with 2 nodes interconnected by 11 channels and a fan has been used for modeling the cooling flow in the drive where the air properties in the different channels have been updated iteratively corresponding to the flow temperatures from the thermal submodel. This is an improvement compared to model used by the external source as they keep the air properties constant in their flow model and thereby introduces an error as the air properties dependency on the temperature is neglected. However, comparing the results achieved in this thesis to the external source with the same air properties and pressure loss have shown to be in good agreement with a deviation of less than 3% for both the flow rate and the mean velocity. The final thermal submodel is a 2D model created in FEMM where the drive has been cut in slices in the axial direction as it has been shown that it is insufficient to just look at one cross-section in the center of the drive. The model is highly fused together with the flow model as the temperature distribution, heat flux and air properties are corrected for each slice which the model from the external source do not incorporate. Comparing the results presented in this thesis with the ones from the external source with the same input parameters and air properties exhibit almost the same values for the maximum temperature with a deviation of only 3%. Another benefit of the presented thermal model compared to the one from the external source is that it shows a more detailed view of the temperature distribution as it is created by the finite element method where the external model is a lumped thermal model and if not created with enough nodes could give misleading results. The thermal model assumes that the only axial heat flow is through the heat transferred to the cooling air. The error in connection with this assumption has been examined and has shown that the axial heat flux in the axial direction of the hottest coil is only 2.6% of the total loss in the coil segment.

The structural part of the model is created by a 3D finite element method program made in Fortran and build of pure hexahedron 20 node elements as these has proved to be superior to both pure tetrahedral and pure hexahedron 8 node finite element mesh. This submodel is like the other submodels an improvement of the model used by the external source as the presented model include the effect of the thermal expansion which has an influence on the air gap and thereby an influence on the pole magnetic pull. This effect has been neglected in the model used by the external source which has been used for comparison. Another improvement is that the pole forces used in the presented model does not rely on only one air gap per pole as the model from the external source do but uses the air gap at each nodal point in the mesh to find the correct nodal force at the different nodes. The main results from the structural model are deformations, Von Mises stresses, eigenvalues and air gap distortion. These values have been compared to the results achieved by the external source and show a somehow larger deviation than for the other submodel except for the results of the air gap distortion, deformation: 42.7%, stress: 50.1%, eigenvalues: 58.2% and air gap: 1.2%. A highly plausible explanation for these high discrepancies are to be found in the boundary condition between the stator and the frame which has been used for the two different models. The presented model assumes that the drive is at its operating temperature and the stator is therefore pressed against the frame which results in a rigid stator-frame boundary condition. The model used by

the external source however simulates the drive in a cold condition where the stator is connected to a lot of beams which again is connected to the frame. These two different boundary conditions of course have an impact on the global stiffness of the structure and therefore on the final result. The boundary conditions at the bearing are also different between the two models where the bearing stiffness in the presented model has been applied to every node of the bearing surface where the model used for comparison only has applied the bearing stiffness to the bottom half of the bearing surface and has added a no rotation boundary condition to the surface as well. The comparison of the two structural models is therefore not completely fair and it is therefore critical that experimental test on the gearless drive are performed to verify the models.

The global integrated multi-physic model has been used in a metaheuristic optimization process using the Evolution Strategies optimization algorithm. The goal of the optimization was initially to minimize the mass of the drive compared with the original drive with dimensions from the external source and secondly the minimization of both the mass and losses compared to the same original drive. The first optimization for minimization of the mass resulted in an impressive reduction of the mass of 8.8% however with a side effect of an increase in losses of 30.3%. The second optimization made for minimization of both the mass and the losses resulted in an bit smaller mass reduction 4.0% compared to the previous optimization, however, this has at the same time also decreased the losses in the drive by 9.9%. The benefit of using Evolution Strategies as an optimization algorithm is that it can optimize several parameters at the same time where none of these have to be in the same physical branch and furthermore it is very easy to implement. However, one of the drawbacks of evolution strategies is that it does not guaranties that the optimal solution will be found but it will at least find a good solution.

8.2 Future aspects

As the presented model is the first generation of a fully integrated multi-physic model of a gearless mill drive combined with the optimization algorithm Evolution Strategies further improvement and verification can be performed toward the next generation of the model. Below is a list of possible directions for future research/work with the presented model.

- Experimental test on the mill drive to verify the presented models, especially the structural model as large deviations have been detected between the presented model and the ABB model used for verification.
- Examine the effect of the end windings and frame chambers with a detailed 3D CFD model.
- Simulating the thermal part in 3D to examine the effect of the axial heat flux.
- Detailed model of the cooling system losses.
- Modeling in time (start up, pole short-circuit, earth quakes).

- Investigation of the boundary condition between the stator and frame.
- Tune both the Evolution Strategies algorithm and the IBEA selector.
- Compare different selectors for the multi-objective optimization.
- Add more objective parameters like different stiffener tubes, removal or additional tubes, frame plates, different winding configuration, different materials.
- Creation of a 3D finite element magnetic model to examine the effect of axial forces due to axial misalignment of the rotor.

References

- ABB Communications (2011). ABB Communications. Press releases.
- ABB Switzerland Ltd. (2009). Gearless mill drives - go gearless. *3BHT 490 275 R0001 REV B*.
- Andersen, S.B., Enemark, S. and Santos, I.F. (2012a). Dynamics and stability of rigid rotors levitated by passive cylinder-magnet bearings and driven/supported axially by punctual contact clutch. *Journal of Sound and Vibration (Submitted)*, Ref. JSV-D-12-01433:1–26.
- Andersen, S.B., Santos, I.F. and Fuerst, A. (2012b). Investigation of Model Simplification and its Influence on the Accuracy in FEM Magnetic Calculations of Gearless Drives. *IEEE Transactions on Magnetics*, 48(7):2166–2177.
- Andersen, S.B.A., Santos, I.F. and Fuerst, A. (2012c). Multi-Physics Modelling of Large Ring Motor for Mining Industry - Combining Electromagnetism, Fluid Mechanics, Mass and Heat Transfer in Engineering Design. *Submitted to Journal of Applied Mathematical Modelling*.
- Andersen, S.B. and Santos, I.F. (2012). Evolution strategies and multi-objective optimization of permanent magnet motor. *Applied Soft Computing*, 12:778–792.
- Arumugam, R., Lowther, D., Krishnan, R. and Lindsay, J. (1985). Magnetic field analysis of a switched reluctance motor using a two dimensional finite element model. *IEEE Transactions on Magnetics*, MAG-21:1883–1885.
- Bader, J., Deb, K. and Zitzler, E. (2008). Faster Hypervolume-based Search using Monte Carlo Sampling. In *Conference on Multiple Criteria Decision Making (MCDM 2008)*. Springer.
- Bader, J. (2011). Hype: An algorithm for fast hypervolume-based many-objective optimization. *Journal of Evolutionary Computation*, 19:45–76.
- Baehr, H.D. and Stephan, K. (2011). *Heat and mass transfer*. Springer, 3 edition.
- Bastos, J.P.A. and Sadowski, N. (2003). *Electromagnetic Modeling by Finite Element Methods*. Marcel Dekker, Inc.
- Bathe, K.J. (1982). *Finite Element Procedures in Engineering analysis*. Prentice Hall.
- Bäck, T. and Hoffmeister, F. (1994). Basic aspects of evolution strategies. *Statistics and Computing*, 4:51–63.

- Bäck, T. and Schwefel, H.P. (1993). An overview of evolutionary algorithms for parameter optimization. *Journal of Evolutionary Computation*, 1:1–23.
- Benzley, S.E., Perry, E., Merkley, K. and Clark, B. (1995). A Comparison of All Hexagonal and All Tetrahedral Finite Element Meshes for Elastic and Elasto-plastic Analysis. *Atomic Energy Commission USA, 4th International meshing roundtable*, pages 179–192.
- Bermudez, D. (2012). GMD fluid flow and temperature calculation program, in-house software, ABB Switzerland Ltd.
- Bertotti, G. (1988). General properties of power losses in soft ferromagnetic materials. *IEEE Transactions on Magnetics*, 24(1):621–630.
- Bhatti, M.A. (2005). *Fundamental Finite Element Analysis and Applications with Mathematica and MATLAB Computations*. John Wiley & Sons Inc.
- Bleuler, S., Laumanns, M., Thiele, L. and Zitzler, E. (2003). PISA - a platform and programming language independent interface for search algorithms. In C.M. Fonseca, P.J. Fleming, E. Zitzler, K. Deb and L. Thiele, editors, *Evolutionary Multi-Criterion Optimization (EMO 2003)*, Lecture Notes in Computer Science, pages 494 – 508. Springer, Berlin.
- Blevins, R.D. (1979). *Formulas for natural frequency and mode shape*. Van Nostrand Reinhold Company.
- Bochnia, D., Hofmann, W. and Hupe, H. (1999). Design optimization of permanent magnet motors by evolution strategies and finite element analysis. In *Ninth International Conference on Electrical Machines and Drives*.
- Boglietti, A., Cavagnino, A., Lazzari, M. and Pastorelli, M. (2003). A simplified thermal model for variable speed self cooled industrial induction motor. *IEEE Transaction on Industry Applications*, 39:945–952.
- Boglietti, A., Cavagnino, A. and Staton, D. (2008). Determination of critical parameters in electrical machine thermal models. *IEEE Transaction on Industry Applications*, 44:1150–1159.
- Boglietti, A., Cavagnino, A., Staton, D., Shanel, M., Mueller, M. and Mejuto, C. (2009). Evolution and modern approaches for thermal analysis of electrical machines. *IEEE Transaction on Industrial Electronics*, 56(3):871–882.
- Bougehey, A., Svalbonas, V. and Jones, S.M. (2000). Supply, installation & commissioning of the worlds largest grinding mill. *Society for Mining, Metallurgy and Exploration - SME annual meeting - CD rom edition*, pages 00–7.

- Bouheraoua, M., Benamrouche, N. and Bousbaine, A. (2012). A more refined thermal model for a totally enclosed fan-cooled induction motor. *Electric Power Components and Systems*, 40:179–194.
- Bracikowski, N., Hecquet, M., Brochet, P. and Shirinskii, S.V. (2012). Multiphysics modeling of a permanent magnet synchronous machine by using lumped models. *IEEE Transaction on Industrial Electronics*, 59(6):2426–2437.
- Casado, D. (2012). GMD Ring Motor - Overall System FEM Analysis - Project: Conga Ball Mill 26ft. Technical report, ABB Switzerland Ltd., LBU Minerals.
- Chen, Y. and Pillay, P. (2002). An improved formula for lamination core loss calculations in machines operating with high frequency and high flux density excitation. *Industry Applications Conference, 2002. 37th IAS Annual Meeting*, 2:759–766.
- Chin, Y. and Staton, D. (2004). Transient thermal analysis using both lumped-circuit approach and finite element method of a permanent magnet traction motor. In *IEEE AFRICON: 7th AFRICON Conference*.
- Christensen, N.T. (2012). Identificering af ækvivalente dynamiske kræfter på mølleforinger i sten maleprocesser - En empirisk metode i frekvens og tids domæner (in Danish) (Identification of equivalent dynamic forces on mill liners in rock grinding processes - An empirical approach in frequency and time domains). Technical report, Technical University of Denmark, Department of Mechanical Engineering.
- Chung, T.K. and Kim, S.K. (1997). Optimal pole shape design for the reduction of cogging torque of brushless dc motor using evolution strategy. *IEEE Transactions on Magnetics*, 33(2):1908–1911.
- Cook, R.D., Malkus, D.S., Plesha, M.E. and Witt, R.J. (2002). *Concepts and Applications of Finite Element Analysis*. John Wiley & Sons Inc., 4 edition.
- Cundev, D. and Cerovsky, Z. (2007). Steady-state analysis of salient poles synchronous motor with damper based on determination of the magnetic field distribution. In *PIERS Proceedings*.
- Deb, K., Agrawal, S., Pratap, A. and Meyarivan, T. (2000). A fast elitist non-dominated sorting genetic algorithm for multi-objective optimization: NSGA-II. In M. Schoenauer, K. Deb, G. Rudolph, X. Yao, E. Lutton, J.J. Merelo and H.P. Schwefel, editors, *Parallel Problem Solving from Nature – PPSN VI*, pages 849–858. Springer, Berlin.
- Deb, K., Mohan, M. and Mishra, S. (2003). A Fast Multi-objective Evolutionary Algorithm for Finding Well-Spread Pareto-Optimal Solutions. KanGAL report 2003002, Indian Institute of Technology, Kanpur, India.

- Dlala, E. (2009). Comparison of models for estimating magnetic core losses in electrical machines using the finite-element method. *IEEE Transactions on Magnetics*, 45(2):716–725.
- Dorigo, M. and Blum, C. (2005). Ant colony optimization theory: A survey. *Theoretical Computer Science*, 344:243–278.
- Dreher, R., Janssen, J., Farnell, D. and Thompson, S. (2004). Matching real world results. In *International ANSYS Conference Proceedings*.
- Drubel, O. and Runge, B. (2004). Temperature rise within the rotor of squirrel cage induction machines with solid iron and laminated rotors during run up and standstill. *Electrical Engineering*, 86:97–103.
- EAnD (1999). EAnDs Engineers Solve Vibration Problems in the Worlds Largest Mill Drive. *EAnD Insight Magazine*, 1(3):1–5.
- EAnD (2000). Antamina, peru - grinding facility analysis. *EAnD Insight Magazine*, 2(1):1–4.
- Eiben, A.E. and Schippers, C.A. (1998). On evolutionary exploration and exploitation. *Fundamenta Informaticae*, 35:35–50.
- EL-Refaie, A. and Shah, M. (2011). Induction machine performance with fractional-slot concentrated windings. *COMPEL: The International Journal for Computation and Mathematics in Electrical and Electronic Engineering*, 31:119–139.
- Filippov, I. (1974). *Fundamental of heat exchange in electrical machines*. Energija Leningrad.
- Fox, R.W., McDonald, A.T. and Pritchard, P.J. (2004). *Introduction to Fluid Mechanics*. John Wiley & Sons Inc., 6 edition.
- Galea, M., Gerada, C. and Raminosa, T. (2012). A thermal improvement technique for the phase windings of electrical machines. *IEEE Transaction on Industry Applications*, 48(1):79–87.
- Geuzaine, C. and Remacle, J.F. (2010). *Gmsh Reference Manual*.
- Glover, F. (1989). Tabu search - part i. *ORSA Journal on Computing*, 1:190–206.
- Glover, F. (1990). Tabu search - part ii. *ORSA Journal on Computing*, 2:4–32.
- Grandy, J. (1997). Efficient computation of volume of hexahedral cells. Technical report, U.S. Department of Energy, Lawrence Livermore National Laboratory.
- Grinbaum, I. (2012). Loss, flow and temperature distribution in GMD, internal report RMBP 2.47.2 on 2012-03-30. Technical report, ABB Switzerland Ltd.

- Hamdani, R. (2000). Ball mill driven with gearless mill drive. *IEEE Cement Industry Technical Conference*, (May):55–68.
- Hughes, E. (2003). Multiple single objective pareto sampling. In *Proceedings of the Congress on Evolutionary Computation (CEC 2003)*, pages 2678–2684. IEEE Press, Canberra, Australia.
- Hughes, E. (2005). Evolutionary many-objectives optimisation: Many once or one many. In G. Greenwood, G. Raidl et al., editors, *Proceedings of the Congress on Evolutionary Computation (CEC 2005)*, pages 222–227. IEEE Press, Piscataway, NJ.
- Humphries, S. (2010). Tutorial: Theory and applications of the maxwell stress tensor. www.fieldp.com.
- Incropera, F.P., DeWitt, D.P., Bergman, T.L. and Lavine, A.S. (2006). *Fundamentals of Heat and Mass Transfer*. John Wiley & Sons Inc., 6 edition.
- Johnson, J.M. and Rahmat-Samii, Y. (1997). Genetic algorithms in engineering electromagnetics. *IEEE Antennas and Propagation Magazine*, 39:7–21.
- Jolly, L., Jabbar, M. and Liu, Q. (2005). Design optimization of permanent magnet motors using response surface methodology and genetic algorithms. *IEEE Transactions on Magnetics*, 41:3928 – 3930.
- Jr., S.H. (2010). Finite-element methods for electromagnetic. www.fieldp.com.
- Jungreuthmayer, C., Bäuml, T., Winter, O., Ganchev, M., Kapeller, H., Haumer, A. and Kral, C. (2011). Heat and fluid flow analysis of an internal permanent magnet synchronous machine by means of computational fluid dynamics. *IEEE International Electric Machines & Drives Conference (IEMDC)*, pages 515–520.
- Kitware, Inc. (2011). *ParaView User's Guide (v3.10) How to unleash the beast!*
- Komeza, K., López-Fernández, X.M. and Lefik, M. (2010). Computer modelling of 3d transient thermal field coupled with electromagnetic field in three-phase induction motor on load. *COMPEL: The International Journal for Computation and Mathematics in Electrical and Electronic Engineering*, 29(4):974–983.
- Kreith, F., editor (2000). *The CRC handbook of thermal engineering*. CRC Press.
- Laumanns, M., Thiele, L., Deb, K. and Zitzler, E. (2002a). Combining convergence and diversity in evolutionary multi-objective optimization. *Evolutionary Computation*, 10(3):263–282.
- Laumanns, M., Thiele, L., Zitzler, E., Welzl, E. and Deb, K. (2002b). Running time analysis of multi-objective evolutionary algorithms on a simple discrete optimization problem. *PPSN VII Proceedings of the 7th International Conference on Parallel Problem Solving from Nature*, pages 44–53.

- Laumanns, M., Thiele, L., Zitzler, E., Welzl, E. and Deb, K. (2002c). Running time analysis of multi-objective evolutionary algorithms on a simple discrete optimization problem. In *Parallel Problem Solving From Nature — PPSN VII*.
- Li, G., Ojeda, J., Hoang, E., Gabsi, M. and Lécivain, M. (2012). Thermal-electromagnetic analysis for driving cycles of embedded flux-switching permanent-magnet motors. *IEEE Transactions on Vehicular Technology*, 61:140–151.
- Li, W., Cao, J. and Zhang, X. (2010). Electrothermal analysis of induction motor with compound cage rotor used for phev. *IEEE Transactions on Industrial Electronics*, 57(2):660–668.
- Meeker, D. (2009). Rotating losses in a outrunner doubly salient permanent magnet generator.
- Meimaris, C. and Boughey, A.M. (2001). Modeling of grinding facilities. *SAG 2001, Mining and Mineral Process Engineering*, pages II–100 – II–111.
- Meimaris, C., Lai, B. and Cox, L. (2001). Remedial design of the worlds largest sag mill gearless drive. *SAG 2001, Mining and Mineral Process Engineering*, pages II–74 – II–83.
- Mellor, P.H., Roberts, D. and Turner, D.R. (1991). Lumped parameter thermal model for electrical machines of TEFC design. *IEE proceedings-B*, 138:205–218.
- Mezani, S., Ibtouen, R., Kechroud, R. and Touhami, O. (2001). Finite element thermal modeling of an induction motor. *Electric Power Components and Systems*, 29:821–834.
- Minghui, Z. and Weiguo, L. (2010). Transient coupled electro-magnetic thermal analysis of a permanent magnet brushless dc motor. In *International Conference on Computer, Mechatronics, Control and Electronic Engineering (CMCE)*.
- Nerg, J., Rilla, M. and Pyrhönen, J. (2008). Thermal analysis of radial-flux electrical machines with a high power density. *IEEE Transactions on Industrial Electronics*, 55(10):3543–3554.
- Nieto, L. and Ahrens, M. (2007). Gearless mill drive protection improvements and its behaviour at minera escondida ltda. In *IEEE Industry Applications Annual Meeting*, pages 1766–1772.
- Olsen, J.B. (2011). Karakterisering af dynamiske kræfter på mølle foringer i sten male processer - En empirisk metode i frekvens domæne (in Danish) (Characterization of Dynamic Forces on Mill Liners in Rock Grinding Processes - An Empirical Approach in Frequency Domain). Technical report, Technical University of Denmark, Department of Mechanical Engineering.

- Pyrhönen, J., Jokinen, T. and Hrabovcová, V. (2008). *Design of Rotating Electrical Machines*. John Wiley & Sons, Ltd.
- Rahideh, A. and Korakianitis, T. (2012). Analytical magnetic field calculation of slotted brushless permanent-magnet machines with surface inset magnets. *IEEE Transactions on Magnetics*, 48:2633–2649.
- Rudolph, G. and Agapie, A. (2000). Convergence properties of some multi-objective evolutionary algorithms. In A. Zalzala and R. Eberhart, editors, *Congress on Evolutionary Computation (CEC2000)*, volume 2, pages 1010–1016. IEEE Press, Piscataway NJ.
- Schwefel, H.P. and Beyer, H.G. (2002). Evolution strategies - a comprehensive introduction. *Natural Computing*, 1:3–52.
- Srinivas, K.N. and Arumugam, R. (2005). Analysis and characterization of switched reluctance motors: Part ii-flow, thermal, and vibration analyses. *IEEE Transactions on Magnetics*, 41:1321–1332.
- Srinivas, K. and Arumugam, R. (2001). Thermal characterization through finite element analysis of the switched reluctance motor. *Proceedings of IEEE Region 10 International Conference on Electrical and Electronic Technology*, pages 819–823.
- Staton, D., Boglietti, A. and Cavagnino, A. (2003). Solving the more difficult aspects of electric motor thermal analysis. *Electric Machines and Drives Conference, IEMDC'03. IEEE International*, 2:747–755.
- Stephan, P., Kabelac, S., Kind, M., Martin, H., Mewes, D. and Schaber, K., editors (2010). *VDI Heat atlas*. Springer, 2 edition.
- Suman, B. and Kumar, P. (2006). A survey of simulated annealing as a tool for single and multiobjective optimization. *Journal of the Operational Research Society*, 57:1143–1160.
- Surahammars Bruks AB (2009). SURA - M400-50A material datasheet.
- Traxler-Samek, G., Zickermann, R. and Schwery, A. (2008). Advanced calculation of temperature rises in large air-cooled hydro-generators. In *Proceedings of the 2008 International Conference on Electrical Machines*.
- Traxler-Samek, G., Zickermann, R. and Schwery, A. (2010). Cooling Airflow, Losses and Temperatures in Large Air-Cooled Synchronous Machines. *IEEE Transactions on Industrial Electronics*, 57:172–180.
- Trigeol, J.F., Bertin, Y. and Lagonotte, P. (2006). Thermal modeling of an induction machine through the association of two numerical approaches. *IEEE Transaction on Energy Conversion*, 21:314–323.

- Veltman, A., Pulle, D.W. and Doncker, R.W.D. (2007). *Fundamentals of Electrical Drives*. Springer.
- Warner, P. (2006). Instability in gearless mill drive motors. *Energize*, pages 38–43.
- White, F.M. (1998). *Fluid Mechanics*. McGraw-Hill, 4 edition.
- Wu, L.J., Zhu, Z., Staton, D., Popescu, M. and Hawkins, D. (2012). Analytical model of eddy current loss in windings of permanent-magnet machines accounting for load. *IEEE Transactions on Magnetics*, 48:2138–2151.
- Zhao, N., Zhu, Z.Q. and Liu, W. (2011). Rotor eddy current loss calculation and thermal analysis of permanent magnet motor and generator. *IEEE Transactions on Magnetics*, 47:4199–4202.
- Zitzler, E. and Künzli, S. (2004). Indicator-based selection in multiobjective search. In *8th International Conference on Parallel Problem Solving from Nature - PPSN VIII*, pages 832–842.
- Zitzler, E., Laumanns, M. and Thiele, L. (2002). SPEA2: Improving the strength pareto evolutionary algorithm for multiobjective optimization. In K. Giannakoglou, D. Tsahalis, J. Periaux, K. Papaliliou and T. Fogarty, editors, *Evolutionary Methods for Design, Optimisation and Control with Application to Industrial Problems. Proceedings of the EUROGEN2001 Conference, Athens, Greece, September 19-21, 2001*, pages 95–100. International Center for Numerical Methods in Engineering (CIMNE), Barcelona, Spain.
- Zitzler, E., Thiele, L. and Bader, J. (2009). On set-based multiobjective optimization. *IEEE Transactions on Evolutionary Computation*, 14:58–79.

Appendix A Appendix

A.1 Data

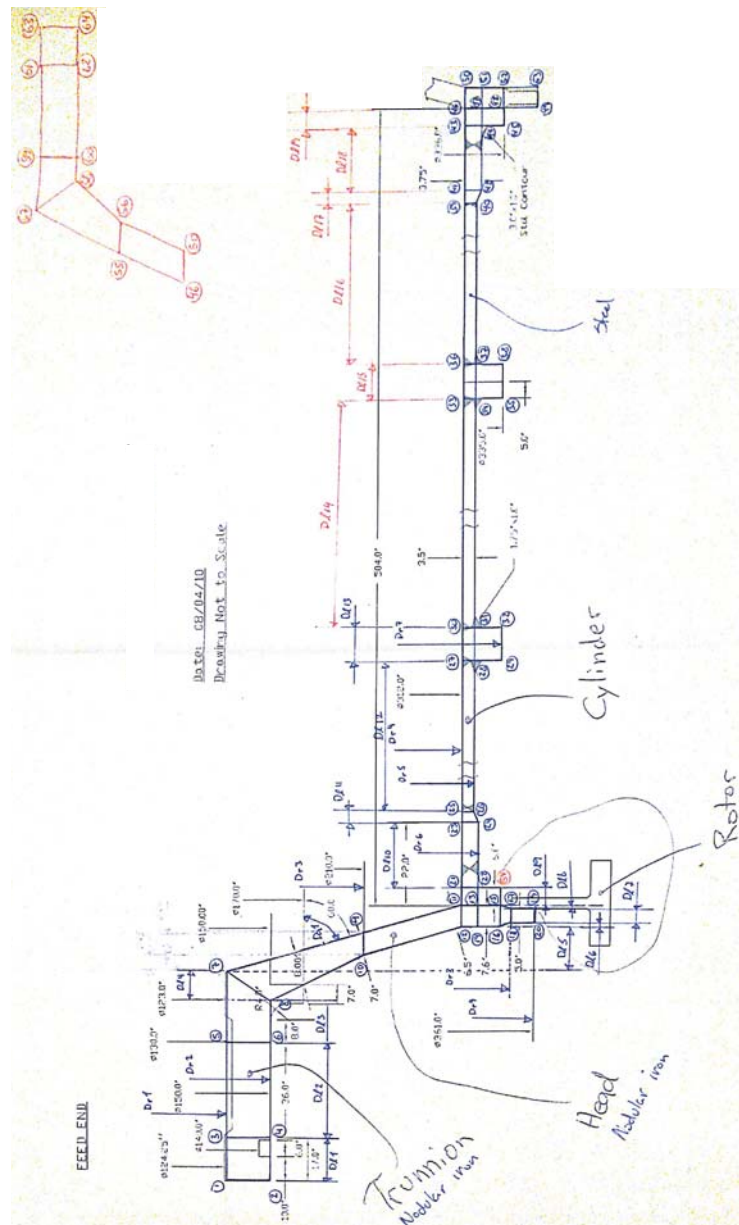


Figure A.1 Drawing of mill drum

A.2 Verification of Fortran code for FD thermal model

Example 5.9 from Incropera et al. (2006) has been used for a simple verification of the Fortran code for the finite difference program. The schematic of the problem in example 5.9 is shown in Fig. A.2 where the wall initially has a heat generation of \dot{q}_1 until steady-state condition has been reached. At this point, the heat generation is increased to \dot{q}_2 until steady-state condition is reached again. The temperatures at these two steady-state conditions are listed in Tab. A.1 which comes from Incropera et al. (2006). Figure A.3 show the temperature distribution for the two steady-state conditions calculated by the Fortran program. The color bars show the maximum and minimum temperatures. Comparing these values with the ones from the example shows a high coherency with only minor discrepancies which can be explained by numerical precision.

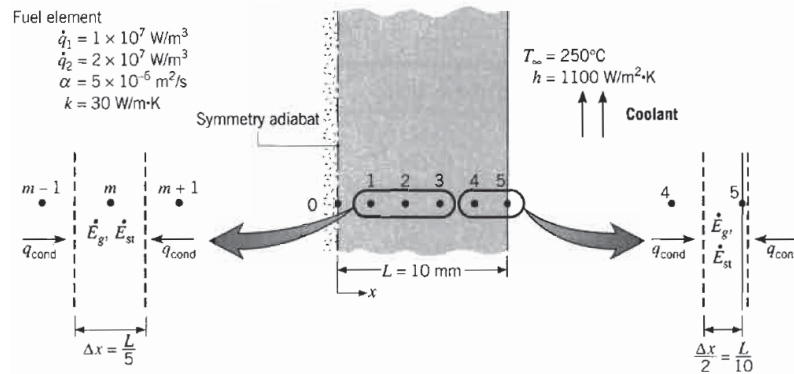


Figure A.2 Schematic of the problem in example 5.9

\dot{q}	T_0	T_1	T_2	T_3	T_4	T_5
1	357.58	356.91	354.91	351.58	346.91	340.91
2	465.15	463.82	459.82	453.15	443.82	431.82

Table A.1 Results from example 5.9, \dot{q}_1 - \dot{q}_2 : heat generation, T_0 - T_5 : temperatures at node 0-5, Incropera et al. (2006)

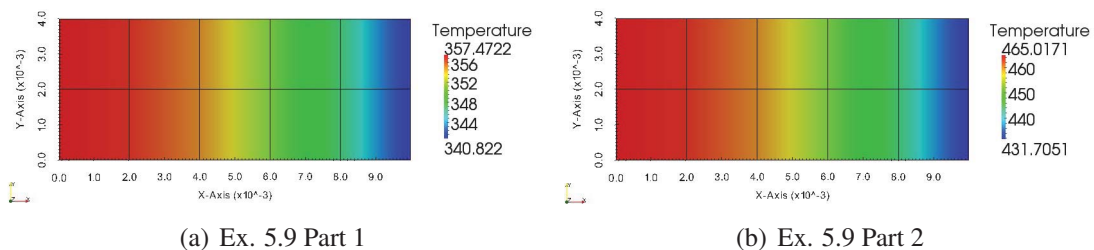


Figure A.3 Ex. 5.9 Part 1 & 2

Publication [P1]

Evolution strategies and multi-objective optimization of
permanent magnet motor

Applied Soft Computing
vol.12, pp.778-792, 2012



Evolution strategies and multi-objective optimization of permanent magnet motor

Søren B. Andersen, Ilmar F. Santos*

Department of Mechanical Engineering, Technical University of Denmark, 2800 Kgs. Lyngby, Denmark

ARTICLE INFO

Article history:

Received 10 May 2011

Received in revised form 9 September 2011

Accepted 18 October 2011

Available online 3 November 2011

Keywords:

Metaheuristic

Permanent magnet motor

Optimization

Evolution strategies

Multi objective optimization

ABSTRACT

When designing a permanent magnet motor, several geometry and material parameters are to be defined. This is not an easy task, as material properties and magnetic fields are highly non-linear and the design of a motor is therefore often an iterative process. From an engineering point of view, we usually want to maximize the efficiency of the motor and from an economic point of view we want to minimize the cost of the motor. As these two things seldom go hand in hand, the goal is to find the best efficiency per cost. The scope of this paper is therefore to investigate the applicability of evolution strategies, ES to effectively design and optimize parameters of permanent magnet motors. Single as well as multi-objective optimization procedures are carried out. A modified way of creating the strategy parameters for the ES algorithm is also proposed and has together with the standard ES algorithm undergone a comprehensive parameter study for the parameters ρ and λ . The results of this parameter study show a significant improvement in stability and speed with the use of the modified ES version. To find the most effective selector for a multi-objective optimization, MOO, of the motor a performance examination of 4 different selectors from the group of programs called PISA has been made and compared for MOO of the efficiency and cost of the motor. This performance examination showed that the indicator based evolutionary algorithm, IBEA, and hypervolume estimation algorithm, HypE, selectors performed almost equally good on this MOO problem where the HypE selector only had a slightly better performance indicator.

© 2011 Elsevier B.V. All rights reserved.

1. Introduction

Metaheuristics is used in combinatorial optimization in discrete and real search space by iteratively trying to improve the current best solution. There have been several proposed metaheuristic algorithms through time which can be used in optimization applications with some of the most commonly known being “hill climber”, “TABU” [1,2], “simulated annealing” [3], “ant colony optimization” [4], “genetic algorithm” [5], and “evolution strategies” [6], to name a few. Metaheuristics, however, does not guarantee that the optimal solutions are ever found but there is a good possibility that a near optimal solution will be determined. This paper gives a theoretical contribution to the application of metaheuristics in the optimization of a permanent magnet motor, more specifically with the use of evolution strategies, ES. Several other authors have used evolutionary algorithms in the quest for optimization of PM motors where [7] optimize the rotor of a PM motor using genetic algorithms and [8] optimize an in-wheel motor using ES. Both articles use FEM in greater or lesser extent where this article

will show the application of ES on analytical equations as FEA is very time consuming and therefore less suited for multi-objective optimization. ES has also been used by Chung and Kim [9] for the optimization of the pole shapes in a BLDC motor for reducing cogging torque where the present work will concentrate on a more global holistic approach. As one usually is not just interested in the optimization of one single parameter like [7–9] and a separate optimization of several parameters might not give a clear picture of the optimal combination of the parameters a multi-objective optimization has to be performed. No such multi-objective optimization based on the cost and efficiency of a PM motor has been found in the literature and is therefore investigated in this paper. The performance of 4 selectors is tested aiming at finding the one which is the most adequate for the problem of PM motor parameter optimization. Several authors also forget to mention in their works how the parameters for their algorithms have been chosen. In the present article, through an extensive parameter tuning, it will be shown that the parameter choice has a major impact on the final outcome like premature or slow convergence of the algorithms. The paper is divided into three main parts. The first part will describe the problem which has to be solved listing its object and fitness parameters. The second part will describe the algorithm of ES in detail and how its parameters have been tuned. This second

* Corresponding author. Tel.: +45 45256269.

E-mail address: ifs@mek.dtu.dk (I.F. Santos).

Nomenclature

p	number of pole pairs
θ	temperature rise in the machine windings [K]
Matr	core material
$\sigma_{F_{tan}}$	tangential stress [Pa]
δ	physical air-gap [m]
Q	number of stator slots
a	number of parallel branches in coil
J_s	stator current density [A/m]
η	efficiency of the PM motor
Cost	cost of materials
μ	number of parent individuals
ρ	number of individuals for reproduction
λ	number of offspring individuals
g	generation number
\mathfrak{P}_p	parent population
\mathbf{y}	object parameter vector
\mathbf{s}	strategy parameter vector
\mathbf{F}	fitness value vector
\mathcal{E}_i	marriage population
s_i	individual i 's strategy parameters
y_i	individual i 's object parameters
F_i	individual i 's fitness value
\mathfrak{P}_o	offspring population
$\tilde{\cdot}$	mutated parameter
\mathbf{a}	individual parameter vector
\mathbf{r}	recombinant
σ	standard deviation
\mathcal{N}	random number from the standard normal distribution
τ_0	learning factor
τ	learning factor
c	proportionality factor
σ^2	variance
α	angle between object vectors
η_{max}	maximum efficiency of PM motor

part will only concentrate on the maximization of a single fitness parameter namely the efficiency of the motor. The third part will describe how to solve a multi-objective optimization problem with conflicting goals by combining ES and PISA where PISA is a group of programs which can be used for solving such multi-objective search problems where the conflicting goals in this problem as explained are the efficiency and the cost of the motor. At the end of the second and third part the findings from the ES algorithm and the motor parameters will be presented and commented on.

2. Parameter optimization of permanent magnet motor

Without getting into the details of how the efficiency of motor is calculated a short description of the motor design will take place. The procedure and equations for the underlying calculations of the motor efficiency can be found in the appendix and follows the approach described in [10]. In Fig. 1 a cross-section of a 3-phase 10-poles PM motor with 12 stator slots is shown where each stator slot contains coils from one or two of the phases as the number of slots divided by the number of poles is a fraction (fractional winding). These coils in the slots can consist of several parallel strains of copper conductors and the size of the stator slots is among other parameters dependent on the allowable current density in the copper conductors. Permanent magnets are mounted around the shaft in such a way that the magnets are magnetized alternately in opposite directions as to create north and south poles. The air gap in the

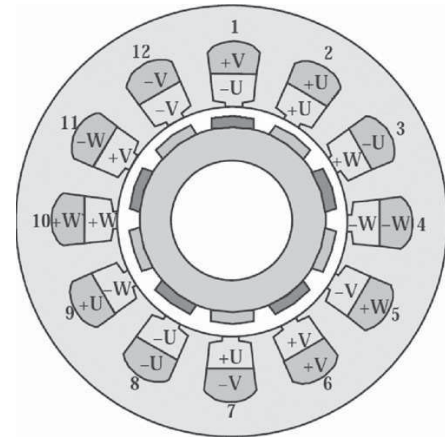


Fig. 1. Schematics of a PM motor [10].

Table 1
Object parameters.

Parameter	Valid range	Unit	Description
p	$[1-6] \in \mathbb{N}$	–	Number of pole pairs
θ	$[60-100] \in \mathbb{R}$	$^{\circ}\text{K}$	Temperature rise in the machine windings
Matr	$[1, 2, 3] \in \mathbb{N}$	–	Core material
$\sigma_{F_{tan}}$	$[20e3-50e3] \in \mathbb{R}$	Pa	Tangential stress
δ	$[0.001-0.020] \in \mathbb{R}$	m	Physical air-gap
Q	$[20-50] \in \mathbb{N}$	–	Number of stator slots
a	$[1-60] \in \mathbb{N}$	–	Number of parallel branches in coil
J_s	$[4e6-6.5e6] \in \mathbb{R}$	A/m	Stator current density

motor is the gap between the surface of the magnet and the stator inner diameter where this inner diameter is determined by the maximum allowable tangential stresses in the motor. As it would be a huge task to take all design parameters into account in this optimization analysis, some of the parameters have been fixed at reasonable values. Some of these fixed values are the shaft power, the speed of the motor, line to line voltage, number of phases and are normally determined by the customer of the motor and specified to match their needs. For getting a complete list of the fixed values we refer to the first table in Appendix. Table 1 shows the object parameters which will be used in this analysis and are the motor variables that can be changed in the search for an optimal design. Most of these parameters have already been explained except the temperature rise which has an influence on the resistance of the conductors and the choice of material which have different magnetic properties. The different parameters valid range come from the literature and “rules of thumb” [10–13]. The fitness values for this optimization problem are the efficiency and the cost of the motor and are kinds of grade explaining the goodness of a specific combination of object parameters. The fitness values are listed in Table 2. The fitness function \mathbf{F} is a function which in the following will be considered a black box and calculate the efficiency and cost of the motor as a function of the object parameters. The fitness function is basically all the equations listed in the appendix

Table 2
Fitness parameters.

Parameter	Description
η	Efficiency of the PM motor
Cost	Cost of materials

```

Procedure  $(\mu/\rho^+\lambda)$ -ES
1 Begin
2    $g = 0$ 
3   initialize  $(\mathfrak{P}_p^{(0)} = \{(\mathbf{y}_m^{(0)}, \mathbf{s}_m^{(0)}, \mathbf{F}(\mathbf{y}_m^{(0)})), m = 1, \dots, \mu\})$ 
4   Repeat
5     For  $i = 1$  to  $\lambda$ 
6        $\mathfrak{E}_i = \text{marriage}(\mathfrak{P}_p^{(g)}, \rho)$ 
7        $s_i = \text{srecombination}(\mathfrak{E}_i)$ 
8        $y_i = \text{yrecombination}(\mathfrak{E}_i)$ 
9        $\tilde{s}_i = \text{smutation}(s_i)$ 
10       $\tilde{y}_i = \text{ymutation}(y_i, \tilde{s}_i)$ 
11       $\tilde{y}_i = \text{repair}_{\text{discrete}}(\tilde{y}_i)$ 
12       $\tilde{F}_i = F(\tilde{y}_i)$ 
13    End
14     $\mathfrak{P}_o^{(g)} = \{(\tilde{y}_i, \tilde{s}_i, \tilde{F}_i), i = 1, \dots, \lambda\}$ 
15    Case Selection type of
16       $(\mu, \lambda) : \mathfrak{P}_p^{(g+1)} = \text{selection}(\mathfrak{P}_o^{(g)}, \mu)$ 
17       $(\mu + \lambda) : \mathfrak{P}_p^{(g+1)} = \text{selection}(\mathfrak{P}_o^{(g)}, \mathfrak{P}_p^{(g)}, \mu)$ 
18    End
19     $g = g + 1$ 
20  Until Termination condition
21 End

```

Fig. 2. General pseudo code of $(\mu/\rho^+\lambda)$ -ES.

which are being used for the calculation of the efficiency and cost of the motor.

3. Evolution strategies

Evolution strategies, ES, were first proposed by Rechenberg and Schwefel in the mid-1960s for numerical optimization. It has since evolved from a simple (1+1) evolution strategy to a more complex $(\mu/\rho^+\lambda)$ with more complex internal routines. One of the benefits of ES is that it is extremely easy to run on parallel computers to decrease the time it takes to evaluate the population of individuals. The following sections explain the $(\mu/\rho^+\lambda)$ -ES which will be used in this paper for optimizing the efficiency of the described PM motor. In a later section the multi-objective optimizing, where we also will look at the cost will be explained but initially we will only look at the efficiency.

3.1. General algorithm of evolution strategies

In Fig. 2 a general pseudo code for evolution strategies (ES) is shown. This section will briefly explain each line of the code and the following sections will give a more thorough explanation of the different part of the ES algorithm. At line #2 the generation counter is initialized for generation zero. At line #3 the initial population is created which consists of μ individuals \mathbf{a}_m each consisting of an object vector \mathbf{y}_m , a strategy vector \mathbf{s}_m and a fitness vector $\mathbf{F}(\mathbf{y}_m)$. $\mathbf{a}_m = (\mathbf{y}_m, \mathbf{s}_m, \mathbf{F}(\mathbf{y}_m))$. Lines #4–20 is the main loop of the algorithm which runs continuously until termination condition is reached in our case until we run out of the allocated time for solving the problem. Lines #5–13 is the loop which generates offspring individuals

who might enter the next generation of parents. The loop will run λ times for each generation producing λ new offspring. At line #6 the marriage procedure is executed which pick ρ individuals from the parent population for reproduction of offspring. Lines #7 and #8 recombine the object and strategy parameters of the ρ parents to form one new offspring individual. At lines #9 and #10 the strategy and object parameters of the newly formed offspring individual is mutated. At line #11 the object parameters are corrected for the discrete space variables. Finally at line #12 the new offspring individual is completed by the addition of its fitness value. Line #14 collects the offspring created to form the offspring population. At lines #15–18 the selection procedure is performed. There are two standard types of selection, a “,” and a “+” selection. This selection procedure decides which of the offspring individuals gets to enter the new parent population of the next generation if any at all. Finally at line #19 the generations counter increases by one and then jumps to line #5 if the termination condition, as said before, has not been reached.

3.2. Marriage

In contrast to evolutionary algorithm with an elitist approach where the marriage process is made by choosing the best individuals of the parent population for reproduction, the marriage process in Evolution Strategies is made by selecting ρ individuals completely random from the parent population. As this does not improve the solution by itself it is obvious that this part of the algorithm is not the main driving force in evolution strategies.

The marriage process is the first part of the algorithm which is performed in the main loop, line 6 in Fig. 2.

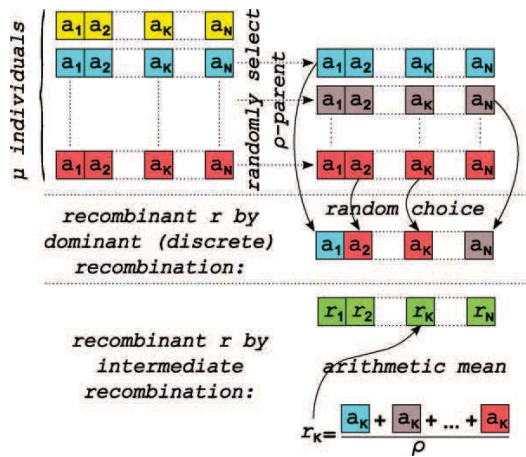


Fig. 3. Standard μ/ρ recombination.

3.3. Recombination

The idea behind recombination is when parents with good genetic material are combined they will also generate offspring with good genetic material. According to [6] there is still an ongoing debate about the usefulness of recombination, however recombination of the strategy parameters has been shown to be mandatory for this mechanism to work according to [14]. Due to this fact, the recombination will be performed on both the object and strategy parameters. A special case of the recombination is when $\rho = 1$ as the individual will be recombined with itself. In other words an exact copy of the individual and so in this case the recombination routine can be skipped.

There are two standard methods of recombination:

- Discrete recombination.
- Intermediate recombination.

According to [14–16] it has been shown that good results have been achieved when using intermediate recombination on strategy parameters and discrete recombination on object variables. We will follow that advice.

3.3.1. Recombination of strategy parameter

As mentioned above intermediate recombination has proved to give a good result when applied to the strategy parameters which is a parameter used to determine the size of the mutation of the object parameters. The vector with the strategy parameters are initially set as the normal standard deviation for each object parameter of the initial population of solutions. The intermediate recombination of the strategy parameters is performed first by randomly selecting ρ parents from the entire population of μ individuals which is performed by the “marriage” routine as described previously. It then calculates the centre of mass of the ρ selected parent vectors $\mathbf{a}_m = (a_{m,1}, \dots, a_{m,N})$ for each strategy parameter as written in Eq. (1) and depicted at the bottom in Fig. 3.

$$\mathbf{r}_k := \frac{1}{\rho} \sum_{m=1}^{\rho} \mathbf{a}_{m,k} \quad (1)$$

The recombination of the strategy parameters can be performed before or after the recombination of the object parameters. In the pseudo code in Fig. 2 it is placed before the recombination of the object parameters at line 7.

3.3.2. Recombination of object parameter

As mentioned above discrete recombination, also called dominant recombination, has proved to give a good result when applied to the object variables. The discrete recombination is performed first by randomly selecting ρ parents from the entire population of μ individuals which again is performed by the “marriage” routine. The routine then randomly selects the object parameters from the ρ individuals for each object parameter until a complete new individual is created. This is written in Eq. (2) and depicted at the top of Fig. 3.

$$\mathbf{r}_k := (\mathbf{a}_{m_k})_k, \quad m_k := \text{Random}\{1, \dots, \rho\} \quad (2)$$

The recombination of the object parameters is performed at line 8 in Fig. 2 but as mentioned before it can also be performed before recombination of the strategy parameters.

If for some reason the intermediate recombination was chosen on the object parameters instead of discrete recombination one should remember that this routine creates values in real space. A correction of the parameters has then to be performed if some or all of the parameters are in discrete space. This correction could be a simple rounding of the parameter values.

3.4. Mutation

Mutation of the object and strategy parameters takes place at lines 9 and 10 in Fig. 2 and is usually the primary source of generic variation. There is currently (2002) no design methodology for the mutation operators but some rules have been proposed by Beyer.

- Reachability.
- Unbiasedness.
- Scalability.

Reachability: It should be possible from a random state to reach any other state within a finite number of mutations or generations.

Unbiasedness: The variation operators should only explore the information of the object space and not use any information about the individuals’ fitness values. Thereby no individual is preferred over another. This leads, in a natural manner, to the principle of maximum entropy and the standard normal distribution.

Scalability: The mutation strength should be tunable to be able to adapt to the properties of the fitness landscape.

3.4.1. Mutation of object parameter

Schwefel and Beyer [6] propose a standard mutation operator for mutating the object parameters in a real valued search space which reads:

Given a vector $\mathbf{s} = \sigma = (\sigma_1, \dots, \sigma_N)$ as the strategy parameter the principle of maximum entropy yields:

$$\tilde{\mathbf{y}} := \mathbf{y} + \mathbf{z} \quad (3)$$

with

$$\mathbf{z} := (\sigma_1 \cdot \mathcal{N}_1(0, 1), \dots, \sigma_N \cdot \mathcal{N}_N(0, 1)) \quad (4)$$

where $\mathcal{N}_i(0, 1)$ is a random number from the standard normal distribution.

3.4.2. Mutation of strategy parameter

For mutating the strategy parameters $\mathbf{s} = \sigma = (\sigma_1, \dots, \sigma_N)$ in Eq. (5) Schwefel suggest using an extended log-normal rule which reads:

$$\tilde{\sigma} := \exp(\tau_0 \cdot \mathcal{N}(0, 1)) \cdot (\sigma_1 \cdot \exp(\tau \cdot \mathcal{N}_1(0, 1)), \dots, \sigma_N \cdot \exp(\tau \cdot \mathcal{N}_N(0, 1))) \quad (5)$$

with

$$\tau_0 = \frac{c}{\sqrt{2N}} \tag{6}$$

$$\tau = \frac{c}{\sqrt{2\sqrt{N}}} \tag{7}$$

where $\mathcal{N}_i(0, 1)$ is a random number from the standard normal distribution and c is a proportionality factor for the learning factors τ_0 and τ .

3.5. Repair

As the above described procedure produces real value object parameters there has to be introduced an extra procedure when working with discrete parameters or a mixture of discrete and real value parameters. This procedure is inserted just before the evaluation by the fitness function at line 11 in Fig. 2. The procedure consists of a simple rounding of the real value to an integer at instances where the parameter is in discrete space.

Furthermore this repair procedure makes sure that the object parameters do not exceed their predefined upper and lower boundaries by moving values outside back onto the boundaries they exceeded. This is not a standard routine in ES but it has to be introduced in this case as the object parameter values is a mixture of real and integer values.

3.6. Selection

The selection routine is the routine which drives the population to better regions by use of the individuals' fitness information. There are two standard types of selection methods in ES which is denoted $(\mu|\rho, \lambda)$ and $(\mu|\rho+\lambda)$. The “-”-sign and the “+”-sign in the notation tells something about how the selection pool for selecting the next generation parent population is created. In the “-” notation the selection pool is made up of only the λ offspring individuals and the current parent population is discarded even in the case of that population containing better solutions. This selection method of course requires that $\lambda > \mu$ as we want to keep a constant size of the parent population. In the “+” notation the selecting pool is made up of both the λ offspring and the μ parents of the current generation.

The actual selection is done simply by selection the μ individuals with the highest fitness value (maximizing) from the selection pool to form the next generation parent population and discarding the remaining solutions. The selection is performed just after the offspring has been created, line 16 for the “-” selection and line 17 for the “+” selection in Fig. 2.

Both types of selection method have their advantages in specific applications. According to [6] the “-” selection performs well on unbounded \mathbb{R}^N search spaces where the “+” selection should be chosen in the case of finite search space. As the problem at hand is defined in finite search space the “+” selection has been chosen as the selection method for this problem.

3.7. Parameter tuning

The ES algorithm explained above consists of the endogenous and exogenous parameters listed in Table 3 below. The exogenous parameters are parameters which remain constant throughout the entire run of the algorithm and are μ, ρ, λ and c . The endogenous parameters are parameters which continuously change and try to adapt to the current situation. These parameters are the standard deviations (mutation strength) \mathbf{s} .

Two different versions of the above mentioned ES algorithm have been tested and will in the following be referred to as ES1 and ES2. Both of these versions have been initiated by randomly

Table 3
Endogenous and exogenous parameters.

Parameter	Description
μ	Size of the parent population
ρ	No. of parents involved in the procreation of one offspring
λ	Size of offspring population
$\mathbf{s} = \sigma = (\sigma_1, \dots, \sigma_N)$	Mutation strength
c	Constant for the learning parameters τ and τ_0

creating μ individuals each consisting of a vector of object parameters with values within the boundaries defined in Table 1. In the ES1 version, which is the standard ES algorithm, the initial vector with strategy parameters is set by calculating the normal standard deviation for each object parameter of the initial population. These strategy parameters follow each individual throughout the entire algorithm and are only changed in the offspring individual through recombination and mutation. In the ES2 version the strategy parameters are continuously being overwritten as the strategy parameters are set by calculating the normal standard deviation for each object parameter of the current generation of the marriage population. The ES2 algorithm is part of the original contribution and is not a standard ES algorithm, however, it will be shown that it performs very well on the problem at hand.

As parameter tuning of all the parameters in Table 3 is a very time consuming task some of these have been fixed. These fixed parameters are μ and c . μ has been set to 20 to have some diversity in the initial population without having a huge population size. The constant c for the learning factors τ and τ_0 have been set to 1 as suggested in [14]. That leaves us with ρ and λ as the tuning parameters. Table 4 shows the tested values of ρ and λ . Each of the tests have been run 10 times for both ES1 and ES2 and a summary of the results from these tests can be seen in Table 5 for the ES1 version and Table 6 for the ES2 version. The 1st column shows the test parameters. The 2nd, 3rd and 4th column show the mean, max and min of the sum of the variances of the normalized object parameters. The 5th column shows the variance of the fitness values. The 6th, 7th and 8th columns show the max, min and mean of the fitness values. The 9th column shows the number of runs that have reached an efficiency of 97.21% which through test with several other algorithms (Hill climber, TABU) has shown with a high probability to be very close to the highest obtainable efficiency. The 10th column shows the percentage of generated invalid solutions which mainly are due to generation of solutions with the requirement that the magnet thickness is larger than the rotor radius. The 11th column show the mean number of generation reached within the arbitrary decided 1.5 min which was allocated for each run of the algorithm. The next section will comment on these results and show more specific results from the tuned algorithms.

3.8. Results and discussion

This section will comment on the test results presented in the previous section and show some results from the two tuned

Table 4
Test parameters.

	$\lambda = 1$	$\lambda = 2$	$\lambda = 5$	$\lambda = 10$	$\lambda = 20$
$\rho = 1$	20/1+1	20/1+2	20/1+5	20/1+10	20/1+20
$\rho = 2$	20/2+1	20/2+2	20/2+5	20/2+10	20/2+20
$\rho = 5$	20/5+1	20/5+2	20/5+5	20/5+10	20/5+20
$\rho = 10$	20/10+1	20/10+2	20/10+5	20/10+10	20/10+20
$\rho = 20$	20/20+1	20/20+2	20/20+5	20/20+10	20/20+20

Table 5
Parameter tuning of ES1.

$(\mu/\rho+\lambda)$	Mean $\left(\frac{\sum(s)}{N}\right)$	Max $\left(\frac{\sum(s)}{N}\right)$	Min $\left(\frac{\sum(s)}{N}\right)$	σ^2 of sol.	Max (sol.)	Min (sol.)	Mean (sol.)	No. of opt. sol.	Still born %	Mean no. of gen.
(20/1+1)	0.062	0.145	0.004	3.24e-004	97.2162	97.1516	97.2041	3 of 10	37.6	1411
(20/1+2)	0.042	0.121	0.001	1.87e-005	97.2180	97.2072	97.2128	6 of 10	29.6	760
(20/1+5)	0.036	0.146	0.000	1.81e-004	97.2180	97.1700	97.2074	4 of 10	29.7	306
(20/1+10)	0.019	0.052	0.001	5.47e-004	97.2179	97.1448	97.1990	3 of 10	36.8	147
(20/1+20)	0.044	0.132	0.002	4.50e-004	97.2181	97.1414	97.2040	3 of 10	33.7	75
(20/2+1)	0.044	0.106	0.003	4.11e-004	97.2178	97.1459	97.2050	4 of 10	40.0	1464
(20/2+2)	0.051	0.110	0.001	1.61e-005	97.2180	97.2086	97.2139	7 of 10	35.8	781
(20/2+5)	0.062	0.167	0.006	4.27e-005	97.2180	97.1969	97.2108	5 of 10	36.5	300
(20/2+10)	0.057	0.104	0.031	2.44e-005	97.2180	97.2058	97.2123	5 of 10	44.5	156
(20/2+20)	0.055	0.124	0.007	2.00e-005	97.2181	97.2072	97.2122	5 of 10	37.9	76
(20/5+1)	0.067	0.118	0.028	1.46e-005	97.2176	97.2071	97.2126	6 of 10	40.3	1438
(20/5+2)	0.067	0.107	0.045	1.61e-005	97.2180	97.2067	97.2145	8 of 10	37.6	751
(20/5+5)	0.050	0.091	0.003	1.55e-005	97.2172	97.2069	97.2106	3 of 10	34.7	304
(20/5+10)	0.082	0.100	0.005	1.87e-005	97.2179	97.2066	97.2121	5 of 10	42.0	159
(20/5+20)	0.074	0.127	0.044	2.11e-005	97.2180	97.2070	97.2133	6 of 10	44.2	75
(20/10+1)	0.093	0.119	0.054	1.68e-005	97.2178	97.2071	97.2108	4 of 10	46.2	1405
(20/10+2)	0.094	0.118	0.070	1.97e-005	97.2179	97.2064	97.2110	4 of 10	44.9	673
(20/10+5)	0.105	0.115	0.068	5.18e-006	97.2174	97.2087	97.2145	9 of 10	45.3	281
(20/10+10)	0.101	0.135	0.075	1.71e-005	97.2173	97.2068	97.2117	5 of 10	45.4	143
(20/10+20)	0.114	0.141	0.081	1.02e-005	97.2164	97.2070	97.2098	2 of 10	47.6	72
(20/20+1)	0.115	0.148	0.098	1.80e-005	97.2177	97.2070	97.2102	3 of 10	44.4	1290
(20/20+2)	0.123	0.188	0.099	1.85e-005	97.2179	97.2053	97.2098	3 of 10	44.9	621
(20/20+5)	0.125	0.165	0.101	2.42e-005	97.2165	97.2011	97.2093	3 of 10	49.1	243
(20/20+10)	0.128	0.175	0.101	1.42e-005	97.2176	97.2056	97.2098	3 of 10	46.3	133
(20/20+20)	0.130	0.156	0.080	3.10e-005	97.2157	97.1973	97.2084	4 of 10	46.0	63

algorithms. The two Tables 5 and 6 show a lot of statistical information. The most important for the evaluation of the algorithm are the mean of the standard deviation (column 2) which is a measurement of the convergence of the entire population together with the gap between max (column 6) and min (column 7) fitness values and the number of fitness values which have reached the limit for a near optimal fitness value (column 9).

Looking at Table 5 for the ES1 algorithm it can be seen that there is one algorithm which separate itself from the other algorithms

by achieving the limit for the near optimal fitness values 9 out of 10 times. This algorithm is the (20/10+5). It also has the highest minimum fitness value. The mean of the standard deviation is not the lowest in the test which means that the algorithm has not fully converged, but as the high success rate and high fitness value are very important in this optimization problem it is still determined to be the most efficient one.

Figs. 4–6 show plots from one of the test runs of the (20/10+5)-ES1. Fig. 4 shows the highest efficiency as a function of the

Table 6
Parameter tuning of ES2.

$(\mu/\rho+\lambda)$	Mean $\left(\frac{\sum(s)}{N}\right)$	Max $\left(\frac{\sum(s)}{N}\right)$	Min $\left(\frac{\sum(s)}{N}\right)$	σ^2 of sol.	Max (sol.)	Min (sol.)	Mean (sol.)	No. of opt. sol.	Still born %	Mean no. of gen.
(20/1+1)	0.000	0.000	0.000	1.59e-002	97.0396	96.6144	96.8099	0 of 10	0.0	1712
(20/1+2)	0.000	0.000	0.000	1.85e-002	96.9310	96.4084	96.7152	0 of 10	0.0	932
(20/1+5)	0.000	0.000	0.000	8.76e-003	97.0765	96.7403	96.8684	0 of 10	0.0	389
(20/1+10)	0.000	0.000	0.000	1.99e-002	96.9992	96.6046	96.7676	0 of 10	0.0	191
(20/1+20)	0.000	0.000	0.000	3.33e-002	97.0294	96.5062	96.7679	0 of 10	0.0	99
(20/2+1)	0.000	0.000	0.000	9.95e-003	97.1022	96.7199	96.9244	0 of 10	0.1	1827
(20/2+2)	0.000	0.000	0.000	1.64e-002	97.1364	96.6333	96.9039	0 of 10	0.1	954
(20/2+5)	0.000	0.000	0.000	1.36e-002	97.1802	96.8045	96.9750	0 of 10	0.4	383
(20/2+10)	0.000	0.000	0.000	1.30e-002	97.1376	96.7453	97.0142	0 of 10	0.6	194
(20/2+20)	0.000	0.000	0.000	1.21e-002	97.2029	96.8259	97.0217	0 of 10	1.1	95
(20/5+1)	0.000	0.001	0.000	1.00e-002	97.2180	96.9193	97.1255	3 of 10	0.8	1742
(20/5+2)	0.000	0.002	0.000	3.28e-003	97.2181	97.0367	97.1768	3 of 10	1.9	863
(20/5+5)	0.000	0.001	0.000	3.32e-003	97.2173	97.0586	97.1852	6 of 10	1.4	369
(20/5+10)	0.001	0.004	0.000	5.34e-003	97.2181	97.0071	97.1771	4 of 10	1.8	179
(20/5+20)	0.001	0.005	0.000	2.28e-003	97.2181	97.0570	97.1957	7 of 10	2.6	90
(20/10+1)	0.001	0.003	0.000	2.18e-003	97.2181	97.0570	97.1964	5 of 10	2.7	1630
(20/10+2)	0.002	0.003	0.000	1.05e-005	97.2181	97.2070	97.2164	9 of 10	3.4	829
(20/10+5)	0.002	0.003	0.000	2.22e-003	97.2181	97.0589	97.1998	7 of 10	2.9	327
(20/10+10)	0.002	0.006	0.000	2.26e-003	97.2181	97.0589	97.2011	8 of 10	3.8	167
(20/10+20)	0.002	0.003	0.000	8.09e-006	97.2181	97.2086	97.2171	9 of 10	5.0	83
(20/20+1)	0.003	0.003	0.001	1.08e-016	97.2181	97.2181	97.2181	10 of 10	6.6	1420
(20/20+2)	0.004	0.012	0.002	2.28e-003	97.2181	97.0589	97.2022	9 of 10	7.4	715
(20/20+5)	0.002	0.003	0.002	1.09e-016	97.2181	97.2181	97.2181	10 of 10	7.8	297
(20/20+10)	0.002	0.003	0.001	2.25e-014	97.2181	97.2181	97.2181	10 of 10	8.8	150
(20/20+20)	0.002	0.004	0.001	1.53e-013	97.2181	97.2181	97.2181	10 of 10	9.1	75

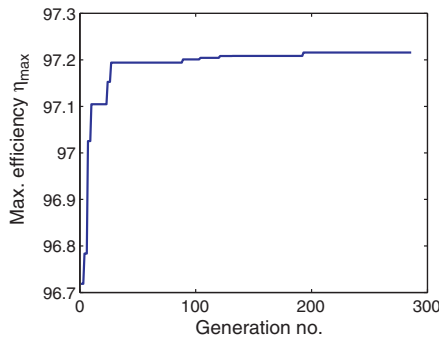


Fig. 4. Efficiency plot of (20/10+5)-ES1.

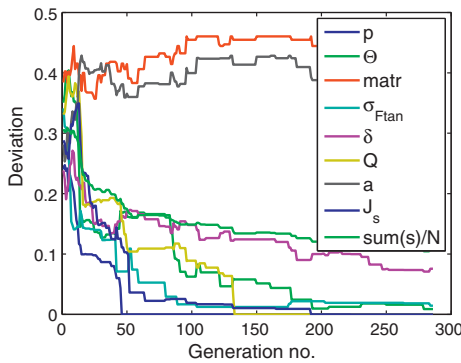


Fig. 5. Normalized standard deviation of a (20/10+5)-ES1.

generation number and it can be seen that it initially converges fast toward higher efficiencies and slows down as it approach the assumed optimal solution of 97.21% as was expected. This convergence tendency can also be seen in the plot of the normalized standard deviation of the 8 object parameters together with the mean sum, Fig. 5. However it is not possible to infer from this plot if the optimal solution is being achieved or just a local maximum. It has therefore to be viewed together with Fig. 4 and the knowledge of the assumed optimal efficiency. Furthermore it is also obvious from the plot in Fig. 5 that not all the object parameters of the population have converged where the most severe ones in this case is the material and the number of parallel branches in the coil which remain almost randomly distributed throughout the entire number of generations. The other object parameters in the population are getting more and more similar as the number of generation

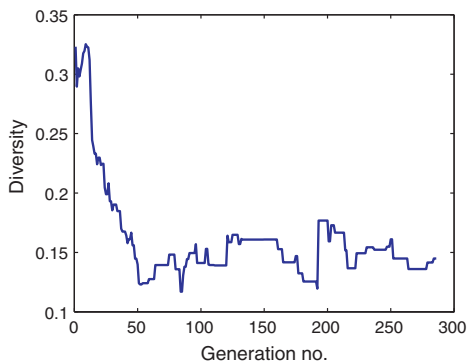


Fig. 6. Diversity of a (20/10+5)-ES1.

Table 7

Best motor design object and fitness parameters.

Parameter	Value ES-1	Value ES-2	Unit	Description
p	2	2	–	Number of pole pairs
Θ	60	60	K	Temperature rise in the windings
Material	3	2	–	Core materials, 1, 2, 3 (see Appendix)
σ_{Ftan}	50,000	48,563	Pa	Tangential stress
δ	7.4199	7.6529	mm	Physical air-gap
Q	20	20	–	Number of stator slots
a	1	1	–	Number of parallel branches in coil
J_s	4,000,000	4,000,000	A/m ²	Stator current density
η	97.2157	97.2181	%	Efficiency

increase even though it is very slowly moving forward. Another indicator for the convergence is the one shown in Fig. 6. It shows the comparison of the angle between the current best object vector and the remaining object vectors calculated by Eq. (8).

$$\cos(\alpha) = \left(\frac{\mathbf{y}_i \cdot \mathbf{y}_j}{\|\mathbf{y}_i\| \cdot \|\mathbf{y}_j\|} \right) \tag{8}$$

This value tells something about how similar the solutions in the population are to the current best solution. The reason for introducing this second convergence indicator is to make sure that the current best solution is not just a stroke of luck as this indicator will have a high value if the current best solution differs markedly from the rest even if the rest of the solutions are similar and the standard deviation is low.

As the algorithm has not fully converged there could be several combinations of object parameters which will have the same fitness value. It can therefore be difficult to choose one solution over another while at the same time knowing with a high probability that it is not the optimal solution. Even though this is the case the parameters of the solution with the highest fitness value from the same test as the one in the plot are shown in Tables 7 and 8 and the geometry is depicted in Figs. 10 and 11. Before commenting on these results we will take a closer look at the results from the ES2 algorithm.

Looking at Table 6 for the ES2 algorithm the most striking difference from the ES1 tests is the extremely low standard deviation in column 2 which means that all the solutions in the population have converged to the same solution. As can be seen this is not the only indicator of an optimal algorithm as one can see that many of the solutions have converged prematurely and found efficiencies below the assumed optimal efficiency. However several of the algorithms performed very well as they reached the success limit of 97.21% for the fitness values 10 out of 10 times and the maximum and minimum fitness values are the same. As it is only marginal's that separate the best ES2 algorithms from each other it has been decided to take a closer look at the (20/20+5)-ES2.

Figs. 7–9 show plots from one of the test runs of the (20/20+5)-ES2. Fig. 7 shows the efficiency as a function of the generation

Table 8

Best motor design dimensions. h_{PM} : magnet height, l : motor length.

Parameter	Value ES-1	Value ES-2	Parameter	Value ES-1	Value ES-2
h_1	0.001	0.001	b_4	0.0172	0.0172
h_2	0.002	0.002	b_{4c}	0.0178	0.0178
h_3	0.005	0.005	b_{5c}	0.0294	0.0294
h_4	0.0517	0.0517	D_r	0.24	0.24
h_5	0.037	0.037	D_{ri}	0.0666	0.0636
h_6	0.0005	0.0005	D_{ryi}	0.1836	0.1811
h_{PM}	0.0281	0.0294	D_s	0.2548	0.2553
h'	0.0005	0.0005	D_{se}	0.4923	0.4932
b_1	0.003	0.003	l	0.1184	0.1180

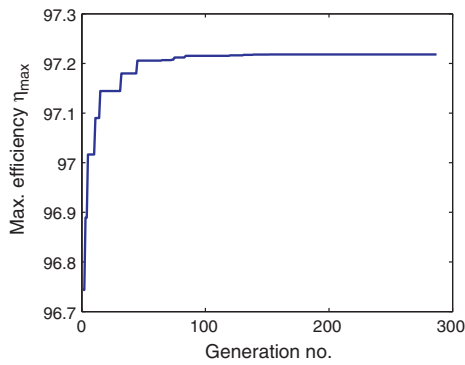


Fig. 7. Efficiency plot of (20/20+5)-ES2.

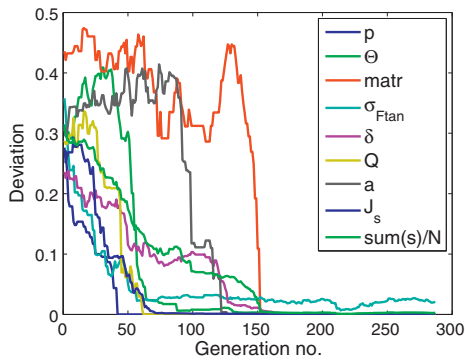


Fig. 8. Normalized standard deviation of a (20/20+5)-ES2.

number and it can be seen that the improvement in efficiency decreases as the optimum is approached as expected. If we look at Fig. 8 we can see in contrast to the ES1 algorithm that almost all of the object parameters have converged to the same value after only half of the time allocated for the test run and there are only a small fluctuation in the parameter for the tangential stress. A further indication of the convergences can be seen in Fig. 9 which again is a comparison of the angles between the object vectors and are almost zero after 150 generations which means that all solutions are basically the same.

As the algorithm has fully converged there is basically only one combination of object parameters as all the solutions in the population are the same and it is therefore very easy to get the parameters for the optimal design. Table 7 shows the found optimal object

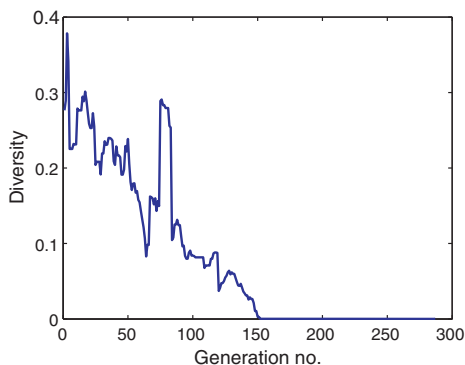


Fig. 9. Diversity of a (20/20+5)-ES2.

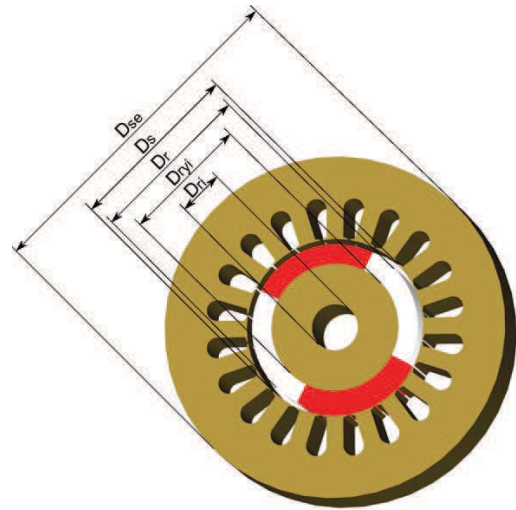


Fig. 10. Best motor design (20/10+5-ES1).

parameters and Table 8 shows the motor dimensions for the shown test run.

Comparing the parameters for the two motor designs Tables 7 and 8 it can be seen that even though the ES1 algorithm did not completely converge the parameters for the two designs are almost identical. The most significant difference is the choice of material where the ES1 and ES2 algorithm respectively has found materials 3 and 2 as the optimal material. This however corresponds well with the findings in Fig. 5 where it can be seen that the material parameter was one of the parameters which did not converge within the time frame set forth. An indication that this could be the motor

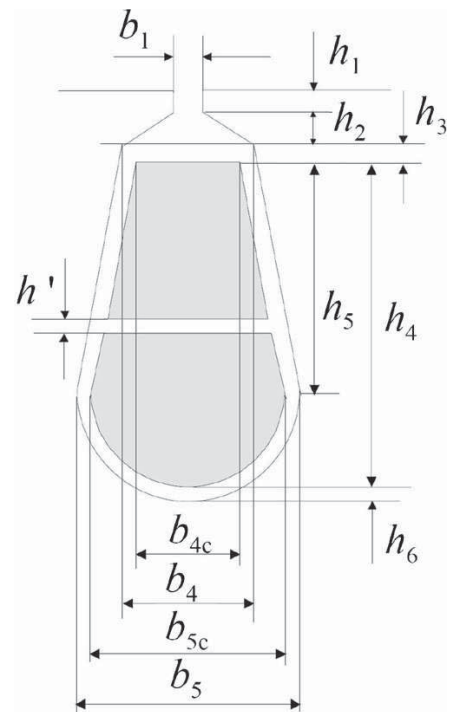


Fig. 11. Slot geometry [10].

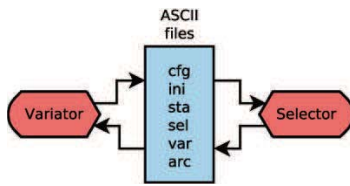


Fig. 12. PISA structure.

design with the highest efficiency is that the current density in both cases is found to the lowest allowed value and thereby the resistive losses in the coils are minimized.

If we compare the two algorithm versions ES1 and ES2 there is no doubt that the ES2 version perform much better on the problem at hand than the ES1 version as it achieves a near optimal solution every time with a very low standard deviation. In other words, the ES2 algorithm is very stable and produces good results every time. For this reason the (20/20+5) ES2 algorithm is the one which has been used in the multi-objective optimization problem which will be described in the next section.

4. Multi-objective optimization using ES and PISA

This section will explain how the multi-objective problem defined in the beginning of this paper (Section 2) has been solved. Furthermore several different algorithms will be compared to examine which one performs best on the problem at hand. For solving this multi-objective optimization problem the previously described ES2 algorithm has been used in conjunction with a free software package called PISA. PISA is a group of programs for solving multi-objective search problems with conflicting goals and is developed and maintained at ETH TIK Zürich, Switzerland.

4.1. PISA structure

The PISA structure operates with two main algorithms. One is called the variator and the other called the selector. These two algorithms run parallel with each other and communicate through ASCII files as symbolized in Fig. 12. The variator is the algorithm that is creating new offspring and calculates their respective fitness values. The fitness value together with an individual id number is then passed to the selector through the ASCII files. The selector then selects which of the individuals has to form the new parent population solely based on the evaluation of their fitness values. The id's of these individuals are then sent back to the variator. The variator then generates new offspring and their fitness values are again sent back to the selector. This ping pong between the variator and selector continues until some stopping criteria have been met. This could be time or number of generation. There are 6 common communication files which are used in the PISA structure for communication between the variator and selector:

- *CFG*: config file containing the size of the problem, μ , ρ , λ and dimension.
- *INI*: file with the initial population fitness values and id's written by the variator.
- *STA*: status file which is used to synchronize the variator and selector.
- *SEL*: file with the next parent population id's written by the selector.
- *VAR*: file with new offsprings fitness values and id's written by the variator.
- *ARC*: archive file with solutions.

For further information on the PISA structure visit their homepage¹ or see [17].

4.1.1. Variator

As explained above the variator is the algorithm in charge of generating new offspring through variation of selected individuals. In this case it is a modified version of the (20/20+5)-ES2 algorithm tuned in Section 3.7. Two modifications have been made to the algorithm. The first is that it has been set up to communicate with the selector through the previously described communication files and the previously used selector has been removed. Secondly there has been added an extra fitness parameter namely the cost. The cost of the motor is simply calculated by determining the mass of the different materials used for a specific solution which is multiplied by a fictive price/mass for the different materials used (magnets, copper and iron). For the sake of reproducibility the used fictive prices/mass is: magnets: 20 \$/kg, iron: 5 \$/kg and copper: 20 \$/kg where the mass of the iron is calculated for a square plate which edges is equal to the diameter of the stator thereby including the scrap material in the price calculation.

4.1.2. Selector

Without getting into the theory behind the selectors the following four different selectors have been chosen for comparison. The parameters for the different selectors have not been changed from their initial values and can maybe be altered to improve their performance, but this is out of the scope of this paper.

- SPAM: set preference algorithm for multi-objective optimization [18].
- SEMO2: simple evolutionary multi-objective optimizer [19].
- IBEA: indicator based evolutionary algorithm [20].
- HypE: hypervolume estimation algorithm for multi-objective optimization [21].

The general function of the selector is that it selects promising individuals from the population which through variation is expected to create new individuals which are able to find the Pareto front. What is a Pareto front? A solution is called Pareto optimal when it is not possible to improve one objective without deteriorating at least one of the others. A set of Pareto optimal solutions constitute the Pareto front. The goal in multi-objective optimization is therefore to find this Pareto front, sometimes also called the Pareto frontier.

4.2. Result and discussion

Before commenting on any of the results a performance indicator has to be defined to be able to compare the different algorithms. This indicator is based on the idea of the Hypervolume indicator [22,23] and is defined as the area between an efficiency of 96% and the Pareto front (see the hatched area of Fig. 13). The reason for not calculating the area from the entire Pareto front is that even though some of the algorithms are better at finding the Pareto front for low values of the efficiency these are not very interesting as no one is interested in this trade-off between cost and efficiency.

The next four Figs. 14–17 show plots of all the individuals of a 5000 generation (20/20+5)-ES2 algorithm for the four different selectors. The found Pareto front has been added to each plot by a solid line connecting the Pareto optimal solutions.

¹ <http://www.tik.ee.ethz.ch/pisa/>.

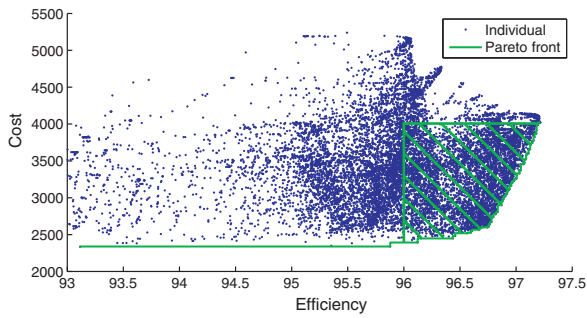


Fig. 13. Area as a performance indicator.

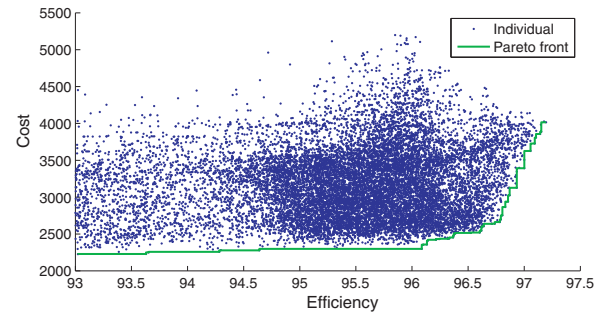


Fig. 16. Pareto front plot with all individuals – variator: 20/20+5-ES2, selector: SPAM, 5000 generations, elapsed time: 5308 s, area: 1422.

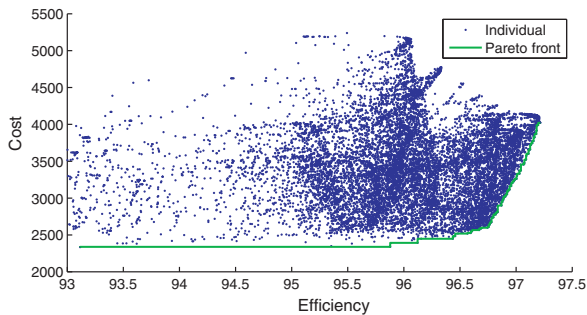


Fig. 14. Pareto front plot with all individuals – variator: 20/20+5-ES2, Selector: HYPE, 5000 generations, elapsed time: 4667 s, area: 1598.

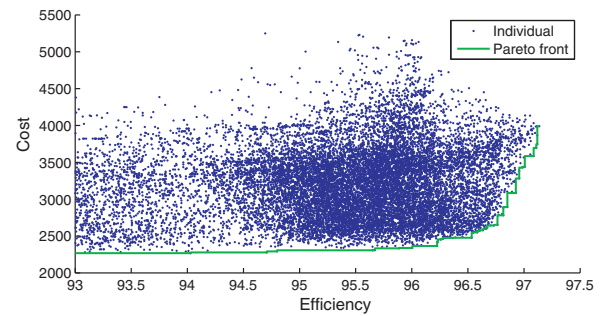


Fig. 17. Pareto front plot with all individuals – variator: 20/20+5-ES2, selector: SEMO2, 5000 generations, elapsed time: 5891 s, area: 1431.

First, looking at Fig. 14 it can be seen that the Pareto front has been found nicely with a high population density at high efficiencies. The algorithm with the HypE selector has been less aggressive at the lowest efficiencies where one loses a lot of efficiency if the cost is reduced just a bit. As mentioned before this area is of less importance as no one is willing to make this sacrifice of the efficiency just to reduce the price a little bit.

Looking at Fig. 15 we again see that there is a nice density of the population close to the Pareto front at high efficiencies. Like as for the algorithm with the HypE selector the algorithm with the IBEA selector is less aggressive at the low efficiencies but we come to the same conclusions as before that this area is of less importance. It has been examined that both the algorithm with the HypE and IBEA selector have found the solution with the highest possible efficiency which is a good indicator that we really have found the Pareto front at least for high efficiencies.

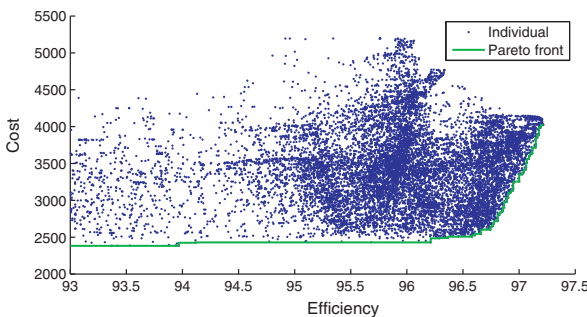


Fig. 15. Pareto front plot with all individuals – variator: 20/20+5-ES2, selector: IBEA, 5000 generations, elapsed time: 4483 s, area: 1587.

Fig. 16 shows the plot for the algorithm with the SPAM selector. Compared with the two previous plots one can see that this algorithm with the SPAM selector is less aggressive at the border of the Pareto front and looks more random with a high population density inside the plot. As we are only interested in Pareto optimal solution this seems like a waste of effort and time to evaluate so many solutions inside the plot.

Fig. 17 shows the plot for the algorithm with the SEMO2 selector. Comparing this algorithm with the one with the HypE and IBEA selector it looks more randomly distributed and is not as aggressive in finding the Pareto front. It has like the SPAM selector a high concentration of individuals inside the plot which is not that useful. If we compare the Pareto front for the four different selectors we can see that they agree well with each other (see Fig. 18). However the algorithms with the SPAM and SEMO2 selectors have not found the maximum efficiency as the algorithms with the HypE and IBEA selectors have. The Pareto front is also better defined with the use of the HypE and IBEA selector as they have been more aggressive toward the Pareto front for high efficiencies. Table 9 summarizes the results from these multi-objective optimization algorithms.

The algorithm with the IBEA and HypE selector is almost equally good but if one should choose one over the other the HypE is deemed to be the winner as it has a slightly higher calculated area. However, the execution time for the 5000 generations is approximately 3 min

Table 9
Evaluation of multi-objective algorithm.

Selector type	Area	Elapsed time	Visual evaluation	η_{max} reached?
SPAM	1422	5308	Random	No
SEMO2	1431	5891	Random	No
IBEA	1587	4483	Aggressive	Yes
HYPE	1598	4667	Aggressive	Yes

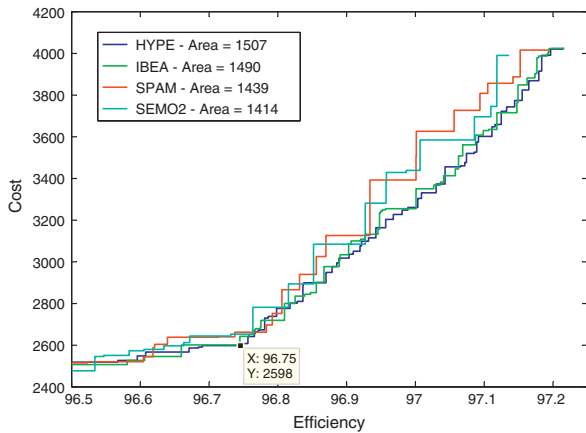


Fig. 18. Comparison of found Pareto fronts.

Table 10
Object and fitness parameters for the best compromise between cost and efficiency.

Parameter	HypE	Unit	Description
p	3	–	Number of pole pairs
Θ	60	K	Temperature rise in the windings
Material	3	–	Core material, 1, 2, 3 (see Appendix)
$\sigma_{F_{tan}}$	43470	Pa	Tangential stress
δ	9.9000	mm	Physical air-gap
Q	20	–	Number of stator slots
a	1	–	Number of parallel branches in coil
J_s	6,500,000	A/m ²	Stator current density
η	96.7456	%	Efficiency
Cost	2598	–	Material cost

slower for the HypE selector than it is for the IBEA selector but time is of less importance in this optimization problem. Another reason for choosing the HypE selector is that it is better at finding the Pareto front for low efficiencies than the IBEA selector, but as this is less important this is not the main reason for choosing the HypE over IBEA.

In a commercial application one would properly chose a solution on the Pareto front where the cost start to increase dramatically if higher efficiencies are needed. Such a solution could be the one marked in Fig. 18 where one would get the highest efficiency for their money. The marked solution's object parameters and motor dimensions are listed in Tables 10 and 11 and come from the use of the HypE selector and a figure of the geometry is depicted in Fig. 19. Comparing these values with the one achieved previously for the motor design with the highest efficiency, Tables 7 and 8, the most striking difference is the high current density in the stator coils and the thicker magnets. This higher current density will cause higher resistive losses but on the other hand require less space for the coils and thereby reducing the occupied space in the stator core.

Table 11
Best compromise motor design dimensions.

Parameter	Value	Parameter	Value
h_1	0.0010	b_4	0.0177
h_2	0.0020	b_{4c}	0.0183
h_3	0.0050	b_{5c}	0.0246
h_4	0.0323	D_r	0.2700
h_5	0.0200	D_{ri}	0.1004
h_6	0.0005	D_{ryi}	0.1948
h_{PM}	0.0376	D_s	0.2898
h'	0.0005	D_{se}	0.4657
b_1	0.0030	l	0.1026

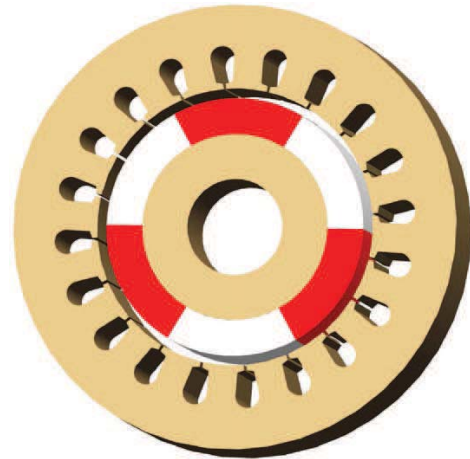


Fig. 19. Best compromise motor design.

The outer diameter can therefore be reduced which in the end will reduce the price of both the iron and copper at the expense of the efficiency. This fits nicely with the shape of the Pareto front where some of the efficiency has been sacrificed to decrease the cost of the motor.

5. Conclusion

A design optimization of a permanent magnet motor with the use of metaheuristics has been presented. The metaheuristics used for this optimization was evolution strategies which have been described in detail in Section 3. Two versions of the ES have been tested and have in the paper been referred to as ES1 and ES2 where the ES1 is a standard ES algorithm and the ES2 is a slightly modified algorithm proposed by the authors. The ES1 version strategy parameters were initially set by calculating the normal standard deviation for each object parameter of the initial population and were only changed in the offspring individual through recombination and mutation. The ES2 version strategy parameters were continuously being overwritten as the strategy parameters were set by calculating the normal standard deviation for each object parameter of the current generation of the marriage population.

The two algorithms have been tuned for the parameters ρ and λ which is the number of parents involved in the procreation of one offspring and the size of the offspring population. The best results from the ES1 version, which is the standard ES algorithm, was achieved by the $(\mu/\rho + \lambda) = (20/10 + 5)$ -ES. Results from this tuned algorithm have been presented, showing that the algorithm did not fully converge within the 1.5 min which was allocated for the run of the algorithm. Even though it did not fully converge it still achieved relatively good results as it reached an efficiency above 97.21% 9 out of the 10 test runs which was the success criteria. The best results from the ES2 version, which was proposed by the authors, was achieved by the $(\mu/\rho + \lambda) = (20/20 + 5)$ -ES. Results from this tuned algorithm have been presented, showing that the algorithm converges fully in less than the 1.5 min which was allocated for the run of the algorithm. This algorithm did not only reach the success criteria of an efficiency of 97.21% but actually found the assumed optimum solution in 10 out of the 10 test runs. For this reason this algorithm was used for the multi-objective optimizing.

The achieved motor parameters and dimensions for the best results from the ES1 and ES2 has been presented and have resulted

in almost identical solutions with the exceptions of choice of core material which did not fully converge in the ES1 algorithm. However the motor parameters achieved seems to be reasonable if one want to create a motor with the maximization of the efficiency as the only goal.

The structure of PISA has briefly been explained which was used in conjunction with the ES2 algorithm for multi-objective optimizing of the efficiency and cost of the motor. Four different selectors together with the ES algorithm have been tested to examine their performance. Results showed that the HypE and IBEA selectors performed best on the problem at hand. They were much more aggressive in the examination of the Pareto front for high efficiencies than the SPAM and SEMO2 selectors which produced more random individuals. It was evaluated that the HypE was the best of the selectors only slightly better than the IBEA selector.

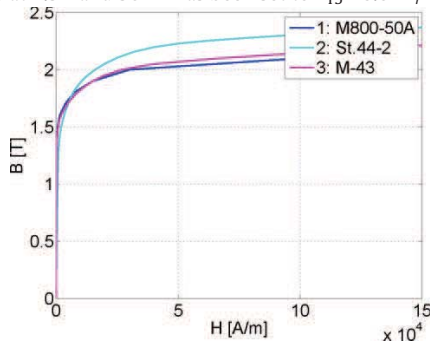
The motor parameters and dimensions for a solution from this MOO which will result in the highest efficiency per cost have been presented. Again the achieved motor parameters seem to be reasonable when they are compared with the values from the single parameter optimization where the volume of the material in the MOO has been minimized to reduce the cost of the motor.

Appendix A. Three-phase permanent magnet motor with rotor surface magnets, a two-layer integral slot winding and open-circuit cooling

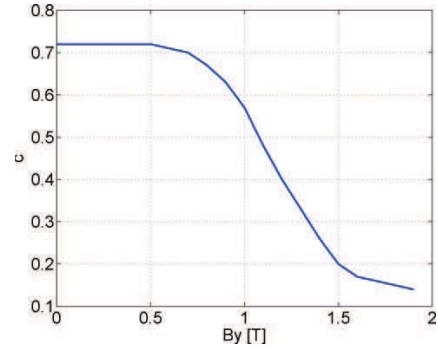
A.1. Initial data of the motor

Parameter	Value	Description
P	160,000	Shaft power [W]
n	41.667	Speed [1/s]
T	$\frac{P}{2\pi n} = 611.1501$	Torque [Nm]
U	690	Line-to-line voltage, [V] star connected
m	3	Number of phases
f	$n \cdot p = 166.6680$	Frequency [Hz]
ω	$2\pi f$	Angular frequency [1/s]
H_c	800,000	Coercivity of the permanent magnets [A/m]
B_r	1.05	Remanence flux of the permanent magnets [T]
μ_0	$4 \cdot \pi \times 10^{-7}$	Permeability of vacuum [Vs/(Am)]
μ_{rec}	$\frac{B_r}{\mu_0 H_c} = 1.0445$	Permeability of the permanent magnet material
σ_{Cu20C}	57×10^6	Conductivity of copper at 20 °C [S/m]
α_{Cu}	3.81×10^{-3}	Temperature coefficient of resistivity for copper [1/K]
k_{Fe}	0.97	Space factor of the stator core
ρ_{Fe}	7600	Density of iron [kg/m ³]
ρ_{PM}	7500	Density of the permanent magnet material [kg/m ³]
ρ_{Cu}	8960	Density of copper [kg/m ³]

BH curve of the lamination material. The specific loss of these materials at 1.5 T and 50 Hz has been set to $P_{15} = 6.6$ W/kg.



Graph for the yoke magnetic voltage calculation.



A.2. Rotor size

Rotor volume V_r

$$V_r = \frac{T}{2\sigma_{Fe} \tau_{an}} \quad (A.1)$$

Ratio of equivalent core length/air-gap diameter and rotor diameter

$$\frac{l'}{D_r} = \chi \approx \frac{\pi}{4p} \sqrt{p} \quad D_r = \sqrt[3]{\frac{4V_r}{\pi \chi}} \quad (A.2)$$

A.3. Core length

Core length in a machine with no cooling channels

$$l = l' - n_p b_{ve} - 2\delta \quad (A.3)$$

A.4. Stator winding

Number of stator slots, stator slot pitch and stator pole pitch

$$Q = 2pmq \quad \tau_u = \pi \frac{D_s}{Q} \quad \tau_p = \pi \frac{D_s}{2p} \quad (A.4)$$

Winding pitch, coil span

$$W = \frac{y}{y_Q} \tau_p \quad y_Q = mq \quad y = \lfloor y_Q \rfloor \quad (A.5)$$

A.5. Air-gap flux density

Fundamental air-gap flux peak density $B_{1peak} = 0.95$ [T].

Effective relative magnet width: $\alpha_{PM} = 0.80$.

Maximum value of the rectangular flux density

$$B_{max} = \frac{\pi B_{1peak}}{4 \sin((\alpha_{PM})\pi/2)} \quad (A.6)$$

A.6. Number of coil turns in a phase winding

Permanent-magnet-induced voltage.

$$E_{PM} = \frac{U}{\sqrt{3}} \quad (A.7)$$

Winding factor

$$k_w(v) = \frac{2 \sin(v(\frac{\pi}{2})) W_{tp} \sin(\frac{v\pi}{2m})}{(Q/mp) \sin(v\pi(\frac{p}{Q}))} \quad (A.8)$$

Number of coil turns in a phase winding

$$N = \frac{\sqrt{2} E_{PM}}{\omega k_w(1) \alpha_{PM} B_{max} \tau_p l'} \quad (A.9)$$

A.7. Number of conductors in a slot

Number of conductors in a slot and number of coil turns in the phase winding

$$z_Q = 2am \frac{N}{Q} \quad N = \frac{Q \cdot z_Q}{2 \cdot a \cdot m} \quad (\text{A.10})$$

A.8. New B_{max}

$$B_{max,new} = \left(\frac{z_{Q,non-rouned}}{z_{Q,selected}} \right) B_{max,old} \quad (\text{A.11})$$

A.9. Width of the stator slot

The tooth width

$$B_d = \frac{l' \tau_u}{k_{Fe}(1 - n_v b_v)} \cdot \frac{B_{max}}{B_{dapp}} \quad (\text{A.12})$$

A.10. Stator slot dimensions

Initial stator current and stator phase voltage

$$I_s = \frac{P}{m\eta U_{sph} \cos(\phi)} \quad U_{sph} = \frac{U}{\sqrt{3}} \quad (\text{A.13})$$

Area of one conductor in a stator slot and wound area of a stator slot

$$S_{Cs} = \frac{I_s}{a j_s} \quad S_{Cus} = \frac{z_Q S_{Cs}}{k_{Cus}} \quad (\text{A.14})$$

The slot dimensions are presented in the table below:

Parameter	Value	Unit
b_1	0.003	m
h_1	0.001	m
h_2	0.002	m
h_3	0.0050	m
h_6	0.0005	m
h'	0.0005	m

Other dimensions are determined as follows:

$$b_4 = \frac{\pi(D_s + 2(h_1 + h_2))}{Q} - b_d \quad (\text{A.15})$$

$$b_{4c} = b_4 + \frac{2\pi h_3}{Q} - 2h_6 \quad b_{5c} = b_{4c} + \frac{2\pi h_5}{Q} \quad (\text{A.16})$$

$$S_{Cus} = \frac{b_{4c} + b_{5c}}{2} h_5 + \frac{\pi}{8} b_{5c}^2 \quad (\text{A.17})$$

Total area of a slot

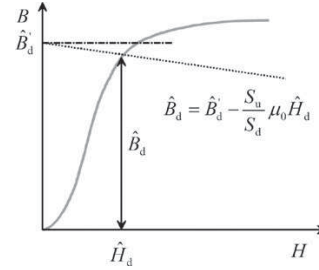
$$S_{slot} = b_1 h_1 + h_2 \left(\frac{b_4}{2} + \frac{b_1}{2} \right) + h_3 \left(b_4 + \frac{\pi h_3}{Q} \right) + \left(\frac{b_4 + b_5}{2} \right) h_5 + \frac{\pi}{8} b_5^2 \quad (\text{A.18})$$

A.11. Magnetic voltage over the tooth

Apparent flux density in stator tooth

$$B_{dapp} = \frac{l' \tau_u B_{max}}{k_{Fe}(1 - n_v b_v) b_d} \quad (\text{A.19})$$

Using the BH curve, we get for the field strengths in the teeth:



Magnetic voltage of the tooth

$$U_{m ds} = H_d (h_3 + h_5) \quad (\text{A.20})$$

The magnetic voltages of the tooth tip and of the rounded part of the tooth are small and may therefore be omitted.

A.12. Height of stator and rotor yokes and permanent magnets. Magnetic voltage of air gap, stator and rotor yokes, and permanent magnet

Factor for reduction of slot opening

$$\kappa = \frac{2}{\pi} \left(\text{atan} \left(\frac{b_1}{2\delta} \right) - \frac{2\delta}{b_1} \ln \left(\sqrt{1 + \left(\frac{b_1}{2\delta} \right)^2} \right) \right) \quad (\text{A.21})$$

Carter factor

$$k_{C1} = \frac{\tau_u}{\tau_u - \kappa b_1} \quad (\text{A.22})$$

Equivalent air gap

$$\delta_e = k_{C1} \delta \quad (\text{A.23})$$

Magnetic voltage of the air gap

$$U_{m \delta e} = \frac{B_{max}}{\mu_0} \delta_e \quad (\text{A.24})$$

Air-gap flux

$$\Phi_m = \alpha_{PM} B_{max} \tau_p l' \quad (\text{A.25})$$

Height of the stator and rotor yoke h_y

$$h_y = \frac{\Phi_m}{2k_{Fe}(1 - n_v b_v) B_y} \quad (\text{A.26})$$

Average stator and rotor yoke slot pitch

$$\tau_y = \frac{\pi D_y}{2p} \quad (\text{A.27})$$

Magnetic voltage of the stator and rotor yoke

$$U_{mys} = c H_{y max} \tau_y \quad (\text{A.28})$$

The permanent magnet flux density B_{PM} is equal to the air-gap flux density $B_{PM} = B_{max}$,

Height of the permanent magnets

$$h_{PM} = \frac{U_{m \delta e} + U_{m ds} + (U_{mys}/2)}{H_c - (H_c/B_r) B_{PM} + (\pi c_r H_{y max r})/2p} + \frac{(\pi c_r H_{y max r} (D_r - h_{yr}))/4p}{H_c - (H_c/B_r) B_{PM} + (\pi c_r H_{y max r})/2p} \quad (\text{A.29})$$

Magnetic voltage of the permanent magnet

$$U_{m PM} = \frac{H_c}{B_r} B_{PM} h_{PM} \quad (\text{A.30})$$

A.13. Stator resistance

Average length of a coil turn

$$l_{av} = 2l + 2.4W_{tp}\tau_p + 0.1 \quad (\text{A.31})$$

Conductivity of copper wire and DC resistance of a phase winding

$$\sigma_{Cu} = \frac{\sigma_{Cu20C}}{1 + \Theta\alpha_{Cu}} \quad R = \frac{Nl_{av}}{\sigma_{Cu}aS_{Cs}} \quad (\text{A.32})$$

A.14. Magnetizing inductance

Effective air gap

$$\delta_{ef} = \frac{U_{m\delta e} + U_{m\delta s} + U_{mPM} + U_{m\delta y}/2 + U_{m\delta r}/2}{U_{m\delta e}} \delta_e \quad (\text{A.33})$$

Magnetizing inductance in d -direction of the two-axis model

$$L_{md} = \frac{m}{2} \cdot \frac{2}{\pi} \cdot \mu_0 \cdot l' \cdot \frac{1}{2p} \cdot \frac{4}{\pi} \cdot \frac{\tau_p}{\delta_{ef}} \cdot (k_w(1) \cdot N)^2 \quad (\text{A.34})$$

As the machine is symmetrical in this case, $L_{mq} = L_{md}$ otherwise the q -axis effective air gap should first be evaluated.

A.15. Air-gap leakage inductance

Air-gap leakage factor

$$\sigma_{\delta s} = \sum_{\substack{v=-\infty \\ v \neq 1}}^{v=+\infty} \left(\frac{\sin((1+2km)W_{tp}(\frac{\pi}{2}))(\sin((1+2km)q\frac{\alpha_u}{2})) / (q\sin((1+2km)\frac{\alpha_u}{2}))}{(1+2km)k_w(1)} \right)^2 \quad (\text{A.35})$$

Air-gap leakage inductance

$$L_{\delta} = \sigma_{\delta s} L_{md} \quad (\text{A.36})$$

A.16. Slot leakage inductance

Slot leakage inductance

$$L_u = \frac{4m}{Q} \mu_0 l' N^2 \lambda_u$$

where

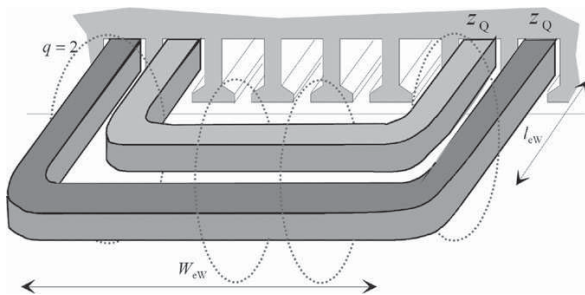
$$\epsilon = 1 - W_{tp} \quad k_1 = 1 - \frac{9}{16}\epsilon \quad k_2 = 1 - \frac{3}{4}\epsilon \quad (\text{A.37})$$

$$\lambda_u = k_1 \frac{h_4 - h'}{3b_4} + k_2 \left(\frac{h_3}{b_4} + \frac{h_1}{b_1} + \frac{h_2}{b_4 - b_1} \ln \left(\frac{b_4}{b_1} \right) \right) + \frac{h'}{4b_4} \quad (\text{A.38})$$

A.17. Tooth tip leakage inductance

$$L_{\sigma d} = \frac{4m}{Q} \mu_0 l' \lambda_d N^2 \quad \lambda_d = k_2 \frac{5(\delta/b_1)}{5 + 4(\delta/b_1)} \quad (\text{A.39})$$

A.18. End winding leakage inductance and reactance



Permeance factor

$$\lambda_w = \frac{2l_{ew}\lambda_{l_{ew}} + W_{ew}\lambda_w}{l_w} \quad (\text{A.40})$$

where

$$W_{ew} = l_w - 2l_{ew} \quad (\text{A.41})$$

End winding leakage inductance

$$L_w = \frac{4m}{Q} qN^2 \mu_0 l_w \lambda_w \quad (\text{A.42})$$

A.19. Synchronous inductance and reactance

Stator leakage inductance

$$L_{s\sigma} = L_{\delta} + L_u + L_{\sigma d} + L_w \quad (\text{A.43})$$

Direct-axis synchronous inductance and reactance

$$L_d = L_{md} + L_{s\sigma} \quad X_d = 2\pi f L_d \quad (\text{A.44})$$

Because there is no saliency in the rotor, the quadrature-axis synchronous inductance is equal to the direct-axis synchronous inductance $L_q = L_d$ and $X_q = X_d$.

A.20. Losses (except stator losses)

The mass of the stator teeth (only the height h_5 is taken into account) for loss calculation. The other parts of the teeth

have a low flux density and are ignored in this simplified calculation.

$$m_d = k_{Fe} \rho_{Fe} Q b_d h_5 l \quad (\text{A.45})$$

Correction coefficients for the core loss calculations, Table 3.2, [10]. $k_{Fed} = 2$ and $k_{Fey} = 1.5$.

Core loss in stator and rotor yoke

$$P_{Fey} = k_{Fey} P_{15} \left(\frac{B_y}{1.5} \right)^2 m_y \left(\frac{f}{50} \right)^{3/2} \quad (\text{A.46})$$

The core loss of the tooth area is calculated using the mass m_d defined above

Mechanical losses consisting of windage and ventilator losses

$$P_{\rho} = k_{\rho} D_r (l + 0.6\tau_p) v_r^2 \quad (\text{A.47})$$

where

$$v_r = \pi n D_r \quad k_{\rho} = 10 [Ws^2/m^4] \quad (\text{A.48})$$

The stator slot openings cause permeance harmonic losses in the rotor surface permanent magnets.

Slot openings b_1 cause a frequency f_{PM} on the rotor surface

$$f_{PM} = nQ \quad (\text{A.49})$$

Fictitious air gap for the loss calculation

$$\delta_{PMEC} = \delta + \frac{h_{PM}}{2\mu_{rec}} \quad (\text{A.50})$$

$$u = \left(\frac{b_1}{2\delta_{PMEC}} \right) + \sqrt{1 + \left(\frac{b_1}{2\delta_{PMEC}} \right)^2} \quad (\text{A.51})$$

$$\beta = \frac{1 + u^2 - 2u}{2(1 + u^2)} \quad (\text{A.52})$$

$$B_0 = \beta B_{max} \quad (\text{A.53})$$

$$k_v = \sqrt{f_{PM} 2\pi \mu_{rec} \mu_0 \frac{\sigma_{PM}}{2}} \quad (A.54)$$

$$\beta_v = \frac{f_{PM} 2\pi}{\pi D_r n} \quad (A.55)$$

$$a_{Rv} = \frac{1}{\sqrt{2}} \sqrt{\sqrt{4 + \left(\frac{\beta_v}{k_v}\right)^4} + \left(\frac{\beta_v}{k_v}\right)^2} \quad (A.56)$$

$$P_{PMEK} = \frac{a_{Rv}}{2} \left(1 + \frac{\tau_u}{2l}\right) \left(\frac{B_0}{\mu_0 \mu_{rec}}\right)^2 \left(\frac{k_v}{\sigma_{PM}}\right) \cdot \pi D_r \alpha_{PM} l \frac{(\sqrt{2} k_v)^2}{\beta_v^2} \quad (A.57)$$

A.21. Stator resistive losses and total losses

Stator resistive losses

$$P_{Cu} = 3I_s^2 R \quad (A.58)$$

Sum of losses

$$P_{loss} = P_{Fe} + P_{Cu} + P_\rho + P_{PMEK} + P_{ex} \quad (A.59)$$

Input power

$$P_{in} = P + P_{loss} \quad (A.60)$$

$$P_{in} = 3 \left(\frac{U_{sph} E_{PM}}{\omega_s L_d} \sin(\delta) + U_{sph}^2 \frac{L_d - L_q}{2\omega_s L_d L_q} \sin(2\delta) \right) \quad (A.61)$$

Direct-axis component of the stator current

$$I_d = \frac{(U/\sqrt{3})(X_q \cos(\delta_{loadinN}) - R \sin(\delta_{loadinN}))}{X_d X_q + R^2} - \frac{E_{PM} X_q}{X_d X_q + R^2} \quad (A.62)$$

Quadrature-axis component of the stator current

$$I_q = \frac{(U/\sqrt{3})(R \cos(\delta_{loadinN}) + X_d \sin(\delta_{loadinN}))}{X_d X_q + R^2} - \frac{E_{PM} R}{X_d X_q + R^2} \quad (A.63)$$

New stator current

$$I_s = \sqrt{I_d^2 + I_q^2} \quad (A.64)$$

If I_s differs more than 1 % from the estimated value, the stator current has to be given a new value and the calculations of Item 25 has to be repeated.

A.22. Efficiency

Efficiency

$$\eta = \frac{P}{P_{in}} 100 \quad (A.65)$$

A.23. Masses of the active materials

Rotor core outer diameter

$$D_{ryi} = D_r - 2h_{PM} \quad (A.66)$$

Mass of permanent magnets

$$m_{PM} = \frac{D_{ryi} + D_{ri}}{2} \pi \alpha_{PM} l h_{PM} \rho_{PM} \quad (A.67)$$

Mass of copper

$$m_{Cu} = \rho_{Cu} (l + 2l_w) Qz_Q S_{cs} \quad (A.68)$$

The mass of the iron (square plates)

$$m_{Fe} = D_{se}^2 l \rho_{Fe} \quad (A.69)$$

References

- [1] F. Glover, Tabu search—part I, ORSA Journal on Computing 1 (1989) 190–206.
- [2] F. Glover, Tabu search—part II, ORSA Journal on Computing 2 (1990) 4–32.
- [3] B. Suman, P. Kumar, A survey of simulated annealing as a tool for single and multiobjective optimization, Journal of the Operational Research Society 57 (2006) 1143–1160.
- [4] M. Dorigo, C. Blum, Ant colony optimization theory: a survey, Theoretical Computer Science 344 (2005) 243–278.
- [5] J.M. Johnson, Y. Rahmat-Samii, Genetic algorithms in engineering electromagnetics, IEEE Antennas and Propagation Magazine 39 (1997) 7–21.
- [6] H.-P. Schwefel, H.-G. Beyer, Evolution strategies—a comprehensive introduction, Natural Computing 1 (2002) 3–52.
- [7] L. Jolly, M. Jabbar, Q. Liu, Design optimization of permanent magnet motors using response surface methodology and genetic algorithms, IEEE Transactions on Magnetics 41 (2005) 3928–3930.
- [8] D. Bochnia, W. Hofmann, H. Hupe, Design optimization of permanent magnet motors by evolution strategies and finite element analysis, in: Ninth International Conference on Electrical Machines and Drives, 1999.
- [9] T.K. Chung, S.K. Kim, Optimal pole shape design for the reduction of cogging torque of brushless dc motor using evolution strategy, IEEE Transactions on Magnetics 33 (2) (1997) 1908–1911.
- [10] J. Pyrhönen, T. Jokinen, V. Hrabovcová, Design of Rotating Electrical Machines, John Wiley & Sons, Ltd, 2008.
- [11] J. Kirtley, Electric Motor Handbook, McGraw-Hill, 2004.
- [12] J.J. Cathey, Electricmachines Analysis and Design Applying MATLAB, 4th Edition, McGraw-Hill Inc., 2001.
- [13] IEEE Std 1776™-2008—Recommended Practice for Thermal Evaluation of Unsealed or Sealed Insulation Systems for AC Electric Machinery Employing Form-Wound Pre-Insulated Stator Coils for Machines Rated 15000 V and Below (2009).
- [14] T. Bäck, H.-P. Schwefel, An overview of evolutionary algorithms for parameter optimization, Journal of Evolutionary Computation 1 (1993) 1–23.
- [15] A.E. Eiben, C.A. Schippers, On evolutionary exploration and exploitation, Fundamenta Informaticae 35 (1998) 35–50.
- [16] T. Bäck, F. Hoffmeister, Basic aspects of evolution strategies, Statistics and Computing 4 (1994) 51–63.
- [17] S. Bleuler, M. Laumanns, L. Thiele, E. Zitzler, PISA - A Platform and Programming Language Independent Interface for Search Algorithms, Tech. Rep., ETH Zürich, Computer Engineering and Networks Laboratory.
- [18] E. Zitzler, L. Thiele, J. Bader, On set-based multiobjective optimization, IEEE Transactions on Evolutionary Computation 14 (2009) 58–79.
- [19] M. Laumanns, L. Thiele, E. Zitzler, E. Welzl, K. Deb, Running time analysis of multi-objective evolutionary algorithms on a simple discrete optimization problem, in: PPSN VII Proceedings of the 7th International Conference on Parallel Problem Solving from Nature, 2002, pp. 44–53.
- [20] E. Zitzler, S. Künzli, Indicator-based selection in multiobjective search, in: 8th International Conference on Parallel Problem Solving from Nature—PPSN VIII, 2004, pp. 832–842.
- [21] J. Bader, Hype: an algorithm for fast hypervolume-based many-objective optimization, Journal of Evolutionary Computation 19 (2011) 45–76.
- [22] J.D. Knowles, L. Thiele, E. Zitzler, A tutorial on the performance assessment of stochastic multiobjective optimizers, Tech. Rep., ETH Zurich, Computer Engineering and Networks Laboratory (2006).
- [23] E. Zitzler, D. Brockhoff, L. Thiele, The hypervolume indicator revisited: on the design of pareto-compliant indicators via weighted integration, in: Evolutionary Multi-Criterion Optimization 4th International Conference, EMO 2007, 2007.

Publication [P2]

Investigation of model simplification and its influence on the accuracy in fem magnetic calculations of gearless drives

IEEE Transactions on Magnetics
vol. 48, No. 7, pp. 2166-2177, July 2012

Investigation of Model Simplification and Its Influence on the Accuracy in FEM Magnetic Calculations of Gearless Drives

Søren B. Andersen¹, Ilmar F. Santos¹, and Axel Fuerst²

¹Department of Mechanical Engineering, Technical University of Denmark, Kgs. Lyngby, 2800, Denmark

²Department of Minerals & Printing, ABB Switzerland Ltd., 5405 Baden 5 Daettwil, Switzerland

Finite-element models of electrical motors often become very complex and time consuming to evaluate when taking into account every little detail. There is therefore a need for simplifications to make the models computational within a reasonable time frame. This is especially important in an optimization process, as many iterations usually have to be performed. The focus of this work is an investigation of the electromagnetic part of a gearless mill drive based on real system data which is part of a larger project building a multiphysics model including electromagnet, thermal, and structural interactions. This multiphysics model will later on be used for simulating and parameter optimization of a gearless mill drive with the use of Evolution Strategies which necessitates the reduction in computation time. What has been investigated is how model simplifications influence the accuracy on the calculated forces and torque coming from the drive where each simplification made is described and justified. To further reduce the evaluation time, it is examined how coarse the mesh can be, while still predicting the results with a high accuracy. From this investigation, it is shown that there are certain ratios between the mesh size in the air gap and the iron core, which will result in an optimal determination of the forces and torque. It will be shown that it is possible, just through simplifications and choosing the correct mesh size, to reduce the computational time by 98%, keeping an accuracy for torque and forces of less than 0.3% and 1.2%, respectively.

Index Terms—Finite-element method magnetic, gearless drives, model accuracy, model simplification, multiphysics.

NOMENCLATURE		\vec{r}	Vector from origin of torque to current position, [m].
i	Index $i \in [x, y, z]$ axis of rotation, [-].	$\vec{i}, \vec{j}, \vec{k}$	Unit vectors, [-].
δ	Kronecker's delta, [-].	A	Area of the integration region, [m ²].
ϵ_0	Permittivity of free space, [F/m].	B_i	Magnetic flux density component, [T].
ϵ_x	Rotor eccentricity component in the x-direction, [m].	E	Electric field strength, [V/m].
ϵ_y	Rotor eccentricity component in the y-direction, [m].	F_i	Electromagnetic force component, [N].
\mathbf{A}	Magnetic vector potential, [Wb/m].	J	Electric current density, [A/m ²].
\mathbf{B}	Magnetic flux density, [T].	r_i	i component of vector from origin of torque to current position, [-].
\mathbf{F}	Electromagnetic force, [N].	V	Volume of the integration region, [m ³].
\mathbf{f}	Lorentz force, [N].		
\mathbf{H}	Magnetic field strength, [A/m].		
\mathbf{S}	Maxwell stress tensor, [N/m ²].		
S_i	Maxwell stress tensor component, [N/m ²].		
\mathbf{T}	Torque tensor, [Nm].		
t	Torque, [Nm].		
μ	Permeability, [H/m].		
μ_0	Permeability of free space, [H/m].		
∇	Del operator, [-].		
\vec{n}	Unit vector normal to the surface, [-].		

I. INTRODUCTION

WHEN optimizing on large multiphysics systems is performed, one usually has to run the simulation models many times to achieve the optimal or near optimal solution. As multiphysics models, which include thermal, structural, and electromagnetics, have a tendency to become highly complex and very time consuming to evaluate, it is necessary to simplify these models in order to speed up the evaluation time without losing too much accuracy. This is in particular very important, if the optimization process is made by use of meta-heuristic [1], such as Evolution Strategies [2]–[4], as these methods require a lot of model iterations to achieve a near optimal solution.

One industrial example of electromagnetic, thermal, and structural dynamic interaction (multiphysics system) can be seen in gearless mill drives (GMDs). As mentioned, a complete multiphysics modeling of large GMDs has to cope with four main areas: structural dynamics, electromagnetism, fluid dynamics, and heat transfer. Based on structural dynamics

Manuscript received August 09, 2011; revised October 13, 2011; accepted January 04, 2012. Date of publication January 23, 2012; date of current version June 21, 2012. Corresponding author: I. F. Santos (e-mail: ifs@mek.dtu.dk).

Color versions of one or more of the figures in this paper are available online at <http://ieeexplore.ieee.org>.

Digital Object Identifier 10.1109/TMAG.2012.2185705

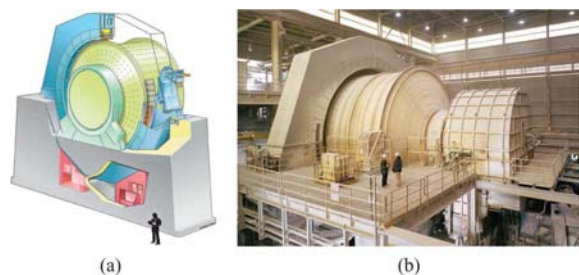


Fig. 1. (a) 3-D schematic of a gearless mill drive [15]. (b) Gearless SAG mill.

movements and deformations of stator housing and rotating structure can be predicted. Based on electromagnetism the dynamic interaction between rotating structure and stator housing can be evaluated. Based on fluid dynamics the interaction forces between rotating structure and journal bearing housing can be described. Finally, based on heat transfer the temperature changes in the stator and journal bearing housings can be estimated. Such temperature changes cause variations of structure dimensions in millimeter and micrometer ranges, respectively, leading to significant changes of magnetic and hydrodynamic interaction forces. Gearless drives/generators are mainly being used in wind turbines, hydro power plants [5], [6], and in mills in the mining industry [7], [8]. The first gearless mill drive was introduced by ABB in 1969 (then Brown Boveri & Cie) and installed at a French company Ciments Lambert-Lafarge in Le Havre [9]. A picture of a gearless mill drive can be seen in Fig. 1, which in most aspects is similar to the one being analyzed.

A gearless mill drive is in principle an ordinary synchronous motor. However, these GMDs have a very large bore diameter compared to their iron length and a high number of poles which is far from a typical synchronous motor design. These drives are wrapped directly onto the mill drum eliminating the gearbox. These kinds of drives can deliver much higher torques than ordinary drives connected to gearboxes, as the structural integrity of the gearboxes are the limiting factor.

Finite-element (FE) modeling and optimization of gearless mill drives is a very complex task. Even with today's powerful computers these FE models demand an enormous long evaluation time, as experienced by the authors of [10], where the starting process of a large 2-pole solid pole synchronous motor was modeled and [11] where a hybrid stepper motor was investigated. To reduce the evaluation time of finite-element models, it is of common practice to model motors in 2-D and afterwards add the three-dimensional effects, such as screwing of the rotor and end windings effect [12].

As also mentioned in [13], many articles present FE simulations without explaining which simplifications/assumptions were made, giving the readers no chance to evaluate the correctness and limitations of such FE models. This paper deals with gearless drives design and modeling toward the optimization of such devices and their dynamic simulation in time domain. The focus of the work is to investigate the electromagnetic part of a gearless drive and to examine how FE model simplifications influence the accuracy on the calculated forces and torque coming from the drive. In this case the goal is to predict the torque and

forces within a $\pm 5\%$ deviation from the actual values which are the usual applied tolerances by the manufactures. These simplifications are done in an attempt to reduce the computation time. It is important to point out that for small electric machines FE models, their simplifications and solutions are combined numerically as well as analytical and nicely reported in the literature, for example [14]. Nevertheless, a lack in the literature is found, when considering FE magnetic modeling of very large electrical machines such as gearless mill drives which has been based on real industrial system data. In this framework the article gives an original contribution to the field of large machines FE magnetic modeling by: a) clearly documenting and validating all simplifications, b) explaining based on the physics of the problem, why the simplifications are made and under which circumstances, and c) exploring an industrial example with real system data of a gearless mill drive with 56 poles and diameter of 10 m. The simplifications are compared against a complete converged model to make the results as trustworthy as possible, as no experimental data is available at this time. The electromagnetic model will later be introduced into the multiphysics global model. Nevertheless this paper is focused only on the electromagnetic modeling.

II. PROBLEM DESCRIPTION

Multiphysics modeling of complex systems can be very time consuming as these models include many geometrical details and have many material properties resulting in a high number of degrees of freedom. There are a lot of strategies to reduce the degree of freedom of a model and consequently the number of equations to be solved. Some of these are:

- use of high order elements;
- manually optimized mesh geometry;
- polygon, square, and triangle elements;
- use of adaptive mesh [16]–[18].

This article will though only concentrate on the use of three node triangular elements and the simplification of the geometry in an attempt to reduce the degree of freedom of the model. Such triangular elements are standard elements in many commercial software packages, for example Maxwell2D.

The aim here is to reduce the complexity of a magnetic model of a gearless drive, which later on has to be implemented in a larger multiphysics model for simulating the dynamic behavior of a complete gearless mill drive.

The method used for simulating the drive is a FEMMagnetic model, which will be shown to converge to a single solution, as the mesh size is reduced. FEMM is a freeware program, and as it will be shown later it has been tested against the commercially available program Maxwell2D and proven to give the same results. The converged model will be used as the base for comparison against any other model examined, as no experimental values are available at the time. First several geometric simplifications will be examined, and the deviation between them and the converged model will be calculated. Simplifications, which have a minor effect on the calculated forces, will then be used for a combined simplified model, which again will be compared with the converged model. This combined simplified model will be used as a base for examination of the mesh size influence on the accuracy.

The goal is therefore to find the most coarse mesh (using three node triangular finite elements), which still leads to reliable results, as this will reduce the number of elements, and thereby the time needed for evaluation. Reliable results in this case is defined as force and torque deviations of less than 5% from the converged model which is the usual applied tolerances by the GMD manufacture.

To verify that the achieved results are not just valid for the rotor eccentricity examined, a second model has been created, where the rotor eccentricity has been altered. A new converged model is here again used as a base for comparison against the simplified models.

Further more the B-field in the air gap and iron core of the drive will be shown to give a visual idea of the amplitudes and field densities, which can be used for simplification purposes.

A. Basic Equations

Magnetostatic problems are problems in which the fields are time-invariant. In this case, the field strength \mathbf{H} and flux density \mathbf{B} must obey (1) and (2):

$$\nabla \times \mathbf{H} = J \quad (1)$$

$$\nabla \cdot \mathbf{B} = 0. \quad (2)$$

The relationship between \mathbf{B} and \mathbf{H} is given in (3) where the proportionality constant μ is the permeability of the material:

$$\mathbf{B} = \mu \mathbf{H}. \quad (3)$$

In cases where the material is nonlinear, the permeability, μ is a function of \mathbf{B} and we have:

$$\mu = \frac{\mathbf{B}}{\mathbf{H}(\mathbf{B})}. \quad (4)$$

The software program FEMM goes about finding a field that satisfies (1)–(3) via a magnetic vector potential approach. Flux density is written in terms of the vector potential, \mathbf{A} , as:

$$\mathbf{B} = \nabla \times \mathbf{A}. \quad (5)$$

Now, this definition of \mathbf{B} always satisfies (2). Then, (1) can be rewritten as:

$$\nabla \times \left(\frac{1}{\mu(\mathbf{B})} \nabla \times \mathbf{A} \right) = J. \quad (6)$$

For a linear isotropic material (and assuming the Coulomb gauge, $\nabla \cdot \mathbf{A} = 0$), (6) reduces to:

$$-\frac{1}{\mu} \nabla^2 \mathbf{A} = J. \quad (7)$$

FEMM retains the form of (6), so that magnetostatic problems with a nonlinear \mathbf{B} - \mathbf{H} relationship can be solved. In the general 3-D case, \mathbf{A} is a vector with three components. However, in the 2-D planar and axisymmetric cases, two of these three components are zero, leaving just the component in the “out of the paper” direction. The advantage of using the vector potential formulation is that all the conditions to be satisfied have been combined into a single equation. If \mathbf{A} is found, \mathbf{B} and \mathbf{H} can then be deduced by differentiating \mathbf{A} .

For calculating the forces, it is of common practice to use Maxwell’s stress tensor [19]–[22], which is particularly suited for this purpose, as the integral depends only on the field distribution outside the object in question. It is for this reason not necessary to know the exact current density distributions within complex anisotropic or nonlinear materials. From the theory of electromagnetism we have, that Lorentz force and Ampere’s law is expressed respectively by (8) and (9)

$$\mathbf{f} = J \times \mathbf{B} \quad (8)$$

$$\nabla \times \mathbf{B} = \mu_0 J. \quad (9)$$

Inserting (9) into (8) and integrating over the volume of the object, one can achieve an expression for the force on the object expressed solely by the B-field present.

$$\mathbf{F} = \frac{1}{\mu_0} \iiint (\nabla \times \mathbf{B}) \times \mathbf{B} dV. \quad (10)$$

Expanding the curl and the cross product, the x, y, and z component of (10) is

$$F_x = \frac{1}{\mu_0} \iiint \left(B_z \frac{\partial B_x}{\partial z} - B_z \frac{\partial B_z}{\partial x} - B_y \frac{\partial B_y}{\partial x} + B_y \frac{\partial B_x}{\partial y} \right) dV \quad (11)$$

$$F_y = \frac{1}{\mu_0} \iiint \left(B_x \frac{\partial B_y}{\partial x} - B_x \frac{\partial B_x}{\partial y} - B_z \frac{\partial B_z}{\partial y} + B_z \frac{\partial B_y}{\partial z} \right) dV \quad (12)$$

$$F_z = \frac{1}{\mu_0} \iiint \left(B_y \frac{\partial B_z}{\partial y} - B_y \frac{\partial B_y}{\partial z} - B_x \frac{\partial B_x}{\partial z} + B_x \frac{\partial B_z}{\partial x} \right) dV. \quad (13)$$

Introducing Maxwell’s stress tensor, (14), where E is the electric field, B is the magnetic field, ϵ_0 is the vacuum permittivity, and μ_0 is the vacuum permeability

$$\mathbf{S}_{ij} = \epsilon_0 \left(E_i E_j - \frac{1}{2} \delta_{ij} E^2 \right) + \frac{1}{\mu_0} \left(B_i B_j - \frac{1}{2} \delta_{ij} B^2 \right). \quad (14)$$

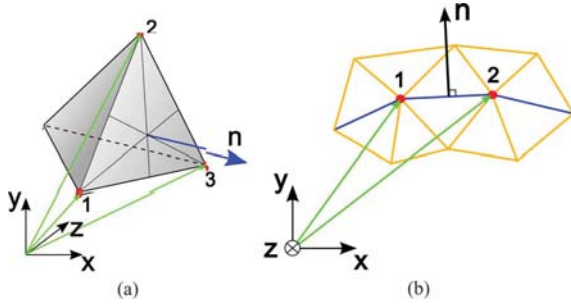


Fig. 2. (a) General case unit vector. (b) FEMM unit vector.

If the field is only magnetic, which is largely true in motors, some of the terms cancel out and we get:

$$\mathbf{S}_{ij} \cong \frac{1}{\mu_0} \left(B_i B_j - \frac{1}{2} \delta_{ij} B^2 \right). \quad (15)$$

Expanding this for the x, y, and z directions we get:

$$\mathbf{S}_x = \frac{1}{\mu_0} \left[\left(B_x^2 - \frac{B_x^2 + B_y^2 + B_z^2}{2} \right) \vec{i} + B_x B_y \vec{j} + B_x B_z \vec{k} \right] \quad (16)$$

$$\mathbf{S}_y = \frac{1}{\mu_0} \left[B_y B_x \vec{i} + \left(B_y^2 - \frac{B_x^2 + B_y^2 + B_z^2}{2} \right) \vec{j} + B_y B_z \vec{k} \right] \quad (17)$$

$$\mathbf{S}_z = \frac{1}{\mu_0} \left[B_z B_x \vec{i} + B_z B_y \vec{j} + \left(B_z^2 - \frac{B_x^2 + B_y^2 + B_z^2}{2} \right) \vec{k} \right]. \quad (18)$$

Now taking the divergence of vector (16) to (18) results in (19)–(21)

$$\nabla \cdot \mathbf{S}_x = \frac{1}{\mu_0} \left[B_x \left(\frac{\partial B_x}{\partial x} + \frac{\partial B_y}{\partial y} + \frac{\partial B_z}{\partial z} \right) - B_y \frac{\partial B_y}{\partial x} - B_z \frac{\partial B_z}{\partial x} + B_y \frac{\partial B_x}{\partial y} + B_z \frac{\partial B_x}{\partial z} \right] \quad (19)$$

$$\nabla \cdot \mathbf{S}_y = \frac{1}{\mu_0} \left[B_y \left(\frac{\partial B_x}{\partial x} + \frac{\partial B_y}{\partial y} + \frac{\partial B_z}{\partial z} \right) - B_x \frac{\partial B_x}{\partial y} - B_z \frac{\partial B_z}{\partial y} + B_x \frac{\partial B_y}{\partial x} + B_z \frac{\partial B_y}{\partial z} \right] \quad (20)$$

$$\nabla \cdot \mathbf{S}_z = \frac{1}{\mu_0} \left[B_z \left(\frac{\partial B_x}{\partial x} + \frac{\partial B_y}{\partial y} + \frac{\partial B_z}{\partial z} \right) - B_x \frac{\partial B_x}{\partial z} - B_y \frac{\partial B_y}{\partial z} + B_x \frac{\partial B_z}{\partial x} + B_y \frac{\partial B_z}{\partial y} \right]. \quad (21)$$

According to (2) the term $((\partial B_x)/(\partial x) + (\partial B_y)/(\partial y) + (\partial B_z)/(\partial z))$ is equal to zero and the first part of the right-hand side can be cancelled. The remaining right-hand-side expressions are similar to the ones in (11), (12), and (13). The force in

the x, y, and z direction on the object can therefore be expressed as:

$$F_x = \iiint \nabla \cdot \mathbf{S}_x dV \quad (22)$$

$$F_y = \iiint \nabla \cdot \mathbf{S}_y dV \quad (23)$$

$$F_z = \iiint \nabla \cdot \mathbf{S}_z dV. \quad (24)$$

Using the divergence theorem to convert the volume integral to a surface integral one achieves:

$$F_x = \iint \mathbf{S}_x \cdot \vec{n} dA \quad (25)$$

$$F_y = \iint \mathbf{S}_y \cdot \vec{n} dA \quad (26)$$

$$F_z = \iint \mathbf{S}_z \cdot \vec{n} dA \quad (27)$$

where \vec{n} is the unit vector normal to the surface. In a general 3-D FE case this normal vector can be expressed as:

$$\vec{n} = \frac{(\mathbf{p}_2 - \mathbf{p}_1)}{|\mathbf{p}_2 - \mathbf{p}_1|} \times \frac{(\mathbf{p}_3 - \mathbf{p}_1)}{|\mathbf{p}_3 - \mathbf{p}_1|} \quad (28)$$

when looking at a triangular segment as shown in Fig. 2(a). \mathbf{p}_1 to \mathbf{p}_3 in (28) are vectors, and marked by arrows in the figure, pointing from the reference system to the corner points of the triangle marked by dots. FEMM however is a 2-D solver, assuming no variation of the B-field in the “out the paper” direction, and the depth into the paper Δz is constant. In this case, the normal vector is as shown in Fig. 2(b), where the contour between the two dots defines the edge of the surface. In this case, the normal vector can, according to Fig. 2(b), be found as:

$$\vec{n} = \vec{n}_z \times \frac{(\mathbf{p}_1 - \mathbf{p}_2)}{|\mathbf{p}_1 - \mathbf{p}_2|} \quad (29)$$

where \vec{n}_z is a unit vector pointing in the z-direction. It is now possible to write a general force law expressed as:

$$\mathbf{F} = \iint \mathbf{S} \cdot \vec{n} dA. \quad (30)$$

The quantity \mathbf{S} is the Maxwell stress tensor for magnetostatic fields

$$\mathbf{S} = \frac{1}{\mu_0} \begin{bmatrix} B_x^2 - B^2/2 & B_x B_y & B_x B_z \\ B_y B_x & B_y^2 - B^2/2 & B_y B_z \\ B_z B_x & B_z B_y & B_z^2 - B^2/2 \end{bmatrix} \quad (31)$$

where $B^2 = B_x^2 + B_y^2 + B_z^2$.

The torque on a differential element can be expressed as:

$$d\mathbf{t} = \vec{\mathbf{r}} \times d\mathbf{F} \quad (32)$$

where \vec{r} is a vector pointing from the origin of torque to the current position

$$\vec{r} = \begin{Bmatrix} r_x \\ r_y \\ r_z \end{Bmatrix} = \begin{Bmatrix} x - x_t \\ y - y_t \\ z - z_t \end{Bmatrix}. \quad (33)$$

Inserting (30) into this, results in:

$$\mathbf{t} = \iint \vec{r} \times (\mathbf{S} \cdot \vec{n}) dA. \quad (34)$$

Expanding the cross product, we can find a torque tensor \mathbf{T} , which satisfies (35), and is a function of the stress tensor (31) and the components of the vector from the torque origin (33):

$$\mathbf{t} = \iint \mathbf{T} \cdot \vec{n} dA \quad (35)$$

$$\mathbf{T} = \begin{bmatrix} (r_y S_{31} - r_z S_{21}) & (r_y S_{32} - r_z S_{22}) & (r_y S_{33} - r_z S_{23}) \\ (r_z S_{11} - r_x S_{31}) & (r_z S_{12} - r_x S_{32}) & (r_z S_{13} - r_x S_{33}) \\ (r_x S_{21} - r_y S_{11}) & (r_x S_{22} - r_y S_{12}) & (r_x S_{23} - r_y S_{13}) \end{bmatrix}. \quad (36)$$

Further information on Maxwell's stress tensor can be found in [23]–[25].

B. The Gearless Drive

Fig. 3 shows a detailed drawing of the gearless drive in question. The drive has an outer diameter of nearly 12 m and a length of just over 1 m. It is a 56-pole 3-phase synchronous motor with DC excited coils on the rotor feed through slip rings. The stator windings are double layer fractional windings connected in a wye (star) configuration, which is the reason for modeling the complete drive, and not just a part of it. Another reason for modeling the complete drive is that the center of the stator and rotor is not coincident in these simulations, and seldom is in a real-life situation due to, e.g., assembly and operational conditions. Usually there is less than 1 mm eccentricity due to assembly and typically another 1 or 2 mm due to operational conditions which mainly is due to thermal effects. Both the rotor and stator core have machined holes, which act as cooling ducts when the sheets are stacked on top of each other. The main parameters of the drive are listed in Table I.

III. IMPLEMENTATION

A. 2-D FEM Magnetic Model

The first assumption that has been made is that the drive can be represented in 2-D to drastically reduce the complexity and computation time needed for simulating the drive. This assumption has, however, not yet been verified, but seems like a reasonable assumption, as the drive is symmetric into the plan, and is over 1 m long. Due to this fact, the end effects are assumed to have a minimal effect on the accuracy of the simulations. The creation and analysis of the FEM model of the gearless drive is carried out with the program FEMM through lua script from

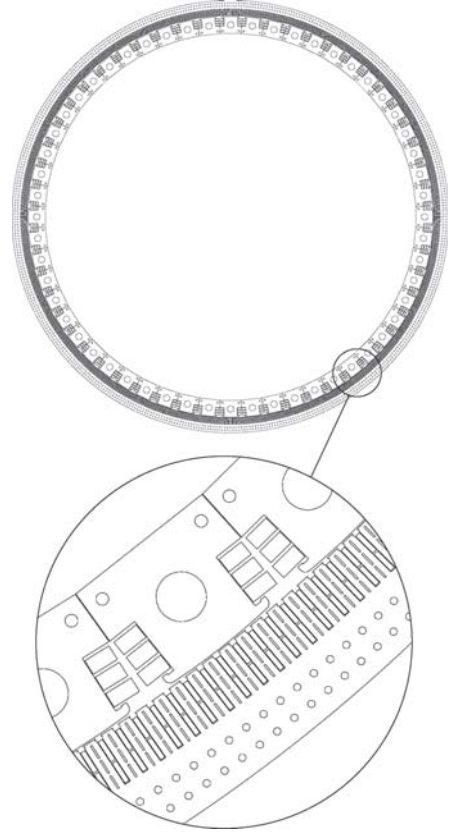


Fig. 3. Detailed rotor and stator geometry.

TABLE I
TYPICAL GMD PARAMETERS

Parameter	Value	Unit
No. of slots	480	-
No. of pole pair	28	-
No. of phases	3	-
Number of slots per pole and phase	2+6/7	-
Stator outer diameter	10.760	m
Max. rotor outer diameter	9.971	m
Rotor inner diameter	9.129	m
Min. nominal air gap	14.500	mm
Length	1.100	m
No. of coil segment per rotor pole	3	-
Coil turns per segment (rotor)	2x17, 1x18	-
Stator winding	double-layer fractional wye	-
Field winding supply current	495	A
Stator windings supply current	2500	A
Rotor core material	St.44-2	-
Stator core material	M-43	-

TABLE II
FEMM PROBLEM DEFINITION

Description	Values
Problem Type	Planar
Length Units	Millimeters
Frequency [Hz]	0
Depth	1100
Solver precision	1e-008
Min Angle	1
AC Solver	Succ. Approx.

MATLAB™. Lua is a programming language, used in this case to send information between the two programs. FEMM has two

ways of calculating the torque and forces, once the model is solved for the B-fields.

One is called line integral, and the other is called block integral [26].

The line integral totals the force produced on a predefined contour in the air gap, derived from Maxwell's stress tensor. Deriving meaningful force results from the line integral requires however some care in the choice of the integration path, which is explained fully in [19], [26].

The block integral/Weighted Stress Tensor block is a volume integral version of Maxwell's stress tensor, that automatically picks a collection of paths for the integration that yield "good" force results. The results are typically more accurate than the Maxwell Stress Tensor line integral, since in some sense, all possible contours have been averaged to yield the Weighted Stress Tensor force result.

Both types of integrations are used in this investigation, where the contour for the line integral is defined as a circle confining the rotor with a radius 2 mm larger than the nominal radius of the rotor.

The boundary condition of the interior of the rotor and the exterior of the stator is set so that the B-field on the boundary is always tangential to the boundary.

The isolation material of the copper conductors is modeled as air, as these isolation materials are nonmagnetic. The coils on the rotor are modeled as one current carrying conductor per segment, where the current in these conductors is the excitation current times the number of coil turns.

As this model is intended as a part of a larger multiphysics model, it is important that it not only predicts the torque with good accuracy, but also the total horizontal and vertical forces. If the rotor and stator center coincide, the resulting forces from the individual poles will cancel each other out, which is not that interesting, and usually not the case in real life. For this reason the rotor eccentricity is set to 7 mm in both the x-direction, ϵ_x , and y-direction, ϵ_y , resulting in an eccentricity of 9.9 mm (68% of the nominal air gap). This is accomplished by shifting the stator, as FEMM calculate the torque around the point $(x, y) = (0, 0)$. It has to be mentioned here that this eccentricity will never be reached in operation as alarms would usually go off at an eccentricity of 3 mm and shut down will happen at an eccentricity of 4 mm. The fascination about these machines is that they can have a bore diameter in excess of 10 m, but are still being manufactured with a precision of some 0.1 mm and operated with an eccentricity of only 1–3 mm. The extremely large eccentricity value used in this analysis is therefore only a theoretical example. To create the maximum torque the drive can deliver, the current in the armature windings is turned in a clockwise direction, as to create a load angle of 90 degrees.

The maximum element size of the mesh can be set individually for the different segments of the model, and is varied to examine its influence on the accuracy.

The material of the rotor core is built up of St.44-2 sheets with a thickness of 3 mm, and the lamination factor is set to 1. This however, is of less importance in this simulation, as the field is constant.

The stator core is built up of M-43 sheets with a thickness of 0.5 mm, and the lamination factor is again set to 1. As for the

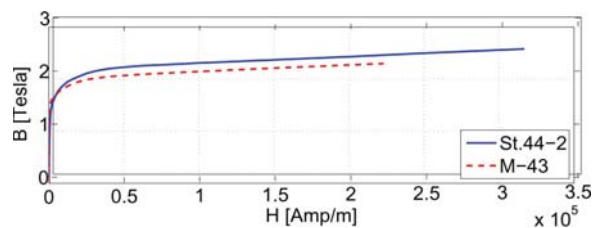


Fig. 4. B-H curves for core materials.

rotor core material, this is of less importance in this simulation, as the field is constant. Both materials are simulated using non-linear material parameters, and the B-H curves for the materials can be seen in Fig. 4.

B. Model Simplifications

To reduce the complexity of the model, the following model simplifications are investigated and compared to the results of a complete converged model.

The first simplification examined is, where the air gap (isolation) between the coils at the rotor and stator core is removed, as indicated in red in Fig. 5(a). This simplification is assumed only to contribute with small errors to the resulting B-field between the rotor and stator, as these air gaps are relatively small compared to the remaining geometry. However, these small air gaps are generating a large amount of small elements in the mesh, which contributes to a longer evaluation time, and is the reason for the simplification.

The second simplification is where the air gap between the rotor poles is removed, as shown in Fig. 5(b), due to the same reason as above, the small mesh elements. This simplification seems reasonable, as the air gaps between the poles are relatively small, and the forces acting between the individual poles are of no interest in this analysis. Furthermore, these air gaps are a long way from the B-field in the air gap between the rotor and stator, the B-field being the main area of interest in these analyses.

The third simplification examined is where the round cooling duct holes in the back iron of the stator are removed, as shown in red in Fig. 5(c). Circular curvatures in FE models usually generate large amounts of mesh elements due to the fact that the curvature is built up of straight lines, and a precise representation of the curvature require a lot of these straight lines. Again, to reduce the number of elements, it is desirable to remove these holes, if possible, without generating large errors to the main results. The validity of this simplification seems reasonable, due to the fact that the flux density at these holes is not so dense, as can be seen in Fig. 11(b). Furthermore, these holes are a long way from the B-field in the air gap between the rotor and stator, which makes it more plausible to only have minor effects on the B-field.

The fourth simplification is where the red holes in Fig. 5(d) are removed. The reason and validity of this simplification is the same as the previously mentioned simplification, that the flux density at the holes is not that dense, which again can be seen in Fig. 11(b), and they are a long way from the B-field of interest.

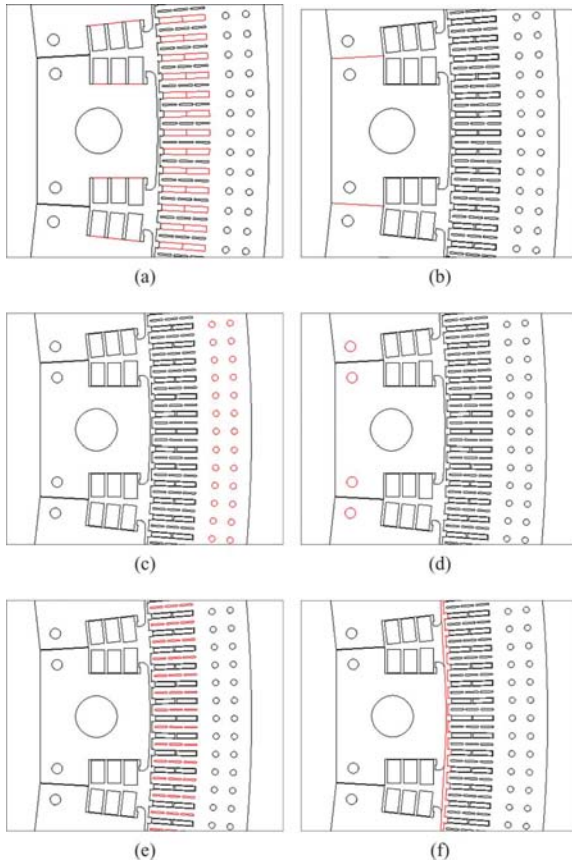


Fig. 5. (a) Air gap between coil and iron parts removed. (b) Air gap between rotor poles removed. (c) Holes in back iron of the stator removed. (d) Small holes in rotor poles removed. (e) Oblong holes in stator core removed. (f) Only a small band in the air gap between rotor and stator has a fine mesh.

The fifth simplification is where the oblong cooling duct holes in the stator fingers are removed, as indicated in red in Fig. 5(e). It is highly desirable to remove these holes, as they are made up of arcs at the ends, and are relatively narrow, which generate a huge amount of small mesh elements, resulting in an increased evaluation time. However it is doubtful that this simplification can be accepted as valid, as some of the stator fingers have a high flux density, as seen in Fig. 11(b), and the oblong holes extend approximately 1/5 of the finger width.

The sixth simplification is where only a small band in the air gap between the rotor and stator has a fine mesh, as indicated in Fig. 5(f). The reason for this simplification is that we are only interested in the B-field in the air gap between the rotor and stator, where the integration of Maxwell's stress tensor is performed. It is therefore assumed to be sufficient to model the air in this area with a dense mesh, and thereby reducing the number of elements, as the remaining air between the rotor poles can be modeled with a coarse mesh.

Finally, a model including all the simplifications, which are shown to have minimal effect on the accuracy are investigated. All the investigated simplifications are listed in Table III, and the results from these simplifications will be shown in the next section.

TABLE III
SIMPLIFICATIONS

No.	Simplification
a	Air gap between coil and iron parts removed
b	Air gap between rotor poles removed
c	Holes in back iron of the stator removed
d	Small holes in rotor poles removed
e	Oblong holes in stator core removed
f	Only a small band in the air gap between rotor and stator has a fine mesh
g	Simplification a, b, c, d and f

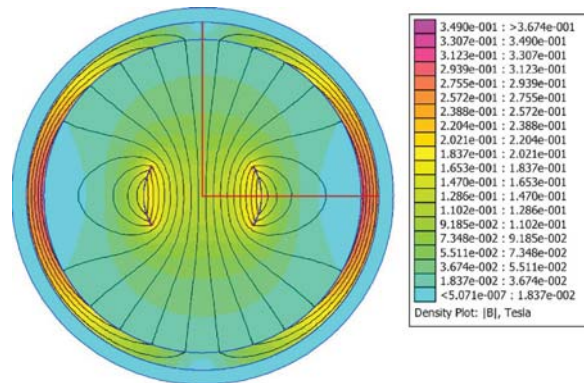


Fig. 6. B-field and flux lines (FEMM).

IV. SIMULATION RESULTS

A. Reliability of FEMM Achieved Results

Due to the fact that the program "Finite Element Method Magnetic" (FEMM) is a freeware program many people might question the reliability of the results achieved with this software program. A test case has therefore been carried out with FEMM and the well known and respected software program called Maxwell2D. The case compares the magnetic fluxes in air and a ring of nonlinear materials created by currents in arc shaped copper bars, Fig. 6. Without getting into the specific details of the model the results will just be presented. The red lines in Fig. 6 indicated the path where the B-field is being evaluated. Fig. 7 shows the absolute values of the B-field on these red lines where B_{tan} is the field normal to the horizontal line and B_{rad} is the field tangential to the vertical line. Both FEMM and Maxwell2D results has been plotted. The results from FEMM has been calculated by one of the authors, Søren B. Andersen, where the results from Maxwell2D has been calculated by Dr. Ing. Grinbaum at ABB Minerals & Printing, Switzerland. It can be seen that there is a very good coherence between these results with only some small deviations at the edge of the ring. These deviations however are assumed to be due to a larger mesh size in the Maxwell2D case as the tendency of the FEMM results fits better as smooth curves are expected instead of wobbling ones. In any case the two programs can be assumed to produce the same results.

B. Investigation of Boundary Condition

In the modeling of the motor an assumption is made, that all the B-fields at the outer diameter of the stator and the inner diameter of the rotor, is tangential to the boundary. This assump-

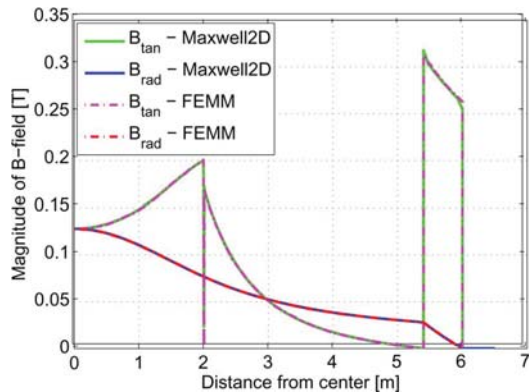


Fig. 7. Maxwell2D vs. FEMM—B-fields.

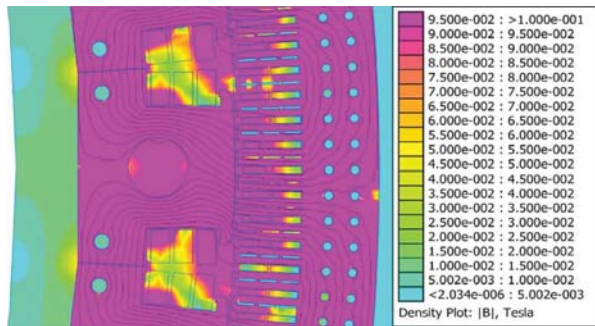
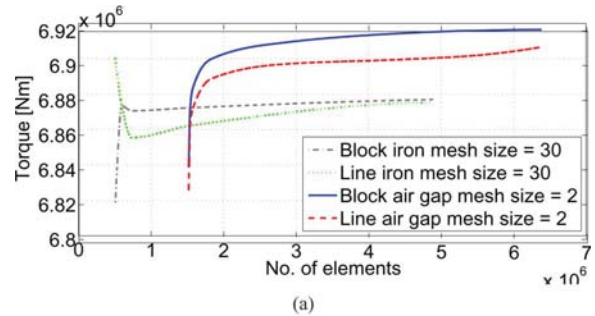


Fig. 8. Investigation of boundary condition.

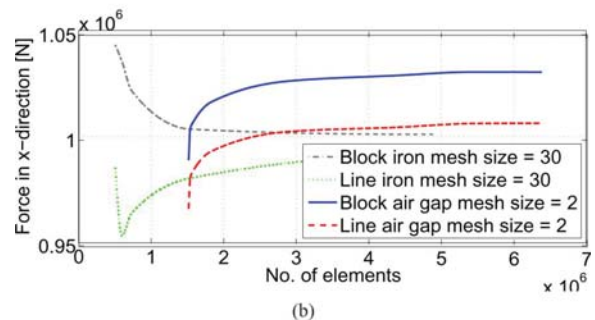
tion is investigated, and shows that, as long as the permeability of the core material is much larger than the permeability of the surrounding air and the material is not close to saturation, the error in connection with this assumption is neglectable. This can also be seen in Fig. 8, which shows that the B-field in the air outside the stator and inside the rotor are less than 0.05 T compared to the iron core, which for the most part, is larger than 1 T and this makes the assumption acceptable.

C. Convergence

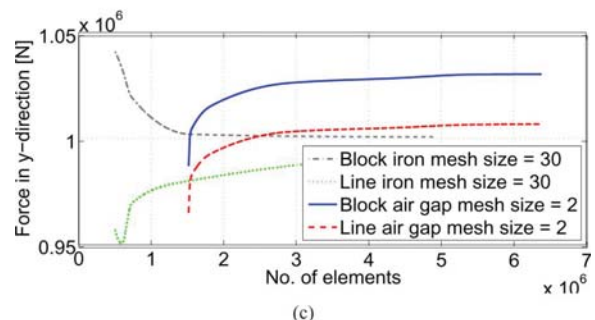
Proving that the described FEMM model converges to a single solution, the convergence is examined by varying the mesh size of the air and iron parts of the complete model, and looking at the convergence of the calculated forces and torque. Figs. 9(a), (b), and (c) show some results from this convergence analysis. The dashed and dot-dashed curves in the figures show the force and torque calculated with a constant iron mesh size of maximum 30 for the block and line integrals respectively, where the air gap mesh size is varied between 1 and 8. The dashed and solid curves show the force and torque calculated with a constant air gap mesh size of maximum 2 for respectively the block and line integrals, where the iron mesh size is varied between 2.7 and 60. As it must be assumed that finer mesh creates more accurate solutions, the dashed and the solid curves are the most interesting ones, where it can be seen that the solid curve (block integral) converges, when the model consists of approximately 5.5 million elements. As explained earlier, the block integrals produce the most accurate results, and the model can therefore be assumed to have converged,



(a)



(b)



(c)

Fig. 9. (a) Convergence of torque, (b) Convergence of force (x-direction), (c) Convergence of force (y-direction).

even though the line integral has not yet completely converged. The solutions, which have been achieved with the model with the finest mesh, are the ones which will be used for comparisons against the simplified models.

D. B-Field

The B-field on the line integration contour in the air gap is plotted for pole 1 and 2 counted CCW from the x-axis, and can be seen in Fig. 10. Fig. 10(a) shows the absolute amplitude of the B-field, and it can be seen that the maximum amplitude for pole 2 is slightly larger than for pole 1, as the air gap at this pole is smaller due to the rotor eccentricity. This is one of the reasons why the complete drive has to be modeled. Furthermore, it can be seen that the B-field drops at each coil slot in the stator, which will create a pulsating B-field as the rotor turns. This has however not been simulated. In Fig. 10(b) the radial B-field is shown. It can be seen that this cannot be assumed to be a sinus shaped B-field, which most simple analytical models assume, which is one of the reasons for creating a complete FE model. The reason why the B-field is not sinusoidal, even though the

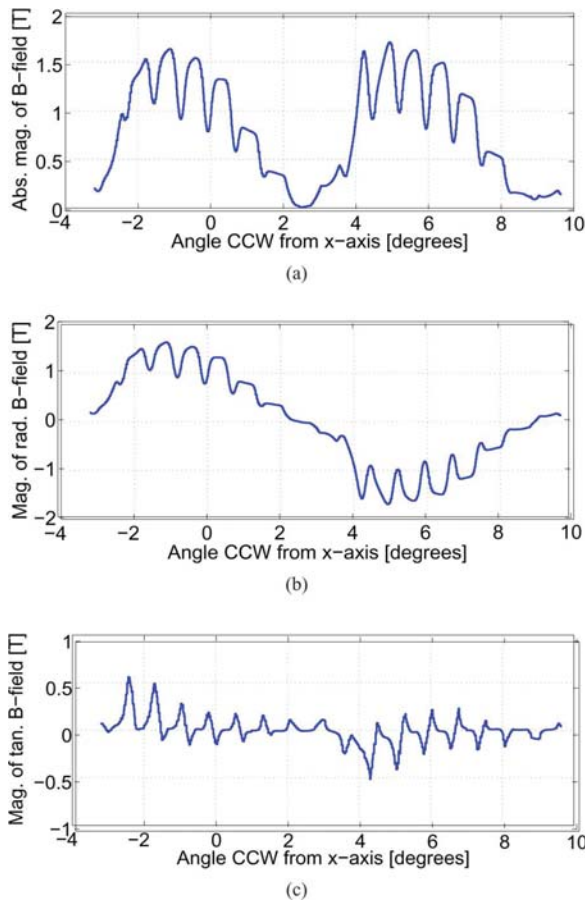


Fig. 10. (a) Abs. B-field in air gap at pole 1 & 2. (b) Radial B-field in air gap at pole 1 & 2. (c) Tangential B-field in air gap at pole 1 & 2.

input current is sinusoidal, is due to the salient poles and the slots in the stator. Finally, the tangential B-field is shown in Fig. 10(c), which is the only field we actually want, as this is the field that creates the torque on the rotor. It can be seen that this field also changes amplitude at each slot in the stator, which is responsible for the torque ripple.

Fig. 11 shows the B-field in the iron and air at pole 1, where it is clear to see that the armature field is turned in a CW direction so as to create the torque. Furthermore the critical areas in the model with high field density can be identified and used for optimization/simplification purposes. In this case the area at both sides of the large hole in the rotor pole have high flux density, which might be optimized by creating a oblong hole, with the same area, aligned in the radial direction. This will create more space beside the hole for the magnetic flux, thereby reducing the density. This has though not been examined, as this article only concentrates on the simplification of FE models for reduction of evaluation time. The thick orange line, actually 49 lines (left arrow), in the air gap in Fig. 11(b) shows the integration paths for the block integrals, and the thin blue line (right arrow) shows the integration path for the line integral, used for calculating the torques and forces. A close up of these lines in the air gap close to the corner of a stator finger (marked by a circle) can be seen

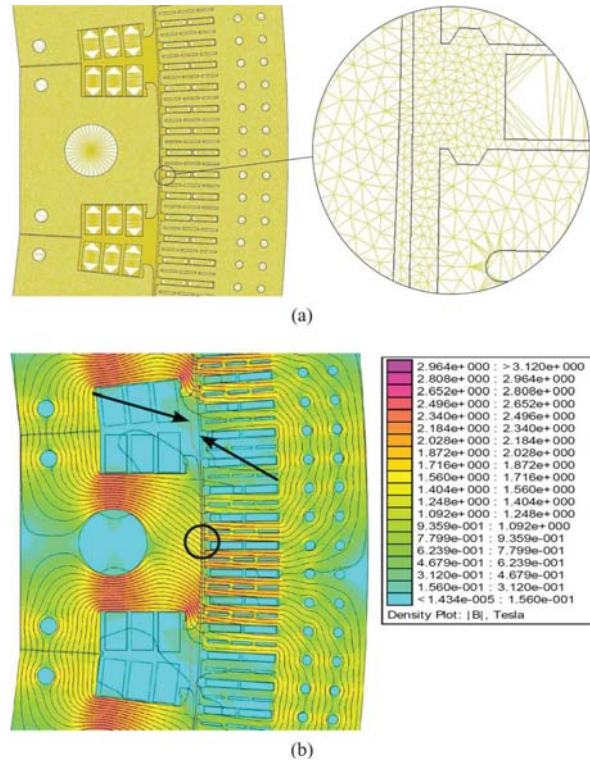


Fig. 11. (a) Section of model mesh with 4.4e6 elements (pole 1). (b) B-field from model with 4.4e6 elements (pole 1).

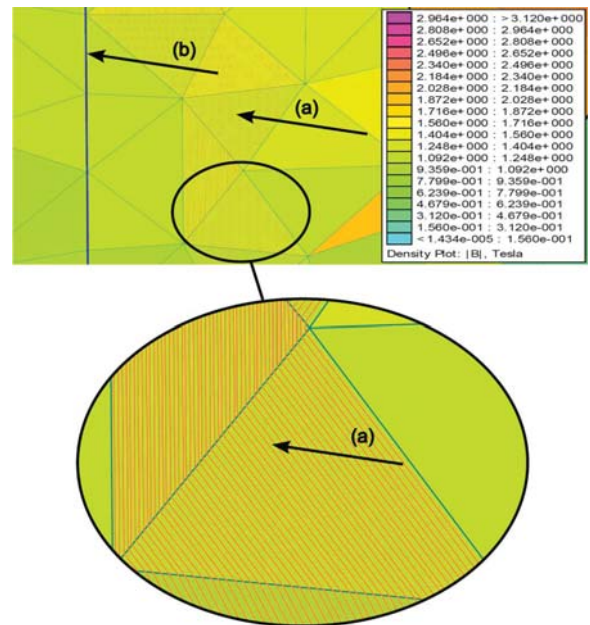


Fig. 12. Close up of air gap at pole 1. (a) 49 block integral paths. (b) Line integral path.

in Fig. 12, where the 49 lines for the block integral are visible, arrow (a). Arrow (b) in Fig. 12 is pointing at the line integral path.

E. Evaluation of Simplifications

To examine how well the previously mentioned simplifications predict the forces and torque, the deviation between the simplified and the complete model are calculated. Figs. 13(a), (b), and (c) show the results from these analyses, where the simplifications (a) to (g) refer to the simplifications listed in Table III. The left bars in the figures are results achieved with the block integral and compared with the block integral results from the complete converged model. The right bars are results achieved with the line integral and compared with the line integral results from the complete converged model. As can be seen, most of the simplifications have only a minor effect on the achieved torque results (less than 2%). However, looking at the forces in Fig. 13(b) and (c), it can be seen that simplification (e) deviates a lot from the converged model results (over 20%). This simplification is the one where the oblong holes in the stator fingers are removed, and it was expected to give large errors, as the iron area of the stator fingers has increased a lot by taking out the oblong holes in an area with high flux density (see Fig. 11(b)). Simplification (g) is a model which combines all the simplifications, which only have introduced minor errors to the results. It can be seen that this model also predicts the forces and torque with only minor deviations. This model, however, still consists of approximately 5.8 million elements, and takes just over 18 h to evaluate on the computer system listed in Table IV. This is, in most cases, an unacceptably long evaluation time. It is therefore investigated how coarse the mesh of the simplified model can be, while still predicting forces and torque with only small errors. The results from this analysis are shown in Fig. 14(a)–(f). Looking at the three left plots, which show the deviations for the block integral, one can see that there is a ratio between the core and air gap mesh size, which will predict the forces very well. This tendency, however, seems only to apply to results from the block integrals, where the results from the line integrals, the last three figures, seem more bumpy and random. Looking just at the block integral results, one can achieve force results with close to 0% deviation with a model with an air gap mesh size of 6 and an iron mesh size of 60. This will produce a model with 247 797 elements, which can be evaluated in less than 25 min on the computer system listed in Table IV. This is a reduction in computation time of more than 98% compared to the complete converged model. Calculating the deviance of this model shows that the torque only deviates -0.23% and the forces -1.15% from the complete converged model. As this ratio in mesh size might only be a characteristic of the specific rotor eccentricity, another rotor eccentricity value is investigated. The rotor eccentricity in the horizontal and vertical direction is therefore changed to 2 mm instead of 7 mm, giving a total eccentricity of 20% of the nominal air gap. The convergence of this new case of investigation is illustrated in Fig. 15. Running this new rotor eccentricity with the mesh size as described above, air gap mesh size of 6 and iron mesh size of 60, one achieves a deviation on the torque of -0.28% and a force deviation of -0.9% . It has been illustrated that this ratio seems to be valid for different states of the model, when using the block integral for calculation of torques and forces.

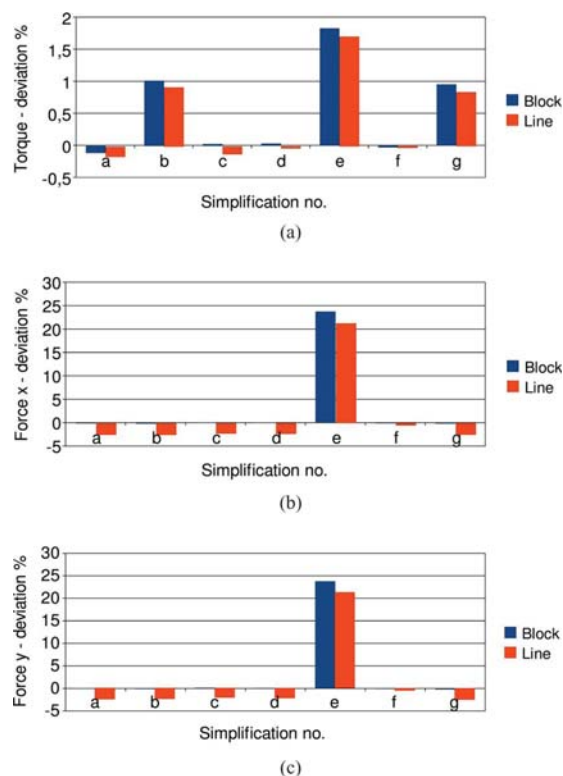


Fig. 13. (a) Deviation in torque due to simplifications. (b) Deviation in horizontal force due to simplifications. (c) Deviation in vertical force due to simplifications.

F. Computation Time

The evaluation time for some of the models is measured. It shows that it is possible to estimate the approximate computation time needed for a simulation, once the number of elements is determined. Fig. 16 shows points from some of the simulations made with the system listed in Table IV and a power curve fit through the points with the related equation, (37). This equation is used for the calculation of time for some of the simulations. All evaluation times mentioned refer to evaluation on this system

$$\text{Time [h]} = 103.48742 \cdot 10^{-9} \cdot \text{Elements}^{1.222232}. \quad (37)$$

G. Main Results

To get an overview of the main results of the described simulations, Tables V and VI list the most important parameters. From Table V it can be seen that the simplifications by themselves do not reduce the evaluation time significant, however they make it possible to create larger mesh elements, which otherwise would not be possible due to the geometry. Table VI shows that the found ratio between the mesh size of the air gap and iron parts is valid for different rotor eccentricities, and that the evaluation time is reduced to just 24 min, which is a reduction of the evaluation time of approximately 98%, keeping the

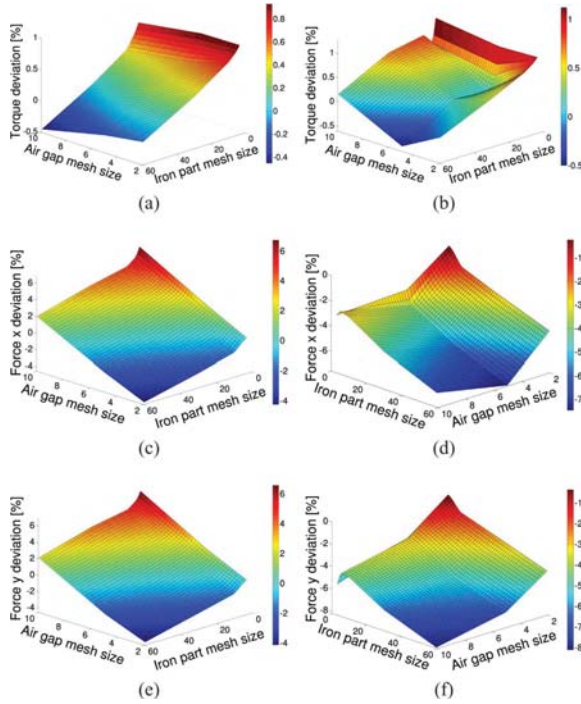


Fig. 14. (a) Torque deviation due to mesh size (block). (b) Torque deviation due to mesh size (line). (c) x-direction force deviation due to mesh size (block). (d) x-direction force deviation due to mesh size (line). (e) y-direction force deviation due to mesh size (block). (f) y-direction force deviation due to mesh size (line).

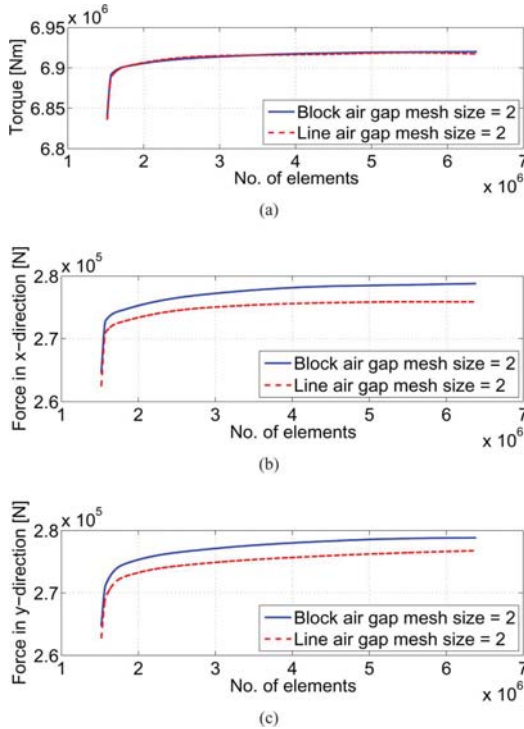


Fig. 15. (a) Convergence of torque. (b) Convergence of force (x-direction). (c) Convergence of force (y-direction).

TABLE IV
COMPUTER SYSTEM

Description	Installed Item
Processor	AMD Athlon 64 X2 Dual Core Processor 6000+
Installed RAM	3.00 GHz
OS	2.00 GB
FEMM version	Windows 7 Professional 64 Bit
	4.2

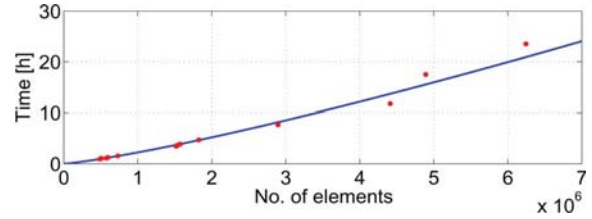


Fig. 16. Computation time.

accuracy for the torque and forces calculation to less than 0.3% and 1.2% respectively.

V. CONCLUSION AND FUTURE ASPECTS

The drive is represented by a 2-D FEM magnetic model, reducing drastically the complexity and computation time needed for simulating forces and torque.

- The boundary condition of the interior of the rotor and the exterior of the stator has been set so that the B-field on the boundary always is tangential to the boundary. The investigation of this assumption shows that as long as the permeability of the core material is much larger than the permeability of the surrounding air, the error in connection with this assumption is neglectable as long as not close to saturation. This will reduce the number of elements, as the surrounding air does not need to be modeled.
- Details at areas with low field densities can be removed inflicting only minor errors to the achieved force and torque results.
- Geometric simplifications do not alone reduce the number of elements and thereby the simulation time significantly. An investigation of the mesh size needed for achieving accurate results has therefore been performed. This investigation shows that there is a certain ratio between mesh size in the air gap and in the iron core of the drive that predicts the forces and torque with only small deviations. Such deviations have been calculated using the complete model and the block integral. A tested ratio of an air gap mesh size of 6 and a iron mesh size of 60 has been shown to give deviation on the torque of -0.23% and forces of -1.17% , when the composed rotor eccentricity has been set to $\epsilon_x = \epsilon_y = 7$ mm (68% of nominal air gap). It has also been verified that this ratio is not only a characteristic of this rotor eccentricity, as a model with a rotor eccentricity of only 2 mm in the horizontal and vertical direction (20% of nominal air gap) show similar results, namely a deviation on the torque of -0.28% and forces of -0.91% . These deviations are way below the acceptable tolerances of $\pm 5\%$ set forth by the GMD manufacture.
- The described simplifications and mesh sizes have proved to reduce the computation time from over 20 h to less than

TABLE V
MAIN SIMPLIFICATION RESULTS

Case	Max. dev. % Block integral Torque/Force	Max. dev. % Line integral Torque/Force	CPU time Hours	Elements
ref.	0/0	0/0	20.45	6,386,726
a	-0.11/-0.12	-0.16/-2.54	19.78	6,211,108
b	1.02/-0.16	0.92/-2.48	20.41	6,376,211
c	0.03/0.09	-0.12/-2.21	20.76	6,465,506
d	0.03/0.05	-0.03/-2.28	20.59	6,422,175
e	1.83/23.76	1.71/21.31	20.37	6,364,553
f	-0.03/-0.14	-0.03/-0.56	18.46	5,862,501
g	0.95/-0.21	0.84/-2.59	18.19	5,791,771

TABLE VI
MAIN MESH SIZE RESULTS (SIMPLIFICATION G)

Mesh size iron / air	Rotor eccen- tricity mm ϵ_x and ϵ_y	Max. dev. % Block integral Torque/Force	CPU time / reduction min. / %	Elements
60 / 6	7	-0.23/-1.17	24 / 98.3	247,797
60 / 6	2	-0.28/-0.91	24 / 98.3	247,227

25 min, which is a reduction in evaluation time of over 98%.

- E) The conclusions from A) to D) are of fundamental importance toward simulating the coupled dynamic behavior of rotor and stator, a future aspect of this research. It is important to highlight that such devices are huge and consist of a large number of poles increasing the complexity of these drives. The dynamic coupling between stator and rotor movements via magnetic forces and torque allows for an accurate simulation of the nonlinear dynamic behavior of gearless drives in time and the performance optimization of such devices.
- F) The calculations were made in 2-D with the assumption that 3-D effects such as end windings and so on could be added afterwards. Neglecting these 3-D effects can only be valid if the results are still sufficiently precise which of course has to be examined. Otherwise these effects have to be found and added to achieve the complete solution.

REFERENCES

- [1] H. A. Taha, *Operations Research: An Introduction*, 8th ed. Englewood Cliffs, NJ: Pearson Prentice Hall, 2007.
- [2] S. B. Andersen and I. F. Santos, "Evolution strategies and multi-objective optimization of permanent magnet motor," *J. Appl. Soft Comput.*, vol. 12, no. 2, pp. 778–792, 2012.
- [3] H.-P. Schwefel and H.-G. Beyer, "Evolution strategies—A comprehensive introduction," *Nat. Comput.*, vol. 1, pp. 3–52, 2002.
- [4] S. B. Andersen, "Evolution strategies and multiobjective optimization—Optimization of PM motor using evolution strategies," Technical University of Denmark, Department of Management Engineering, Tech. Rep., 2010.
- [5] L. Wang, R. W. Cheung, Z. Ma, J. Ruan, and Y. Peng, "Finite-element analysis of unbalanced magnetic pull in a large hydro-generator under practical operations," *IEEE Trans. Magn.*, vol. 44, no. 6, pp. 1558–1561, Jun. 2008.
- [6] W. Li, S. Ding, H. Jin, and Y. Luo, "Numerical calculation of mult-coupled fields in large salient synchronous generator," *IEEE Trans. Magn.*, vol. 43, no. 4, pp. 1449–1452, Apr. 2007.
- [7] R. A. Errath, "15000-hp gearless ball mill drive in cement—Why not!," *IEEE Trans. Ind. Appl.*, vol. 32, no. 3, pp. 663–669, 1996.
- [8] L. Nieto and M. Ahrens, "Gearless mill drive protection improvements and its behaviour at Minera Escondida Ltda.," in *IEEE Industry Applications Annu. Meeting*, 2007, pp. 1766–1772.
- [9] H. U. Wurgler, "The world's first gearless mill drive," *IEEE Trans. Ind. Gen. Appl.*, vol. IGA-6, no. 5, pp. 524–527, 1970.
- [10] Y. Li, S. Ho, W. Fu, and W. Liu, "An interpolative finite-element modeling and the starting process simulation of a large solid pole synchronous machine," *IEEE Trans. Magn.*, vol. 45, no. 10, pp. 4605–4608, Oct. 2009.
- [11] A. Oswald and H. G. Herzog, "Investigation of the usability of 2D- and 3D-FEM for a hybrid stepper motor," in *Proc. IEEE Int. Electric Machines and Drives Conf. (IEMDC '09)*, 2009, pp. 535–542.
- [12] A. Arkkio, "Analysis of Induction Motors Based on the Numerical Solution of the Magnetic Field and Circuit Equations," Ph.D. dissertation, Acta Polytechnica Scandinavica Helsinki, Finland, 1987.
- [13] H. Bärnklaue and T. Bach, "Experience with model simplifications for making a large FEM calculation case computable," in *18th Int. Conf. Electrical Machines*, 2008, p. 5.
- [14] A. Abdel-Razek, J. Coulomb, M. Feliachi, and J. Sabonnadiere, "The calculation of electromagnetic torque in saturated electric machines within combined numerical and analytical solutions of the field equations," *IEEE Trans. Magn.*, vol. MAG-17, no. 6, pp. 3250–3252, Nov. 1981.
- [15] ABB, "Gearless mill drives—Go gearless," ABB Switzerland Ltd Brochure, 2009.
- [16] Z. Cendes and D. Shenton, "Adaptive mesh refinement in the finite element computation of magnetic fields," *IEEE Trans. Magn.*, vol. MAG-21, no. 5, pp. 1811–1816, Sep. 1985.
- [17] H.-S. Choi, H.-S. Kim, and S.-Y. Hahn, "An adaptive mesh generator based on nodal errors," *IEEE Trans. Magn.*, vol. 36, no. 4, pp. 1619–1622, Jul. 2000.
- [18] F. Fernandez, Y. Yong, and R. Ettinger, "A simple adaptive mesh generator for 2-D finite element calculations," *IEEE Trans. Magn.*, vol. 29, no. 2, pp. 1882–1885, Mar. 1993.
- [19] W. Cai, P. Pillay, and K. Reichert, "Accurate computation of electromagnetic forces in switched reluctance motors," in *Proc. Fifth Int. Conf. Electrical Machines and Systems*, 2001.
- [20] J. Mizia, K. Adamiak, A. R. Eastham, and G. E. Dawson, "Finite element force calculation: Comparison of methods for electric machines," *IEEE Trans. Magn.*, vol. 24, no. 1, pp. 447–450, Jan. 1988.
- [21] K. Boughrara, B. L. Chikouche, R. Ibtouen, D. Zarko, and O. Touhami, "Analytical model of slotted air-gap surface mounted permanent-magnet synchronous motor with magnet bars magnetized in the shifting direction," *IEEE Trans. Magn.*, vol. 45, no. 2, pp. 747–758, Feb. 2009.
- [22] Z. Ren, "Comparison of different force calculation methods in 3d finite element modelling," *IEEE Trans. Magn.*, vol. 30, no. 5, pp. 3471–3474, Sep. 1994.
- [23] S. Humphries, "Tutorial: Theory and applications of the Maxwell stress tensor," [Online]. Available: www.fieldp.com 2010
- [24] S. H. Jr, "Finite-element methods for electromagnetic," [Online]. Available: www.fieldp.com 2010
- [25] J. P. A. Bastos and N. Sadovskii, *Electromagnetic Modeling by Finite Element Methods*. New York: Marcel Dekker, 2003.
- [26] D. Meeker, *Finite Element Method Magnetics—User's Manual Ver. 4.2* 2009.

Publication [P3]

Dynamics and Stability of Rigid Rotors Levitated by Passive
Bar-Magnet Bearings and Driven/Supported Axially by
Punctual Contact Clutch

Journal of Sound and Vibration

ref. JSV-D-12-01433

Submitted

Dynamics and Stability of Rigid Rotors Levitated by Passive Cylinder-Magnet Bearings and Driven/Supported Axially by Punctual Contact Clutch

Søren B. Andersen, Søren Enemark and Ilmar F. Santos

Department of Mechanical Engineering, Technical University of Denmark, 2800 Kgs. Lyngby, Denmark.

Abstract

A stable rotor - supported laterally by passive magnetic bearings and longitudinally by magnetic forces and a clutch - losses suddenly its contact to the clutch and executes abruptly longitudinal movements away from its original equilibrium position as result of small increases in angular velocity. Such an unstable behavior and its reasons are thoroughly theoretically as well as experimentally investigated in this work. In this context, this paper gives a theoretical and experimental contribution to the problem of two dimensional passive magnetic levitation and one dimensional contact stability dictated by mechanical-magnetic interaction. The behavior of passive multi-cylinder magnetic bearings (MCMB) is thoroughly theoretically as well as experimentally investigated. The contact dynamics between a clutch and a rotor supported by MCMB using several configurations of magnet distribution is also theoretically and experimentally studied. Such investigations lead to: a) clear physical explanation about the reasons of the rotor unstable behavior, loosing its contact to the clutch; b) an accurate prediction of the threshold of stability based on the nonlinear rotor-bearing model, i.e. maximum angular velocity before the rotor misses its contact to the clutch as a function of rotor, bearing and clutch design parameters.

Keywords: Passive Magnetic Bearing, Magnetic forces, Magnetic Field, Stability, Natural frequencies, Mode Shapes

Nomenclature

Roman Symbols

a	acceleration [m/s ²]
a_n	outpointing unit normal vector [-]
a_θ	unit vector, spherical/cylindrical [-]
a_φ	unit vector, cylindrical [-]
a_R	unit vector, spherical [-]
a_r	unit vector, cylindrical [-]
a_z	unit vector, cylindrical [-]
J_{ms}	current density of the surface of the magnet [A/m ²]
J_m	current density of the interior of the magnet [A/m ²]
m	magnetic dipole [A m ²]
F	force [N]
I	mass moment of inertia [kg m ²]
M	moment [Nm]
M_C	magnetization vector [A/m]
n	unit normal vector [-]
R	reaction force vector from clutch [N]
r	position vector [m]
r₀	position of rotor tip [m]
T	transformation matrix [-]
v	velocity vector [m/s]
A	vector magnetic potential [T m ²]
B	magnetic flux density [T]
B_r	magnetic remanence [T]
A	surface area of cylinder-magnet [m ²]
a	radius of cylinder-magnet [m]
a_n	radius of bearing to center of magnets [m]
g	gravity constant [m/s ²]
h	height of cylinder-magnet [m]
i	bearing magnet
i⁺	bearing magnet that rotor is angled towards
I_c	current [A]
K	positive constant [-]
l	length [m]
l_x	distance from rotor tip to center of rotor magnet [m]

l_{cur}	length of electrical current [m]
m	mass [kg]
M_C	magnetization constant [A/m]
R_C	reaction force [N]
r	magnet in rotor
R_p	distance [m]
s	clutch inclination [-]
V	volume of cylinder-magnet [m ³]
v	velocity [m/s]
z₀	chosen constant displacement [m]

Greek Symbols

α	Cardan angle [rad]
β	Cardan angle [rad]
γ	imbalance phase [rad]
Ω	angular velocity of reference system [rad/s]
ω	angular velocity of rotor [rad/s]
μ	friction coefficient
μ₀	vacuum permeability, 4π · 10 ⁻⁷ H/m
φ	variable angle above x-axis in xy-plane [rad]
τ	clutch moment [Nm]
ζ	variable in z-direction [rad]

Subscripts

*	representing quantities in xz-plane independent of y
0	origo
a	point a, rotor magnet 1
b	point b, imbalance mass
B1	coordinate system B1
B2	coordinate system B2
c	point c, center of gravity
d	point d, rotor magnet 2
g	gravity
I	coordinate system I
K	clutch
n	normal
rel	relative
t	tangential
U	imbalance mass

1. Introduction

Due to the advent of rare-earth magnets the development of magnetic materials has been accelerated in the last few decades [1, 2]. Passive magnetic bearings, exploring the advantages of magnetic material properties, allow friction free suspensions without the need of expensive electronics and control systems. The simplicity makes such type of bearings extremely attractive to different engineering applications. Passive magnetic bearings are normally manufactured using permanent magnets magnetized either axially or radially. The properties of such bearings strongly depend on the magnet material, its magnetic polarization and the dimensions of the magnets used [3]. One of the first investigations concerning passive magnetic bearings with permanent magnets (magnetized radially or axially) have been done by Yonnet [4, 5].

The use of either 2-D and 3-D analytical calculations for the determination of the magnetic field or of the magnetic forces created between ring permanent magnets or numerical procedures are common approaches while designing such electro-mechanical machine element [6, 7, 8, 9]. Some authors have also proposed semi-analytical expressions of the magnetic field created by ring permanent magnets [10, 11] in order to reduce the high computational costs. Methods for calculating such forces and additionally stiffness coefficients among ring passive magnetic bearings are thoroughly treated in [12, 13]. Experimental validation of magnetic force models are presented and discussed in [14] using arrays of cylindrical permanent magnets.

An interpretation of Earnshaw's Theorem (1842) is that permanent magnetic levitation of a rigid body is impossible [15]. Instability and low damping are the two most important drawbacks of passive magnetic levitation. Nevertheless, since the beginning of the nineties a spinning top is offered in toy shops, able to rotate contactless for minutes over a permanent magnetic plate built by ring magnets. The interaction of the six degree of freedom of this fast top with the magnetic field is discussed in details in [16, 17] with the classical methods of rotor dynamics and gyroscopic stabilization. Additionally, other types of stabilization can be found in the literature, namely by means of passive electro-dynamical actuation - thoroughly theoretically investigated in [18, 19] and experimentally shown in [19] - or by classical active actuation, industrially adopted in small and large machines [20]. The linear and nonlinear vibration behaviour of simple rigid rotors [21] and simple spring-mass systems [22] interacting with passive magnetic rings is also theoretically as well as experimentally treated in the literature.

In this framework this paper gives two main theoretical and experimental contributions to the problem of rotors under passive magnetic levitation. Firstly, the modeling of passive multi-cylinder magnetic bearings (MCMB) is theoretically as well as experimentally investigated using two different approaches. It is worth highlight that there are several ways of calculating magnetic forces between rings and most engineering applications reported in the literature deal with several ring permanent magnets. MCMB can be designed by circumferentially distributing multiple axially-magnetized cylinders around the rotor, generating isotropic as well as anisotropic bearing stiffness. Several configurations of magnet distribution are theoretically as well as experimentally studied in this work. Secondly, the axial stabilization of the rotor is obtained by means of punctual contact to a mechanical clutch. The contact dynamics between rotor and clutch is thoroughly investigated. The reasons of the rotor unstable behavior, which loses its contact to the clutch, are explained. In the context, the importance of design parameters as residual unbalance, contact friction coefficient and clutch geometry are elucidated. Finally, an accurate prediction of the threshold of stability, i.e. maximum angular velocity before the rotor misses its contact to the clutch, is achieved by means of the nonlinear rotor-bearing model presented.

2. Physical System and Mechanical Model

The test-rig used for proving and verification of the concept and mathematical models of the proposed passive cylinder-magnet bearings is shown in Fig. 1. The device consists of six main parts which are:

- (1) Passive cylinder-magnet bearings
- (2) Imbalance ring with a screw
- (3) Passive rotating cylinder-magnets
- (4) Rotor
- (5) Punctual contact clutch
- (6) DC-motor

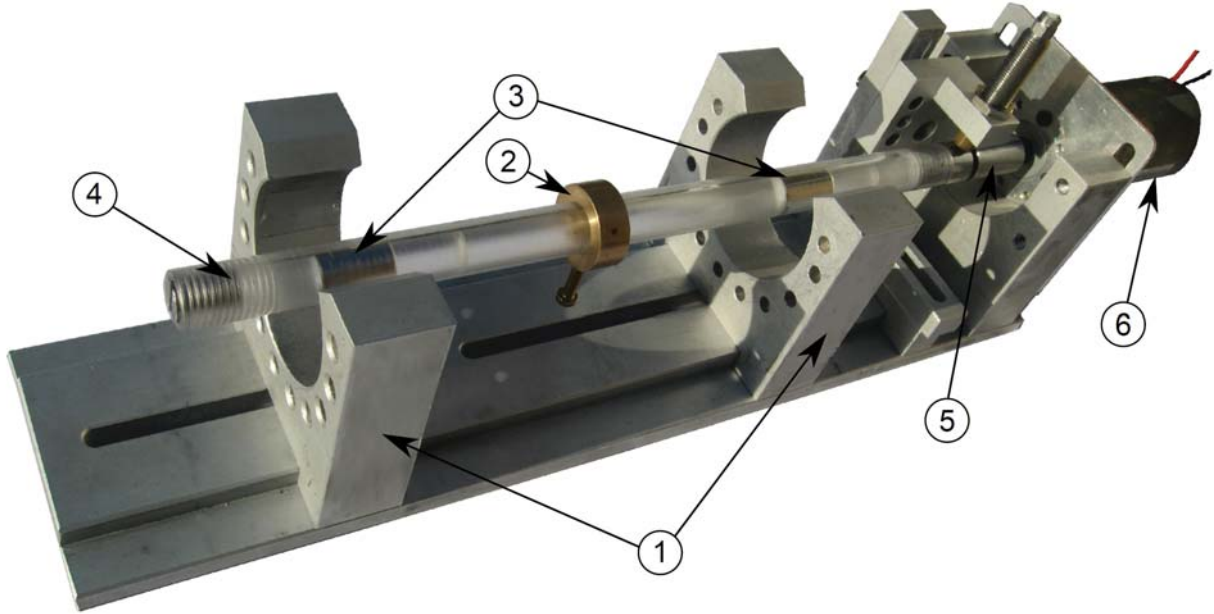


Figure 1: Experimental setup: (1) Passive cylinder-magnet bearings, (2) Imbalance ring with a screw, (3) Passive cylinder-magnets, (4) Rotor, (5) Punctual contact clutch, (6) DC-motor

The rotor (4) is levitated in the two horseshoe shaped bearing houses (1) which contain several cylinder-magnets arranged in a circular pattern. These permanent magnets form a magnetic field around the rotor which repels similar cylinder-magnets (3) embedded in the rotor and thereby counteracting the gravity forces. As the shape of the magnetic field generated by the bearings attempts to push the rotor in one of the axial direction the bearings has been shifted slightly to assure an axial force on the rotor toward the clutch (5). The clutch consists of a round metal disc with an inverted cone shape which works exclusively by friction forces between the clutch and the rotor tip. This clutch is firmly attached to a DC-motor (6) which can be used for controlling the rotational speed of the rotor. Four of the mentioned six main parts will in the following be described in more details.

2.1. Rotor

The rotor illustrated in Fig. 2(a) has a diameter of 15 mm and a length of 287 mm weighing 135 g. It is composed of 5 different materials, Plexiglas, brass, carbon steel, stainless steel and NdFeB magnets. The main part of the rotor consists of Plexiglas due to its non-magnetic properties and does therefore not interfere with the magnetic field from the two embedded cylinder-magnets, see Fig. 2(b). The tip at the end of the rotor, away from the embedded magnets, are made of carbon steel to be able to record the deflection of the rotor with the use of proximitors. The rotor end with the steel tip is chamfered with an inclination greater than that of the internal cone in the clutch to insure that there will only be a point contact between the rotor and the clutch. A brass ring with a screw is attached at the center of the rotor to simulate the effects of imbalance.

2.2. Passive Cylinder-Magnets

The magnets used in the bearings are sintered rare-earth neodymium magnets also known as NdFeB and are the strongest type of permanent magnets to date. The dimensions of the chosen cylinder-magnets for this test-rig are $\text{Ø}10 \times 20$ mm for both the bearing and rotor magnets and they are magnetized in their axial direction (z-direction in Fig.3(b)). A picture of one of the magnets is seen in Fig. 3(a) and Tab. 1 lists their magnetic properties. The information of interest in Tab. 1 is in this case the magnetic remanence, B_r . The correlation between the magnetic remanence and the magnetization constant M_c , which will be used later, is given as:

$$M_c = B_r \cdot \mu_0 \quad [\text{A/m}] \quad (1)$$

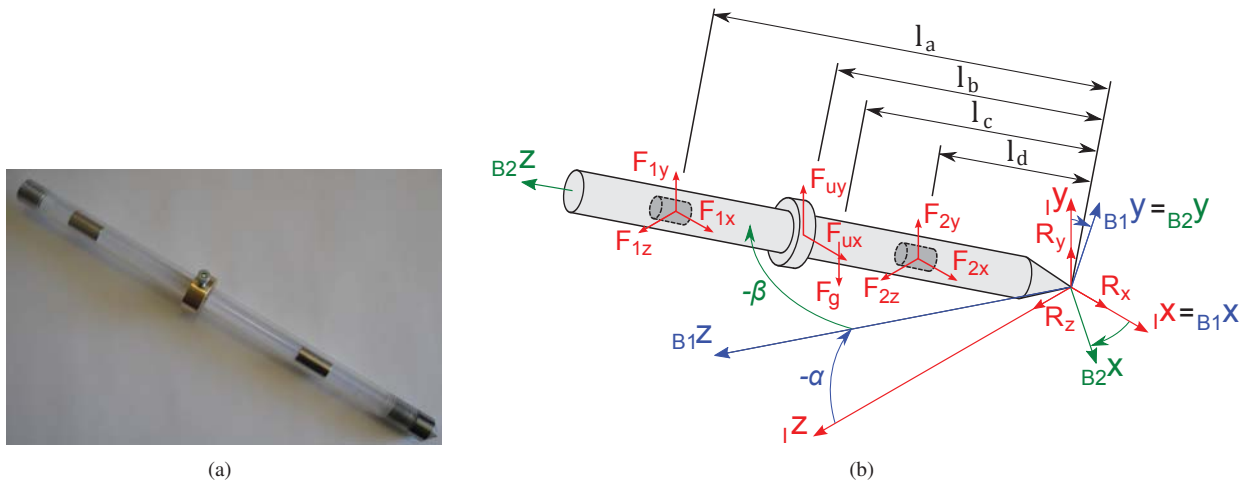


Figure 2: Rotor with embedded permanent cylinder-magnet and imbalance ring. (a) Physical system, (b) Mechanical model illustrating the parameters used in the mathematical modelling. F_1 & F_2 : magnetic reaction forces, F_u : imbalance forces, F_g : gravity force, R : clutch reaction forces, l_a : length to magnet 1, l_b : length to imbalance forces, l_c : length to gravity force, l_d : length to magnet 2.

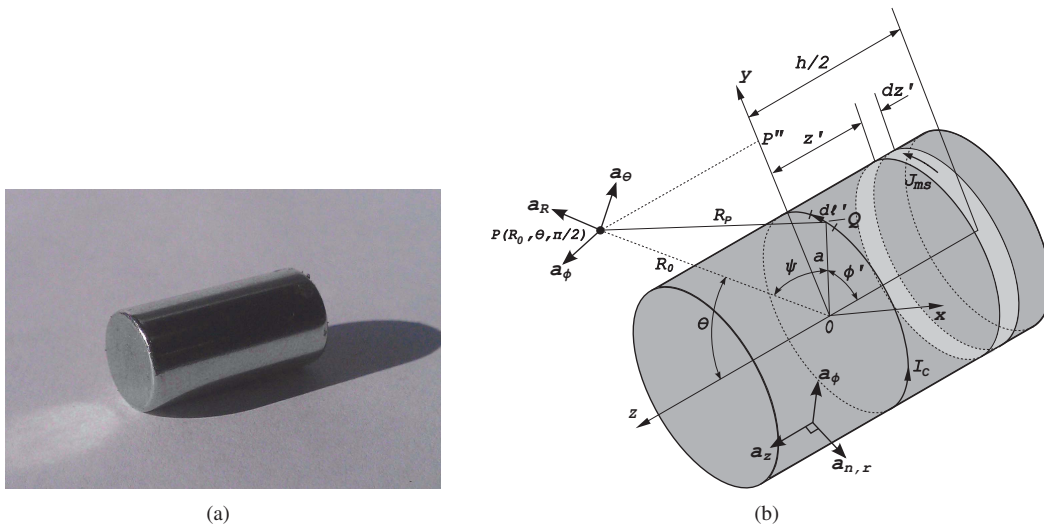


Figure 3: Cylinder-magnet used to build passive magnetic bearings with different configurations, illustrating the parameters used in the mathematical modelling.

Sintex Grade	Remanence B_r T [kG]		Coercivity HCB kA/m [kOe]		Intrinsic Coercivity H_{CI} kA/m [kOe]	Max. energy product $(B \cdot H)_{max}$ kJ/m ³ [MGoe]		Working temp. T_w L/D=0.7 °C
	Typical	min.	Typical	min.		Typical	min.	
SIX-N35	1.21 [12.1]	1.17 [11.7]	915 [11.5]	860 [10.8]	>955 [>12]	279 [35]	263 [33]	<80

Table 1: Magnetic properties provided by the company Sintex a/s

From the table it is seen that the magnetic remanence is in the range of 1.17 to 1.21 T, hence, the magnetization constant is determined to be in the range of 931 to 963 kA/m. These values will later be compared against experimental achieved results.

2.3. Passive Cylinder-Magnet Bearings

The passive cylinder-magnet bearing houses, Fig. 4, are made of aluminum due to its non-magnetic properties as not to interfere with the generated magnetic field. Holes have been machined into the horseshoe shaped bearing houses in an evenly spaced circular pattern where the cylinder-magnets can be placed in different configurations to generate different shapes of the bearing's magnetic field. Two different sizes of bearings have been made, Fig. 4(b) and Fig. 4(c), with two different magnet center diameters and thereby also a different maximum number of magnets. The large bearings have a magnet center diameter of 66 mm and the small bearings have a magnet center diameter of 46 mm.

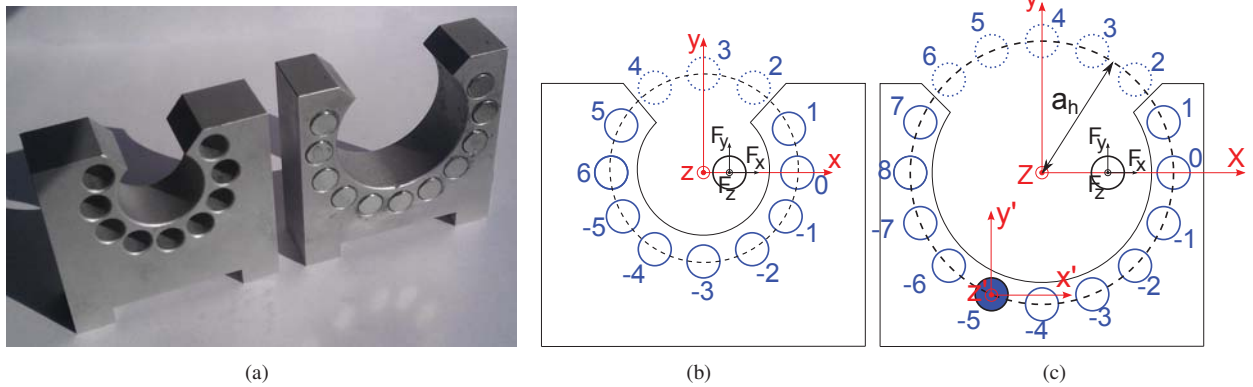


Figure 4: (a) Small and large permanent magnet bearing houses without and with permanent magnets. (b) Mechanical model and parameters for the small bearing. (c) Mechanical model and parameters for the large bearing.

2.4. Motor and Punctual Contact Clutch

The clutch, Fig. 5, is made of a round stainless steel bar where an inverted cone shape has been machined with a surface inclination $s \cong 0.57$, Fig. 5(b). The clutch has two main purposes:

- 1) to keep the rotor from moving in the axial direction
- 2) to rotate the rotor exclusively by friction forces between clutch and rotor

The clutch is firmly attached to the shaft of a DC-motor which can rotate the clutch and thereby the rotor making it possible to control the rotation speeds of the rotor.

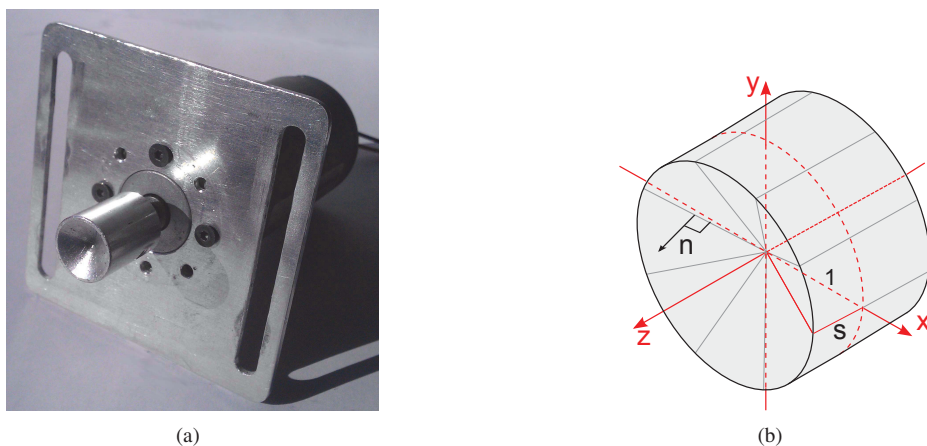


Figure 5: Motor and clutch.

3. Mathematical Modeling

The mathematical model of the test rig have been split up into three main parts: rotor model, clutch model and bearing model which in the following will be explained in more details but first the kinematics of the rotor and the clutch will be described.

3.1. Kinematics of Rigid Rotor and Punctual Contact Clutch

3.1.1. Rotor

The equations of motion of the rotor will be expressed in a moving coordinate system, here called B2, which moves with the rotor but does not rotate around the longitudinal axis of the rotors. The used coordinate systems are defined as shown in Fig. 2(b) where system I (red) is a fixed reference system. System B1 (blue) is defined as system I rotated by the angle α around its ${}_I X$ axis. System B2 (green) is defined as system B1 rotated by the angle β around its ${}_{B1} Y$ axis. In other words the equations of motion is expressed in Cardan angles, Ref.[23].

The transformation matrix from system I to system B1 and from system B1 to system B2 are:

$${}_{B1} \mathbf{T}_I = \begin{bmatrix} 1 & 0 & 0 \\ 0 & \cos(\alpha) & -\sin(\alpha) \\ 0 & \sin(\alpha) & \cos(\alpha) \end{bmatrix} \quad {}_{B2} \mathbf{T}_{B1} = \begin{bmatrix} \cos(\beta) & 0 & \sin(\beta) \\ 0 & 1 & 0 \\ -\sin(\beta) & 0 & \cos(\beta) \end{bmatrix} \quad (2)$$

The transformation matrix from system I to system B2 is therefore:

$${}_{B2} \mathbf{T}_I = {}_{B1} \mathbf{T}_I \cdot {}_{B2} \mathbf{T}_{B1} \quad (3)$$

Usually the rotor tip is positioned in the clutch center (0, 0, 0), but the rotor tip is able to slide at the clutch and actually also fly in free space. Therefore generally the rotor tip has the coordinates ${}_I \mathbf{r}_0 = (x, y, z)$. The position vectors from the tip of the rotor to the point of attack for the different forces illustrated in Fig. 2(b) are:

$${}_{B2} \mathbf{r}_{F_1} = \begin{pmatrix} 0 \\ 0 \\ l_a \end{pmatrix} \quad {}_{B2} \mathbf{r}_{F_U} = \begin{pmatrix} 0 \\ 0 \\ l_b \end{pmatrix} \quad {}_{B2} \mathbf{r}_g = \begin{pmatrix} 0 \\ 0 \\ l_c \end{pmatrix} \quad {}_{B2} \mathbf{r}_{F_2} = \begin{pmatrix} 0 \\ 0 \\ l_d \end{pmatrix} \quad (4)$$

The angular velocity of the system B2 is a sum of the time derivative of the angles α and β viewed as vectors.

$${}_{B2} \boldsymbol{\Omega} = {}_{B2} \dot{\boldsymbol{\alpha}} + {}_{B2} \dot{\boldsymbol{\beta}} = {}_{B2} \mathbf{T}_{B1} \cdot \begin{pmatrix} \dot{\alpha} \\ 0 \\ 0 \end{pmatrix} + \begin{pmatrix} 0 \\ \dot{\beta} \\ 0 \end{pmatrix} = \begin{pmatrix} \dot{\alpha} \cos \beta \\ \dot{\beta} \\ \dot{\alpha} \sin \beta \end{pmatrix} \quad (5)$$

The rotor angular velocity is equal to the angular velocity of the reference system plus the rotation of the rotor around its longitudinal axis (${}_{B2} z$ -axis).

$${}_{B2} \boldsymbol{\omega} = {}_{B2} \boldsymbol{\Omega} + {}_{B2} \dot{\boldsymbol{\gamma}} = \begin{pmatrix} \dot{\alpha} \cos \beta \\ \dot{\beta} \\ \dot{\alpha} \sin \beta + \dot{\gamma} \end{pmatrix} \quad (6)$$

The linear acceleration of the rotor center of gravity can expressed as:

$$\begin{aligned} {}_{B2} \mathbf{a} &= {}_{B2} \mathbf{T}_I \cdot {}_I \mathbf{a}_0 + {}_{B2} \boldsymbol{\Omega} \times ({}_{B2} \boldsymbol{\Omega} \times {}_{B2} \mathbf{r}_g) + {}_{B2} \dot{\boldsymbol{\Omega}} \times {}_{B2} \mathbf{r}_g \\ &= \begin{pmatrix} \ddot{x} \cos \beta + \ddot{y} \sin \alpha \sin \beta - \ddot{z} \cos \alpha \sin \beta + l_c \dot{\alpha}^2 \sin \beta \cos \beta + l_c \ddot{\beta} \\ \ddot{y} \cos \alpha + \ddot{z} \sin \alpha + 2l_c \dot{\alpha} \dot{\beta} \sin \beta - l_c \ddot{\alpha} \cos \beta \\ \ddot{x} \sin \beta - \ddot{y} \sin \alpha \cos \beta + \ddot{z} \cos \alpha \cos \beta - l_c \dot{\alpha}^2 \cos^2 \beta - l_c \ddot{\beta}^2 \end{pmatrix} \end{aligned} \quad (7)$$

3.1.2. Punctual Contact Clutch

The shape of the inverted cone in the clutch shown in Fig. 5(b) can be expressed as:

$$\mathbf{P}(u, \theta) = (u \cdot \cos \theta, u \cdot \sin \theta, s \cdot u), \quad u \in [0; 5 \text{ mm}], \theta \in [-\pi; \pi], \quad (8)$$

in Cartesian coordinates in reference system I. When the rotor tip is in contact with the clutch it is necessary to know the unit normal vector, \mathbf{n} , of the clutch in relation to friction as will be explained later on. In Cartesian coordinates in reference system I it can be written as:

$$\mathbf{n} = \left\{ \begin{array}{c} -\frac{s \cdot x}{\sqrt{s^2+1} \sqrt{x^2+y^2}} \\ -\frac{s \cdot y}{\sqrt{s^2+1} \sqrt{x^2+y^2}} \\ \frac{1}{\sqrt{s^2+1}} \end{array} \right\} \quad (9)$$

Furthermore it is given that $z = s \sqrt{x^2 + y^2}$ when the rotor is in contact with the clutch. By differentiating the rotor tip position at the clutch surface twice with respect to time the velocity, \dot{z} , and acceleration, \ddot{z} , in the z-direction are obtained as:

$$\begin{aligned} \dot{z} &= \frac{s}{\sqrt{x^2 + y^2}} (x\dot{x} + y\dot{y}) \\ \ddot{z} &= -\frac{\dot{z}^2}{s \sqrt{x^2 + y^2}} + \frac{s}{\sqrt{x^2 + y^2}} (\dot{x}^2 + \dot{y}^2 + x\ddot{x} + y\ddot{y}) \end{aligned} \quad (10)$$

The transformation matrix from the initial coordinates to the clutch coordinates are as follows:

$${}^k \mathbf{T}_I = \left[\frac{\partial \mathbf{P}}{\partial u} / \left\| \frac{\partial \mathbf{P}}{\partial u} \right\|} \quad \frac{\partial \mathbf{P}}{\partial \theta} / \left\| \frac{\partial \mathbf{P}}{\partial \theta} \right\|} \quad \mathbf{n} \right] = \begin{bmatrix} \frac{\cos(\theta)}{\sqrt{s^2+1}} & -\frac{u \sin(\theta)}{\sqrt{u^2}} & -\frac{sx}{\sqrt{s^2+1} \sqrt{x^2+y^2}} \\ \frac{\sin(\theta)}{\sqrt{s^2+1}} & \frac{u \cos(\theta)}{\sqrt{u^2}} & -\frac{sy}{\sqrt{s^2+1} \sqrt{x^2+y^2}} \\ \frac{s}{\sqrt{s^2+1}} & 0 & \frac{1}{\sqrt{s^2+1}} \end{bmatrix} \quad (11)$$

It is important to highlight that the normal vector, \dot{z} and \ddot{z} has singularities at $(x, y) = (0, 0)$. To get around this it is assumed that the coupling is a flat plate as long as $\sqrt{x^2 + y^2} \leq 0.25 \text{ mm}$. This means that there will be an ‘‘artificial’’ and rough transition at 0.25 mm from the center of the coupling. The justification for this assumption is that in praxis neither the coupling nor the rotor will be completely pointy and have a more or less flat surface in the center as a result of manufacturing methods.

3.2. Rotor Model

The equations of motion of the rotor can be expressed by Newton’s second law and Euler’s moment equation, Ref. [24], where the summation of forces in Newton’s second law (the left hand side) can according to Fig. 2(b) be written as:

$$\begin{aligned} \sum {}_{B_2} \mathbf{F} &= {}_{B_2} \mathbf{T}_I \cdot ({}_I \mathbf{F}_1 + {}_I \mathbf{F}_2 + {}_I \mathbf{F}_g + {}_I \mathbf{R}) + {}_{B_2} \mathbf{F}_U \\ &= {}_{B_2} \mathbf{T}_I \cdot \left(\left\{ \begin{array}{c} F_{1x} \\ F_{1y} \\ F_{1z} \end{array} \right\} + \left\{ \begin{array}{c} F_{2x} \\ F_{2y} \\ F_{2z} \end{array} \right\} + \left\{ \begin{array}{c} 0 \\ -mg \\ 0 \end{array} \right\} + \left\{ \begin{array}{c} R_x \\ R_y \\ R_z \end{array} \right\} \right) + \left\{ \begin{array}{c} m_b r_b \dot{\gamma}^2 \cos \gamma \\ m_b r_b \dot{\gamma}^2 \sin \gamma \\ 0 \end{array} \right\} \end{aligned} \quad (12)$$

The right hand side of Newton’s second law can be written as:

$$\begin{aligned} m \cdot {}_{B_2} \mathbf{a} &= m \cdot \left({}_{B_2} \mathbf{T}_I \cdot {}_I \mathbf{a}_0 + {}_{B_2} \mathbf{\Omega} \times ({}_{B_2} \mathbf{\Omega} \times {}_{B_2} \mathbf{r}_g) + {}_{B_2} \mathbf{\Omega} \times {}_{B_2} \mathbf{r}_g + \underbrace{2\mathbf{\Omega} \times \mathbf{v}_{rel}}_{=0} + \underbrace{\mathbf{a}_{rel}}_{=0} \right) \\ &= m \cdot \left\{ \begin{array}{c} \ddot{x} \cos \beta + \ddot{y} \sin \alpha \sin \beta - \ddot{z} \cos \alpha \sin \beta + l_c \dot{\alpha}^2 \sin \beta \cos \beta + l_c \ddot{\beta} \\ \ddot{y} \cos \alpha + \ddot{z} \sin \alpha + 2l_c \dot{\alpha} \dot{\beta} \sin \beta - l_c \ddot{\alpha} \cos \beta \\ \ddot{x} \sin \beta - \ddot{y} \sin \alpha \cos \beta + \ddot{z} \cos \alpha \cos \beta - l_c \dot{\alpha}^2 \cos^2 \beta - l_c \ddot{\beta} \end{array} \right\} \end{aligned} \quad (13)$$

where the two last terms is zero as the rotor is modeled as a rigid body and thereby the relative velocity and acceleration of the center of mass is zero. By setting Eq. (12) equal to Eq. (13) the first 3 of the needed 6 equations have been

derived. The last 3 equations are to be found using Euler's moment equation.

The summation of the moments around origo (the left hand side) can be expressed as:

$$\begin{aligned} \sum_{B_2} \mathbf{M}_0 &= \begin{Bmatrix} 0 \\ 0 \\ l_a \end{Bmatrix} \times ({}_{B_2} \mathbf{T}_I \cdot {}_I \mathbf{F}_1) + \begin{Bmatrix} 0 \\ 0 \\ l_b \end{Bmatrix} \times {}_{B_2} \mathbf{F}_U + \begin{Bmatrix} 0 \\ 0 \\ l_c \end{Bmatrix} \times ({}_{B_2} \mathbf{T}_I \cdot {}_I \mathbf{F}_g) + \begin{Bmatrix} 0 \\ 0 \\ l_d \end{Bmatrix} \times ({}_{B_2} \mathbf{T}_I \cdot {}_I \mathbf{F}_2) + \begin{Bmatrix} 0 \\ 0 \\ \tau \end{Bmatrix} \\ &= \begin{Bmatrix} -M_z \sin \alpha - l_b m_b r_b \dot{\gamma}^2 \sin \gamma - M_y \cos \alpha \\ M_y \sin \alpha \sin \beta - M_z \cos \alpha \sin \beta + M_x \cos \beta + l_b m_b r_b \dot{\gamma}^2 \cos \gamma \\ \tau \end{Bmatrix} \end{aligned} \quad (14)$$

where

$$\begin{Bmatrix} M_x \\ M_y \\ M_z \end{Bmatrix} = \begin{Bmatrix} l_a F_{1x} + l_d F_{2x} \\ l_a F_{1y} + l_d F_{2y} - l_c mg \\ l_a F_{1z} + l_d F_{2z} \end{Bmatrix} \quad (15)$$

is the x , y and z moment components defined in reference system I and τ is the moment transferred to the rotor through the clutch.

The right hand side of the Euler moment equation can be derived to:

$$\begin{aligned} {}_{B_2} \mathbf{I}_0 \cdot \frac{d}{dt} {}_{B_2} \boldsymbol{\omega} + {}_{B_2} \boldsymbol{\Omega} \times ({}_{B_2} \mathbf{I}_0 \cdot {}_{B_2} \boldsymbol{\omega}) + {}_{B_2} \mathbf{r}_g \times (m \cdot {}_{B_2} \mathbf{a}_0) &= \\ \begin{Bmatrix} -l_c m (\ddot{z} \sin \alpha + \ddot{y} \cos \alpha) + (I_z - I_y - I_x) \dot{\beta} \dot{\alpha} \sin \beta + I_x \ddot{\alpha} \cos \beta + I_d \dot{\beta} \dot{\gamma} \\ l_c m (\dot{y} \sin \alpha \sin \beta - \dot{z} \cos \alpha \sin \beta + \dot{x} \cos \beta) + (I_x - I_z) \dot{\alpha}^2 \cos \beta \sin \beta - \dot{\alpha} \dot{\gamma} I_z \cos \beta + I_y \ddot{\beta} \\ I_z \ddot{\alpha} \sin \beta + (I_z + I_y - I_x) \dot{\alpha} \dot{\beta} \cos \beta + I_z \dot{\gamma} \end{Bmatrix} \end{aligned} \quad (16)$$

where the inertia matrix ${}_{B_2} \mathbf{I}_0$ is diagonal because of symmetry. Setting Eq. (14) equal to Eq. (16) the last three needed equation of motion for the rotor are obtained.

3.3. Punctual Contact Clutch Model and Representation of Contact Forces, $\mathbf{R} = \{R_x, R_y, R_z\}$

The interaction between the rotor and the clutch can be explained by 3 different states. The first state is when there is sufficient friction between the rotor and the clutch thereby restricting the rotor from sliding on the clutch surface. The second state is when the friction between the rotor and the clutch is not sufficient resulting in movement of the rotor tip on the clutch surface. The third state is when there is not any contact between the clutch and the rotor as the rotor have been pushed away from the clutch. Before commenting further on the three states the normal reaction force and tangential force are defined as, see Fig. 2(b) and Fig. 5(b):

Normal reaction force:

$$R_n = \|\mathbf{R}_n\| = \mathbf{R} \cdot \mathbf{n} \quad \text{where} \quad \mathbf{R} = \begin{Bmatrix} R_x \\ R_y \\ R_z \end{Bmatrix} \quad (17)$$

The tangential reaction force:

$$R_t = \|\mathbf{R}_t\| = \|\mathbf{R} - \mathbf{R}_n\| \quad \text{where} \quad \mathbf{R}_n = (\mathbf{R} \cdot \mathbf{n}) \mathbf{n} \quad (18)$$

3.3.1. State I

In state I the friction between the rotor and the clutch is sufficient to restricting the rotor from sliding on the clutch surface. This can be described as:

$$\mu R_n \geq R_t \quad (19)$$

As the end of the rotor is not sliding on the clutch means that it is either in the center (0,0,0) or rotating in circles in a plane normal to the z-axis. As the clutch has a constant rotational speed $\dot{\gamma}$ the velocity and acceleration of the rotor tip can be written as:

$$\ddot{x} = -\dot{\gamma}^2 x, \quad \dot{x} = -\dot{\gamma} y, \quad \ddot{y} = -\dot{\gamma}^2 y, \quad \dot{y} = \dot{\gamma} x \quad (20)$$

As the rotor is not moving in the z-direction \ddot{z} must be zero and the remaining six unknowns, $\ddot{\alpha}$, $\ddot{\beta}$, R_x , R_y , R_z and τ , can be determined by the six equation of motion described in Sec. 3.2. After solving, it has to be checked if Eq. (19) is valid. Otherwise the rotor must be in one of the other mentioned states.

3.3.2. State II

In state II the friction between the rotor and the clutch is not sufficient to prohibit the rotor from sliding on the clutch surface. The friction force is now directly dependent on the tangential force and can be written as:

$$\mu R_n = R_t \quad (21)$$

It is in the calculation assumed that the kinematic and static coefficient of friction has the same value. In this state the friction force is opposite the relative motion, \mathbf{v}_{rel} , between the rotor end and the clutch. To describe this both the relative speed and reaction forces are to be transformed to a coordinate system that follows the surface of the clutch. In this coordinate system it can be written as:

$${}_K R_1 + K \cdot {}_K v_{1,rel} = 0 \quad \text{and} \quad {}_K R_2 + K \cdot {}_K v_{2,rel} = 0 \quad (22)$$

where $({}_K R_1, {}_K R_2, {}_K R_3) = {}_K \mathbf{R} = {}_K \mathbf{T}_I \cdot \mathbf{R}$ and similar $({}_K v_{1,rel}, {}_K v_{2,rel}, {}_K v_{3,rel}) = {}_K \mathbf{v}_{rel} = {}_K \mathbf{T}_I \cdot \mathbf{v}_{rel}$. Assuming initially that the positive constant K is known the eight unknowns, \ddot{x} , \ddot{y} , $\ddot{\alpha}$, $\ddot{\beta}$, R_x , R_y , R_z and τ can be found with the six equation of motion from Sec. 3.2 together with the two equations, Eq. (22). The value of K is determined iteratively so that Eq. (21) also is satisfied.

However a problem arise in the transition between state I and II as the relative velocity \mathbf{v}_{rel} between the rotor end and the clutch is zero. This will result in an infinite number of solutions to Eq. (22). To overcome this transition problem Eq. (22) is solved for the reaction forces, ${}_K R_1$ and ${}_K R_2$ under the assumption that the rotor is still in state I. This can be written as:

$${}_K R_1 - K \cdot {}_K R_1^{(1)} = 0 \quad \text{and} \quad {}_K R_2 - K \cdot {}_K R_2^{(1)} = 0 \quad (23)$$

where ${}_K R_1^{(1)}$ and ${}_K R_2^{(1)}$ is the reaction forces found under the assumption that the system is still in state I. This assumption allows the tangential force to change size but not direction in the transition between the two states and seams like a reasonable assumption.

3.3.3. State III

In state III the rotor and the clutch is no longer in contact with each other. The system is in this state if the normal force R_n in state I is zero or no solution for K in state II can be found. As there is not any contact between the rotor and clutch all the contact forces and moments, R_x , R_y , R_z and τ , between the rotor and the clutch are zero. This result in only six unknowns which can be solved by the six equation of motion defined in Sec. 3.2.

3.4. Cylinder-Magnet Bearing Model and Representation of Forces \mathbf{F}_1 and \mathbf{F}_2

Two different bearing models are proposed and will later be compared against each other and results experimentally achieved. The first model is an exact model without any assumptions and the other one is created with some minor assumptions to ease the computations.

3.4.1. Exact Solution of Magnetic Field - Method A

In this section an exact solution for the magnetic flux density \mathbf{B} around a cylinder-magnet is presented. This is found using an expression for the magnetic vector potential \mathbf{A} , because the curl of \mathbf{A} is \mathbf{B} (Ref. [25] p. 214):

$$\mathbf{A}(x, y, z) = \frac{\mu_0}{4\pi} \int_V \frac{\nabla \times \mathbf{M}_C}{R_p} dV + \frac{\mu_0}{4\pi} \int_A \frac{\mathbf{M}_C \times \mathbf{a}_n}{R_p} dA \quad (24)$$

For this kind of magnets, it is not possible to find an analytical solution, but it is possible to reduce the amounts of computations, in order to find a numerical solution, radically.

The cylinder-magnets in the bearings lies along the z -axis and they have a constant magnetization vector: $\mathbf{M}_c = (0, 0, M_c)$, see Fig. 3(b). The value of the magnetization constant M_c is found experimentally as will be shown in Sec. 4.2.2. Since $\nabla \times \mathbf{M}_c = \mathbf{0}$ the first integral in Eq. ((24)) is eliminated. $\mathbf{M}_c \times \mathbf{a}_n$ is only nonzero at the sides of the magnets and not on the end surfaces, see Fig. 3(b). Here $\mathbf{a}_n = (\cos \phi, \sin \phi, 0)$. Every points Q on the surface of the cylinder-magnet can be described as $Q = (a \cos \phi, a \sin \phi, \zeta)$. The distance R to an arbitrary point outside the magnet $P = P(x, y, z)$ from Q is

$$R_p = \left| \overrightarrow{QP} \right| = \sqrt{x^2 - 2ax \cos \phi + y^2 - 2ay \cos \phi + a^2 + (z - \zeta)^2} \quad (25)$$

With this in hand, it is possible to rewrite the vector potential:

$$\mathbf{A} = \frac{\mu_0}{4\pi} \int_A \frac{\mathbf{M}_c \times \mathbf{a}_n}{R_p} dA = \frac{aM_c\mu_0}{4\pi} \int_{-h/2}^{h/2} \int_{-\pi}^{\pi} \frac{(-\sin \phi, \cos \phi, 0)}{R_p} d\phi d\zeta \quad (26)$$

Now the curl is done in order to find \mathbf{B} , because it is not possible to do the double integration analytically.

$$\mathbf{B} = (B_x, B_y, B_z) = \nabla \times \mathbf{A} = \frac{aM_c\mu_0}{4\pi} \int_{-h/2}^{h/2} \int_{-\pi}^{\pi} \left(\frac{(z - \zeta) \cos \phi}{R_p^3}, \frac{(z - \zeta) \sin \phi}{R_p^3}, \frac{a - x \cos \phi - y \sin \phi}{R_p^3} \right) d\phi d\zeta \quad (27)$$

Because of rotation symmetry around the z -axis, y is set to zero, so the \mathbf{B} -field is only found in the xz -plane (represented by a star) for values of x higher than a . It is possible to show that B_y^* is zero (because of rotation symmetry). As mentioned it is not possible to do the double integrations analytically. Though, it is possible to integrate over the variable ϕ .

$$B_x^*(x, z) = \frac{M_c\mu_0}{2\pi} \int_{-h/2}^{h/2} \frac{z - \zeta}{R_2 x} \left[\left(\frac{2ax}{R_1^2} + 1 \right) E_E - E_K \right] d\zeta \quad (28)$$

and

$$B_z^*(x, z) = \frac{M_c\mu_0}{2\pi} \int_{-h/2}^{h/2} \frac{1}{R_2} \left[\left(\frac{2a(x+a)}{R_1^2} - 1 \right) E_E + E_K \right] d\zeta \quad (29)$$

where

$$R_1 = \sqrt{(x-a)^2 + (z-\zeta)^2}, \quad R_2 = \sqrt{(x+a)^2 + (z-\zeta)^2} = \sqrt{R_1 + 4ax}, \quad (30)$$

$$E_K = \text{EllipticK} \left(2 \frac{\sqrt{ax}}{R_2} \right) \quad \text{and} \quad E_E = \text{EllipticE} \left(2 \frac{\sqrt{ax}}{R_2} \right)$$

EllipticK and EllipticE are two functions called the 'Complete Elliptic Integral of the First Kind' and the 'Complete Elliptic Integral of the Second Kind' respectively. They are not algebraic functions, but are known to programs as Maple and MATLAB.

The integrals have to be calculated for multiple points in the xz -plane, then an interpolation can be used. In this work they are solved in the intervals of $x \in [a; 2a_h - a]$ and $z \in [-h; h]$. The adequate number of points in the grid is evaluated in a convergence analysis in section 4.1. Only half of the integrals are independent because of symmetry: $B_x^*(x, z) = -B_x^*(x, -z)$ and $B_z^*(x, z) = B_z^*(x, -z)$.

When interpolation functions of B_x^* and B_z^* are found, \mathbf{B} in space can be found this way

$$\mathbf{B} = (B_x, B_y, B_z) = \left(\frac{x}{R_3} B_x^*(R_3, z), \frac{y}{R_3} B_x^*(R_3, z), B_z^*(R_3, z) \right), \quad (31)$$

where $R_3 = \sqrt{x^2 + y^2}$.

3.4.2. Simplified Solution of Magnetic Field - Method B

This section will describe an analytical method for estimating the B-field from a cylinder-magnet by introducing some minor assumptions. As a consequence of the postulate $\nabla \cdot \mathbf{B} = 0$, the B-field can be expressed as the curl of another field, the vector magnetic potential \mathbf{A} , as shown in Eq. (32).

$$\mathbf{B} = \nabla \times \mathbf{A} \quad (32)$$

where the vector magnetic potential is defined for a current carrying loop as, Ref. [25]:

$$\mathbf{A} = \frac{\mu_0 I_c}{4\pi} \oint_{C'} \frac{d\mathbf{l}'}{R_p} \quad (33)$$

Figure 3(b), show a current carrying loop with a current I_c where the B-field in point P located at $P(R_0, \theta, \pi/2)$ is to be found. It can be written that:

$$d\mathbf{l}' = (-\mathbf{a}_x \sin \phi' + \mathbf{a}_y \cos \phi') a d\phi' \quad (34)$$

Due to symmetry, there will be another current element $I_c d\mathbf{l}'$ on the other side of the y-axis, that will contribute an equal amount to \mathbf{A} in the $-\mathbf{a}_x$ direction, but will cancel the contribution of $I_c d\mathbf{l}'$ in the \mathbf{a}_y , direction.

The vector magnetic potential \mathbf{A} in Eq. (33) can now be written in spherical coordinates as:

$$\mathbf{A} = \mathbf{a}_\phi \frac{\mu_0 I_c a}{2\pi} \int_{-\pi/2}^{\pi/2} \frac{\sin \phi'}{R_p} d\phi' \quad (35)$$

Solving this with the condition that $a^2 \ll R_0^2$ gives:

$$\mathbf{A} = \mathbf{a}_\phi \frac{\mu_0 I_c a^2}{4\pi R_0^2} \sin \theta \quad (36)$$

The B-field from a current carrying loop at point P can now be found by inserting Eq. (36) in Eq. (32). Solving this gives us:

$$\mathbf{B} = \frac{\mu_0 I_c b^2}{4\pi R_0^3} (\mathbf{a}_R 2 \cos \theta + \mathbf{a}_\theta \sin \theta) \quad (37)$$

Now only the equivalent current of a permanent magnet need to be determine to establish an expression for the B-field.

A permanent magnet can be thought of as consisting of small current carrying loops (magnetic dipoles), which all have been orientated in the same direction. By summing up all these magnetic dipoles \mathbf{m} over the volume \mathbf{V} of the magnet gives us the magnetization vector \mathbf{M}_c :

$$\mathbf{M}_c = \lim_{\Delta v \rightarrow 0} \frac{\sum_{k=1}^{n\Delta v} \mathbf{m}_k}{\Delta v} \quad (A/m) \quad (38)$$

where n is the number of atoms per volume. The current density for a magnet can be expressed by this magnetization vector as

$$\mathbf{J}_m = \nabla \times \mathbf{M}_c \quad (39)$$

$$\mathbf{J}_{ms} = \mathbf{M}_c \times \mathbf{a}_n \quad (40)$$

While assume that \mathbf{M}_c is uniform inside the magnet, the current of a neighbor dipole flows in the opposite direction, and thereby canceling each other out leaving no net current in the interior. Leaving only a net surface current density.

Figure 3(b) show a cylinder-magnet with a differential increment in the z-direction. Rewriting Eq. (40) in cylindrical coordinates gives

$$\begin{aligned} \mathbf{J}_{ms} &= (\mathbf{a}_z M_c) \times \mathbf{a}_r \\ \mathbf{J}_{ms} &= M_c \mathbf{a}_\phi \end{aligned} \quad (41)$$

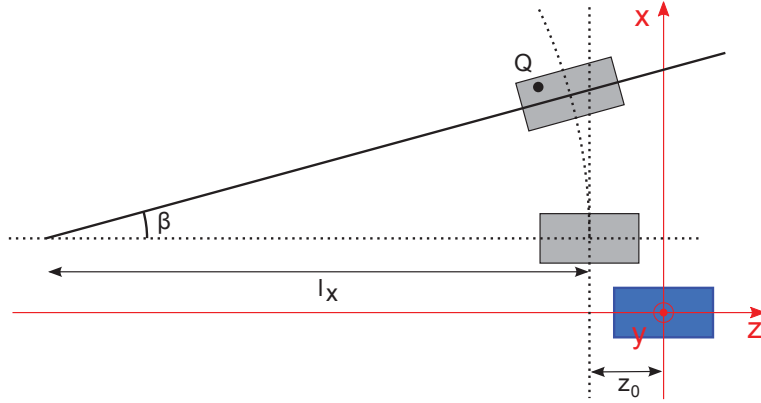


Figure 6: Sketch of bearing magnets and rotor magnets, when calculating magnetic forces, seen from the top.

By integrating over the entire length of the magnet, the total current density can be expressed as:

$$\mathbf{J}_{ms} = \int_{-h/2}^{h/2} M_c \mathbf{a}_\varphi dz = M_c \mathbf{a}_\varphi h \quad (42)$$

The equivalent current on the surface can therefore be expressed as $I_c = M_c h$. Substituted this into Eq. (37) gives the B-field in a given point from a current carrying loop, when the magnitude of the magnetization vector is known.

$$\mathbf{B} = \frac{\mu_0 M_c h a^2}{4\pi R_0^3} (\mathbf{a}_R 2 \cos \theta + \mathbf{a}_\theta \sin \theta) \quad (43)$$

The total magnetic field from all the magnets in the bearing can then be found by assuming that each magnet can be modeled as consisting of several evenly distributed current carrying loops along the magnets longitudinal direction. The total magnetic field in a point can then be found by superposition of the B-field contribution from every current loop in the bearing where the current in each loop is I_c divided by the number of loops in one magnet. A more detailed explanation can be found in Ref. [25].

3.4.3. Magnetic Forces Coupled to Rotor Movements - Method A

The found magnetic flux density has to be used in order to find the forces between the magnets in the bearing and the magnet in the rotor. The rotor can move freely in two dimensions, when only considering state I, which therefore acquire that the sum of forces acting on the rotor magnet is found on this surface (bend plane). Again a lot of computational power can be saved simply by a super-positioning of a few simpler cases.

Magnetic Forces. The calculation of the sum of forces acting on the rotor magnet is split into two parts. First the force \mathbf{F}_i from an arbitrary magnet in the bearing, called i , acting on the magnet in the rotor, called r , in some relevant positions, is found. The calculations shown here are for the large bearings.

A magnetic flux density creates a force acting on electrical currents. In the same way, passive magnets are affected, and mathematically they are transformed into electrical currents as it is shown here, Ref. [25] pp. 215 and 247, Ref. [26]:

$$\mathbf{F}_i = I_{cur} I_c \times \mathbf{B} = \int_{A_r} (\mathbf{M}_{C,r} \times \mathbf{a}_{n,r}) \times \mathbf{B}_i dA_r \quad (44)$$

First $\mathbf{M}_{C,r}$ and $\mathbf{a}_{n,r}$ is found in the fixed coordinate system I shown in Fig. 4(c) and Fig. 6, where r is only moving in half of the xz -plane. The rotor is fixed in the bottom and has a positive angle β to the z -axis as shown in Fig. 6. The transformation of the rotor coordinates, which is $B2$ with $y = 0$, into the fixed coordinates I is done by using ${}_I \mathbf{T}_{B2}$, where $\alpha = 0$.

All magnets are identical, which means that ${}_{B2}\mathbf{M}_{c,r} = (0, 0, M_c)$ in r -coordinates. $\mathbf{M}_{c,r} \times \mathbf{a}_{n,r}$ is again only non-zero at the sides of the magnet. The integration, Eq. (44), is done in the fixed coordinate system, and therefore a transformation is made:

$${}_I(\mathbf{M}_{c,r} \times \mathbf{a}_{n,r}) = {}_I\mathbf{T}_{B2} \cdot \left(\begin{pmatrix} 0 \\ 0 \\ M_c \end{pmatrix} \times \begin{pmatrix} \cos \phi \\ \sin \phi \\ 0 \end{pmatrix} \right) = \begin{pmatrix} -M_c \sin \phi \cos \beta \\ M_c \cos \phi \\ M_c \sin \phi \sin \beta \end{pmatrix} \quad (45)$$

\mathbf{B}_i is found in the previous section and are functions of the point in space $P(x, y, z)$ at the surface of r . $P(x, y, z)$ is found:

$$P(x, y, z) = - \begin{pmatrix} x_i \\ y_i \\ l_x + z_0 \end{pmatrix} + {}_I\mathbf{T}_{B2} \cdot \begin{pmatrix} a \cos \phi \\ a \sin \phi \\ l_x + \zeta \end{pmatrix} = \begin{pmatrix} -x_i + (l_x + \zeta) \sin \beta + a \cos \phi \cos \beta \\ -y_i + a \sin \phi \\ -l_x - z_0 + (l_x + \zeta) \cos \beta - a \cos \phi \sin \beta \end{pmatrix} \quad (46)$$

$(x_i, y_i) = (a_h \cos \frac{i\pi}{8}, a_h \sin \frac{i\pi}{8})$ are the coordinates from the center of the bearing to a magnet i in the bearing. The force \mathbf{F}_i acting on r from i is determined by integrating over ϕ and ζ , and by that cover all of the side of the magnet i :

$$\mathbf{F}_i = \int_{A_r} \begin{pmatrix} -M_c \sin \phi \cos \beta \\ M_c \cos \phi \\ M_c \sin \phi \sin \beta \end{pmatrix} \times \begin{pmatrix} B_{x_i} \\ B_{y_i} \\ B_{z_i} \end{pmatrix} dA_r = aM_c \int_{-h/2}^{h/2} \int_{-\pi}^{\pi} \begin{pmatrix} -B_{y_i} \sin \phi \sin \beta + B_{z_i} \cos \phi \\ B_{x_i} \sin \phi \sin \beta + B_{z_i} \sin \phi \cos \beta \\ -B_{x_i} \cos \phi - B_{y_i} \sin \phi \cos \beta \end{pmatrix} d\phi d\zeta \quad (47)$$

This double integration has to be done numerically, since $\mathbf{B} = \mathbf{B}(x, y, z)$ is an interpolation function. The integration has to be done for varying value of β in the interval $[0; \arctan \frac{a_h - a}{l_x + z_0}]$. For every value of β , \mathbf{F}_i is found for $i = 0, 1, \dots, 8$ for the large bearing.

Bearing force field. With these calculations in hand it is possible to find the total magnetic force acting on the magnet r from a choice of combinations of magnets i in the bearing. Because of symmetry it is possible to find the force from magnet $i = -7, -6, \dots, -1$:

$$F_x(i) = F_x(-i) \quad , \quad F_y(i) = -F_y(-i) \quad \text{og} \quad F_z(i) = F_z(-i), \quad (48)$$

cf. the numbering of the magnets i in the bearing.

The total force \mathbf{F}_T acting on r is a sum of the forces from the chosen configuration of bearing magnets. When the rotor is angled towards another magnet i^+ in the bearing, the total force can be found by using another specific configuration of bearing magnets and then make a transformation.

$$\mathbf{F}_T = \begin{bmatrix} \cos \frac{\pi i^+}{8} & -\sin \frac{\pi i^+}{8} & 0 \\ \sin \frac{\pi i^+}{8} & \cos \frac{\pi i^+}{8} & 0 \\ 0 & 0 & 1 \end{bmatrix} \cdot \mathbf{F}_T^+, \quad (49)$$

Here \mathbf{F}_T^+ is the total force acting on r , when moving towards bearing magnet i^+ , where the configuration of bearing magnets is rotated so it fits with a corresponding movement in the xz -plane towards bearing magnet $i^+ = 0$. This can be done for all $i^+ = -7, -6, \dots, 8$ bearing magnets, by which all valid positions of the rotor is represented well if an interpolation is done between the grid points.

The same method is used for the small bearing. Here the angles in Eq. (49) are $\frac{\pi i^+}{6}$, the same is the case for x_i and y_i in Eq. (46).

3.4.4. Magnetic Moments Coupled to Rotor Movements - Method A

The forces acting on the rotor magnet are not equally distributed, which results in a moment around the center of the magnet. These moments will of course also affect the movement of the rotor and will be visible in the Euler equation. As known, $\mathbf{M} = \mathbf{r} \times \mathbf{F}$, and therefore the moments can be found altering Eq. (44).

$$\mathbf{M}_i = \int_{A_r} \mathbf{r}_{oQ} \times (\mathbf{M}_{c,r} \times \mathbf{a}_{n,r}) \times \mathbf{B}_i dA_r \quad (50)$$

Here the arm \mathbf{r}_{oq} is the vector from the geometrical center of the magnet to dA_r :

$$\mathbf{r}_{oq} = {}_I\mathbf{T}_{B2} \cdot \begin{Bmatrix} a \cos \phi \\ a \sin \phi \\ \zeta \end{Bmatrix} = \begin{Bmatrix} \zeta \sin \beta + a \cos \phi \cos \beta \\ a \sin \phi \\ \zeta \cos \beta - a \cos \phi \sin \beta \end{Bmatrix} \quad (51)$$

The rest of the procedure of determining the moments is the same as for the forces with exception of Eq. (48), which is opposite for moments:

$$M_x(i) = -M_x(-i) \quad , \quad M_y(i) = M_y(-i) \quad \text{and} \quad M_z(i) = -M_z(-i), \quad (52)$$

Examples of the magnetic moments can be seen in Fig. 21 and Fig. 22.

3.4.5. Magnetic Forces Coupled to Rotor Movements - Method B

An electric charge q moving in a electric field \mathbf{E} and a magnetic field \mathbf{B} at a velocity \mathbf{u} can be described by Lorentz's force equation:

$$\mathbf{F} = q(\mathbf{E} + \mathbf{u} \times \mathbf{B}) \quad (53)$$

As no electric fields are present in the system, the equation can be reduced to:

$$\mathbf{F} = q\mathbf{u} \times \mathbf{B} \quad (54)$$

It is again assumed that each magnet can be thought of as several current carrying loops stacked on top of each other in the z-direction however for simplicity we will initially just look at one. Looking at a differential element $d\mathbf{l}$ of a loop with a cross section area S , and assume that there are N charge carriers per volume moving at a velocity of \mathbf{u} in the direction of $d\mathbf{l}$ it can written:

$$d\mathbf{F} = NqS |\mathbf{u}| d\mathbf{l} \times \mathbf{B} \quad (55)$$

As $NqS |\mathbf{u}|$ equals the current in the loop, Eq. (55) can be rewritten as:

$$d\mathbf{F} = I d\mathbf{l} \times \mathbf{B} \quad (56)$$

The total magnetic force can now be found by integrating over the entire loop C :

$$\mathbf{F} = I \oint_C d\mathbf{l} \times \mathbf{B} \quad (57)$$

where I was found in a previous section to:

$$I_c = M_c h \quad (58)$$

Inserting Eq. (58) into Eq. (57) gives:

$$\mathbf{F} = M_c h \oint_C d\mathbf{l} \times \mathbf{B} \quad (59)$$

which is the force on one current carrying loop in a B-field. The total force on one magnet is now found by summation of the force contribution for all the loops on the rotor magnet. Again the current in each loop on the magnet is I_c divided by the number of loops in the magnet.

3.4.6. Magnetic Moments Coupled to Rotor Movements - Method B

As mentioned in Sec. 3.4.4 the forces acting on the rotor magnet are not equally distributed, which results in a moment around the center of the magnet. This has of course to be taken into account even thou its effect on the system might be fairly small. It is again known that the moment can be calculated as:

$$\mathbf{M} = \mathbf{r} \times \mathbf{F} \quad (60)$$

By use of this the moment contribution from a single current loop can be found as:

$$\mathbf{F} = M_c h \oint_C \mathbf{r}_{oq} \times (d\mathbf{l} \times \mathbf{B}) \quad (61)$$

where \mathbf{r}_{oq} is a vector pointing from the center of the magnet to $d\mathbf{l}$. By sum up all the moment contribution for all the current carrying loops in the magnet one can determine the total moment around the magnet center.

4. Theoretical and Experimental Results

In this section the described mathematical models will be validated through convergence analyses and comparisons with experimental data. Furthermore the models will be used to carry out simulations in order to find resonance frequencies and explain the instability phenomenon that the rotor exhibits at high angular velocities.

4.1. Convergence analyses

For Method A a convergence analysis has been carried out in order to determine appropriate grid lengths so that the magnetic forces have converged. Here there are three types of grids: (a) At the rotor in the bearing creating the B-field, (b) The B-field interpolation grid around the magnet in the rotor, and (c) the surface grid of the magnet in the rotor in order to determine the forces and moments. The analyses are done on the forces between two magnets with a radial distance (x) of 20 mm and a displacement in their length directions (z) of 4 mm. These values are comparable with the ones in the following experiments.

In (a) the grid is determined by the distances between the points where $\zeta \in [-h/2; h/2]$ is evaluated. The convergence results are shown in Fig. 7(a). The errors in repulsing forces are compared to a grid length of 0.2 mm. Here it is seen that the errors both in F_x and F_z should be below 1 % as long as the grid length is smaller than 2 mm, which is equivalent to 10 integration points.

In (b) the grid is two dimensional, one in $x \in [a; 2a_h - a]$ and one in $z \in [-h; h]$. Fig. 7(b) shows that errors do not behave as regularly as in (a), but that the errors should be below 1 %, when the grid length is chosen to be 1.5 mm. This is equivalent to around 40 times 25 points for the large bearing.

In (c) the grid is again two dimensional, one in $\phi \cdot a \in [-a\pi; a\pi]$ and one in $\zeta \in [-h/2; h/2]$. Figure 7(c) shows that a grid length of 1.5 mm should give errors less than 1 % equivalent to 21 times 14 grid points.

The following calculations with the use of method A are made with these found grid sizes.

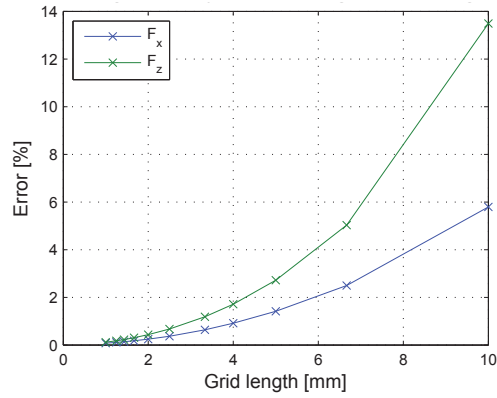
Likewise, a convergence analysis has been performed for Method B. Now it is investigated how many points are needed around each current carrying loop as well as how many current carrying loops are needed per magnets to predict the forces with a high accuracy. The convergence analysis has been performed by evaluating the force between two magnets. Figure 8 show the results from the analysis of the needed number of points around each current loop when number of loops has been kept constant at 100 loops per magnet. What can be concluded from this is that increasing the number of points above 6 points per loop does not increase the accuracy significantly. However it has been chosen to continue with 10 points per loop to be sure that it has converged. Figure 9 show the results from the convergence analysis of the number of needed loops per magnet. It can be seen that it is possible to achieve results that only deviates 1% from the fully converged model when modeling with 100 loops per magnet which is the number of loops chosen to continue with. The reason for not choosing a higher number of loops is that the computation time needed will increase by the square of number of loops per magnet.

4.2. Parameters of Cylinder-Magnet Bearing

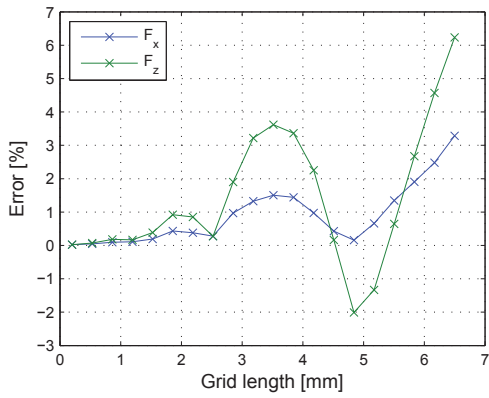
To verify the complete model the magnetic flux density and the force field had initially to be determined. This has been done through some simple experiments which will be explained below but before the magnetic flux density and the force field can be determined theoretically the magnetization M_C of the magnets had to be found experimentally. These simple experiments were also used for comparing the two methods (A: exact and B: simplified) for predicting the magnetic flux density.

4.2.1. Magnetic B-Field

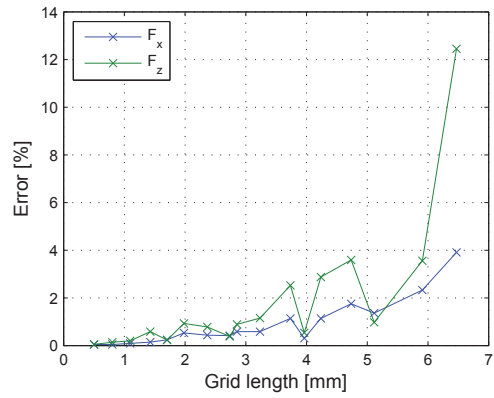
The test setup for measuring the **B** field around a magnet and determination of the magnetization constant M_C is shown in Fig. 10 where a Hall sensor has been fixed to a table (1). The test magnet has then been fixed on a horizontal brass rod (2) which is firmly attached to a vertical-electric ruler (3). The Hall sensor has then been connected to a power supplier (4) as input and a voltmeter (5) as output. The distance between the center of the magnet and the Hall-sensor has been varied in steps between 10 mm and 50 mm and the measured magnetic field density from the Hall-sensor has been recorded. The measured values of the magnetic field density from four different test magnets have been plotted in Fig. 11 together with their mean value. The magnetization constant M_C has been determined using the mean value of the measurements.



(a) B-field grid on first magnet



(b) B-field grid around second magnet



(c) force grid on second magnet

Figure 7: Convergence analysis on the grid lengths used in the evaluation of Method A.

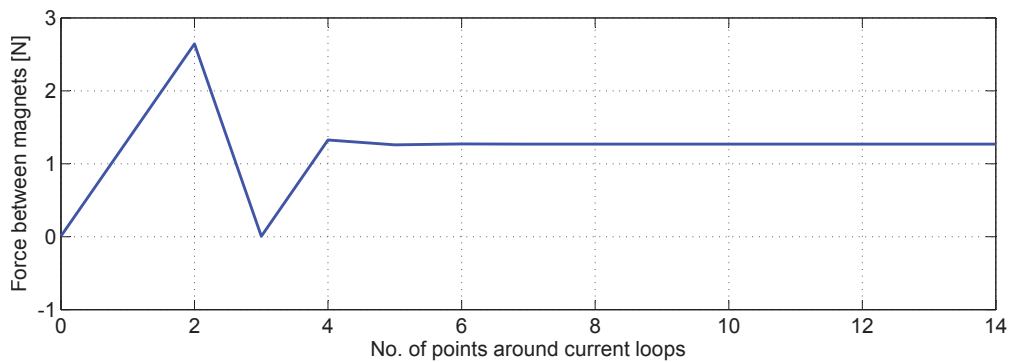


Figure 8: Convergence analysis of needed no. of points around current loops

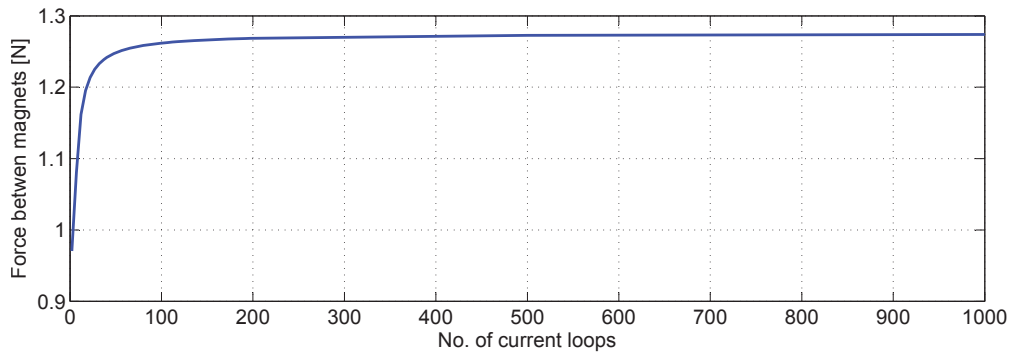


Figure 9: Convergence analysis of needed no. of current loops per magnet

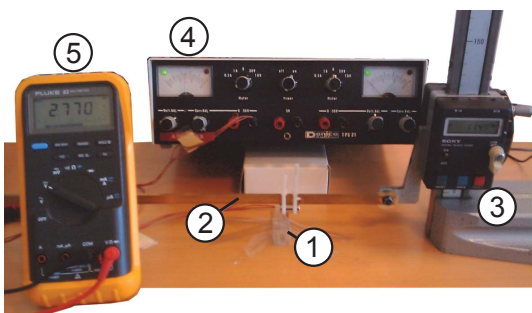


Figure 10: Test setup for measuring magnetic fields. (1) Hall sensor, (2) Brass rod, (3) Vertical-electric ruler, (4) Power supplier, (5) Voltmeter

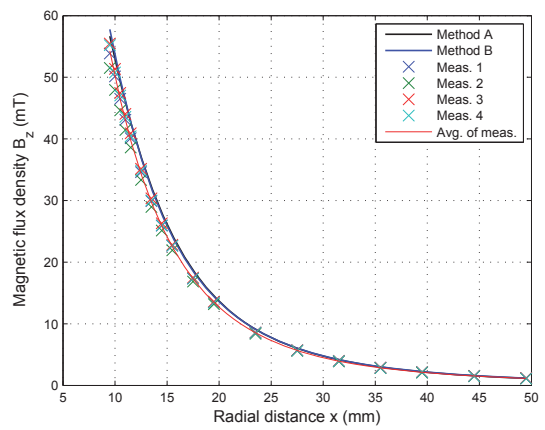


Figure 11: Comparison of experimental and theoretical achieved magnetic fields

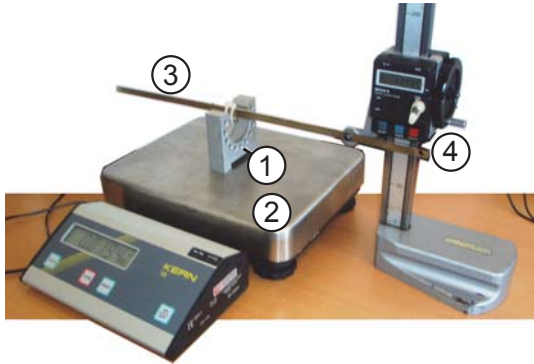


Figure 12: Test setup for measuring magnetic force. (1) Bearing house, (2) Scale, (3) Brass rod, (4) Vertical-electric ruler

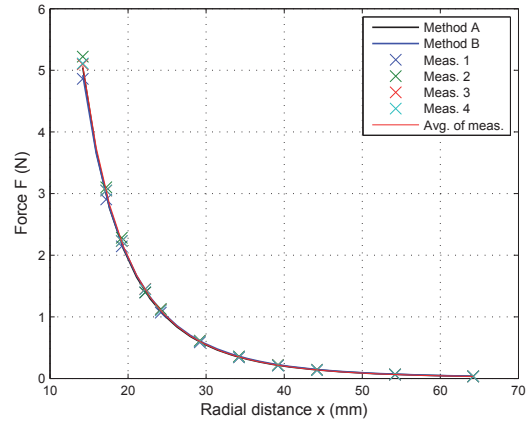


Figure 13: Comparison of experimental and theoretical achieved magnetic forces

4.2.2. Magnetic Forces

The test setup used for measuring the repulsive force between two magnets is shown in Fig. 12. A permanent magnet has been fixed in the bottom hole of one of the bearing houses (1) which is made of aluminum. Under the bearing house there was a scale (2), which made it possible to record the force exposure in terms of weight change. The second magnet had then been fixed on a horizontal brass rod (3) which was firmly attached to a vertical-electric ruler (4), making it possible to modify and record the distances.

The distance between the centers of the two magnets has then been varied in steps between 15 mm and 65 mm and the measured weight change from the scale has been recorded. The measured values of the weight change from four different test magnets converted into force exposure have been plotted in Fig. 13 together with their mean value.

As seen in Fig. 13 it has been possible to determine M_c for both methods A and B, so the graphs are very accurately on top of the measurements. It can actually be difficult to distinguish between the black, blue and red line, representing method A, method B and the measurements mean. The determined magnetization however is different for each of the methods:

$$M_{c,A} = 9.35 \cdot 10^5 \frac{A}{m} \quad \text{and} \quad M_{c,B} = 9.65 \cdot 10^5 \frac{A}{m} \quad (62)$$

$M_{c,B}$ varies 3% from method A, which can be explained by the approximations that are made, as described in Sec. 3.4.2. Apart from the different magnetizations the two different methods do not differ from each other. Comparing the experimental found values for the magnitude of magnetization vector with the one provided by the manufacture, Sec. 2.2, it can be seen that the values correspond very well with each other.

4.3. Verification of the Principle of Superposition for Magnetic Forces

Several experiments have been performed to verify the possibility of using the principle of superposition for magnetic forces as proposed in the theory section. These experiments are similar to the one explained in previous section where the force was measured on a scale however several magnets have now been placed in the bearing house at the same time. Figure 14 shows the results from these experiments where the forces in the y-direction has been measured as a function of the displacement of the rotor magnet in the y and z direction. A simulated surface plot has been plotted on top of the experimentally achieved curves where it can be seen that there are an almost excellent coherence between the achieved results. Looking a bit closer at the two curves, Fig. 15 ($z = 0$ mm) and Fig. 16 ($z = 10$ mm) reveals however that there are a tiny deviation between the simulation and the experiment for the one with the 10 mm shift. Assuming that the magnet during the experiment was turned $\beta = 0.75^\circ$ which has been simulated in simulation 2 one would get a perfect fit between the curves. This is a highly plausible error as it has no been possible to detect such small angular misalignments in the test setup. To verify that the principle of superposition also apply

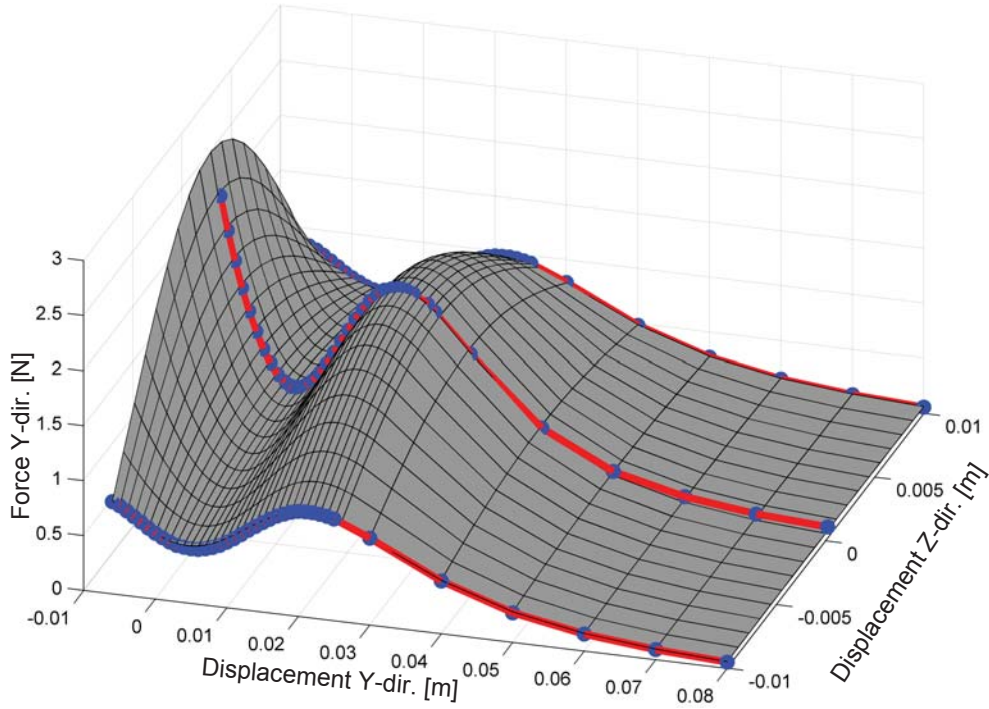


Figure 14: Force in y-dir. when rotor magnet is displaced in the y-dir. and z-dir., $x = 0$, Bearing magnet configuration: [1 5 -1 -3 -5], small bearing. See Fig.4(b). Gray surface is simulated and red lines with blue markers are experimentally measured values.

to the forces in the axial direction a similar experiment has been performed where the forces in the z-direction has been measured as a function of the displacement in the z-direction. The results from this experiment together with a simulated surface plot are shown in Fig. 17 and it can again be seen that there is a very good coherence between the results. It is therefore concluded that the principle of superposition is valid for summing up magnetic forces on current loops and thereby permanent magnets.

4.4. Coupled Rotor-Bearing Statics and Linear and Nonlinear Dynamics

To verify the proposed mathematical models several experiments were made with different configuration of the magnetic bearings including two different sizes of bearing houses. Table 2 shows the configurations of the three experiments that were made to verify the models. The magnets are numbered according to Fig. 4(b) and Fig. 4(c).

4.4.1. Natural Frequencies and Mode Shapes

The natural frequencies of the rotor have been measured and simulated using small perturbation to the rotor and evaluating its movements around its equilibrium position. The results from these experiments and simulations are shown in Tab. 2. From the table it can be seen that the frequencies only deviates approximately 10% from the measured values which must be concluded to be an acceptable deviation considering the rapid change in radial forces if there are just a small error in the shift z_0 of the bearings. For example if $z_{0,1}$ is shifted 0.6 mm in the simulation in respect to experiment 1, the simulation predicts natural frequencies that deviates only up to 5 % from the experiments and not up to 13 % as listed in the table.

Figure 18 shows the two first mode shapes from experiment 1 where it is possible to detect the gyroscopic effect as the path of the rotors nodal points create an ellipse rather than just moving in a straight line. Further more it can be seen that the two modes act in the horizontal and the vertical plane. This is due to the configuration of the bearing which is symmetric around the yz-plane. Had it not been configured in at symmetric way this would not be the case and the modes would not follow the horizontal and the vertical plane.

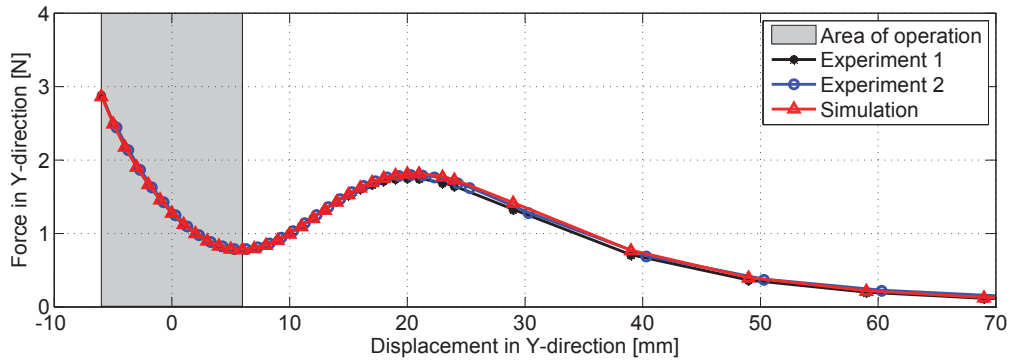


Figure 15: Force in y-dir. when rotor magnet is displaced in the y-dir., $x = 0, z = 0$, Bearing magnet configuration: [1 5 -1 -3 -5], small bearing. See Fig.4(b).

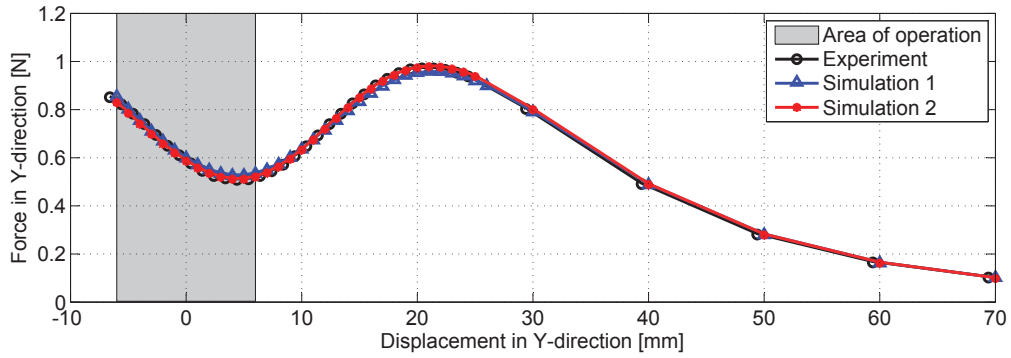


Figure 16: Force in y-dir. when rotor magnet is displaced in the y-dir., $x = 0, z = 10$, Bearing magnet configuration: [1 5 -1 -3 -5], small bearing. See Fig.4(b). Simulation 1: $\alpha = 0.0^\circ, \beta = 0.0^\circ$, Simulation 2: $\alpha = 0.0^\circ, \beta = 0.75^\circ$

Experiment	1	2	3
Setup			
$z_{0,1}$ (mm)	8	8	2
$z_{0,2}$ (mm)	-	5	5
Bearing 1	small	small	large
Bearing 2	-	large	large
Magnets 1	-5, -3, -1, 1, 5	-5, -3, -1, 1, 5	-6, -4, -2, 1, 7
Magnets 2	-	-6, -2, 1, 7,	-6, -4, -2, 1, 7
Natural frequency			
<i>Measured (Hz) mode 1</i>	4.0	4.0	4.3
<i>Simulated (Hz) mode 1</i>	4.5	3.7	4.7
<i>Deviation (%) mode 1</i>	13	-8	9
<i>Measured (Hz) mode 2</i>	7.3	7.6	5.8
<i>Simulated (Hz) mode 2</i>	8.0	8.4	5.9
<i>Deviation (%) mode 2</i>	10	11	2

Table 2: The experiment set-ups and natural frequencies. The first two rows (z_0) denotes the offset between the rotor and the bearing magnets. Index 1 is the bearing furthest away from the clutch. The next two rows indicates whether it is a large or small bearing that was used. The next two rows indicates where the magnets were added in the bearing, see numbering in figure 4(b) and 4(c). The last lines denote the simulated and measured natural frequencies.

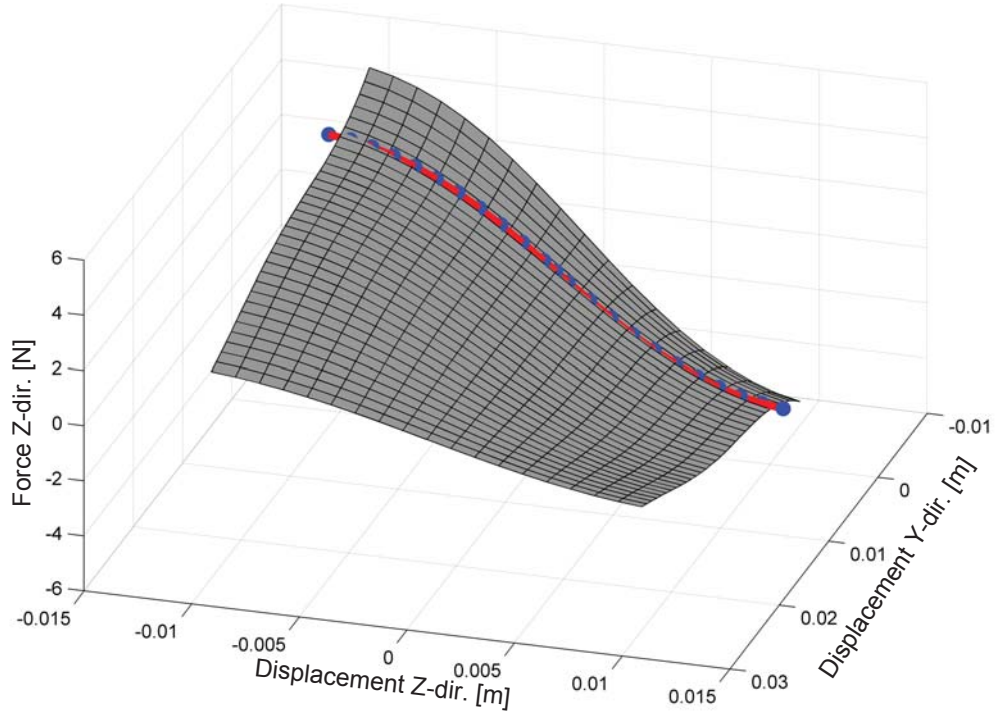


Figure 17: Force in z-dir. when rotor magnet is displaced in the y-dir. and z-dir., $x = 0$, Bearing magnet configuration: [1 5 -1 -3 -5], small bearing. See Fig.4(b). Gray surface is simulated and red lines with blue markers are experimentally measured values.

To give an idea of the nonlinearities of these kinds of bearings the force and moment intensity for experiment 2 has been plotted in Fig. 19, Fig. 20, Fig. 21 and Fig. 22. In these figures the force and moment intensity in the z-direction is indicated by colors and the force and moment intensity and vector direction in the xy-plane is indicated by arrows.

4.4.2. Stability and Instability - “Punctual Contact Clutch - Rotor”

At a given rotational speed an instability phenomena occurs where the rotor is being pushed away from the clutch and a good distance along its axial direction. One interesting element of this instability phenomenon is that the rotor exhibits an incredibly stable behavior prior to being shot out of the test rig. An explanation for this phenomena can be found by taking a closer look at the forces between the rotor and clutch together with the geometry of the clutch. Through simulation, see Fig. 23(a) and 23(b), it is possible to show that the mean value of tangential reaction force R_t , in which the projection of the thrust force on the clutch surface, greatly depends on the rotational speed. The higher the rotational speed of the rotor becomes, the higher the mean value of the tangential force between the clutch and the rotor becomes. The mean value of the normal force R_n on the other hand hardly change size due to the rotational speed. This means that when the tangential force becomes large enough, so that it is equal to the friction force μR_n , the rotor will begin to slip and enters state II. Due to the inverted cone shape of the clutch such a slip will lead to a shift of the rotor in the axial direction resulting in smaller offset values, $z_{0,1}$ and $z_{0,2}$, between the bearings and the rotor magnets. When that happens the force, F_z , from both bearings become larger (numerically smaller) and eventually end up being positive. When the sum of F_z from the two bearings is positive, the rotor will be pushed away from the clutch and the unstable state has been reached, state III. The maximum angular velocity (threshold of stability) before rotor-clutch misses contact depends on the set-up: the number of magnets in the bearing and the shifts $z_{0,1}$ and $z_{0,2}$ of the bearings in relation to the rotor magnets and magnitude of imbalance.

Some assumptions have been made to the model for predicting the instability limit where one of them is, as mentioned in Sec. 3.3.2, that the clutch is modeled as being a flat plate, when $\sqrt{x^2 + y^2} < 0.25$ mm. Another assumption is that the instability limit in the model has been defined as the highest rotational speed at which the rotor is still in state I,

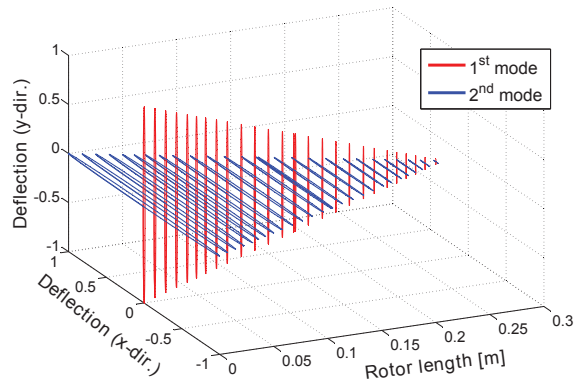


Figure 18: Two first theoretically calculated mode shapes from experiment 1 @ 72 Hz

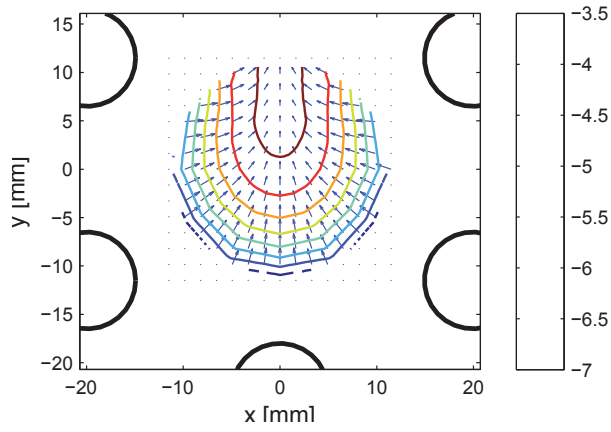


Figure 19: Theoretically calculated force field of small bearing from experiment 2

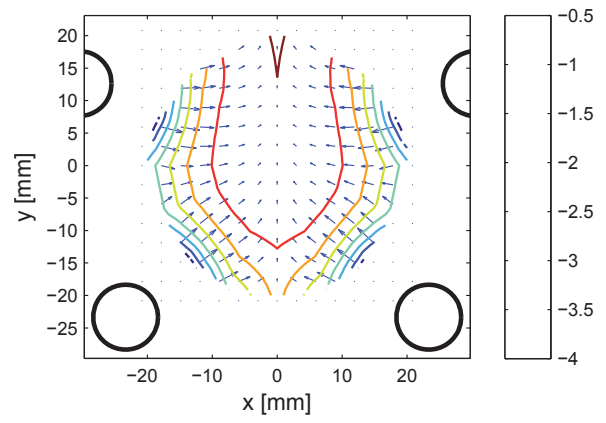


Figure 20: Theoretically calculated force field of large bearing from experiment 2

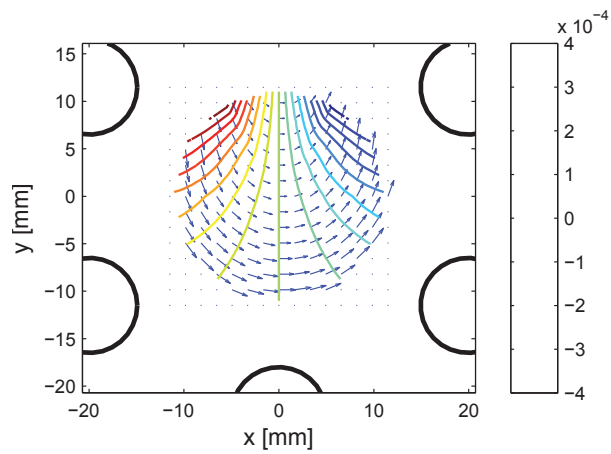


Figure 21: Theoretically calculated moment field of small bearing from experiment 2

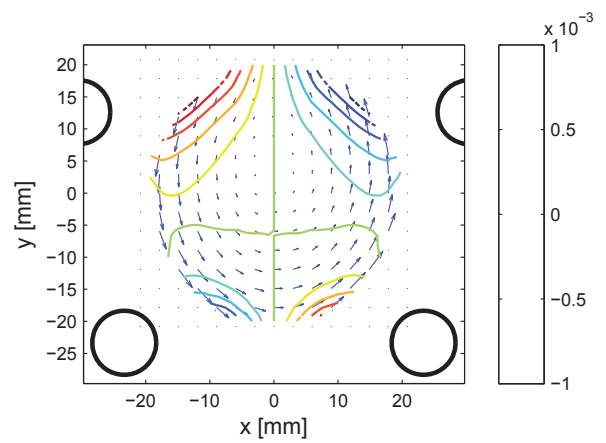


Figure 22: Theoretically calculated moment field of large bearing from experiment 2

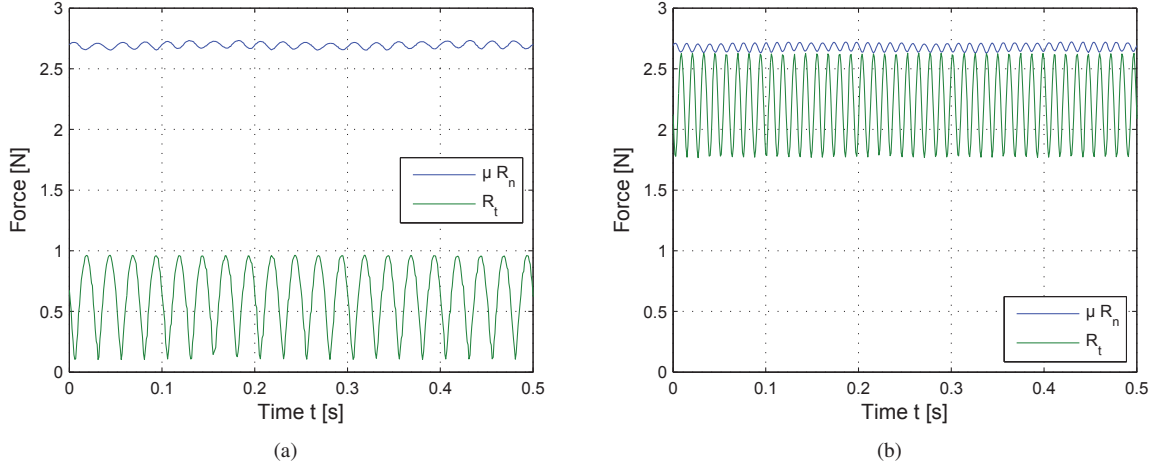


Figure 23: Simulated results of the two components of the reaction forces as functions of time for the second experiment. (a) rotation speed of 40 Hz and (b) rotation speed of 82 Hz. When the tangential reaction force R_t reach the normal force multiplied by the coefficient of friction μR_n (the friction force), the system will switch to state II, and the instability limit is reached.

and the tip of the rotor is placed at $(0,0,0)$ over longer period of time. This definition, however, not entirely correct as instability first occurs when entering state III, has been used for several reasons: Simulations in other situations than state I take an incredibly long time. Furthermore, differential equations are not continuous in time in the transitions between the different states, which disturbs the Matlab ode45 function and require very small time steps.

Force fields are determined when the tip of the rotor is at $(0,0,0)$, giving two coupled faults when not in state I:

1. shifting the rotor from the center, the tip coordinates (x, y) will change as to create an angle between the magnet in the rotor and the magnets in the bearings which differs from those assumed in the simulation. This has an influence on F_z , although it might be insignificant.
2. shifting the rotor from the center, the relative shifts $z_{0,1}$ and $z_{0,2}$ between the bearings and the rotor magnets will also change due to the design of the clutch. This is not taking into account in the calculation of the force fields, and has a major impact on F_z .

Based on the graphs in Fig. 23, it might be interesting to see exactly what the relationship is between the forces and speed. In Fig. 24 such results are shown for experiment no. 2, where the points are simulated values and the lines are regressions. Since forces vary over time (relatively periodic) the mean values are considered. The minimum of μR_n and maximum of R_t is also considered, as the instability threshold is reached (or close to being reached) when they have the same value.

As mentioned, the mean value of friction force is constant as a function of revolutions likewise is the amplitude, resulting in a steady minimum value. The maximum value of R_t depends on the square of the rotational speed from 25 Hz and up. The mean value also depend on the square of the revolution, again from 25 Hz and at lower frequencies, it has a more constant character.

The reason that the tangential force depends on the square of the revolution, lies in the force imbalance that has the size $F_u = m_b r_b \dot{\gamma}^2$ where $\dot{\gamma}$ is the rotation speed. R_t depends almost linearly on F_u (when angles α and β are small), making R_t dependent on $\dot{\gamma}^2$.

The amplitude of the normal force is almost independent on the increasing rotational speed, if the initial conditions are well set. This means that the oscillations are almost steady as well for frequencies much higher than the eigenfrequencies.

To verify that the proposed model can predict the angular velocity threshold some experiments was made with the

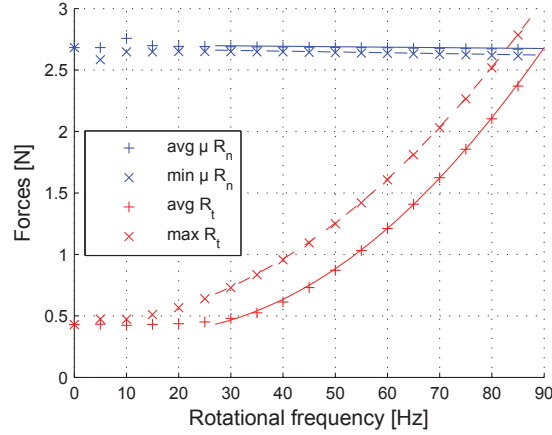


Figure 24: The size of the reaction forces as a function of the rotational speed from the simulated experiment 2. Since reaction forces vary over time the mean, minimum and maximum values were used appropriately. Points are simulated values and lines are regressions.

Parameter	Value	Unit	Comments
Rotor inertia, $I_x = I_y$	$3.45 \cdot 10^{-3}$	[kg m ²]	around origo
Rotor mass, m	0.135	[kg]	incl. imbalance ring
Rotor total length	0.278	[m]	
Distance to center of gravity, l_c	0.134	[m]	measured from origo
Clutch inclination, s	0.57	[-]	$s = z/x$
Rotor tip inclination, s	1.00	[-]	$s = z/x$
Rotor imbalance	$5.04 \cdot 10^{-5}$	[kg m]	

Table 3: Simulation parameters.

same configurations as those described in Sec. 4.4.1. For each of these experimental set-ups some measurements was made to determine the frequency at which the rotor was thrown away from the clutch. The results from these experiments are found in Tab. 4. At each setup there was made several measurements and the average of these is the one written in the table. The angular velocity threshold depended highly on the current oscillations as even minor remaining transient oscillation will result in higher radial forces at the clutch which will ruin the results. Despite the fact that the rotor is highly stable prior to it being pushed away from the clutch, small changes in oscillation amplitude result in relatively large changes in the size of friction and tangential forces. The experimental results are compared with simulations in such a way that the friction coefficient is determined in order to meet the results of the experiments. When comparing the results from the three simulations a very good coherence between the found friction coefficients from the three simulations are found. From the literature Ref. [27] and Ref. [28] the table value of the friction coefficient for steel on steel is listed to be between 0.57 and 0.74 and as the clutch and rotor tip are made of stainless steel and carbon steel respectively these values must be assumed to be fairly accurate for this case. Comparing these values with the simulated values it can be seen that the simulated values are right in the center of the table value range.

Experiment	1	2	3
Measured frequency [Hz]	72	82	35
Simulated friction coefficient μ	0.64	0.67	0.68

Table 4: Experimental results of rotor instability limit in the three experiments in Tab. 2. From the simulation the friction coefficient is calculated in order to meet the results from the experiments. This is when the simulations goes from state I to II.

5. Conclusion

A mathematical model of a system with a rotor supported laterally by passive multi-cylinder magnetic bearings and longitudinally by magnetic forces and a clutch is presented and experimentally verified. The presented bearings are constructed in a way making them highly configurable as to create symmetric as well as asymmetric bearing stiffnesses. This is an improvement compared to passive magnetic bearings consisting of only one ring magnet as asymmetric stiffness is in many rotordynamic application an advantage. Two different models for predicting the B-field and F-field in the bearings are proposed both assuming that the principle of superposition can be applied for the summation of the B-field created by the different bearing magnets. These models are validated through experiments and deliver good agreement between theory and experiments when using slightly different magnetization constant for the two models. However the value of these magnetization constants are still within the manufacture provided values for both of the models. The natural frequencies of the rotor-bearing system are found through both experiments and simulation which again show a good agreement between the theoretically and experimentally achieved results. However it has to be pointed out that the natural frequencies are extremely sensitive to the initial displacement z_0 between the rotor and bearing magnets making the precision in the experimental setup highly important. The reason for the angular threshold of the rotor-bearing system is explained by the use of the presented model and reveal friction coefficients of the rotor-clutch very close to table values. The most important design parameters affecting the threshold of stability are the rotor residual unbalance, friction coefficient between rotor and clutch and finally the geometry of the clutch surface.

References

- [1] B. Bochenkov, S. Lutz, A review of modern materials of permanent magnets, IEEE Electrical Engineering (2004) 201.
- [2] C. S. J., D. J. B., L. H. C. t, R. V. S, Rare-earth permanent magnets: New magnet materials and applications, Materials Science Forum 315 - 317 (1999) 77–83.
- [3] P. Campbell, Permanent magnet materials and their application, UK. Cambridge University Press.
- [4] J. P. Yonnet, Passive magnetic bearings with permanent magnets, IEEE Trans. Magn. MAG-14 (1978) 803–805.
- [5] J. P. Yonnet, Permanent magnet bearings and couplings, IEEE Trans. Magn. MAG-17, no. 1 (1981) 1169–1173.
- [6] B. Azzerboni, E. Cardelli, A. Tellini, Computation of the magnetic field in massive conductor systems, IEEE Trans. Magn. 25, no. 6 (1989) 4462–4473.
- [7] R. Ravaut, G. Lemarquand, The three exact components of the magnetic field created by radially magnetized tile permanent magnet, Progress In Electromagnetics Research PIER 88 (2008) 307–319.
- [8] E. P. Furlani, S. Reznik, A. Kroll, A three-dimensional field solution for radially polarized cylinders, IEEE Trans. Magn. 31, no. 1 (1995) 844–851.
- [9] G. Akoun, J. P. Yonnet, 3d analytical calculation of the forces exerted between two cuboidal magnets, IEEE Trans. Magn. MAG-20, no. 5 (1984) 1962–1964.
- [10] J. P. Selvaggi, S. Salon, O. M. Kwon, M. V. K. Chari, Computation of the three dimensional magnetic field from solid permanent-magnet bipolar cylinders by employing toroidal harmonics, IEEE Trans. Magn. 43(10) (2007) 3833–3839.
- [11] K. K. E. Levi, Z. Zabar, L. Birenbaum, Restoring force between two noncoaxial circular coils, IEEE Trans. Magn. 32, no. 2 (1996) 478–484.
- [12] R. Ravaut, G. Lemarquand, V. Lemarquand, Force and stiffness of passive magnetic bearings using permanent magnets. part 1: Axial magnetization, IEEE Trans. Magn. 45, no. 7 (2009) 2996–3002.
- [13] R. Ravaut, G. Lemarquand, V. Lemarquand, Force and stiffness of passive magnetic bearings using permanent magnets. part 2: Axial magnetization, IEEE Trans. Magn. 45, no. 9 (2009) 3334–3342.
- [14] D. Vokoun, G. Tomassetti, M. Beleggia, I. Stachiv, Magnetic forces between arrays of cylindrical permanent magnets, Journal of Magnetism and Magnetic Materials 323 (2011) 55–60.
- [15] S. Earnshaw, On the nature of the molecular forces which regulate the constitution of the lumiferous ether, Trans. Camb. Phil. Soc. 7 (1842) 97–112.
- [16] R. Gash, M. Lang, Levitron – rein permanentmagnetische lagerung eines rotors, (in german), ZAMM – Zeitschrift für Angewandete Mathematik und Mechanik 80, 2 (2000) 137–144.
- [17] T. Azukizawa, S. Yamamoto, N. Matsuo, Feasibility study of a passive magnetic bearing using the ring shaped permanent magnets, IEEE Trans. Magn. 44, no. 11 (2008) 4277–4280.
- [18] J. Detoni, F. Impinna, A. Tonoli, N. Amati, Unified modelling of passive homopolar and heteropolar electrodynamic bearings, Journal of Sound and Vibration 331 (2012) 4219–4232.
- [19] A. Tonoli, N. Amati, F. Impinna, J. G. Detoni, A solution for the stabilization of electrodynamic bearings: Modeling and experimental validation, ASME Trans. Journal of Vibration and Acoustics 133(2) (2002) 021004–1 021004–10.
- [20] G. Schweitzer, E. H. Maslen, Magnetic Bearings – Theory, Design and Application to Rotating Machinery, Springer Verlag, Berlin, 2009.
- [21] T. Inoue, Y. Ishida, Vibration of the rigid rotor supported by a repulsive magnetic bearing (influences of magnetic anisotropies of magnets), ASME J. Vibr. Acoust. 131 (2009) 031002.
- [22] A. D’Angola, G. Carbone, L. Mangialardi, C. Serio, Non-linear oscillations in a passive magnetic suspension, International Journal of Non-Linear Mechanics 41 (2006) 1039–1049.

- [23] P. E. Nikraves, Computer-aided analysis of mechanical systems, Prentice-Hall, Inc., 1988.
- [24] I. F. Santos, Dinâmica de sistemas mecânicos - Modelagem, simulação, visualização, verificação, Makron Books Ltda., 2001.
- [25] D. K. Cheng, Field and Wave Electromagnetics, Addison-Wesley Publishing Company, 1983.
- [26] M. Baatz, M. Hyrenbach, Method of calculating the magnetic flux density and forces in contact-free magnetic bearings, European Transactions on Electrical Power 1 (1991) 195–199.
- [27] J. F. Sullivan, Technical physics, John Wiley & Sons Inc., 1988.
- [28] I. S. Grigoriev, E. Z. Meilikhov, Handbook of physical quantities, CRC Press, 1997.

Publication [P4]

Multi-physics Modelling of Large Ring Motor for Mining
Industry - Combining Electromagnetism, Fluid mechanics,
Mass and Heat Transfer in Engineering Design

Journal of Applied Mathematical Modelling
ref. AMM13853

Submitted

Multi-Physics Modelling of Large Ring Motor for Mining Industry - Combining Electromagnetism, Fluid Mechanics, Mass and Heat Transfer in Engineering Design

Søren B. Andersen^a, Ilmar F. Santos^{a,*}, Axel Fuerst^b

^a*Department of Mechanical Engineering, Technical University of Denmark, 2800 Kgs. Lyngby, Denmark*

^b*Department of Minerals, ABB Switzerland Ltd, 5405 Baden, Switzerland*

Abstract

This paper presents an improved completely interconnected procedure for estimating the losses, cooling flows, fluid characteristics and temperature distribution in a gearless mill drive using real life data. The presented model is part of a larger project building a multi-physic model combining electromagnet, thermal and structural interactions. This multi-physic model will later on be used for simulating and parameter optimization of a gearless mill drive. What has been proposed is a multi-physic model where the core losses are determined through a series of static finite element magnetic calculations applied to the principle of separation of losses where the losses of each harmonic are summed up. These losses have then be used in the thermal part of the model as heat generation and is modeled by the finite difference and finite element method. The cooling flow, which properties are updated iteratively according to the heat flux transferred to the fluid, is modeled as a lumped model with two nodes interconnected by 11 channels and one pump. The flow model is based on Bernoulli's energy equation and solved by Newton-Raphson method. All the results from the three physical areas have been verified and have shown to be in good agreement with the found values.

Keywords: Multi physics, ring motor, electromagnetic, eddy current losses, hysteresis losses, resistive losses, cooling flow, heat transfer, finite element, finite difference.

*Corresponding author

Email addresses: sban@mek.dtu.dk (Søren B. Andersen), ifs@mek.dtu.dk (Ilmar F. Santos)

Nomenclature

α	Kinetic energy coefficient, [-]	K	Loss coefficient, [-]
α	Thermal diffusivity, [m ² /s]	k_f	Fluid thermal conductivity, [W/(m·K)]
α_{ref}	Temperature coefficient of resistivity, [1/°C]	k_{Cu}	Thermal conductivity of copper [W/(m·K)]
\bar{V}	Mean velocity, [m/s]	$k_{eq,rx}$	Equivalent thermal conductivity in x-dir. of rotor coil pack [W/(m·K)]
μ	Dynamic viscosity, [(N·s)/m ²]	$k_{eq,ry}$	Equivalent thermal conductivity in y-dir. of rotor coil pack [W/(m·K)]
μ_s	Dynamic viscosity at the heat transfer boundary surface temperature, [(N·s)/m ²]	$k_{eq,sx}$	Equivalent thermal conductivity in x-dir. of stator coil pack [W/(m·K)]
ν	Kinematic viscosity, [m ² /s]	$k_{eq,sy}$	Equivalent thermal conductivity in y-dir. of stator coil pack [W/(m·K)]
Ω	Rotational speed, [Hz]	k_{ins}	Thermal conductivity of insulation [W/(m·K)]
ω	Frequency, [Hz]	K_{SC}	Loss coefficient, sudden contraction, [-]
ρ	Density, [kg/m ³]	K_{SE}	Loss coefficient, sudden expansion, [-]
ρ_{ele}	Element density, [kg/m ³]	L	Length, [m]
ρ_{ref}	Electrical resistivity, [Ω ·m]	L_e	Equivalent length, [m]
A	Area, [m ²]	$L_{active,r}$	Active coil length (rotor), [m]
A_r	Copper cross section area of parallel strands (rotor), [m ²]	$L_{active,s}$	Active coil length (stator), [m]
A_s	Copper cross section area of parallel strands (stator), [m ²]	L_{con}	Connection of coil bars at the ends, [m]
$A_{Coil,r}$	Cross-section area of the coil packs in one rotor pole [m ²]	LCu	Length of copper [m]
$A_{Coil,s}$	Cross-section area of one coil pack in the stator [m ²]	$L_{end,r}$	End windings (rotor), [m]
$A_{Cu,r}$	Cross-section area of the copper part of one rotor pole [m ²]	$L_{end,s}$	End windings (stator), [m]
$A_{Cu,s}$	Cross-section area of the copper part of one stator coil pack [m ²]	L_{ins}	Length of insulation [m]
$A_{Fe,r}$	Cross-section area of the iron part of one rotor pole [m ²]	L_{jump}	Jump of coil bars between slots, [m]
$A_{Fe,s}$	Cross-section area of the iron part of the stator [m ²]	L_{motor}	Axial length of the motor [m]
A_{wire}	Cross section area of wire, [m ²]	L_{twist}	Twist of copper strand in active length, [m]
B	B-field, [T]	L_{wire}	Wire length, [m]
C_e	Eddy current loss coefficient, [W/(kg·T ² ·Hz)]	$Loss_{Cu,s}$	Copper loss in stator, [W]
C_h	Hysteresis loss coefficient, [W/(kg·T ² ·Hz)]	m	Harmonic number, [-]
C_p	Specific heat capacity of air at constant pressure, [J/(kg·K)]	n	Number of elements, [-]
$C_{s,ele}$	Element stacking factor, [-]	n_{poles}	Number of poles [-]
D	Diameter/major diameter, [m]	n_{slots}	Number of slots [-]
d	Minor diameter, [m]	Nu	Nusselt number, [-]
e	Roughness, [m]	P	Wetted perimeter, [m]
ele	Element number, [-]	p	Pressure, [Pa]
f	Friction coefficient, [-]	$P_{Fe,total}$	Total iron losses, [W]
g	Gravitational acceleration, [m/s ²]	Pr	Prandtl number, [-]
h	Heat transfer coefficient, [W/(m ² ·K)]	R_{ref}	Reference resistance, [Ω]
h_{lm}	Minor loss, [Nm/kg]	$R_{wire,r}$	Wire resistance (rotor), [Ω]
h_{lT}	Total energy loss, [Nm/kg]	$R_{wire,s}$	Wire resistance (stator), [Ω]
h_l	Major loss, [Nm/kg]	R_{wire}	Wire resistance, [Ω]
I_{exc}	Excitation current (DC), [A]	Re	Reynolds number, [-]
I_{ph}	Phase current (peak), [A]	T_s	Heat transfer boundary surface temperature, [°C]
		T_{ini}	Initial temperature after the cooler [°C]
		T_{wire}	Wire temperature, [°C]
		V	Volume, [m ³]
		V_{ele}	Element volume, [m ³]
		z	Vertical distance, [m]

1. Introduction

All electric motors generate heat due to losses in windings and iron core which, if not predicted correct, could have fatal consequences for the operation of the device. This is increasingly important for large and very expensive motors like gearless mill drives in mineral mining mills [1, 2, 3] which also is very costly in downtimes and therefore require high reliability. It is of common practice in thermal modeling of motors to use the lumped thermal method, [4, 5, 6, 7, 8], however if higher level of details is desired one needs to move to more refined methods like finite difference [9, 10] and/or finite element method [11, 5, 12, 13]. These types of methods can give a highly accurate and clear view of the temperature distribution within the motor if the convection coefficient has been determined with a high accuracy which is one of the major hurdles in heat transfer simulations. This convection coefficient is highly dependent on the fluid properties, channel geometry and the channel flow rate and can only be determined through experiments. Several empirical equations [14, 15, 16] have however been formulated which is specially optimized for different channel geometries and parameter ranges. But before the convection coefficient can be determined knowledge of the flow is needed. If high level of detail is desired numerical CFD can be used for predicting the flow as in [17], however, these 3D simulations is very computationally expensive and less suited for iterative optimization. Another and fast way of determine the flow is as described in [18] by the use of Bernoulli's energy equation where the pressure losses from the different channel segments can be summed up. These losses are split into what is called major and minor losses where the major losses are head losses in straight channel with constant cross section and minor losses are head losses due to inlet/outlet condition, fittings, valves, bends and other devices which create a resistance in the fluid flow. These head losses can again only be determined through experiments but as before some empirical equations and constants for common components can be found in the literature [16, 19]. The electromagnetic losses in the motor are what's generating the heat and consist of two main types of losses. The core losses which are generated by eddy current and hysteresis in the iron parts as the magnetic field oscillates and the resistance losses as current flow through the coils. The core losses can be determined through a series of static finite element simulation as described in [20, 21, 22, 23, 24] and the resistance losses can be found when the resistance and the current are known [25].

The presented model is a completely interconnected multi-physic model incorporating electromagnetic losses, cooling flow and mass transfer, fluid

characteristics and temperature and heat transfer where Grinbaum [26] and Bermudez [27], used for comparison, only use partly interconnected models. Grinbaum’s [26] model only include one cooling channel for the rotor and one for the stator with constant fluid properties and is based on a lumped model looking only at one cross section of the drive. Bermudez’s [27] model is based on several lumped models at different cross section positions and also uses constant fluid properties and losses found by Grinbaum [26]. The presented electromagnetic submodel is a numerical model which predict the core losses with higher accuracy than Grinbaum [26] as it takes all the losses for the desired number of harmonics into account and not just the losses due to the fundamental frequency as in [26].

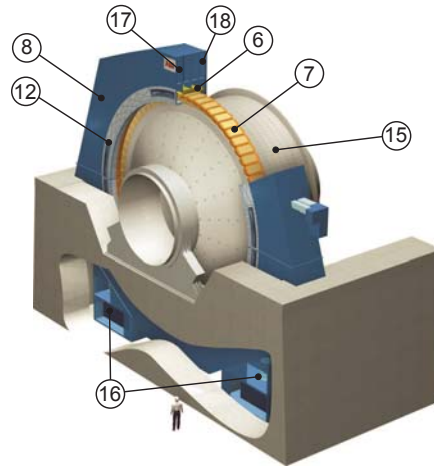
An computational multi-physic tool is created to aid gearless drive design, taking into consideration electromagnetism, fluid mechanics, mass and heat transfer, and in the near future will be linked to the flexible structural behavior of stator and rotor (solid mechanics model). The different models are validated against data and results presented in selected literatures. The global multi-physic model is afterwards used to predict the steady-state thermal characteristics of stator and rotor accurately in all desired positions.

2. Gearless mill drives

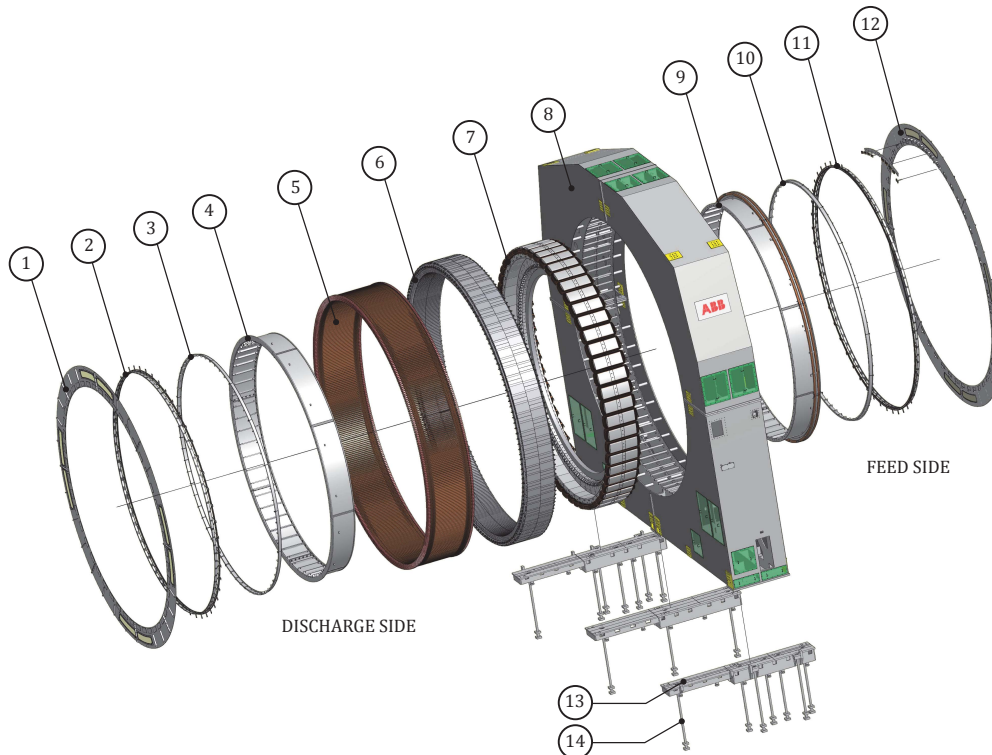
Gearless drives/generators are mainly being used in wind turbines, hydro power plants and in mills in the mining industry, where the latter is the one being analyzed here. The first gearless mill drive was introduced by ABB in 1969 (then Brown Boveri & Cie) and installed at France’s Ciments Lambert-Lafarge in Le Havre, [28]. A picture of a gearless mill drive can be seen in Fig. 1a and Fig. 1b and an exploded view can be seen in Fig. 1c, which in most aspect is similar to the one being analyzed. A gearless mill drive (GMD) is in principle an “ordinary” synchronous motor. However, these GMD’s has a very large bore diameter compared to their iron length and a high number of poles which is fare from a typical synchronous motor design. These drives are wrapped directly on to the mill drum (15) eliminating the gearbox and giving it its name, namely gearless drive. These kinds of drives can deliver much higher torques than ordinary drives connected to gearboxes, as the structurally integrity of the gearboxes are the limiting factor. The stator (6) of the drive is fixed in the stator frame (8) which forms large chambers (17) (18) on each side of the stator for the entering and exiting of the cooling flow. The rotor poles (7) are mounted pole per pole on the mill drum flange and its coils are fed through as slip ring system (9). A stator cover (1) and sealing system (2) are added on both sides of the stator frame to build a



(a) SAG mill with a gearless drive



(b) Drawing of a SAG mill



(c) Exploded view of a gearless drive

Figure 1: ① Stator cover, ② Sealing system, ③ Sealing protection cover, ④ Rotor cover, ⑤ Stator winding, ⑥ Stator core, ⑦ Rotor poles, ⑧ Stator frame (with holding plates and key bars), ⑨ Rotor cover with slip rings, ⑩ Sealing protection cover, ⑪ Sealing system, ⑫ Stator cover with brushes holder, ⑬ Sole plate, ⑭ Anchor bolts, ⑮ Mill drum, ⑯ Fan and coolers, ⑰ Inlet side chamber, ⑱ Outlet side chamber.

closed cooling system and to protect the drive for external dust from the rough environment. The cooling fans and coolers (16) are placed at each bottom corner of the stator frame and force cooling air into the inlet side chamber (17), through the cooling channels and air gap between the rotor and the stator and finally into the other side chamber (18) which is the inlet for the coolers.

3. Electromagnetic loss model

The global loss model consists of two types of losses, the core losses and the resistance losses. The core losses are losses in the iron part due to oscillation of the magnetic B-field within the material and the resistance losses are losses in the coils as current passes through them.

3.1. Eddy current & hysteresis losses

There are two major types of core losses in electrical machines. One is due to eddy currents and the other is due to hysteresis. One way of determine these losses is described in the following based on the procedure described in [20], [21], [22] and [23]. Through a series of static FEM calculations applied to the principle of separation of losses it is possible to estimate the core losses. This principle assume that it is possible to treat the different losses separately by assuming that the average losses in a material can be split up into hysteresis losses and eddy current losses. The hysteresis losses are defined as the oscillation frequency of the B-field in the material times the square of the peak value of the B-field times a loss coefficient times the mass, Eq.1. The equation for the eddy current losses looks almost the same, however, it is not just a function of the frequency but of the square of the oscillation frequency, Eq.2. The two loss coefficients C_h and C_e , for hysteresis and eddy current losses respectively, are based on material loss curves provided by the material manufacture and will be determined in Sec.3.2.

$$P_h = C_h \cdot \omega \cdot B^2 \cdot \rho \cdot V \quad (1)$$

$$P_e = C_e \cdot \omega^2 \cdot B^2 \cdot \rho \cdot V \quad (2)$$

With the equation for hysteresis and eddy current losses it is possible to estimate the total losses in a material experiencing a sinusoidal induced B-field with the oscillation frequency ω and peak value B by the use of Eq.3:

$$P_{loss} = P_h + P_e = (C_h \cdot \omega + C_e \cdot \omega^2) B^2 \cdot \rho \cdot V \quad (3)$$

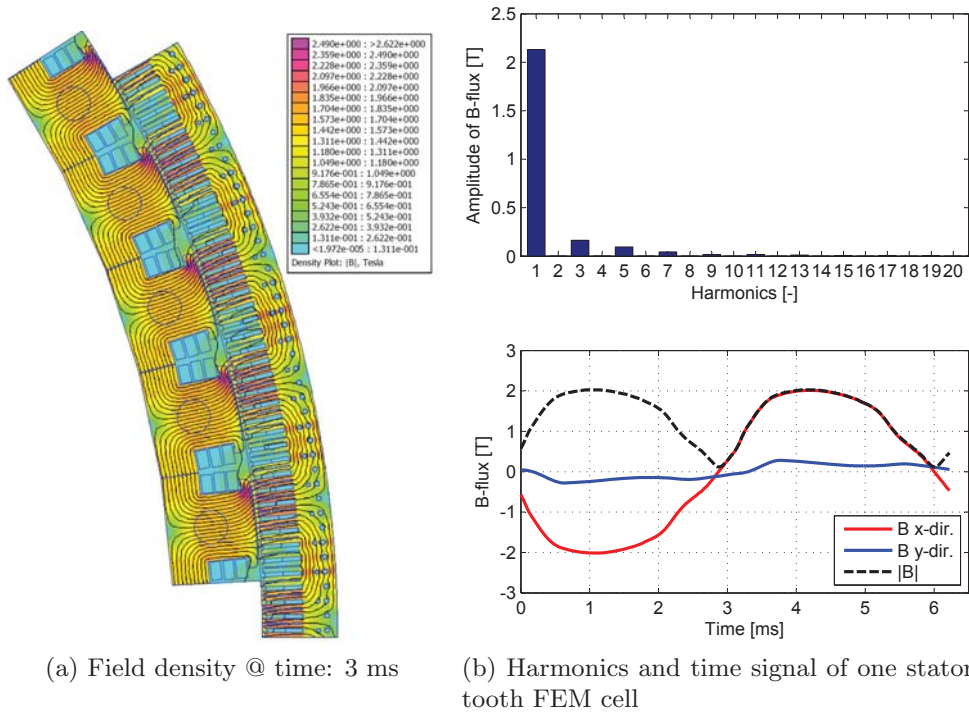


Figure 2: B-field in the center of a finite element cell in the stator tooth at rated currents, speed and torque.

This equation is only valid for sinusoidal B-field with a constant oscillation frequency and amplitude. However, in most cases the material is not just exposed to one frequency but several frequencies at the same time. By creating a series of magneto static simulations [29] where the rotor is rotated at least one pole pitch and the B-field in the centroid of every finite element cell is recorded for each step it is possible to extract the amplitude of the B-field of each harmonic frequency in each cell by applying Fast Fourier Transformation, Fig. 2b. If the rotor is rotated only one pole pitch the vector containing the B-field for the FFT has to be extended to cover 2 pole pitches by adding a copy of the calculated value with a sign change for the stator as the B-field in the stator for the next pole pitch would be the same as the first but with opposite sign. The rotor will however experience the same B-field for the second pole pitch which therefore has to be added without a sign change. The square of the amplitude of each harmonic at the

centroid of each element cell can now be found by the use of Eq. 4, 5 and 6:

$$\mathbf{B}_{x,\text{fft}} = |\text{fft}([\mathbf{B}_x; \pm\mathbf{B}_x])| \cdot \frac{2}{2 \cdot n_{\text{step}}} \quad (4)$$

$$\mathbf{B}_{y,\text{fft}} = |\text{fft}([\mathbf{B}_y; \pm\mathbf{B}_y])| \cdot \frac{2}{2 \cdot n_{\text{step}}} \quad (5)$$

$$\mathbf{B}^2 = \mathbf{B}_{x,\text{fft}} \circ \mathbf{B}_{x,\text{fft}} + \mathbf{B}_{y,\text{fft}} \circ \mathbf{B}_{y,\text{fft}} \quad (6)$$

where \mathbf{B}_x and \mathbf{B}_y are matrices containing the B-field for every element cell and steps for the x and y direction respectively. The corresponding frequency associated with each of the harmonic can be found by Eq. 7 where the last half of the entries are zeroed out as not to count each harmonic twice as the upper half of the FFT is just a mirror of the lower half.

$$\boldsymbol{\omega} = \frac{n_{\text{poles}}}{2} \cdot \Omega_{\text{base}} \cdot \boldsymbol{\omega}_m \circ \boldsymbol{\omega}_m \quad (7)$$

where

$$\boldsymbol{\omega}_m = [0, 1, 2, \dots, n_{\text{step}}, 0, \dots, 0]_{1 \times 2 \cdot n_{\text{step}}} \quad (8)$$

With the use of Eq. 3 for each of the above found frequencies and corresponding amplitude of each finite element cell it is possible by summation to find the total iron loss, Eq. 9.

$$P_{Fe,\text{total}} = \frac{(\mathbf{C}_h \circ \boldsymbol{\omega} + \mathbf{C}_e \circ \boldsymbol{\omega} \circ \boldsymbol{\omega}) \cdot \mathbf{B}^2 \cdot (\boldsymbol{\rho}_{ele} \circ \mathbf{V}_{ele})^T}{C_{s,ele}} \cdot \frac{n_{\text{poles}}}{n_{\text{polepair}}} \quad (9)$$

where $\boldsymbol{\rho}_{ele}$ and \mathbf{V}_{ele} are vectors containing the density and volume of every element cell. The $C_{s,ele}$ in Eq. 9 is the element stacking factor and is introduced in the equation to take the reduced iron volume into account. The last fraction in Eq. 9 is to be added if the FEM model is a reduced model as shown in Fig. 2a where n_{poles} in this case is equal to 5. A flow diagram of the loss calculation procedure is shown in Fig. 3.

3.2. Determination of hysteresis & eddy current loss coefficients

Before the losses can be determined by Eq. 9 the two loss coefficients C_h and C_e has to be estimated. This can be done with the help of the loss curves provided by the manufacturer/distributor of the core material. As an example the loss curves for electric steel SURA M400-50A which is used for the stator core can be seen as the full bold curves in Fig. 4. These curves show the losses in W/kg in this case for four different sinusoidal oscillations frequencies of the B-field. By using Eq. 3 as an approximation

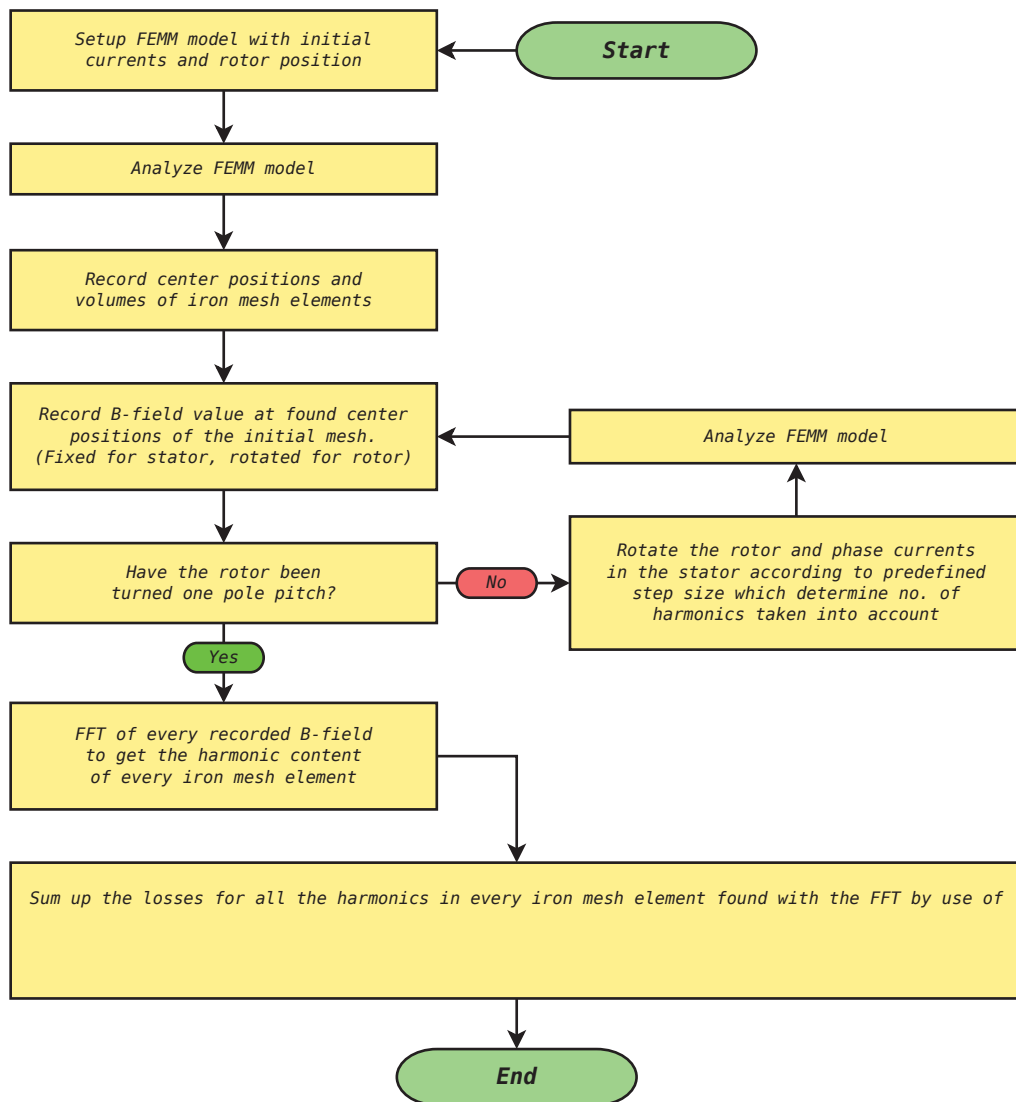


Figure 3: Electromagnetic losses - Flow diagram of core loss calculation procedure

polynomial one can achieve the loss coefficients as the values which best fit the manufacture provided curves. In this case the loss coefficients has been found to $C_h = 0.019831 \text{ W}/(\text{kg}\cdot\text{T}^2\cdot\text{Hz})$ and $C_e = 0.00018393 \text{ W}/(\text{kg}\cdot\text{T}^2\cdot\text{Hz}^2)$ and the approximation polynomial with these values are indicated by the dotted curves in Fig. 4).

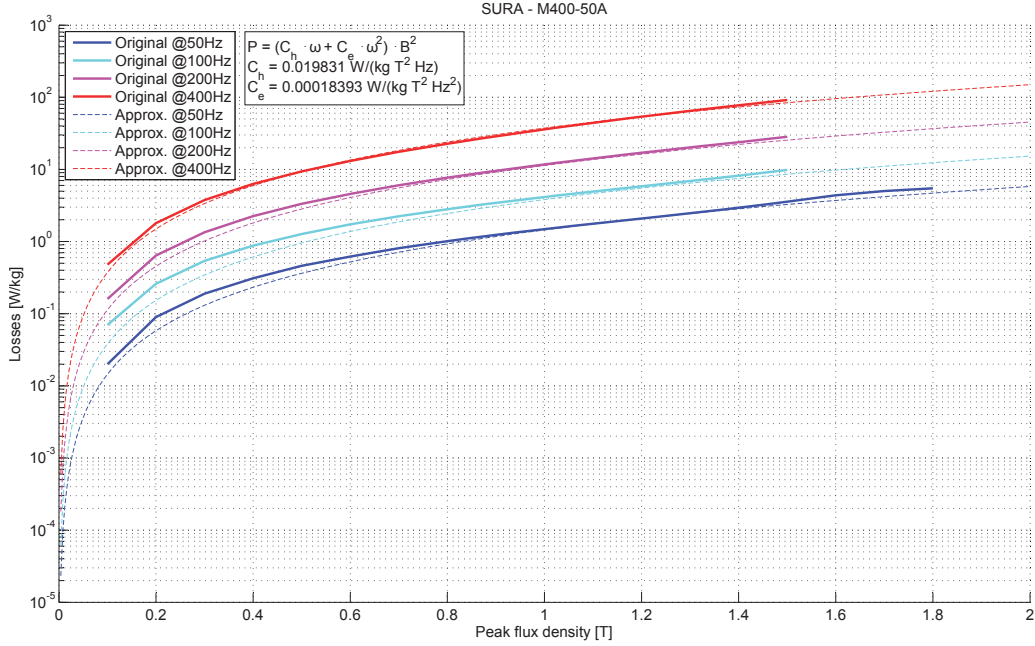


Figure 4: SURA - M400-50A Loss Curve [30]

3.3. Copper resistive losses

The majority of losses in an electrical motor originate from the resistive losses in the copper coils of the stator and the rotor. For this the resistance of the coils has initially to be determined. The resistance of a material with a constant cross section area is proportional to the length and can be found by Eq. 10 where ρ_{ref} is the proportionality constant called electrical resistivity.

$$R_{ref} = \rho_{ref} \cdot \frac{L_{wire}}{A_{wire}} \quad (10)$$

The subscript “ref” refers to the reference temperature T_{ref} at which the resistance R_{ref} is found. This reference temperature is in the literature usually 20°C. As the coil temperature in the motor most likely is much higher than this the resistance of the copper has to be corrected for this increase in temperature. If the temperature change is not too large this can be accomplished by the use of Eq. 11 where α_{ref} is an empirically found constant called the temperature coefficient of resistance. As Eq. 11 is a linear approximation it is important that α_{ref} has been found for the same reference temperature as R_{ref} has been calculated, respecting the Taylor

approximation of $R_{wire}(T)$ around $T = T_{ref}$.

$$R_{wire} = R_{ref} \cdot (1 + \alpha_{ref} \cdot (T_{wire} - T_{ref})) \quad (11)$$

Once the temperature of the copper coils are found the resistive losses can be found by Eq. 12 and Eq. 13 for stator and rotor coils respectively.

$$Loss_{Cu,s} = R_{wire,s} \cdot \left(\frac{I_{ph}}{\sqrt{2}} \right)^2 \quad (12)$$

$$Loss_{Cu,r} = R_{wire,r} \cdot I_{exc}^2 \quad (13)$$

The reason for the $\sqrt{2}$ in Eq. 12 is that I_{ph} is the peak phase current which need to be the RMS current before it is squared, Ref. [31].

4. Fluid flow model

4.1. Energy equation - Bernoulli's equation

For the flow calculation we have that the energy equation, Ref.[18], also called Bernoulli's equation named after Daniel Bernoulli who first proposed it can be written as:

$$\left(\frac{p_1}{\rho} + \alpha_1 \frac{\bar{V}_1^2}{2} + gz_1 \right) - \left(\frac{p_2}{\rho} + \alpha_2 \frac{\bar{V}_2^2}{2} + gz_2 \right) = h_{l_T} = \sum h_l + \sum h_{l_m} \quad (14)$$

The two first terms in brackets on the left hand side represent each the mechanical energy at a specific cross section of a pipe and the terms on the right hand side represent the irreversible losses between two cross sections due to heat generation and heat transfer losses. This equation can be used for calculating the pressure losses between two cross section of a pipe with constant cross section area. Assuming that $\alpha_1 \cdot \frac{\bar{V}_1^2}{2} = \alpha_2 \cdot \frac{\bar{V}_2^2}{2}$ and neglecting the effect of the gravitation, $z_1 = z_2$ the equation can be simplified to:

$$\frac{p_1}{\rho} - \frac{p_2}{\rho} = h_{l_T} = \sum h_l + \sum h_{l_m} \quad (15)$$

These assumptions will be used throughout the entire paper. As indicated in the equation the total energy loss, h_{l_T} , can be split up as the sum of minor losses, h_{l_m} , plus the sum of major losses, h_l . The next sections will explain how these losses can be determined.

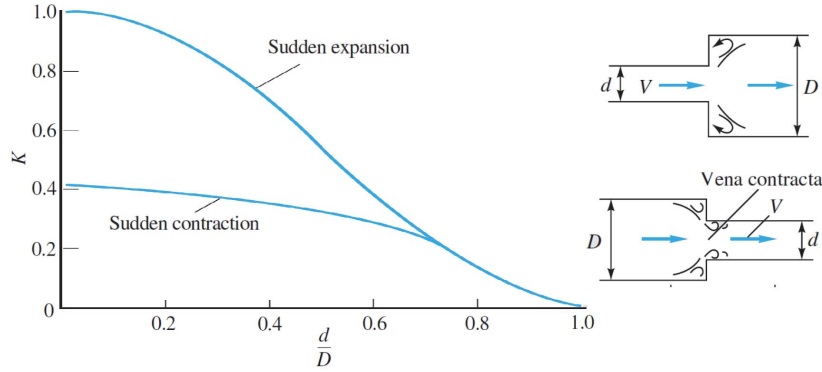


Figure 5: Fluid loss coefficient for expansion and contraction, [19]

4.2. Head losses

Head losses can, as explained, be divided into minor losses and major losses. Minor losses consist of losses due to inlet and outlet conditions, sudden expansion and contraction of pipes, bends in pipes, valves and fittings. These losses are usually small compared to the total loss in systems consisting of long pipes with constant cross section areas, hence the name minor losses. Major losses which usually are the dominant losses are due to viscous friction between the pipe and the fluid which generate heat which are stored in the fluid and/or dissipated through the pipe walls.

4.2.1. Minor losses

The minor losses can be defined in two ways, either by the loss coefficient or an equivalent length as shown in Eq.16

$$h_{l_m} = K \frac{\bar{V}^2}{2} = f \frac{L_e}{D} \frac{\bar{V}^2}{2} \quad (16)$$

where K is the loss coefficient and L_e is the equivalent pipe length which result in equivalent losses. These constants can only be determined experimentally and are shown in Fig. 5 and Eq. 17 and Eq. 18 for pipe enlargement and contraction. Loss coefficient for other fittings, valves and bends can be found in [18] and [19].

$$K_{SE} = \left(1 - \frac{d^2}{D^2}\right)^2 \quad (17)$$

$$K_{SC} \approx 0.42 \left(1 - \frac{d^2}{D^2}\right)^2 \quad (18)$$

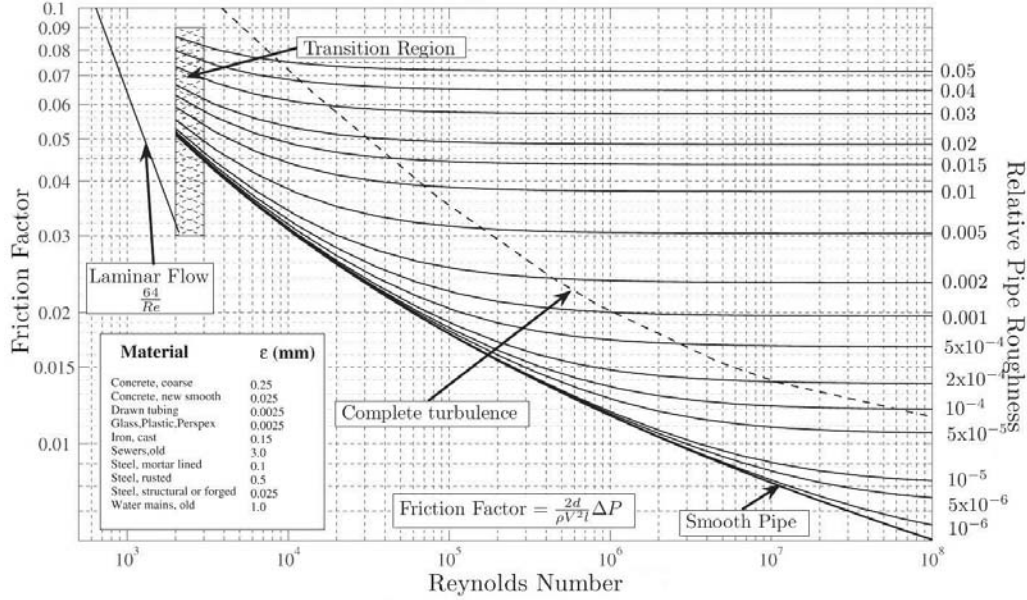


Figure 6: Moody diagram, [32]

4.2.2. Major losses

Major losses are losses due to viscous friction between a fluid and its boundaries which generate heat that are stores in the fluid itself and/or dissipated through its boundaries. The major losses are dependent on the length/diameter ratio of the pipe, the mean velocity of the flow and the friction factor which tell something about the friction between the fluid and the inner surface of the pipe. For a fully developed flow in a round pipe the major loss can be determined by:

$$h_l = f \frac{L}{D} \frac{\bar{V}^2}{2} \quad (19)$$

There are two ways of determine the Darcy-Weisbach friction factor f , either by the use of the Moody's diagram Fig. 6 or by the use of Darcy-Weisbach equation, Eq. 20, for the laminar regime and Colebrooks equation, Eq. 21 for the turbulent regime where the last one cannot be solved analytically but has to be solved iteratively.

$$f = \frac{64}{Re} \quad (20)$$

$$\frac{1}{f^{0.5}} = -2.0 \cdot \text{Log} \left(\frac{e/D}{3.7} + \frac{2.51}{Re \cdot f^{0.5}} \right) \quad (21)$$

Before the friction factor can be determined the Reynolds number has to be known to determine if the flow is in the laminar or turbulent regime. This can be found by Reynolds equation, Eq. 22.

$$Re = \frac{\rho \cdot \bar{V} \cdot D}{\mu} \quad (22)$$

4.3. Non-circular channels & hydraulic diameter

All the above theory and equations explain how it is possible to calculate flow and pressure losses in circular pipes. As this is far from the only type of channels used for fluids there is a need for estimating an equivalent diameter for other geometries. This diameter is called the hydraulic diameter and is defined as, Ref.[19]:

$$D_h = \frac{4A}{P} \quad (23)$$

where A is the cross section area and P is the wetted perimeter of the channel. For a rectangular channel the hydraulic diameter would therefore be:

$$D_h = \frac{4 \cdot h \cdot w}{2 \cdot (h + w)} \quad (24)$$

where h is the height and w is the width of the channel. The above equation will, according to [18], give results with acceptable accuracy for a height/width ratio of approximately $1/4 \leq h/w \leq 4$. Beyond this ratio and for irregular shaped channels experimental values must be used.

4.4. Fluid flow model description

Figure 7a show a section of the rotor and the stator of the gearless drive which is analyzed and Fig. 7b show a close-up of approximately one stator tooth including coils. The green rectangles and circles indicate the cooling flow channels which are used in the calculations. Even though not all of the channels are rectangles it is assumed to only have minor effect on the accuracy as long as the cross section area of the channels and the perimeter are comparable. Each of the channels is numbered according to the number in the blue circle beside the channels. It is this number that has been referred to in Tab. A.3 in appendix which show the dimensions used for the channels. Every subsequent content will use this numbering of the channels for both the flow and heat calculation. Table A.3 also show how many parallel channels there are of the different channels in the motor. This number of channels is based on the number of poles and number of

slots of the motor which can be found in appendix Tab. A.4. The system is assumed to have two nodes, one at each end of the motor. All the channels are connected to these two nodes resulting in a pressure drop between the nodes. To counteract this pressure drop a fan has been connected between the nodes as well. A diagram of the system can be seen in Fig. 8 and the pressure characteristics of the fan including cooler which is used in the calculation is shown in appendix Fig. A.1.

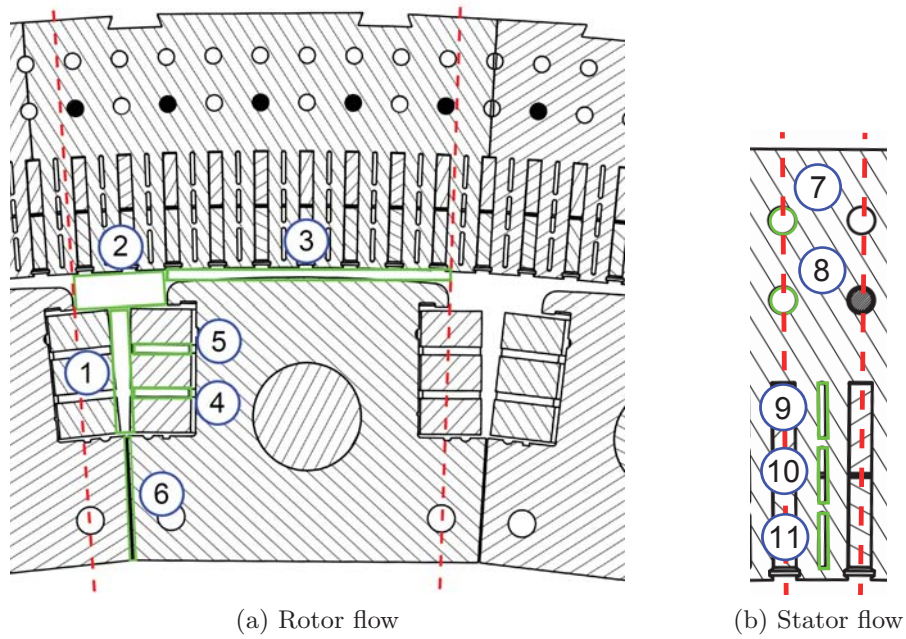


Figure 7: Fluid flow model - Cooling channels through motor

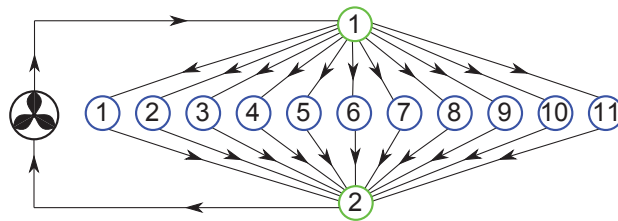


Figure 8: Fluid flow model - Flow diagram of motor cooling

5. Heat transfer model

Two different models are made for modeling the heat distribution in the gearless drive. The first assume that it is sufficient to look only at a cross section in the center of the gearless drive, assuming that the cooling flow temperature can be kept constant at an elevated temperature compared to the outlet temperature of the cooler, equivalent to that half of the losses are transferred into the fluid. Furthermore, the coil losses used are assumed to be constant in the axial direction and are calculated at an assumed 90°C copper temperature. The second model is more refined as it is sliced in several pieces in the axial direction where the cooling flow temperature in the different channels are constantly updated by the heat flux transferred to the fluid from the previous cross section slice. Furthermore, the coil losses are updated iteratively according to the coil temperature of the current slice. The cooling flow temperature of the first slice is determined as the temperature of the flow from the cooler, where the losses from the end windings are added. The temperatures of the end winding are assumed to be the same as the winding temperature of the first slice, which again is found iteratively. The mass flow for both models are determined with air properties equivalent to the air properties in the different channels in the center of the drive which is the same for all the channels in the center slice model and different for the different channels in the multi sliced model. If the initial guesses of these air properties are not within an acceptable error the whole model is run again with updated air properties from the previous calculation. A flow diagram of the calculation procedure for the multi sliced model can be seen in Fig. 9.

The center slice model is simulated with both the explicit finite difference method and the finite element method where the multi sliced model is only modeled with the finite element method due to the time consuming explicit finite difference method. The explicit finite difference model is programed in FORTRAN and the finite element models are created in the program FEMM. The following will shortly describe the models with major focus on the finite difference model.

5.1. Finite difference thermal model - Equations and implementation

The energy balance equation state that the energy that enters a control volume plus the energy that is generated in the control volume must equal the energy stored in the control volume. This can be written as:

$$\dot{E}_{in} + \dot{E}_{gen} = \dot{E}_{st} \quad (25)$$

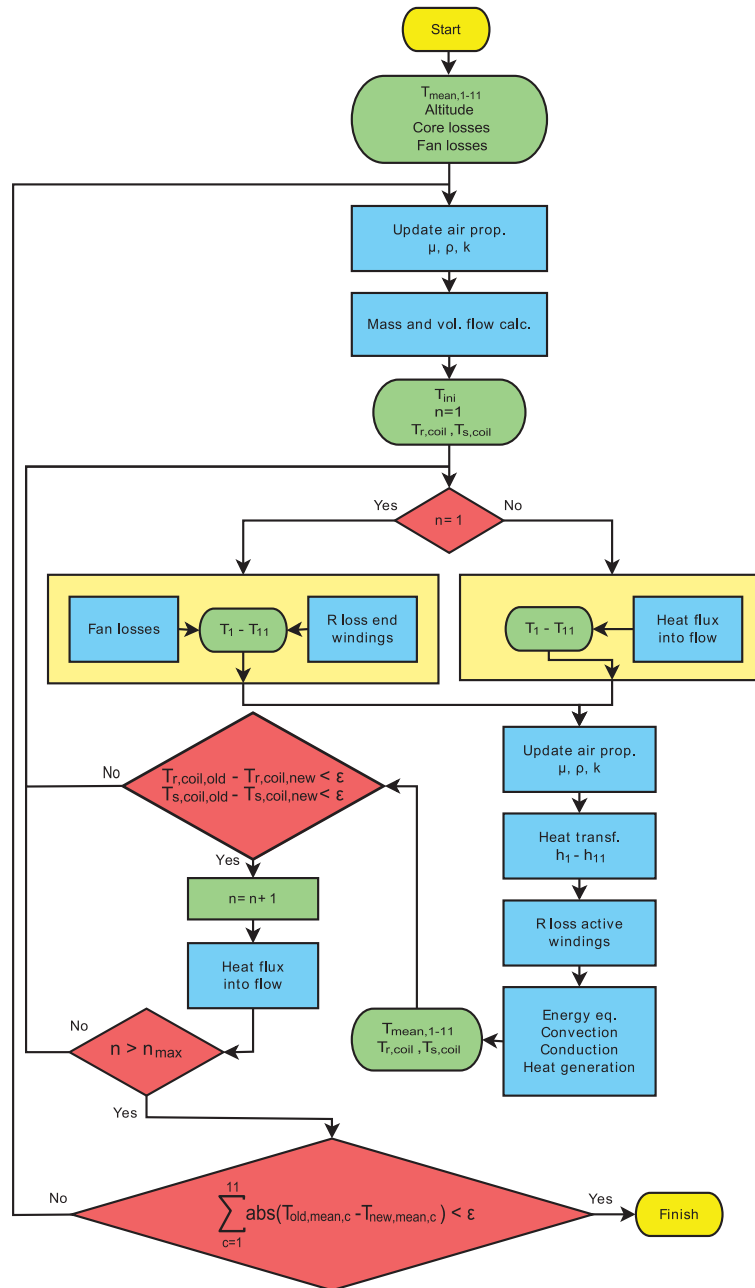


Figure 9: Flow diagram for iterative flow and temperature calculations

where energy that leaves the control volume is added as negative energy flow. The energy that enters/leaves the control volume could be due to conduction between the control volume and the neighbor material through

the control volumes sides. Another source of energy leaving/entering the control volume is through convection between the control volumes sides and a heating/cooling fluid.

When solving for the nodal temperature, $T_{m,n}$, there are 4 general situations which are illustrated in Fig. 10. In case a) the node is an internal node where only heat generation in the control volume, indicated by the colored box, and conduction between neighbor control volumes can occur.

The energy flow done by conduction can be found by:

$$\begin{aligned}
q_{cond} = & \underbrace{L \cdot \Delta y \frac{k_{m+1,n}}{\Delta x} (T_{m+1,n}^t - T_{m,n}^t)}_{\text{Conduction with node}_{m+1,n}} + \underbrace{L \cdot \Delta x \frac{k_{m,n-1}}{\Delta y} (T_{m,n-1}^t - T_{m,n}^t)}_{\text{Conduction with node}_{m,n-1}} \\
& + \underbrace{L \cdot \Delta y \frac{k_{m-1,n}}{\Delta x} (T_{m-1,n}^t - T_{m,n}^t)}_{\text{Conduction with node}_{m-1,n}} + \underbrace{L \cdot \Delta x \frac{k_{m,n+1}}{\Delta y} (T_{m,n+1}^t - T_{m,n}^t)}_{\text{Conduction with node}_{m,n+1}} \quad (26)
\end{aligned}$$

where the 4 terms on the RHS are conduction through the control volumes 4 edges.

The term for the energy generation, if there is any, is just the volumetric energy rate multiplied by the volume of the control volume as shown in Eq. 27.

$$q_{gen} = \dot{q} \cdot L \cdot \Delta x \cdot \Delta y \quad (27)$$

The stored energy in the control volume can be expressed as the density multiplied by the heat capacity multiplied by the volume multiplied by the time derivative of the temperature as shown in Eq. 28

$$q_{st} = \rho_{solid} \cdot C_{solid} \cdot L \cdot \Delta x \cdot \Delta y \frac{T_{m,n}^{t+dt} - T_{m,n}^t}{dt} \quad (28)$$

In case b), c) and d) in Fig. 10 some of the control volume has been removed compared with case a) where convection has been added. Due to the smaller control volume Eq. 26, 27 and 28 has to be corrected for this reduction. As an example the conduction in the $(m+1, n)$ and $(m, n-1)$ directions of case b), under the assumption that $\Delta x = \Delta y$, would only be half of that of case a) as the area has been reduced to half in these two directions. For the heat generation in case b), again under the assumption that $\Delta x = \Delta y$, would be reduced to 3/4 of that of case a) as the volume has been reduced to 3/4.

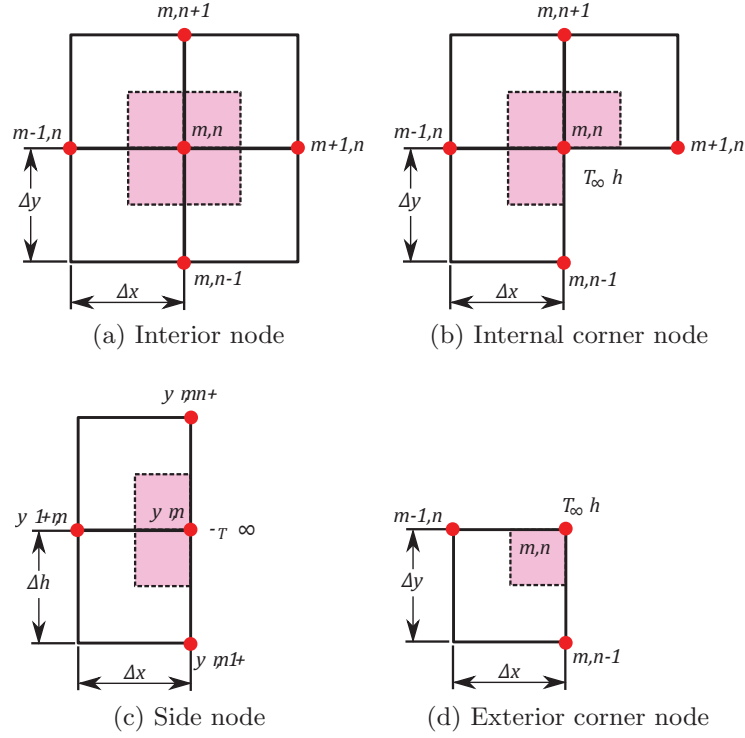


Figure 10: Finite difference cases, [14]

The convective energy from a fluid at constant temperature where $\Delta x = \Delta y$ can be determined by:

$$q_{conv} = h \cdot L \cdot \Delta x (T_{conv} - T_{m,n}^t) \quad (29)$$

This expression for the convective energy is independent of being in case b), c) or d) as long as $\Delta x = \Delta y$. This is due to the fact that the convective area is the same for the three different cases.

Combining Eq. 25 to Eq. 29 and rearranging it is possible to determine the temperature at time $t + dt$ when the temperature distribution at time t is known.

$$T_{m,n}^{t+dt} = \frac{(q_{cond} + q_{conv} + q_{gen}) \cdot dt}{\rho_{solid} \cdot C_{solid} \cdot L \cdot \Delta x \cdot \Delta y} + T_{m,n}^t \quad (30)$$

For modeling an adiabatic or symmetry line boundary condition the expression for the conduction Eq. 26 has to be corrected. This is most easily done by adding this boundary effect to the thermal conductivity constant of the solid. If looking at case d) as an example and assume that the convection surface has been perfectly insulated. This will result in

that $k_{m+1,n} = k_{m,n+1} = 0$ as no convection occur in these direction and $k_{m-1,n} = k_{m,n-1} = k_{solid}/2$ as only half of the conductive area is available under the assumption that $\Delta x = \Delta y$. The generated and stored energy, Eq. 27 and Eq. 28, has of course to be corrected as well according to the volume of the control volume.

In cases where to different materials meet in a control volume the thermal conductivity in the direction of the boundary between the two materials has to be changed to $k_{equivalent} = (k_{solid,1} + k_{solid,2})/2$.

5.2. Forced convection & thermal conduction

To be able to calculate the convection between a fluid and a solid the heat transfer coefficient h has to be determined. This is normally done by the use of empirical equations and is defined by:

$$h = \frac{k_f}{D_h} \cdot Nu \quad (31)$$

There are many different empirical equations for determining the Nusselt number, Nu , which is specially optimized for different geometries and parameter ranges. This paper will only focus on the determination of the Nusselt numbers for forced convection in internal channel flows.

For internal turbulent flow Kreith [15] suggests that the Nusselt number is to be found by the empirical equation:

$$Nu = \frac{(f/2) \cdot (Re - 1000) \cdot Pr}{1 + 12.7 \cdot (f/2)^{0.5} \cdot (Pr^{2/3} - 1)} \cdot \left(1 + \left(\frac{D}{L}\right)^{2/3}\right) \cdot \left(\frac{T_f}{T_s}\right)^{0.45} \quad (32)$$

which is valid for the following ranges:

$$0.6 \leq Pr \leq 2000, 2300 \leq Re \leq 10^6, 0 \leq \frac{D}{L} \leq 1$$

and f is defined as:

$$f = (1.58 \cdot \ln(Re) - 3.28)^{-2} \quad (33)$$

The Prandtl number, Pr , can be found by Eq. 36.

For internal laminar flow Incropera et al. [14] suggest that the Nusselt number is to be found by the empirical equation:

$$Nu = 1.86 \cdot \left(\frac{Re \cdot Pr}{(L/D)}\right)^{1/3} \cdot \left(\frac{\mu}{\mu_s}\right)^{0.14} \quad (34)$$

which is valid for the following ranges:

$$0.6 \leq Pr \leq 5, Re \leq 2300, 0.0044 \leq \frac{\mu}{\mu_s} \leq 9.75, Nu \geq 3.66$$

In the case that the Nusselt number found by Eq. 34 falls below $Nu = 3.66$, Incropera et al. [14] suggest that Eq. 35 is to be used instead.

$$Nu = 3.66 + \frac{0.0668 \cdot (L/D) \cdot Re \cdot Pr}{1 + 0.04 \left((L/D) \cdot Re \cdot Pr \right)^{2/3}} \quad (35)$$

which is valid for the following ranges:

$$Re \leq 2300, Nu < 3.66$$

The Prandtl number used above to find the Nusselt number is another dimensionless number frequently used in heat calculation and is defined as the ratio of momentum and thermal diffusivity:

$$Pr = \frac{\nu}{\alpha} = \frac{C_p \cdot \mu}{k_f} \quad (36)$$

5.3. Dependency of fluid characteristics on temperatures and altitude changes

As the properties of air changes at different temperatures and pressures which has a significant influence on the flow and heat transfer results it is of utmost importance that these are estimated as precise as possible. As all calculations are made in 2D the most correct air temperature to use for the calculations must be the average air temperature in the center of the motor. In Tab. A.4 all the losses from the iron, copper and fan are listed. Using these losses together with the initial temperature after the cooler it is possible to estimate the temperature in the center of the motor by assuming that half of the copper and iron losses are at that point transferred to the fluid. The losses of the fan has to be added to these losses as it is placed after the cooler and therefore contribute to the increase in temperature. The center temperature can be found as:

$$T_{mid} = \frac{Loss_{fan} + (Loss_{Fe,s} + Loss_{Fe,r} + Loss_{Cu,s} + Loss_{Cu,r})/2}{\dot{m} \cdot C_p} + T_{ini} \quad (37)$$

This equation has to be solved iteratively as the center air temperature is dependent on the mass flow and specific heat capacity which again is dependent on the center air temperature. As air pressure decrease with the

altitude the pressure has to be determined with the help of Eq. 38 and the altitude from Tab. A.4.

$$p_{alt} = p_0 \cdot \left(1 - \frac{T_{lap} \cdot h_{alt}}{T_0}\right)^{\frac{g \cdot M}{R \cdot T_{lap}}} \quad (38)$$

It is now possible to calculate the remaining needed properties by the use of Eq. 39 to 42:

$$\rho_{air} = p_{alt} \cdot \frac{M}{R \cdot (273.15 + T_{mid})} \quad (39)$$

$$\mu = \mu_0 \frac{T_0 + C}{(273.15 + T_{mid}) + C} \left(\frac{273.15 + T_{mid}}{T_0}\right)^{3/2} \quad (40)$$

$$C_p = 4.44 \cdot 10^{-7} \cdot (273.15 + T_{mid})^3 - 3.33 \cdot 10^{-5} \cdot (273.15 + T_{mid})^2 - 6.99 \cdot 10^{-2} \cdot (273.15 + T_{mid}) + 1.02 \cdot 10^3 \quad (41)$$

$$k_f = 7.6686 \cdot 10^{-5} \cdot (273.15 + T_{mid}) + 3.0438 \cdot 10^{-3} \quad (42)$$

5.4. Heat transfer model in the solid parts

The schematics of the motor for the heat transfer analysis is shown in Fig. 11 with the dimensions listed in appendix Tab. A.1. The different colors indicate the different material where gray is iron, M400-50A for the stator and St.42 for the rotor. The yellow color is the insulation material and the brownish color is the copper/coil packs. The red lines on the edges of the solids indicate surfaces which have convection with the cooling flow found in previous section. The blue lines indicate adiabatic boundary conditions which are either a symmetry line or a surface which are considered to have no heat flux passing through it. The stator section is modeled with parallel symmetry lines at the sides which are acceptable assumptions as the radius of the rotor is large and the error in connection with this assumption will therefore be minimal. The coils in the rotor and stator do not just consist of copper but of copper bars wrapped in one or several layers of insulations. Figure 12 show the schematics of the coil packs for the stator and rotor. The different layers of insulation are assumed to be made of the same material (glass fiber composite, 66% glass fiber, 33% epoxy). Looking at Fig. 12b it can be seen that each copper bar in the rotor coil pack is wrapped in 0.105 mm of insulation. By taking the sum of the insulation length and divide it by the sum of length per conductivity of the different materials one can

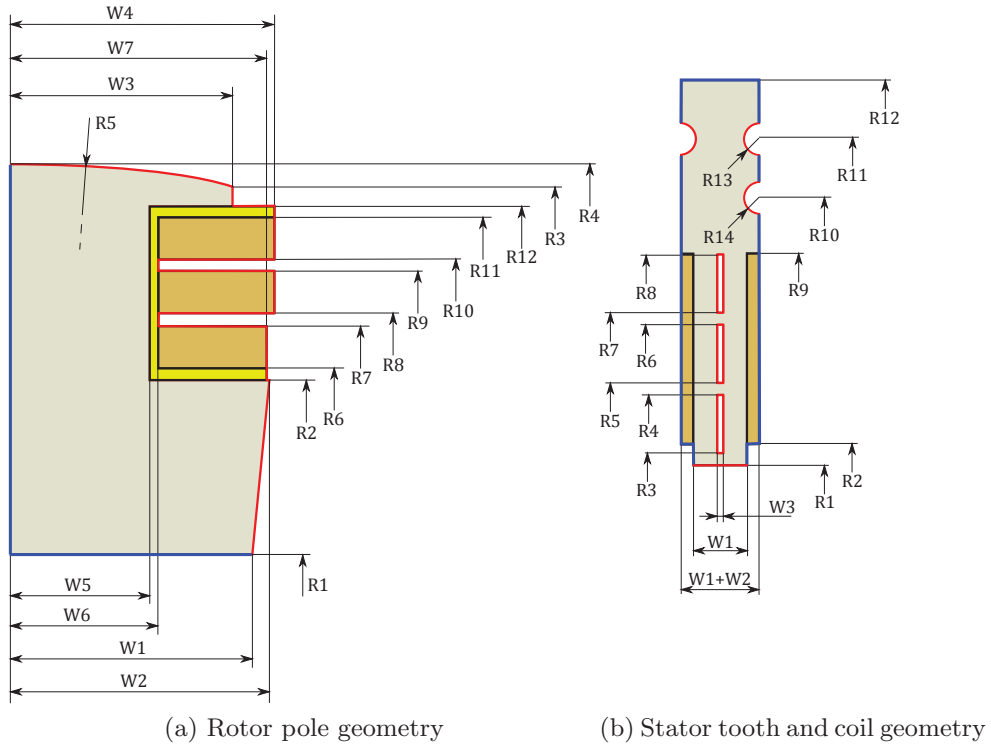


Figure 11: Stator and rotor geometry

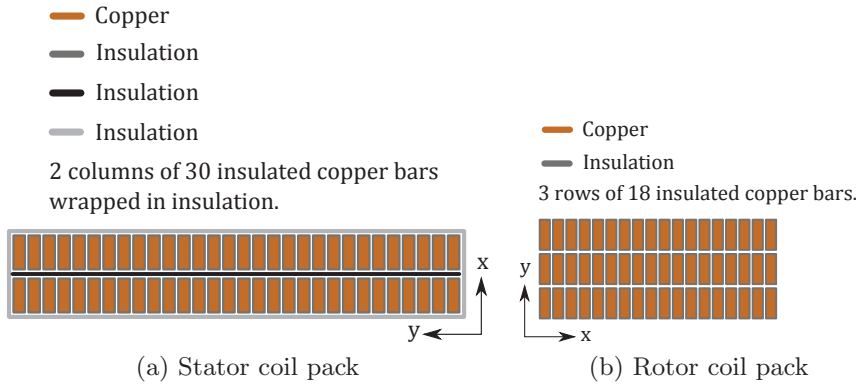


Figure 12: Rotor & stator coil packs

achieve an equivalent conductivity. For the x and y direction of the rotor copper pack this can be found as:

$$k_{eq} = \frac{L_{ins} + L_{Cu}}{L_{ins}/k_{ins} + L_{Cu}/k_{Cu}} \quad (43)$$

Stator			Rotor		
Yoke	[kW]	19.1	Pitch	[kW]	4.9
Teeth	[kW]	20.6	Pitch SC	[kW]	3.8
Teeth SC	[kW]	1.8			
Coil DC	[kW]	328.7	Field windings	[kW]	229.2
Coil AC	[kW]	4.4			
Total Fe losses	[kW]	41.5	Total Fe losses	[kW]	8.7
Total Cu losses	[kW]	333.1	Total Cu losses	[kW]	229.2

Table 1: Electromagnetic losses - Losses at 75°C calculated by Grinbaum [26] using only the 1st harmonic.

In a similar way this can be done for the stator pack Fig. 12a. In the x direction this will however just be done starting from the copper bar of one of the columns and to the outer surface of the insulation as no conduction will occur through the center due to symmetry.

6. Comparison of models

6.1. Electromagnetic loss model

The estimation of the coil length for calculating the resistance losses consists of several different length contributions to the most obvious active coil length. These contributions comes from the twisting of the copper strands in the active part of the stator, connection between upper and lower coil segments, jump between slots in the stator and finally the end windings. The found lengths and cross section areas of the coils are listed in appendix Tab. A.2 and are the values used in the following calculations. To evaluate the presented loss model a simulation is made with rated currents, speed and torques of the gearless drive while assuming that the copper coils are kept at a constant temperature of 75°C. Similar calculations has been carried out by Grinbaum [26] using the same assumptions but based on analytical equations. Results from [26] can be seen in Tab. 1 and results from the finite element model can be seen in Tab. 2. Before a comparison can be made it is important to note that the loss model used in [26] only takes the first harmonic into account when estimating the losses where the finite element model can estimate as many harmonics as the machine precision allows. For this reason two simulations are made to estimate the losses coming only from the fundamental frequency and losses coming from the first 80 harmonics. Both results are listed in Tab. 2. As can be seen there is a significant increase in the estimated core losses when using the first 80 harmonics as basis for the calculation compared to only the fundamental frequency. However, in order to allow a comparison between the different loss

Parameter		Value
Rotor core loss	[W]	536.42
Rotor core loss (only 1 st harmonic taken into account)	[W]	0.00
Stator core loss	[kW]	48.80
Stator core loss (only 1 st harmonic taken into account)	[kW]	41.86
Total core loss	[kW]	49.27
Loss/core volume (rotor)	[W/m ³]	41.15
Loss/core volume (stator)	[W/m ³]	4251.14
Stator resistance loss @ 75 °C (incl. end windings)	[kW]	347.72
Stator resistance loss in active part @ 75 °C	[kW]	167.92
Stator resistance loss/coil pack volume @ 75 °C	[kW/m ³]	77.1
Rotor resistance loss @ 75 °C (incl. end windings)	[kW]	230.54
Rotor resistance loss in active part @ 75 °C	[kW]	162.72
Rotor resistance loss/coil pack volume @ 75 °C	[kW/m ³]	76.8
Average torque	[MNm]	13.61
Mechanical power	[MW]	15.96

Table 2: Electromagnetic losses - Results from the FEMM loss calculation using the first 80 harmonics at rated current, speed and torque based on [29].

calculation approaches, namely presented in [26] and in this work, only the fundamental frequency will be initially considered. Table 3 list the results from the finite element model and the results from [26] both considering only the fundamental frequency. Good agreement for stator core losses, rotor and stator resistance losses can be seen in Tab. 3 with only minor deviations, except for rotor core losses. However, as the rotor core is not experiencing a B-field with the fundamental frequency it is obvious that the losses for this will be zero. The reason for this is that the only oscillation of the B-field in the rotor core comes from the rotor passing the slots and the fractional stator windings where the stator is experience the fundamental frequency due to the pulsating phase currents in the stator. However, taking the first 80 harmonics into account it is seen that the total losses is not zero even though the losses are small as the B-field is almost constant within the rotor core material and only small oscillations occur at the top of the pole shoes. All in all the finite element model has been verified against analytical results and proved to give similar results under similar assumptions. The core losses used in the following sections are the losses found from the first 80 harmonics.

6.2. Fluid flow model

For validation of fluid flow model data, preliminary results from Bermudez [27] using the same input as the present model are used and listed in Tab. 4. The channel numbers refers to the numbering in Fig. 7. The results show a

Parameter		Value FEM	Value [26]	Deviation
Rotor core loss (only 1 st harmonic)	[kW]	0.0	8.7	∞
Stator core loss (only 1 st harmonic)	[kW]	41.9	41.5	0.95%
Rotor resistance loss @ 75 °C	[kW]	230.5	229.2	0.6%
Stator resistance loss @ 75 °C	[kW]	347.7	333.1	4.2%

Table 3: Electromagnetic losses - Comparison of loss results, [26].

Channel number	Hydraulic diameter [m]	flow rate [m ³ /s]	Mean vel. [m/s]	Pressure drop [Pa]
1	0.0491	4.89	15.04	170.0
1 [27]	0.0634	5.77	15.98	170.0
<i>Deviation</i>	<i>22.6%</i>	<i>15.3%</i>	<i>5.9%</i>	<i>0.0%</i>
2	0.0945	9.19	16.84	170.0
3	0.0346	7.70	14.18	170.0
2+3 [27]	0.0585	16.03	15.72	170.0
<i>Deviation</i>		<i>5.4%</i>	<i>1.3%</i>	<i>0.0%</i>
4+5	0.0197	2.72	10.96	170.0
4+5 [27]	0.0208	2.68	11.08	170.0
<i>Deviation</i>	<i>5.3%</i>	<i>1.5%</i>	<i>1.1%</i>	<i>0.0%</i>
6	0.0049	0.06	2.94	170.0
6 [27]	-	-	-	170.0
7	0.0235	2.56	11.70	170.0
7 [27]	0.0235	2.56	11.73	170.0
<i>Deviation</i>	<i>0.00%</i>	<i>0.0%</i>	<i>0.3%</i>	<i>0.0%</i>
8	0.0195	0.81	10.77	170.0
8 [27]	0.0195	0.81	10.76	170.0
<i>Deviation</i>	<i>0.00%</i>	<i>0.0%</i>	<i>0.1%</i>	<i>0.0%</i>
9+10+11	0.0108	3.68	7.80	170.0
9+10+11 [27]	0.0110	3.58	7.78	170.0
<i>Deviation</i>	<i>1.8%</i>	<i>2.8%</i>	<i>2.6%</i>	<i>0.0%</i>

Table 4: Fluid flow model - Results and comparison to Bermudez [27], (same input).

deviation of the fluid flow rate of less than 3%, except for channel 1 and 2+3 which had a deviation of 15.3% and 5.4%. However adding up the flow rate in these channels and compare the total flow rate for these channels result in a deviation of 0.1% which could indicate a different split up of the air gap at the rotor. Accepting this as the cause of deviation, there is a relative good agreement in all the cases.

6.3. Heat transfer model

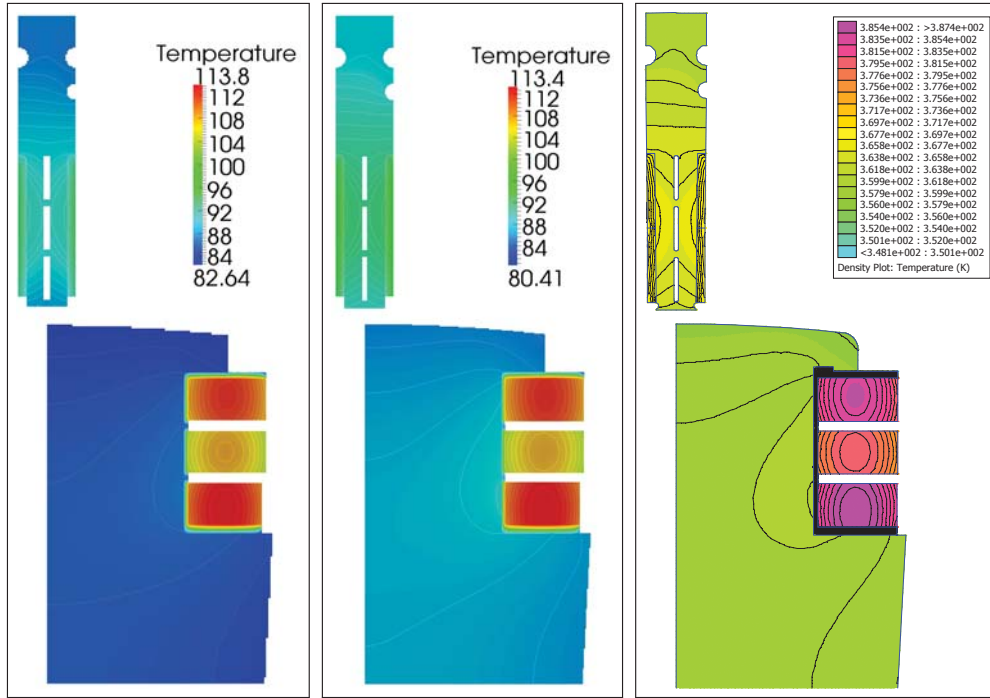
For the center slice thermal model four different grid sizes are used for the finite difference model, two for the stator and two for the rotor. The grid sizes are chosen as to best represent the geometry of the different parts with the coarsest grid possible. To examine the accuracy of the results with

the coarse grid an extra simulation is carried out with a twice as fine grid. The entire grid used are of equal side length, $\Delta x = \Delta y$. The following grid sizes are used for the stator and the rotor:

$$\begin{aligned}
 \text{Stator} & : \quad \Delta x = \Delta y = 2.00 \text{ mm} \\
 & \quad \Delta x = \Delta y = 1.00 \text{ mm} \\
 \text{Rotor} & : \quad \Delta x = \Delta y = 2.50 \text{ mm} \\
 & \quad \Delta x = \Delta y = 1.25 \text{ mm}
 \end{aligned}$$

Figure 13 show the results of the converged steady-state temperatures of the rotor and stator achieved with the finite difference method together with results from the finite element model. Figure 13a is for the coarse grid, Fig. 13b is for the fine grid and Fig. 13c is for the finite element model. As a proof of convergence of the finite difference model the coldest and warmest part of the copper and iron are plotted in Fig. 14 where it can be seen that the steady-state has been reached after approximately 30 simulated hours and it converges toward the finite element results. As it is difficult to read the exact temperatures from Fig. 13 the coldest and warmest temperatures are listed in Tab. 5. Furthermore the deviation between the achieved temperatures values for the fine and coarse grid and between the FD and FEM model is added to the table. It can be seen that the increase in refinement does not make a large change in the found temperatures, only a deviation of approximately 1.5%. However looking at the increase in computational time spend per iteration and the maximum possible time step Δt shown in Tab. 6 it is not worth the effort as other part of the calculations are connected with higher errors. One obvious reason for the deviation in the stator temperature for the two different grid sizes is that the cooling channels in the tooth for the coarse grid is actually modeled with a width of 8 mm due to the size and placement of the grid where it are modeled as 6 mm in the fine grid case which are the actual width of the cooling channels. This increase in modeled cooling channel width will of course increase the surface area for the convection slightly and thereby decreasing the temperature in the solid parts. From Tab. 5 it must be concluded that the three models produce results with almost same accuracy.

To validate the results obtained by using the three models, comparisons are done with results and data presented by Grinbaum [26] under almost the same conditions as the one used in the simulations. Table 7 show these results together with the ones found by the FEMM model. As can be seen there is only minor deviation between the temperature results. It must therefore with a high probability be concluded that the models produce similar



(a) Finite difference, Rotor: $\Delta x = \Delta y = 2.5$ mm, stator: $\Delta x = \Delta y = 1.25$ mm, Stator: $\Delta x = \Delta y = 2$ mm (b) Finite difference, Rotor: $\Delta x = \Delta y = 1$ mm, Stator: $\Delta x = \Delta y = 1$ mm (c) Finite element method

Figure 13: Finite difference Steady-State and finite element temperatures of rotor and stator, Center slice model

results under the same assumptions.

The multi sliced model which updates cooling flows and copper losses due to the increasing temperatures in the axial direction is only modeled by FEMM due to the time consuming explicit finite difference model as many iterations have to be performed. As a comparison between the computational time for one slice the two finite difference models takes 20 hours and 1 hours respectively where the FEM model takes approximately 1 second to compute 1 slice. The multi sliced model consists of 40 slices evenly distributed over the total length of the gearless drive. Figure 15 show the temperature distribution of the center and the two end slices found by the FEMM model and Fig. 16 show the cooling flow temperatures in the different channels. It is obvious from this that the center slice model is too simple as the temperature difference between the two end slices is 31.1°C for the warmest part. Furthermore the warmest temperature is 30.0°C warmer than what

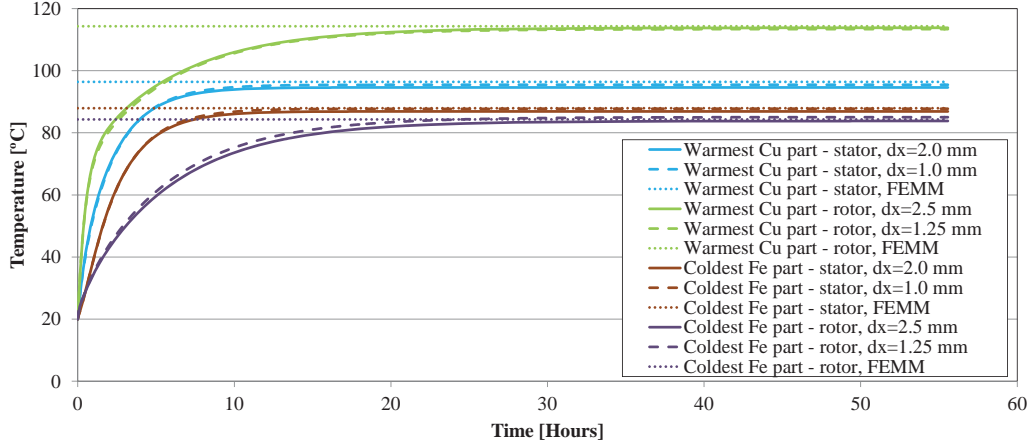


Figure 14: Maximum and minimum temperatures in stator and rotor poles, Center slice model

	$\Delta x = 2.5$ [mm]	$\Delta x = 1.25$ [mm]	Dev. [%]	FEMM	Dev. [%]
Cu rotor max. [°C]	113.8	113.4	0.4	114.3	0.4
Cu rotor min. [°C]	103.9	102.7	1.2	102.4	1.5
Fe rotor max. [°C]	87.7	87.2	0.6	87.7	0.0
Fe rotor min. [°C]	83.8	85.0	1.4	84.3	0.6
	$\Delta x = 2.0$ [mm]	$\Delta x = 1.0$ [mm]	Dev. [%]	FEMM	Dev. [%]
Cu stator max. [°C]	94.6	95.5	2.0	96.4	1.9
Cu stator min. [°C]	89.2	90.0	0.9	91.3	2.3
Fe stator max. [°C]	91.5	92.3	0.9	93.2	1.8
Fe stator min. [°C]	86.9	87.7	0.9	87.9	1.1

Table 5: Rotor and stator max. and min. temperatures, Center slice model

was found by the first model. For validating the multi sliced model, comparisons with data and results obtained in Bermudez [27] using the same input as the present model are carried out and presented in Tab. 8. The difference between the results could, among other things, be explained by the fact that Bermudez [27] uses Dittus-Boelters equation for calculating the Nusselt number which is for smooth channels with a Reynolds number above 10,000 and is therefore less suited for these cases. Furthermore, there is a difference in the mass flow at the same differential pressure which could be explained by the fact that the author of [27] assumes that the air properties in the channels are the same for all the channels. Moreover, small discrepancies in the geometry used for the flow calculation are also verified.

It is assumed in all the models that no axial heat flux is present in the solid parts of the drive. The only axial heat transfer occurring is in cooling

	Δx [mm]	Max. Δt [ms]	CPU time/step [ms]	Steady-state CPU time [h]
Rotor	1.25	20	10.25	15.375
Stator	1.00	20	3.16	4.740
Rotor	2.50	100	2.49	0.747
Stator	2.00	100	0.78	0.234

Table 6: Finite difference model computation time, Intel core I5 CPU M450@2.4GHz, OS Windows 7 64-bit, Steady-state @ 30 simulated hours

	FEMM	[26]	Deviation	Deviation
Rotor max.	109.1 °C	109.5 °C	0.4 °C	0.4%
Stator max.	104.7 °C	104.9 °C	0.2 °C	0.2%
Volume flow	31.4 m ³ /s	32.9 m ³ /s	1.5 m ³ /s	4.6%
Loss/coil vol. stator	96891 W/m ³	96891 W/m ³	0.0 W/m ³	0.0%
Loss/vol. stator iron	5729 W/m ³	5729 W/m ³	0.0 W/m ³	0.0%
Loss/coil vol. rotor	70657 W/m ³	70657 W/m ³	0.0 W/m ³	0.0%
Loss/vol. rotor iron	621 W/m ³	621 W/m ³	0.0 W/m ³	0.0%

Table 7: Temperature comparison with data and results provided by Grinbaum [26], Center slice model

fluid as heat is transferred from the solids to the fluid through the walls of the cooling channels. To investigate the error in connection with this assumption a simulation has been carried out where the axial heat flux of the warmest coil has been found (bottom rotor coil). The axial heat flux for this coil is found to be 41.6 W which is approximately 8.6% of the total loss in that coil segment. The axial heat flux in the core material is much smaller than in the copper coils as this is laminated steel sheets and has a conductivity coefficient of $k \approx 0.5658$ W/(m·K) in the axial direction perpendicular to the sheet plan, [33]. The conductivity coefficient parallel to the sheets plan is 26 W/(m·K) which is 46 times larger than the conductivity perpendicular to the sheet plan. This assumption will however only overestimate the temperature rise in the gearless drive and will therefore not predict lower temperatures which could be fatal for the operation and lifespan of the drive.

	FEMM	[27]	Deviation	Deviation
Rotor max.	144.3 °C	147.7 °C	3.4 °C	2.3%
Stator max.	127.5 °C	123.8 °C	3.7 °C	3.0%
Mass flow	20.45 kg/s	19.55 kg/s	0.90 kg/s	4.6%
Vol. flow	31.60 m ³ /s	31.43 m ³ /s	0.17 m ³ /s	0.5%
Pressure loss	170.0 Pa	170.0 Pa	0.0 Pa	0.0%

Table 8: Temperature comparison of multi sliced model against Bermudez [27] results, (same inputs)

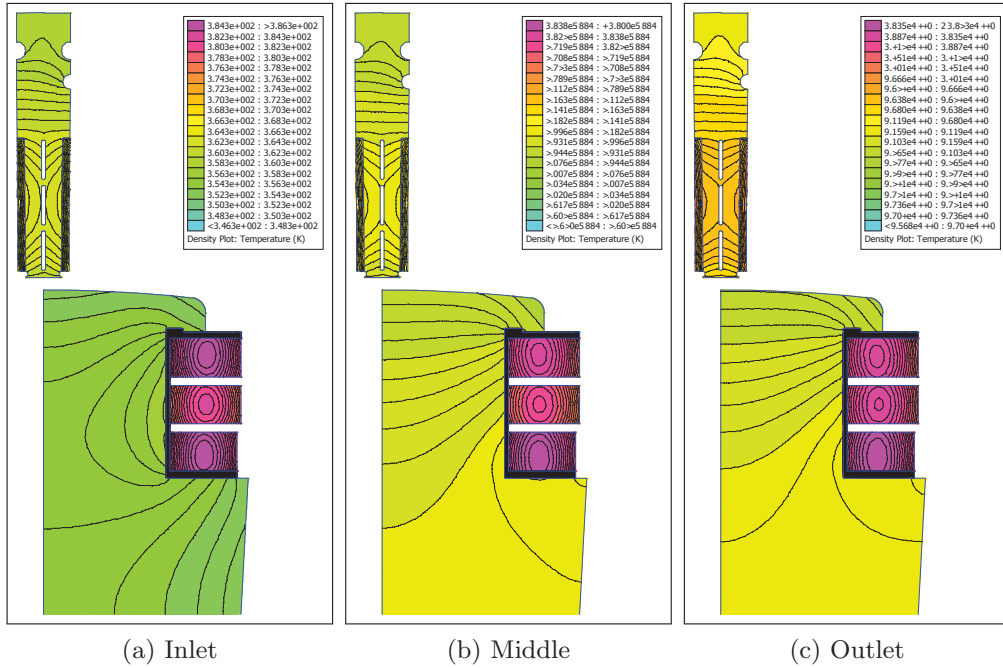


Figure 15: Temperature distribution with updated copper resistance losses, Multi sliced model

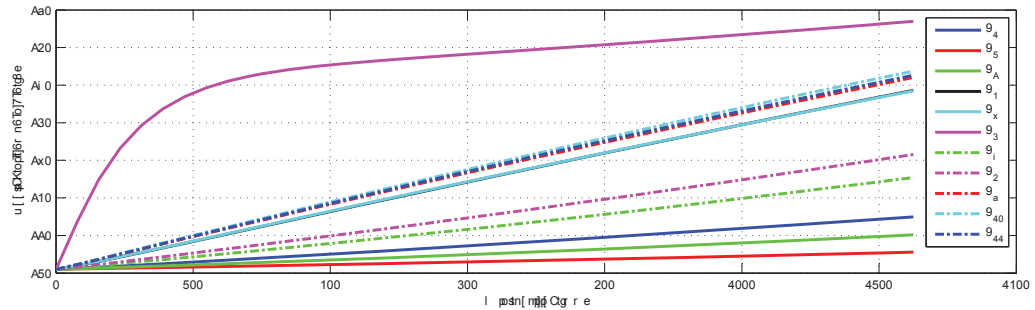


Figure 16: Cooling air temperatures, Temperature updated copper resistance losses, Multi sliced model

7. Results and discussions

The previous section has presented a comparison of the different sub-models which showed a good correlation between estimated values with only minor deviation. This is however only true as long as the input for the different submodels has been modified to match each other. What will be shown below is a comparison between the original values obtained from

Parameter		Value [27]	Value FEMM	Deviation
Stator core loss	[kW]	65.5	48.8	34.2%
Stator winding loss	[kW]	370@90°C	379.2@89.5°C-127.5°C	2.4%
Rotor core loss	[kW]	31.6	0.5	6220%
Rotor winding loss	[kW]	266.9@90°C	263.4@104.4°C-144.3°C	1.3%
Fan losses	[kW]	120.0	106.3	12.9%

Table 9: Losses - Results and comparison of losses found by Iossif [26] and used in Bermudez [27], (original).

[26] and [27] where the pressure loss in the cooling channels and the outlet temperature from the cooler are the only values which has been kept the same in all the models.

Table 9 show a comparison between the losses found by the FEMM model and the original losses used by Bermudez [27] which are calculated by Iossif [26]. The most eye catching in the table are the found core losses which deviate a lot. One reason for this high deviation can be explained by the fact that Iossif [26] only uses the fundamental frequency for the core losses. To compensate for the lack of losses coming from the remaining harmonics some additional losses of 72.6kW has been distributed evenly between the stator core loss, rotor core loss and fan losses where the losses in the FEMM model comes from the eddy current and hysteresis losses for the 1st 80 harmonics. The deviation in the winding losses can be explained by the fact that the losses in Bermudez [27] have been estimated at a constant copper temperature for both rotor and stator where the FEMM model updates the copper temperatures and thereby the losses in the windings.

Table 10 show a comparison between the cooling flow results of the presented model and the original result found by Bermudez [27]. It can be seen that even though the input losses for the two models deviates highly it only has a minor influence on the fluid flow calculations as these are almost identical to the previous flow comparison Tab. 4.

Table 11 show a comparison between the temperature distribution of the presented multi sliced thermal FEMM model and the original result found by Bermudez [27]. As can be seen there are large deviations between the results achieved by the two models especially when comparing against the lower temperature results. This could among other things be explained by the fact that the cooling flow properties are kept constant in [27] for all the channels whereas the properties of the fluid in the completely interconnected model are updated for the different channels and in the axial direction of the drive. An other reason could be, as explained earlier, that Bermudez [27]

Channel number	Hydraulic diameter [m]	flow rate [m ³ /s]	Mean vel. [m/s]	Pressure drop [Pa]
1	0.0491	4.89	15.04	170.0
1 [27]	0.0634	5.68	15.73	170.0
<i>Deviation</i>	<i>22.6%</i>	<i>13.9%</i>	<i>4.4%</i>	<i>0.0%</i>
2	0.0945	9.19	16.84	170.0
3	0.0346	7.70	14.18	170.0
2+3 [27]	0.0585	15.80	15.49	170.0
<i>Deviation</i>		<i>6.9%</i>	<i>0.1%</i>	<i>0.0%</i>
4+5	0.0197	2.72	10.96	170.0
4+5 [27]	0.0208	2.70	11.17	170.0
<i>Deviation</i>	<i>5.3%</i>	<i>0.7%</i>	<i>1.9%</i>	<i>0.0%</i>
6	0.0049	0.06	2.94	170.0
6 [27]	-	-	-	170.0
7	0.0235	2.56	11.70	170.0
7 [27]	0.0235	2.58	11.79	170.0
<i>Deviation</i>	<i>0.00%</i>	<i>0.8%</i>	<i>0.8%</i>	<i>0.0%</i>
8	0.0195	0.81	10.77	170.0
8 [27]	0.0195	0.82	10.86	170.0
<i>Deviation</i>	<i>0.00%</i>	<i>1.2%</i>	<i>0.8%</i>	<i>0.0%</i>
9+10+11	0.0108	3.68	7.80	170.0
9+10+11 [27]	0.0110	3.67	7.97	170.0
<i>Deviation</i>	<i>1.8%</i>	<i>0.3%</i>	<i>2.1%</i>	<i>0.0%</i>

Table 10: Fluid flow model - Results and comparison to Bermudez [27], (original).

	FEMM	[27]	Deviation	Deviation
Rotor coil	104.4 °C - 144.3 °C	141.0 °C - 158.0 °C	36.6 °C - 13.7 °C	26.0% - 8.7%
Stator coil	89.5 °C - 127.5 °C	128.8 °C	39.3 °C - 1.3 °C	30.5% - 1.0%
Tooth	88.6 °C - 124.0 °C	118.4 °C	29.8 °C - 5.6 °C	25.2% - 4.7%
Core	85.6 °C - 120.7 °C	115.7 °C	30.1 °C - 5.0 °C	26.0% - 4.3%
Mass flow	20.45 kg/s	20.61 kg/s	0.16 kg/s	0.8%
Vol. flow	31.60 m ³ /s	31.23 m ³ /s	0.37 m ³ /s	1.2%
Pressure loss	170.0 Pa	170.0 Pa	0.0 Pa	0.0%

Table 11: Temperature comparison of multi sliced model against Bermudez [27] results, (original)

uses Dittus-Boelters equation for calculating the Nusselt number which is for smooth channels with a Reynolds number above 10,000 and is therefore less suited for this case. As the Nusselt number have a direct influence on the convective heat transfer this would of course have a major impact on the thermal results. Finally the resistance losses from the windings are kept constant in the axial direction in Bermudez [27] where these are updated in the presented global interconnected model according to the temperature of the specific axial position.

It is evident from the above comparison that it is of the utmost im-

portance that as many parameters as possible are updated between the submodels as well as inside the submodels. This update can most easily be done by creating a completely interconnected model, as the one presented in this paper, which iteratively updates the parameters based on intermediate results from other submodels or the submodel itself. By creating such a model as the one presented here it is also possible to completely eliminate the risk of forgetting to update all the parameters and thereby insure more reliable results. This section has demonstrated the strength of a completely interconnected model compared to several separate models where not all parameters are updated automatically but kept constant throughout the simulations.

8. Conclusion

The work presented in this paper has shown that modeling only a single cross section in the center of the drive with constant coil and cooling fluid temperatures is insufficient. The fluid and coil temperatures have to be updated in the axial direction as this contributes to a significant increase in losses and thereby an increase in core and coil temperatures. Furthermore the temperature in the core material in the axial direction has shown to be far from constant which is a further indication that the single cross section model is insufficient. As the air temperature in the different cooling channels change the presented thermal submodel update the air properties corresponding to the air temperature of the specific channels at the specific axial positions giving a more accurate estimate of the heat convection coefficient. This is an improvement of [26] and [27] used for comparisons as none of these models update the air properties in this way but use constant air properties in all the cooling channels. Another improvement of the heat convection coefficient estimate compared to [27] is that the presented model use three different empirical equations for estimating the Nusselt number for internal channel flows. These three equations covers the complete range from laminar to turbulent flow in smooth and rough channels whereas [27] only use Dittus-Boelters equation for calculating the Nusselt number. As the Dittus-Boelters equation is only for smooth channels with a Reynolds number above 10,000 (turbulent flow) this might result in less accurate estimates. The presented thermal FEM and FD submodel is also an improvement over [26] and [27] if a higher level of detail is needed/wanted as [26] and [27] are based on lump models and only predict the average temperature within each lump. The finite difference method with explicit equations is, however, not well suited for modeling the multi sliced model case with updated fluid

flow and copper losses as it is computationally expensive compared with the finite element method. The two presented finite difference models takes ~ 20 hours and ~ 1 hours respectively to compute 1 slice where the FEMM model takes approximately 1 second to do it. If it is chosen to use the finite difference method anyway it has been shown that there is no significant loss in accuracy by choosing a coarse grid for the finite difference model as long as the grid does not violate the boundaries of the different solid parts too much. However, a significant reduction in computation time is gained by choosing a coarse grid. In this case the CPU time was 20 times larger as the grid size was reduced to half the size. Like the cooling air properties was updated in the thermal submodel the presented fluid flow submodel also update the air properties in the different channels. These air properties are updated corresponding to the center air temperature of the specific channels which result in a more accurate flow as the fluid temperature is not the same in all the channels resulting in different viscosities and densities. This is also an improvement of models [26] [27] used for comparisons as these models use constant air properties in all the cooling channels resulting in less accurate flow estimates. In all the presented models including [26] and [27] it is assumed that the only axial heat flux occurring is in the cooling fluid as heat is transferred from the solids to the fluid. An investigation of the heat flux in the warmest coil is shown to be 41.6 W for the presented case which is approximately 8.6% of the total loss in the coil segment. This assumption however only overestimate the temperature rise in the gearless drive and will therefore not predict lower temperatures which could be fatal for the operation and lifespan of the drive. This axial conduction in the solid parts could in the future be implemented by iteratively adding the conductive heat flux from the previous and the subsequent slice to the current slice.

A completely interconnected multi-physic model has been presented showing the importance of updating the parameters between the models which is one of the major strength of a completely interconnected model compared to several separate models where not all parameters are updated automatically but kept constant throughout the simulations.

9. Thanks

The authors would like to thank Dr. Iossif Grinbaum and Daniel Bermudez from ABB Switzerland Ltd. who has been most helpful in taking time to providing data, results and software programs for comparisons of the different sub models described in this paper.

Appendix A. Data

Parameter	Stator [m]	Rotor [m]	Parameter	Stator [m]	Rotor [m]
R1	5.400	4.955	R12	5.750	5.372
R2	5.415	5.135	R13	0.012	-
R3	5.410	5.328	R14	0.010	-
R4	5.462	5.384	W1	$4.830 \cdot 10^{-2}$	0.2584
R5	5.470	1.870	W2	$1.970 \cdot 10^{-2}$	0.2679
R6	5.522	5.145	W3	$6.000 \cdot 10^{-3}$	0.2140
R7	5.530	5.196	W4	-	0.2605
R8	5.582	5.207	W5	-	0.1620
R9	5.585	5.258	W6	-	0.1665
R10	5.659	5.269	W7	-	0.2553
R11	5.700	5.320			

Table A.1: Rotor and stator dimensions cf. Fig. 11

Parameter	Value	Description
L_{twist} [mm]	25.0	Twist of copper strand in active length (stator per bar)
L_{con} [mm]	120.0	Connection of coil bars at the ends (stator per bar)
L_{jump} [mm]	72.12	Jump of coil bars between slots (stator per bar)
$L_{end,s}$ [mm]	1173.0	End windings (stator per bar)
$L_{active,s}$ [mm]	1250	Active coil length (stator per bar)
A_s [m ²]	$9.8658 \cdot 10^{-4}$	Copper cross section area of parallel strands (stator)
$L_{end,r}$ [mm]	3313	End windings (rotor all poles)
$L_{active,r}$ [m]	7950	Active coil length (rotor all poles)
A_r [m ²]	$245.85 \cdot 10^{-6}$	Copper cross section area of parallel strands (rotor)

Table A.2: Electromagnetic losses - Data of length and cross section areas of copper coils

Channel no.	1	2	3	4	5	6
a, width [mm]	28.1	137.5	428.0	94.0	94.0	2.5
b, height [mm]	193.0	72.0	18.0	11.0	11.0	180.0
D, diameter [mm]	-	-	-	-	-	-
L, length [mm]	1250.0	1250.0	1250.0	1250.0	1250.0	1250.0
e, roughness [mm]	0.3	0.3	0.3	0.3	0.3	0.3
No. of channels	60	60	60	120	120	60
Channel no.	7	8	9	10	11	
a, width [mm]	-	-	6.0	6.0	6.0	
b, height [mm]	-	-	52.0	52.0	52.0	
D, diameter [mm]	23.5	19.5	-	-	-	
L, length [mm]	1250.0	1250.0	1250.0	1250.0	1250.0	
e, roughness [mm]	0.3	0.3	0.3	0.3	0.3	
No. of channels	504	252	504	504	504	

Table A.3: Fluid flow model - Channel dimensions

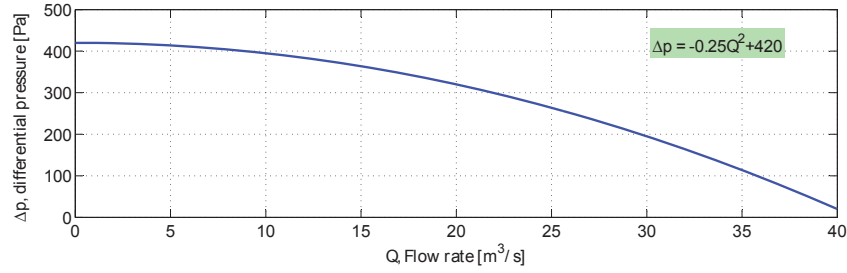


Figure A.1: Fluid flow model - Pressure characteristic of fan incl. cooler

Parameter	Value	Description
H_{alt}	4100	Altitude [m]
$C_{s,ele}$	0.97	Lamination stacking factor
$A_{Fe,r}$	$179.90 \cdot 10^{-3}$	Cross-section area of the iron part of one rotor pole [m ²]
$A_{Fe,s}$	9.6548	Cross-section area of the iron part of the stator [m ²]
$A_{Cu,r}$	$26.060 \cdot 10^{-3}$	Cross-section area of the copper part of one rotor pole [m ²]
$A_{Cu,s}$	$0.9866 \cdot 10^{-3}$	Cross-section area of the copper part of one stator coil pack [m ²]
$A_{Coil,r}$	$28.254 \cdot 10^{-3}$	Cross-section area of the coil packs in one rotor pole [m ²]
$A_{Coil,s}$	$1.728 \cdot 10^{-3}$	Cross-section area of one coil pack in the stator
L_{motor}	1.250	Axial length of the motor [m]
T_{ini}	36.4	Initial temperature after the cooler [°C]
n_{poles}	60	Number of poles [-]
n_{slots}	504	Number of slots [-]

Table A.4: Fluid flow model - General parameters

References

- [1] L. Nieto, M. Ahrens, Gearless mill drive protection improvements and its behaviour at minera escondida ltda., in: IEEE Industry Applications Annual Meeting, 2007, pp. 1766–1772.
- [2] A. Boughey, V. Svalbonas, S. M. Jones, Supply, installation & commissioning of the worlds largest grinding mill, Society for Mining, Metallurgy and Exploration - SME annual meeting - CD rom edition (2000) 00–7.
- [3] R. Hamdani, Ball mill driven with gearless mill drive, IEEE Cement Industry Technical Conference (May) (2000) 55–68.
- [4] J. Nerg, M. Rilla, J. Pyrhönen, Thermal analysis of radial-flux electrical machines with a high power density, IEEE Transactions on Industrial Electronics 55 (10) (2008) 3543–3554.
- [5] M. Galea, C. Gerada, T. Raminosa, A thermal improvement technique

- for the phase windings of electrical machines, *IEEE Transaction on Industry Applications* 48 (1) (2012) 79–87.
- [6] P. H. Mellor, D. Roberts, D. R. Turner, Lumped parameter thermal model for electrical machines of TEFC design, *IEE proceedings-B* 138 (1991) 205–218.
- [7] D. Staton, A. Boglietti, A. Cavagnino, Solving the more difficult aspects of electric motor thermal analysis, *Electric Machines and Drives Conference, IEMDC'03. IEEE International* 2 (2003) 747–755.
- [8] N. Bracikowski, M. Hecquet, P. Brochet, S. V. Shirinskii, Multiphysics modeling of a permanent magnet synchronous machine by using lumped models, *IEEE Transaction on Industrial Electronics* 59 (6) (2012) 2426–2437.
- [9] O. Drubel, B. Runge, Temperature rise within the rotor of squirrel cage induction machines with solid iron and laminated rotors during run up and standstill, *Electrical Engineering* 86 (2004) 97–103.
- [10] H. D. Baehr, K. Stephan, *Heat and mass transfer*, 3rd Edition, Springer, 2011.
- [11] G. Li, J. Ojeda, E. Hoang, M. Gabsi, M. Lécrivain, Thermal–electromagnetic analysis for driving cycles of embedded flux-switching permanent-magnet motors, *IEEE Transactions on Vehicular Technology* 61 (2012) 140–151.
- [12] K. Srinivas, R. Arumugam, Thermal characterization through finite element analysis of the switched reluctance motor, *Proceedings of IEEE Region 10 International Conference on Electrical and Electronic Technology* (2001) 819–823.
- [13] S. Mezani, R. Ibtouen, R. Kechroud, O. Touhami, Finite element thermal modeling of an induction motor, *Electric Power Components and Systems* 29 (2001) 821–834.
- [14] F. P. Incropera, D. P. DeWitt, T. L. Bergman, A. S. Lavine, *Fundamentals of Heat and Mass Transfer*, 6th Edition, John Wiley & Sons Inc., 2006.
- [15] F. Kreith (Ed.), *The CRC handbook of thermal engineering*, CRC Press, 2000.

- [16] P. Stephan, S. Kabelac, M. Kind, H. Martin, D. Mewes, K. Schaber (Eds.), VDI Heat atlas, 2nd Edition, Springer, 2010.
- [17] C. Jungreuthmayer, T. Bäuml, O. Winter, M. Ganchev, H. Kapeller, A. Haumer, C. Kral, Heat and fluid flow analysis of an internal permanent magnet synchronous machine by means of computational fluid dynamics, IEEE International Electric Machines & Drives Conference (IEMDC) (2011) 515–520.
- [18] R. W. Fox, A. T. McDonald, P. J. Pritchard, Introduction to Fluid Mechanics, 6th Edition, John Wiley & Sons Inc., 2004.
- [19] F. M. White, Fluid Mechanics, 4th Edition, McGraw-Hill, 1998.
- [20] D. Meeker, Rotating losses in a outrunner doubly salient permanent magnet generator, <http://www.femm.info/wiki/CoreLossCalculation> (2009) 1–11.
- [21] E. Dlala, Comparison of models for estimating magnetic core losses in electrical machines using the finite-element method, IEEE Transactions on Magnetics 45 (2) (2009) 716–725.
- [22] G. Bertotti, General properties of power losses in soft ferromagnetic materials, IEEE Transactions on Magnetics 24 (1) (1988) 621–630.
- [23] Y. Chen, P. Pillay, An improved formula for lamination core loss calculations in machines operating with high frequency and high flux density excitation, Industry Applications Conference, 2002. 37th IAS Annual Meeting 2 (2002) 759–766.
- [24] N. Zhao, Z. Q. Zhu, W. Liu, Rotor eddy current loss calculation and thermal analysis of permanent magnet motor and generator, IEEE Transactions on Magnetics 47 (2011) 4199–4202.
- [25] M. Bouheraoua, N. Benamrouche, A. Bousbaine, A more refined thermal model for a totally enclosed fan-cooled induction motor, Electric Power Components and Systems 40 (2012) 179–194.
- [26] I. Grinbaum, Loss, flow and temperature distribution in GMD, internal report RMBP 2.47.2 on 2012-03-30, Tech. rep., ABB Switzerland Ltd. (2012).
- [27] D. Bermudez, GMD fluid flow and temperature calculation program, in-house software, ABB Switzerland Ltd. (2012).

- [28] H. U. Wurgler, The world's first gearless mill drive, *IEEE Transactions on Industry and General Applications* IGA-6 (5) (1970) 524–527.
- [29] S. B. Andersen, I. F. Santos, A. Fuerst, Investigation of model simplification and its influence on the accuracy in FEM magnetic calculations of gearless drives, *IEEE Transactions on Magnetics* 10.1109/TMAG.2012.2185705.
- [30] Surahammars Bruks AB, SURA - M400-50A material datasheet (2009).
- [31] A. Veltman, D. W. Pulle, R. W. D. Doncker, *Fundamentals of Electrical Drives*, Springer, 2007.
- [32] S. Beck, R. Collins, *Moody diagram*, university of sheffield (2008).
- [33] I. Filippov, *Fundamental of heat exchange in electrical machines*, Energija Leningrad, 1974.

DTU Mechanical Engineering
Section of Solid Mechanics
Technical University of Denmark

Nils Koppels Allé, Bld. 404
DK- 2800 Kgs. Lyngby
Denmark
Phone (+45) 4525 4250
Fax (+45) 4593 1475
www.mek.dtu.dk
ISBN: 978-87-90416-95-9

DCAMM
Danish Center for Applied Mathematics and Mechanics

Nils Koppels Allé, Bld. 404
DK-2800 Kgs. Lyngby
Denmark
Phone (+45) 4525 4250
Fax (+45) 4593 1475
www.dcam.dk
ISSN: 0903-1685